NLR TECHNICAL PUBLICATION

TP 97482 U

ADAPTATION OF STRUCTURED GRIDS BASED ON WEIGHTED LEAST SQUARES FORMULATIONS

by

R. Hagmeijer

This investigation has been carried out to obtain the degree of Ph.D. from the Delft University of Technology

Division : Fluid Dynamics
Prepared : RH/
Approved : BO/

Completed : 971002
Order number : 526501
Typ. : RH

Summary

Computational grids are used for the discretisation of partial differential equations (PDE's) such that solution of the resulting system of algebraic equations for the discrete values of the dependent variables provides an approximation to the solution of the system of PDE's. When the discretisation of the partial differential equations (PDE's) is fixed, it is the local distribution of grid points, in terms of density and smoothness, that determines the accuracy of the numerical solution. The present thesis deals with adaptation of so-called single-block structured grids with a fixed number of grid points, as a tool to provide automatic control over the distribution of these grid points.

The thesis consists of four parts:

- In the first part the so-called *Equidistribution Principle* is introduced which forms the basis for the grid adaptation techniques developed. After a brief discussion on grid quality the literature is reviewed on existing techniques and the thesis objectives are formulated.
- The second part contains the theoretical background:
  - The one-dimensional equidistribution principle is reviewed and cast in two different variational formulations to interpret the function of this principle.
  - An extension of the equidistribution principle to three dimensions is developed. One of the variational formulations of the one-dimensional equidistribution principle is extended to a Weighted Least Squares formulation suitable for problems in more dimensions. It is shown that four well-known grid adaptation methods from the literature can be cast into this extended formulation. These methods are compared and their pro's and con's are identified.
  - The so-called Compound Weighted Least Squares formulation is introduced to eliminate some of the shortcomings that are identified. It is shown that there exist two explicit interpretations of this formulation in terms of applying the equidistribution principle in each dimension. For two-dimensional problems an invertibility theorem is presented that shows that the adapted grid is non-overlapping. Such a theorem does not exist for most methods presented in the literature.
- The third part contains the application of the developed theory to two- and three-dimensional aerodynamic problems.
  - The theoretical results of the second part are used to develop a robust and powerful grid adaptation algorithm suitable for the computation of viscous compressible flow in two dimensions. A considerable effort is put into the specification of the weight functions in the adaptation equations, the adaptation of highly stretched grid cells that occur in boundary layers, and the solution of problems that arise when a structured

grid is connected to itself as occurs in so-called C-topology grids. The algorithm is demonstrated by application to computations of the flow around two different airfoils.

- A similar development is described to obtain a grid adaptation algorithm suitable for the computation of viscous compressible flow in three dimensions. The algorithm is applied to a variety of 3D aerodynamic problems including a transonic wing, a transonic wing-body combination, a delta wing, and a rocket-propelled space vehicle.

- The fourth part contains the summary and the conclusions of the present study.

Acknowledgements

The research presented in this thesis would not have been possible without the support of a large number of people and organizations.

I express my sincere gratitude to Prof.dr.ir. H.W.M. Hoeijmakers, as my promotor, for reading the successive parts and versions of the manuscript carefully, and giving me strong support by means of comments, suggestions and encouragements. I have enjoyed the numerous discussions we had over the past years on the subject of the thesis, which, time after time, gave me new momentum to carry on with the work. His support explicitly contributed to the quality and completeness of this thesis.

I am very grateful to my wife Monique who continuously supported me both mentally and physically (thanks for the great catering!) over more than six years. She was always willing to celebrate with me when I sometimes exclaimed that I just had invented a wonderful and new idea, while at the same time she would comfort me in the event that I would return ten minutes later having discovered that something was wrong with the invention.

There is a number of people that I thank for their contribution to this thesis:

- Ir. K.M.J. de Cock for his enthusiasm and constructive cooperation during the initial year of the work;
- Dr.ir. F.J. Brandsma for his support with the airfoil calculations with the MUTU2D code, and for the cooperation on the subject of delta wings,
- Ir. A.K. Poortman for his work on the RAE2822 and NLR8602 airfoil and the numerous interesting discussions;
- Dr. B. Oskam, head of the Theoretical-Aerodynamics department of NLR, for his general support and his critical comments on my manuscript of the article published in *Journal of Computational Physics*;
- Prof.dr. Ph. Clément and Dr.ir. G. Sweers of the Department of Pure Mathematics of the Delft University of Technology, for the extremely constructive and enjoyable cooperation on the article published in *Numerische Mathematik*; it was a real pleasure to work in such an open, inspiring and interdisciplinary atmosphere;
- Ir. F. Ernst for his work on an initial-grid generator;
- Ir. J.C. Kok for his constructive cooperation and fruitful discussions on the subject of 3D flow-calculations for wings;
- my fellow researchers from all over Europe that participated within the EUROMESH and ECARP projects of the CEC BRITE-EURAM programme, for the numerous technical discussions and presentations;

- Dr.ir. J.J.W. van der Vegt for the numerous discussions on grid adaptation;
- the ENFLOW-team (Prof.dr.ir. J.W. Boerstoel, Dr.ir. S.P. Spekreijse, Ing. A. Kassies and Ir. J.C. Kok) for the use of the ENFLOW flow-simulation system for all 3D flow calculations.

Finally I thank a number of organizations:

- the National Aerospace Laboratory NLR, as my employer, for the use of its computer-network and the possibility to work on this thesis during non-standard hours, and also for the possibility to include work in this thesis that was partially funded by NLR (BRITE/EURAM and the 1995-1996 VKI Lecture Series Programme),
- the Commission of the European Communities CEC for the possibility to include work that was partially funded by the CEC within:
  (i) the BRITE/EURAM 1042 EUROMESH project, Contract Number AERO.0018.C(H), and
  (ii) the BRITE/EURAM ECARP project, Contract Number AERO-CT92-0031;
- the Netherlands Agency for Aerospace Programmes NIVR, for the possibility to include work on delta-wings in this thesis, performed by NLR within the framework of the European collaborative programme WEAG-TA15;
- the European Space Agency ESA, for the possibility to include work in this thesis that was funded by ESA within "Technology Developments in Aerothermodynamics for Reusable Launchers", as part of the FESTIP programme;
- the Von Karman Institute for Fluid Dynamics VKI for the possibility to include work, partially funded by VKI, that was part of the "27th Computational Fluid Dynamics" course in the 1995-1996 VKI Lecture Series Programme.

Contents

4 Tables
79 Figures

(164 pages in total)

This page is intentionally left blank.

1 Introduction

This chapter contains a general introduction on the subject of grid adaptation. A major part of the material included has been presented previously during the "27th Computational Fluid Dynamics"-course of the 1995-1996 Lecture Series Programme of the Von Karman Institute for Fluid Dynamics (Refs. [30] and [31]).

Computational grids are used for the discretisation of partial differential equations (PDE's) such that solution of the resulting system of algebraic equations for the discrete values of the dependent variables provides an approximation of the solution of the (system of) PDE's. The accuracy of the numerical solution depends on:

1. the computational method used,
2. the computational grid, and
3. the solution itself.

The computational method determines which derivatives appear in the truncation error of the discretised PDE's while the computational grid and the solution itself determine the magnitude of derivatives.

Let for example the function $x(\xi)$ define a non-uniform grid in one-dimensional physical space as the image of a uniform grid in one-dimensional computational space:

$$x_i = x(\xi_i), \quad i = 1, ..., N; \quad \xi_i = i/(N-1). \tag{1}$$

An approximation of the first derivative of a function $f(x)$ with respect to x is:

$$f_x = f_\xi \xi_x = f_\xi / x_\xi = \frac{f_{i+1} - f_{i-1}}{x_{i+1} - x_{i-1}} + T.E. \tag{2}$$

The truncation error $T.E.$ is $O((N-1)^{-2})$ and the leading term in the $T.E.$ is a function of higher order derivatives of $x(\xi)$ with respect to ξ and $f(x)$ with respect to x, i.e., a function of both the computational grid as well as the solution.

That the solution of the problem at hand is incorporated in the truncation error prohibits *a priori* tuning of the grid point locations other than:

- global refinement by increasing the number of nodes in each direction,

- increasing the node density locally in regions of high surface curvature,
- increasing the node density locally in regions of geometry discontinuities
- for viscous flows, increasing the node density locally in regions near solid walls,
- tuning to an estimate of the flow solution obtained from experience or from theory.

As an alternative a typical computation could start on a given initial grid and during the course of the flow computation the grid could be adjusted to the developing flow solution. This explicitly illustrates the subject of the present thesis: Adaptation of the computational grid simultaneously or quasi-simultaneously with the flow solution with the goal to increase the computational accuracy. This approach implies that the result of the numerical simulation is not only the discrete flow solution but also the location of the grid points. The location of the grid points is such that the flow solution will be smoothly distributed over the grid points. The consequence is that for each flow condition the grid is different.

The present thesis deals with adaptation of so-called single-block structured grids. A single-block structured grid is defined as the image of a uniform grid in $[0, 1]^n$ ($n = 1$ denotes the unit interval, $n = 2$ denotes the unit square and $n = 3$ denotes the unit cube) under a given regular map to the physical domain, see Fig. 1. By a regular map we mean that it is continuous, one-to-one and

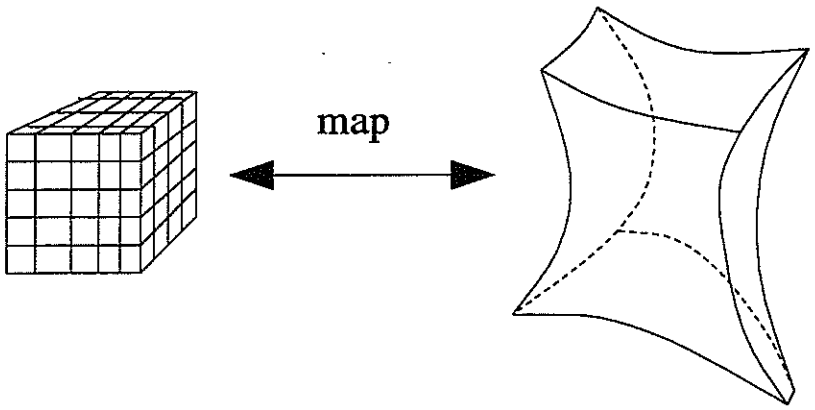

Fig. 1 Definition of single-block structured grid.

invertible. Structured grid adaptation can not be carried out by local addition or subtraction of grid points since this would destroy the structure of the grid. Global addition or subtraction of grid points is indeed possible by simply changing the grid dimensions, but is not very efficient. If the flow solution requires local refinement of the grid then global refinement would add also points in other locations. The alternative is grid point movement. If local grid refinement is required the grid could be arranged such that locally points are moved towards the particular spot,

while some distance away grid points stay at almost fixed positions. Grid adaptation by point (node) movement is less efficient and effective than local grid refinement possible with so-called unstructured grids (see e.g. Refs. [69], [70], [71]). A large class of modern CFD methods for viscous high-Reynolds-number flows, however, is based on discretisation of the Navier-Stokes equations on **structured** grids incorporating highly stretched cells, typically with aspect ratios of 1:1000 or 1:10,000. This is the motivation to put effort in the development of grid adaptation methods based on node movement within structured grids.

A basic concept for the generation and adaptation of structured grids is to identify grid lines (in 2D) and grid surfaces (in 3D) as iso-lines and iso-surfaces of scalar functions that are defined in the physical domain. Figure 2 shows an example of two families of iso-lines in the unit square, each corresponding to a different scalar function. The points of the structured grid are subsequently constructed as the intersections of these two families of iso-lines. From this concept it is straightforward to define:

Adaptation of structured grids is equivalent to adaptive construction of scalar functions over the physical domain.

1.1 One-dimensional Equidistribution Principle

In one-dimensional problems an adaptive grid consists of a number of points along the coordinate axis with the point distribution tuned to the solution of the problem. The goal of the adapted grid is to provide a set of points that is most suitable for discretisation of the equations that govern the problem. The use of finite-differences introduces a truncation error which depends on both the grid and the solution of the problem. To minimise the truncation error one can tune the mesh size to the local behaviour of the solution. Let the variation of the solution be measured in some sense by a strictly positive weight function, then the following *Equidistribution Principle* can be applied:

$$(weight\ \ function) \times (meshsize) = constant$$

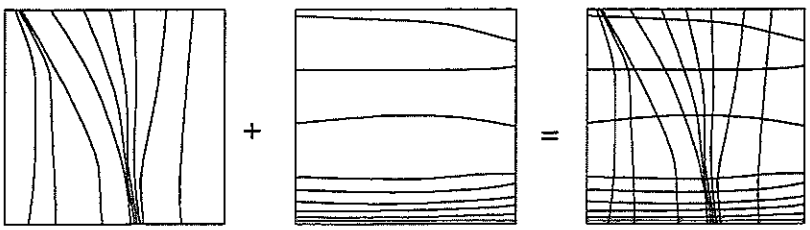

Fig. 2 Two families of iso-lines of two different scalar functions combined into a single computational grid.

As a result the mesh size will be small where the weight function is large and, vice versa, the mesh size will be large where the weight function is small. This principle plays a key role in the development of many adaptation methods not only for one-dimensional problems, but also for multi-dimensional problems.

Mathematically the equidistribution principle can be formulated as:

$$w(x)x_\xi = constant, \tag{3}$$

where $x(\xi) : [0,1] \mapsto [0,L] \in \mathcal{R}$ is the map that defines the grid and $w(x) : [0,L] \in \mathcal{R} \mapsto D \in \mathcal{R}^+$ is the weight function. Once the adaptive map $x(\xi)$ is obtained by solving Eq. (3) the adaptive grid is constructed as the image of a uniform grid on the unit interval under the map $x(\xi)$, see Eq. (1). Examples of weight functions incorporating first and/or second derivatives of the solution are presented and discussed by Thompson [65]. One of these examples concerns the following weight function:

$$w(x) = \sqrt{1 + f_x^2}, \tag{4}$$

where $f(x)$ is the problem solution of the one-dimensional problem. It is easily verified that substitution of $w(x)$ given by Eq. (4) into the equidistribution principle (3) yields:

$$\sqrt{x_\xi^2 + f_\xi^2} = constant, \tag{5}$$

meaning that grid points are equally distributed over the graph $(x, f(x))^T$. In case $f(x)$ is a monotonically increasing function of x, another interesting possibility is to take:

$$w(x) = f_x. \tag{6}$$

It is again easily verified that substitution of $w(x)$ given by expression (6) into the equidistribution principle (3) yields:

$$f_\xi = constant, \tag{7}$$

meaning that f has become a linear function of ξ.

Eiseman [21] presents a dozen ways to formulate the equidistribution principle, ranging from the differential statement given by Eq. (3) to variational statements. We will select a few of these formulations that are representative for many adaptation methods found in the literature, see Fig. 3.

- Evolutionary Statement

$$\frac{\xi_i^{k+1}}{\langle w \rangle^i} = \frac{1}{2}\left(\frac{\xi_{i-1}^k}{w^{i-\frac{1}{2}}} + \frac{\xi_{i+1}^k}{w^{i+\frac{1}{2}}}\right); \quad \frac{1}{\langle w \rangle^i} = \frac{1}{2}\left(\frac{1}{w^{i-\frac{1}{2}}} + \frac{1}{w^{i+\frac{1}{2}}}\right), \tag{8}$$

- Finite-Difference Statement

$$\frac{\xi_{i+1} - \xi_i}{w^{i+\frac{1}{2}}} - \frac{\xi_i - \xi_{i-1}}{w^{i-\frac{1}{2}}} = 0, \tag{9}$$

- Differential Statement

$$\frac{d}{dx}\frac{\xi_x}{w} = 0, \tag{10}$$

- Variational Statement I

$$minimise \quad K[\xi] = \frac{1}{2}\int_\Omega \frac{\xi_x^2}{w} dx, \tag{11}$$

- Variational Statement II

$$minimise \quad F(\xi_1, ..., \xi_N) = \frac{1}{2}\sum_i \frac{(\xi_{i+1} - \xi_i)^2}{w^{i+\frac{1}{2}}}. \tag{12}$$

All of these statements are related to each other as is illustrated in Fig. 3. Starting from Variational Statement I we have two possibilities: either we discretise the integral and obtain Variational Statement II, or we derive the Euler-Lagrange equation associated with Variational Statement I and arrive at the Differential Statement. The Finite-Difference Statement is obtained by either discretising the Differential Statement or derive the zero-gradient condition to satisfy the Variational Statement II. Finally the Evolutionary Statement is obtained by applying the Jacobi iteration technique to the Finite-Difference Statement.

1.2 Extension to two dimensions

In view of the observation that grid generation or adaptation in two and three dimensions can be considered as the construction of suitable scalar functions, see Fig. 2, the objective of the present section is to:

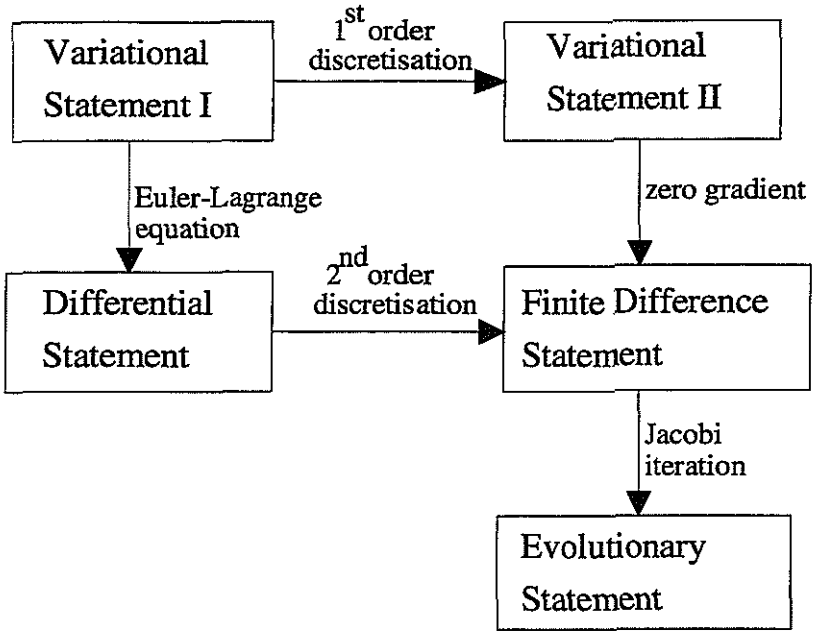

Fig. 3 Relations between various formulations of the equidistribution principle.

Find computational coordinates $\xi(x,y)$ and $\eta(x,y)$ such that iso-ξ and iso-η contours projected on the physical domain form a smooth grid that is adapted to some given scalar function, say $\rho(x,y)$.

For simplicity, but without loss of generality, we assume for the moment that the physical domain, say Ω, is the unit square and that the initial grid is a uniform grid with square cells. Like the formulation of the one-dimensional equidistribution principle we can give a number of statements for the generation of an adapted grid in Ω:

- Evolutionary Statement

$$\frac{\xi_{ij}^{k+1}}{\langle w \rangle^{ij}} = \frac{1}{4}\left(\frac{\xi_{i-1,j}^{k}}{w_1^{i-\frac{1}{2},j}} + \frac{\xi_{i,j-1}^{k}}{w_2^{i,j-\frac{1}{2}}} + \frac{\xi_{i+1,j}^{k}}{w_1^{i+\frac{1}{2},j}} + \frac{\xi_{i,j+1}^{k}}{w_2^{i,j+\frac{1}{2}}}\right), \quad \xi \equiv (\xi,\eta)^T, \tag{13}$$

with

$$\frac{1}{\langle w \rangle^{ij}} = \frac{1}{4}\left(\frac{1}{w_1^{i-\frac{1}{2},j}} + \frac{1}{w_2^{i,j-\frac{1}{2}}} + \frac{1}{w_1^{i+\frac{1}{2},j}} + \frac{1}{w_2^{i,j+\frac{1}{2}}}\right), \tag{14}$$

- Finite-Difference Statement

$$\frac{\xi_{i+1,j}-\xi_{i,j}}{w_1^{i+\frac{1}{2},j}}-\frac{\xi_{i,j}-\xi_{i-1,j}}{w_1^{i-\frac{1}{2},j}}+\frac{\xi_{i,j+1}-\xi_{i,j}}{w_2^{i,j+\frac{1}{2}}}-\frac{\xi_{i,j}-\xi_{i,j-1}}{w_2^{i,j-\frac{1}{2}}}=0 \tag{15}$$

- Partial Differential Statement

$$\frac{\partial}{\partial x}(\frac{\xi_x}{w_1})+\frac{\partial}{\partial y}(\frac{\xi_y}{w_2})=0, \quad \frac{\partial}{\partial x}(\frac{\eta_x}{w_1})+\frac{\partial}{\partial y}(\frac{\eta_y}{w_2})=0, \tag{16}$$

- Variational Statement I

$$K[\xi,\eta]=\frac{1}{2}\int_\Omega\{\frac{\xi_x^2}{w_1}+\frac{\xi_y^2}{w_2}+\frac{\eta_x^2}{w_1}+\frac{\eta_y^2}{w_2}\}d\Omega, \tag{17}$$

- Variational Statement II

$$F(\xi_{i,j};i=1,..,N;j=1,...,N)=$$

$$\frac{1}{2}\sum_i\sum_j\{\frac{\|\xi_{i+1,j}-\xi_{i,j}\|^2}{w_1^{i+\frac{1}{2},j}}+\frac{\|\xi_{i,j+1}-\xi_{i,j}\|^2}{w_2^{i,j+\frac{1}{2}}}\} \tag{18}$$

Note that if the two weight functions are both identical to one, each of the above formulations represents the Laplace equations for both ξ and η.

It was noted by Thompson [65] that, if the grid is determined by PDE's, we need an appropriate grid to obtain the solution of the computational coordinates $(\xi,\eta)^T$ as functions of the physical coordinates $(x,y)^T$ on a general 2D domain. To construct such a grid we need in turn to solve PDE's: hence we have arrived at an "chicken or egg" problem (who was first?). To circumvent this problem Thompson proposed to interchange the roles of the dependent and independent variables. As a consequence the equations for x and y as functions of ξ and η have to be solved on the rectangular computational domain. The grid in the computational domain is simply uniform. Thompson evaluated this approach for the Poisson equations:

$$\nabla^2\xi=P(x,y), \quad \nabla^2\eta=Q(x,y), \tag{19}$$

which can be transformed into (summation convention):

$$g^{ij}\frac{\partial^2\mathbf{x}}{\partial\xi^i\partial\xi^j}+P_k\frac{\partial\mathbf{x}}{\partial\xi^k}=0, \tag{20}$$

where $\mathbf{x} = (x, y)^T$, $\xi^1 = \xi$, $\xi^2 = \eta$, $P_1 = P$, and $P_2 = Q$, and g^{ij} is the contravariant metric tensor (summation convention):

$$g^{ij} = \frac{\partial \xi^i}{\partial x^k} \frac{\partial \xi^j}{\partial x^k}. \tag{21}$$

Note that due to the transformation we have exchanged uncoupled linear PDE's (19) for coupled quasi-linear PDE's (20).

While for the initial grid the above described transformation is necessary to generate the grid points, the situation for grid adaptation is quite different since an initial grid is then already present, which can be used to solve the grid adaptation equations. Furthermore, weight functions that are involved in the grid adaptation process are functions of the physical coordinates $(x, y)^T$, e.g., containing the density gradient. Hence when the grid adaptation equations are transformed and solved for the physical coordinates as functions of the computational coordinates then evaluation of the weight functions $w(x, y)$ at the updates of the points in physical space requires interpolation of the flow solution at every iteration. Therefore it is beneficial to solve the linear equations directly for the computational coordinates $(\xi, \eta)^T$ as functions of the physical coordinates $(x, y)^T$ and to invert the resulting map numerically to obtain the physical coordinates as functions of the computational coordinates afterwards. This is illustrated in the next chapters of this thesis.

1.3 Grid quality

In the first section of this chapter it is pointed out that the accuracy of the flow solution calculated on a computational grid depends on the characteristics of that grid and on the characteristics of the flow field. Hence the quality of a grid can only be discussed in view of the flow field that is calculated on it. Actually one wants to control the error of the numerical flow solution compared to the exact flow solution. But since the exact flow solution is unknown a priori, one can try to control the truncation error of the discretisation of the PDE instead and hope that this implies control over the solution error.

Several authors [48], [35], [64], [68], [45], [43], [61] have studied the accuracy of finite-difference schemes on curvilinear meshes. In this section we use the work of Lee and Tsuei [43] to discuss some general characteristics of the truncation error that is introduced when convection terms are discretized on a curvilinear coordinate system:

$$\rho u \frac{\partial f}{\partial x} + \rho v \frac{\partial f}{\partial y} = A + T_E. \tag{22}$$

Here $(\rho u, \rho v)$ is a given density flow-field, A is an approximation of the convection terms and T_E is the associated truncation error. When the first derivatives of the convected property f are discretized using second-order upwind differences and when the first derivatives of x and y with respect to the computational coordinates ξ and η are discretised using second-order central differences then the truncation error can be expressed as:

$$T_E = T_{E1} + T_{E2} + T_{E3}. \tag{23}$$

T_{E1} contains all terms with first derivatives of f with respect to x, e.g. $x_{\xi\xi\xi} f_x$, T_{E2} contains all terms with second derivatives of f with respect to x, e.g. $x_\xi x_{\xi\xi} f_{xx}$, and T_{E3} contains all terms with third derivatives of f with respect to x, e.g. $x_\xi^3 f_{xxx}$.

Lee and Tsuei [43] draw a number of conclusions from their study:

(i) Reducing the grid size locally by altering the function $x(\xi)$ does not ensure error reduction since if the number of grid points is fixed T_{E1} is independent of local grid size. Increasing the smoothness of the grid will reduce T_{E2} which is the leading term in the truncation error (first-order of accuracy in terms of the physical grid size). Orthogonality is not a must to eliminate T_{E2} while in the limit of a uniform parallel grid T_{E2} is eliminated. Both grid uniformity and grid orthogonality do not affect T_{E3}.

(ii) If the grid lines are aligned with the velocity vector, many terms in T_{E2} and T_{E3} will become zero.

(iii) Test problems show that grid orthogonality does not guarantee truncation error reduction, since in general the optimal grid arrangement is strongly dependent on the flow field.

Reduction of the local truncation error induced by discretisation of the PDE's at hand can be used to reduce the error in the numerical flow solution. The success of this strategy however depends on the local condition of the PDE's. In not-well conditioned cases sufficient reduction of the solution error may require extremely small truncation errors. For the aerodynamicist it is important that global coefficients like lift, drag and pitching moment are accurately predicted. This requires that the global accuracy of the numerical flow solution must be sufficient. For the more critical flow conditions the aerodynamicist also requires accurate predictions of local characteristics like surface pressure and skin friction distributions, location of flow separation and transition.

In the present thesis we do not define grid quality in terms of truncation errors since the evaluation would be excessively complex for the Navier-Stokes equations. A measure for the accuracy of the numerical flow solution with respect to the exact flow field cannot be used since exact solutions are not known in general. Therefore we assess the grid quality by comparison of results obtained

on adapted grids with results obtained on globally refined grids and with results obtained from measurements in physical experiments.

1.4 Survey of the literature

In this section we present a number of grid adaptation examples from the literature published primarily during the last six years. It is noted that this is by no means an extensive overview, and we refer to the excellent overviews of Thompson [62], Eiseman [21], [22], [23], Thompson and Weatherill [66] and the recent one by Baker [2]. For general theory on grid generation the reader is referred to the text books of Thompson, Warsi and Mastin [65], and Knupp and Steinberg [42], and the paper on variational formulations by Warsi and Thompson [72].

Concepts The evolutionary approach has been exploited amongst others by Eiseman et al., e.g. [24], and Pao and Abdol-Hamid [50]. They use the alternate direction adaptation approach which is convenient for dynamic adaptation (closely coupled to each iteration of the flow computation). Eiseman [20], and Connett et al., e.g. [15], use the concept of prescribing a displacement for each node based on its position with respect to the surrounding nodes. Benson and McRae [5] use a parametric domain to adapt the grid points based on movement towards a center of "mass".

The finite-difference approach has been exploited amongst others by Nakahashi and Deiwert [49]. They use a tension and torsion spring analogy and solve the system of equations to minimise the potential energy in the spring system.

Within the PDE formulation the adaptation approach of Kim and Thompson [40] is a practical extension of the widely used elliptic grid generation approach of Thompson [63]. Eiseman [21] shows that the PDE formulation is a subset of the PDE formulation that is obtained from the extension to adapted grids of the variational formulation of the Laplace equations. Adaptation is achieved by including weight functions in the control functions (the source terms) of the Poisson system. The weight functions measure the gradients of the flow solution. In references [46] and [58] the implementation of these concepts into industrial grid generation systems is demonstrated. Lee and Loellbach, e.g. [44], use a parametric domain and adapt the points in response to source potentials. The parametric map is based on the initial grid. After adaptation the points are mapped back to the physical space. Another interesting PDE approach is described by Catherall [12] who developed a mixture of PDE's called the LPE system, using a weighted sum of Laplace, Poisson and Equidistribution equations. In this way user-defined control is obtained over smoothness, deviation from the initial grid and over adaptation.

Within the class of variational methods one has the functional presented by Winslow [74] which consists of the integration of the weighted gradients of the computational coordinates. The adaptation algorithm is isotropic because a single weight function is used.

The functional proposed by Eiseman [21] is an extension of the Winslow functional incorporating a different weight function for each coordinate direction enabling anisotropic adaptation.

Brackbill and Saltzman [9] developed a composite functional as the weighted sum of three separate functionals accounting for smoothness, orthogonality and adaptivity, respectively. This results in fairly complex PDE's but enables explicit control over these three grid quality properties that influence the discretisation errors in the flow solution.

Also very interesting is the functional developed by Jaquotte, e.g., [37], which resembles the deformation of elastic material. While direct minimisation of this functional may require considerable computational effort, the recently exploited approach of Coussement [18] based on the solution of the associated Euler-Lagrange equations is promising.

Dvinsky [19] introduced the minimisation of an 'energy' integral resembling the smooth distribution of a grid over the graph of a monitor surface. This can be interpreted as a solution of the Laplace equation on the monitor surface described by the Laplace-Beltrami equations. Extension of this method to multiple monitor surfaces has been explored by Spekreijse et al. [60].

Finally a functional enabling anisotropic grid adaptation has been proposed by the present author et al. [28], [27], [29] which is extensively discussed in the remaining part of this thesis.

Applications for 3D Euler Some adaptation results for 3D structured grids suitable for solution of the Euler equations have been presented in [40], [67], [13] and [51]. Kim and Thompson [40] compared their control function (Poisson) approach to the variational approach of Brackbill and Saltzman [9] by application on a 3D grid around the ONERA M6 wing. Their conclusion is that both approaches have basically the same potential but the control function approach should be the more promising tool due to shorter computing times and higher sensitivity to the flow solution. Tu and Thompson [67] apply the control function approach within the EAGLE 3D code to an eight-block finned body of revolution at transonic speeds, obtaining an improved quality of the aerodynamic simulation. Catherall [13] and Le Pape et al. [51] obtain adaptive solutions for the ONERA M6 wing with the LPE method [12] and the Jaquotte functional [37] respectively showing adaptation with respect to the λ shock on the upper wing surface and improved resolution at the leading edge.

Applications for 2D Navier-Stokes Some adaptation results for 2D structured grids suitable for solution of the Navier-Stokes equations have been presented in [47], [41], [57], [33] and [28]. Luong, Thompson and Gatlin [47] show applications of the control function approach [40] for two low-Reynolds-number flows; a backward-facing step and a turnaround duct. Klopfer [41] presents some impressive results for a hypersonic high-Reynolds-number flow over a cylinder with an impinging shock introducing shock-shock and shock/boundary-layer interactions. Klopfer uses a hyperbolic grid adaptor which is possible because the grid away from the cylinder is free to move. Slater, Liou and Hindman [57] show a strong coupling between flow solver and grid adaptor resulting in dynamic adaptation. They apply their method, based on the Brackbill and Saltzman equations [9], to a supersonic high-Reynolds-number shock/boundary-layer interaction. Finally Hall and Zing [33] present adaptive viscous airfoil computations using the control function approach formulated by Eiseman [21]. Compared to grid independent flow solutions they succeed to improve significantly on the accuracy of the aerodynamic coefficients. The results of Hagmeijer [28] for the RAE2822 airfoil are discussed in detail in chapter 5.

Applications for 3D Navier-Stokes Some adaptation results for 3D structured grids suitable for solution of the Navier-Stokes equations have been presented in [36],[39],[6],[34] and [29]. Harvey, Acharya and Lawrence [36] apply the tension and torsion spring analogy of Nakahashi and Deiwert [49] to the hypersonic high-Reynolds-number flow calculation over a cone. Kania [39] shows results obtained with an 3D extension of the 2D method of Connett et al. [15] for the supersonic high-Reynolds-number flow over a blunted cone and the transonic high-Reynolds-number flow over a fuselage forebody. Bockelie and Smith [6] show results for hypersonic high-Reynolds-number flow over a re-entry body using a multi-phase alternate direction algorithm. Henderson, Huang, Lee and Choo [34] use the method developed by Lee and Loellbach [44] to adapt grids for the computation of high-Reynolds-number flows over a blunt fin and over the ONERA M6 wing. The results of Hagmeijer and Kok [29] for the ONERA M6 wing are discussed in detail in chapter 5.

1.5 Thesis objectives and overview

The objectives of this thesis are:

- to review one-dimensional adaptation principles,
- to extend these principles to multi-dimensional problems based on variational principles,
- to use the developed theory to obtain robust and useful grid adaptation algorithms for realistic aerodynamic problems,
- to demonstrate the obtained algorithms in applications to realistic aerodynamic problems.

It is recognised that the development of theory is essential for the construction of adaptation algorithms. It is also recognised that the transfer of these algorithms from the level of relatively simple test problems on rectangular or cubic domains to the level of realistic and practical aerodynamic problems requires a significant effort. Hence, both elements are incorporated here.

The thesis consists of four parts:

- In the first part, consisting of the present chapter, the so-called *Equidistribution Principle* is introduced which forms the basis for the techniques developed. After a brief discussion on grid quality the literature is reviewed on existing grid adaptation techniques and the thesis objectives are formulated.
- The second part, consisting of chapters 2,3 and 4, contains the theoretical background:
  - In chapter 2 the one-dimensional equidistribution principle is reviewed and cast in two different variational formulations to interpret the function of this principle.
  - In chapter 3 an extension of the equidistribution principle to three dimensions is developed. One of the variational formulations of the one-dimensional equidistribution principle is extended to a Weighted Least Squares formulation suitable for problems in more dimensions. It is shown that four well-known grid adaptation methods from the literature can be cast into this extended formulation. These methods are compared and their pro's and con's are identified.
  - In chapter 4 the so-called Compound Weighted Least Squares formulation is introduced to eliminate some of the shortcomings that are identified. It is shown that there exist two explicit interpretations of this formulation in terms of applying the equidistribution principle in each dimension. For two-dimensional problems an invertibility theorem is presented that shows that the adapted grid is non-overlapping. Such a theorem does not exist for most methods presented in the literature.
- The third part, consisting of chapters 2,3 and 4, contains the application of the developed theory to two- and three-dimensional aerodynamic problems.
  - In chapter 5 the theoretical results of the second part are used to develop a robust and powerful grid adaptation algorithm suitable for the computation of viscous compressible flow in two dimensions. A considerable effort is put into the specification of the weight functions in the adaptation equations, the adaptation of highly stretched grid cells that occur in boundary layers, and the solution of problems that arise when a structured grid is connected to itself as occurs in so-called C-topology grids. The algorithm is demonstrated by application to computations of the flow around two different airfoils.

- In chapter 6 a similar development is described to obtain a grid adaptation algorithm suitable for the computation of viscous compressible flow in three dimensions. The algorithm is applied to a variety of 3D aerodynamic problems including a transonic wing, a transonic wing-body combination, a delta wing, and a rocket-propelled space vehicle.

- The fourth part, consisting of chapter 7, contains the summary and the conclusions of the present study.

2 Equidistribution Principle

2.1 Introduction

This chapter describes an extensive discussion of the equidistribution principle already mentioned in the introduction. In many articles on grid adaptation in two or three dimensions this principle is cited as having a potential for extension to multiple dimensions [21], [65]. We will derive the equidistribution principle from a variational formulation employing a functional that provides a clear interpretation and reveals the objective of grid adaptation. Two different approaches are presented, both of which describe a map from the one-dimensional interval $[0, L]$ to the auxiliary unit interval $[0, 1]$. The first approach describes the map $x(\xi) : [0, 1] \mapsto [0, L]$ and is called the "direct formulation". The second approach describes the inverse map $\xi(x) : [0, L] \mapsto [0, 1]$ and is called the "inverse formulation". Both approaches are relevant since the direct formulation involves a functional that enables a clear interpretation of the underlying principle and the inverse formulation involves a functional that indicates a convenient way for extension to multiple dimensions.

2.2 Direct Formulation

Let the function to which the grid has to be adapted be $f(x) : [0, L] \mapsto \mathcal{R}$. The objective is to find a map $x(\xi) : [0, 1] \mapsto [0, L]$ such that the adapted grid is constructed as a uniform grid on $[0, 1]$ which is mapped to $[0, L]$ by the map $x(\xi)$. It is assumed that the grid serves to discretise a differential equation of which the function $f(x)$ is a solution.

The differential equation for $f(x)$ can be transformed such that ξ becomes the independent variable. The transformed equation, containing derivatives of $f(x)$ and x with respect to ξ, can be discretised on a uniform grid in ξ. The accuracy of the obtained discretisation strongly depends on the smoothness of the functions $f(x)$ and x with respect to ξ. Therefore it is worthwhile to construct the function $x(\xi)$ such that both $f(x)$ and x become smooth functions of ξ. We will try to construct the function $x(\xi)$ such that the derivatives f_ξ and x_ξ are as close to constants as is possible using the following variational problem:

Variational Problem 2.1 *Find a function* $x(\xi)$: $[0, 1] \mapsto \mathcal{R}$ *and the constants* $a, b \in \mathcal{R}$ *with* $x(0) = 0$ *and* $x(1) = L$ *such that the functional* $K[x(\xi), a, b]$ *is minimised, with* K *given by*

$$K[x(\xi), a, b] = \frac{1}{2} \int_0^1 \{(f_\xi - a)^2 + (x_\xi - b)^2\} d\xi. \tag{24}$$

K can be evaluated by expansion of the quadratic terms and by using the identity $f_\xi = f_x x_\xi$:

$$K[x(\xi), a, b] = \frac{1}{2}\int_0^1 (1 + {f_x}^2) x_\xi^2 d\xi \; - aF \; - bL \; + \frac{1}{2}(a^2 + b^2), \tag{25}$$

where $F = f(L) - f(0)$. Since K is stationary we have:

$$\frac{\partial K}{\partial a} = 0, \quad \Rightarrow a = F; \quad \frac{\partial K}{\partial b} = 0, \quad \Rightarrow b = L, \tag{26}$$

hence a and b are equal to the mean values of f_ξ and x_ξ on the interval $[0, 1]$, respectively. Since the last three terms in Eq. (25) do not depend on $x(\xi)$ the following variational formulation is equivalent with Problem (24) if we are only interested in the map $x(\xi)$:

Variational Problem 2.2 *Find a function* $x(\xi)$*:* $[0, 1] \mapsto \mathcal{R}$ *with* $x(0) = 0$ *and* $x(1) = L$ *such that a functional* $K^*[x(\xi)]$ *is minimised, with* K^* *given by*

$$K^*[x(\xi)] = \frac{1}{2}\int_0^1 w(x)^2 x_\xi^2 d\xi, \quad w(x) = \sqrt{1 + {f_x}^2}. \tag{27}$$

The functional $K^*[x_\xi]$ in Problem 2.2 is one of the functionals suggested by Thompson (ref. [65]).

The Euler-Lagrange (EL) equation associated with the variational problems (24) and (27) is [17]:

$$\frac{\partial}{\partial x} F(x, x_\xi, \xi) - \frac{d}{d\xi}\frac{\partial}{\partial x_\xi} F(x, x_\xi, \xi) = 0, \tag{28}$$

where $F(x, x_\xi, \xi)$ is the integrand of expression (27). Equation (28) can be evaluated to:

$$- w(x)\frac{d}{d\xi}\left(w(x)x_\xi\right) \; = 0, \tag{29}$$

finally leading to the *Equidistribution Principle*:

$$w(x)x_\xi \; = constant. \tag{30}$$

It is noted that Eq.(30) can be evaluated to:

$${x_\xi}^2 + {f_\xi}^2 \; = constant, \tag{31}$$

which expresses that the magnitude of the derivative of the graph $(x, f(x))$ with respect to ξ is constant.

2.3 Inverse Formulation

This section aims at obtaining a variational formulation for the inverse map $\xi(x) : [0, L] \mapsto [0, 1]$ instead of the map $x(\xi)$ itself. This is a relevant topic in relation to extension to three dimensions because in that case three different maps from the three dimensional physical domain to the unit interval are constructed. The combination of these maps provides a map from the physical domain to the unit cube. The following variational formulation is employed:

Variational Problem 2.3 *Find a function* $\xi(x)$: $[0, L] \mapsto [0, 1]$ *and the constant* $c \in \mathcal{R}$ *with* $\xi(0) = 0$ *and* $\xi(L) = 1$ *such that the functional* $K[\xi(x), c]$ *is minimised, with* K *given by*

$$K[\xi(x), c] = \frac{1}{2}\int_0^L (\frac{\xi_x}{w(x)} - c)^2 dx, \quad w(x) = \sqrt{1 + {f_x}^2}. \tag{32}$$

Observation of the integrand shows directly that the solution of the variational problem (2.3) is given by the equidistribution principle (30) which can be written as:

$$\frac{\xi_x}{w(x)} = c, \tag{33}$$

since then $K[\xi(x), c]$ is zero, which is the smallest possible value.

The constant c in (33) is easily derived from the boundary conditions $\xi(0) = 0$ and $\xi(L) = 1$:

$$c = \frac{1}{\int_0^L w(x)\, dx}. \tag{34}$$

Although we have found the solution (33) to variational problem (2.3) directly we should derive the solution more formally from the viewpoint of extension to multiple dimensions. In multiple dimensions it will be impossible to find the solution of the variational problem without solving the EL equation.

We start by employing the equation for the constant c, stating that the first derivative of K with respect to c must be zero:

$$\frac{\partial K}{\partial c} = 0, \quad \Rightarrow c = \frac{1}{L}\int_0^L \frac{\xi_x}{w(x)}\, dx. \tag{35}$$

From this expression it appears that the constant c is a functional of ξ_x and so the EL equations will not be of the relatively simple form that can be found in Courant and Hilbert (ref. [17]).

In order to circumvent this difficulty, again in view of extension of the present variational formulation to the multiple-dimensional problem, it is proposed to multiply the integrand in Eq. (32) with a strictly positive function $\alpha(x)$ which is unknown for the moment. Hence the modified functional becomes:

$$K^*[\xi(x), c] = \frac{1}{2}\int_0^L \alpha(x)\,(\frac{\xi_x}{w(x)} - c)^2 dx. \tag{36}$$

which is still minimised by Eq. (33). But now the equation to determine the constant c becomes:

$$\frac{\partial K}{\partial c} = 0, \quad \Rightarrow c = \frac{\int_0^L \alpha(x)\frac{\xi_x}{w(x)}\,dx}{\int_0^L \alpha(x)dx}. \tag{37}$$

This expression is not a functional of ξ_x if we choose $\alpha(x) \equiv w(x)$:

$$c = \frac{\int_0^L \xi_x\,dx}{\int_0^L w(x)\,dx} = \frac{1}{\int_0^L w(x)\,dx}. \tag{38}$$

Hence our functional K^* becomes:

$$K^*[\xi(x), c] = \frac{1}{2}\int_0^L w(x)\,(\frac{\xi_x}{w(x)} - c)^2 dx. \tag{39}$$

Before determining the EL equation we first evaluate K^* to:

$$K^*[\xi(x), c] = \frac{1}{2}\int_0^L \frac{{\xi_x}^2}{w(x)} dx \; - \frac{1}{2}c. \tag{40}$$

Since the last term does not depend on the map $\xi(x)$ we finally have the following equivalent variational problem formulation if we are only interested in the map $\xi(x)$:

Variational Problem 2.4 *Find a function* $\xi(x)$: $[0, L] \mapsto [0, 1]$ *with* $\xi(0) = 0$ *and* $\xi(L) = 1$ *such that a functional* $K^{**}[\xi_x]$ *is minimised, with* K^{**} *given by*

$$K^{**}[\xi(x)] = \frac{1}{2}\int_0^L \frac{{\xi_x}^2}{w(x)} dx. \tag{41}$$

Functional K^{**} in Problem 2.4 is again one of the functionals proposed by Thompson (ref. [65]).

The Euler-Lagrange (EL) equation associated with the variational problems (39) and (41) is [17]:

$$\frac{\partial}{\partial \xi} G(\xi, \xi_x, x) - \frac{d}{dx} \frac{\partial}{\partial \xi_x} G(\xi, \xi_x, x) = 0, \tag{42}$$

where $G(\xi, \xi_x, x)$ is the integrand in Eq. (41). Eq. (42) can be evaluated to:

$$-\frac{d}{dx}\left(\frac{\xi_x}{w(x)}\right) = 0, \tag{43}$$

finally leading to the equidistribution principle (33).

2.4 Example

To illustrate the effects of the equidistribution erinciple the following scalar function $f(x)$ is employed:

$$f(x) : [0, 1] \mapsto \mathcal{R}^+; \quad f(x) = tanh(10x), \tag{44}$$

which is initially represented on the uniform grid shown in fig. 4a. In fig. 4b x and f are plotted as functions of ξ. The actual adaptation of the uniform grid is obtained by application of the equidistribution principle. Direct integration of Eq. (33) leads to an explicit expression for the inverse map $\xi(x)$:

$$\xi(x) = \frac{\int_0^x w(x)dx}{\int_0^L w(x)dx}, \quad w(x) = \sqrt{1 + f_x^2}, \tag{45}$$

which can be numerically evaluated by using the trapezoidal rule. Finally the map $x(\xi)$ can be obtained by linear interpolation. The resulting plots of x and f as functions of ξ are presented in fig. 4c, which demonstrates the equal distribution of "non-smoothness" over the functions $x(\xi)$ and $f(x(\xi))$ upon adaptation, such that ${x_\xi}^2 + {f_\xi}^2$ is constant (see Eq. (31)). Finally the adapted grid is presented in fig. 4d, which also shows that the grid points are equidistantly distributed along the curve $(x(\xi), f(\xi))$.

2.5 Conclusions

We have presented two different variational formulations of the *Equidistribution Principle* that is used for grid adaptation:

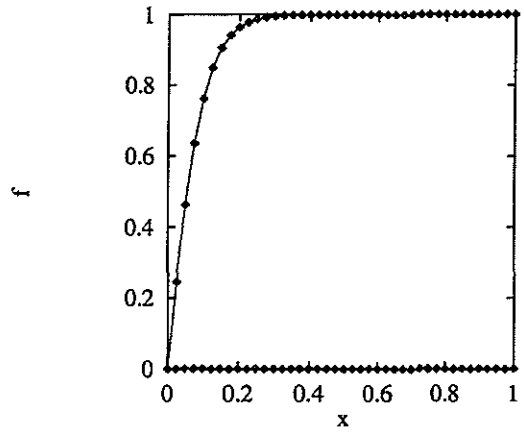

a) $f(x)$ on initial grid.

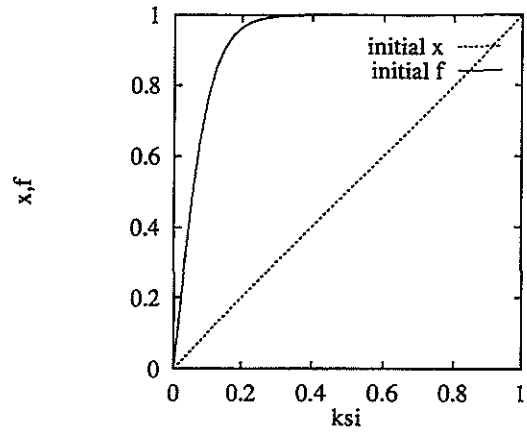

b) Initial $x(\xi)$ and $f(\xi)$.

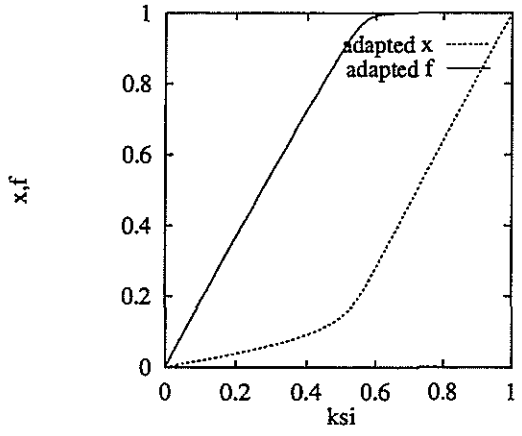

c) Adapted $x(\xi)$ and $f(\xi)$.

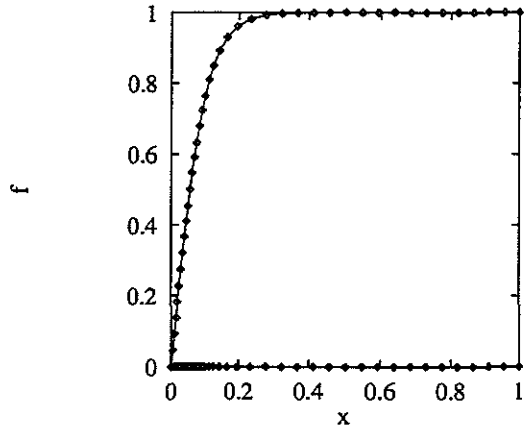

d) $f(x)$ on adapted grid.

Fig. 4 Model problem for equidistribution principle in 1D.

- the *direct formulation* which describes the function $x(\xi)$, and
- the *inverse formulation* which describes the function $\xi(x)$.

Both formulations aim at constructing a map between x and ξ in such a way that both x and $f(x)$ become smooth functions of ξ in the sense that their first derivative with respect to ξ is optimally

close to being constant:

$$x_\xi \approx constant, \quad f_\xi \approx constant.$$

The variational problems both have the same unique solution

$$x_\xi{}^2 + f_\xi{}^2 = constant,$$

expressing that the magnitude of the derivative of the graph $(x, f(x))$ with respect to ξ is constant.

The solution of the variational problems can be written in the more general forms

$$w(x)x_\xi = constant,$$

and

$$\frac{\xi_x}{w(x)} = constant,$$

with

$$w(x) = \sqrt{1 + f_x^2}.$$

These forms show that the products $w(x)x_\xi$ and $\xi_x w(x)^{-1}$ are equally distributed over the unit interval. The equidistribution principle in these forms can also be used with other choices for the weight function $w(x)$, e.g. involving second-order derivatives of f with respect to ξ (e.g. see [65] and [21]).

The inverse formulation is of particular interest here since it enables extension to multiple dimensions which is the subject of the next chapter.

3 Weighted Least Squares Formulation

3.1 Introduction

The present chapter aims at extending the analysis presented in the previous chapter towards a formulation that is suitable for three-dimensional problems. In chapter 2 the objective was to map the interval $[0, L] \subset \mathcal{R}$ to the unit interval $[0, 1] \subset \mathcal{R}$, whereas in this chapter the objective is to map the three-dimensional physical domain $\Omega \subset \mathcal{R}^3$ to the unit cube $[0, 1]^3 \subset \mathcal{R}^3$. Once such a map is constructed, say $\xi(x)$: $\Omega \subset \mathcal{R}^3 \mapsto [0, 1]^3$, the inverse of that map, $x(\xi)$, $[0, 1]^3 \mapsto \Omega \subset \mathcal{R}^3$, can be used to map a uniform rectangular grid in the unit cube to a curvilinear grid in the physical domain Ω.

As a preparation it is first described how the physical domain $\Omega \subset \mathcal{R}^3$ is mapped to the unit interval. This map is based on a weighted least squares (WLS) formulation. Then it is derived how the map of Ω to the unit cube is constructed by combination of three separate maps from Ω to the unit interval. In section 3.3 a number of examples from the literature is discussed cast in the present WLS formulation.

3.2 WLS Formulation

3.2.1 Map of $\Omega \subset \mathcal{R}^3$ to the unit interval

The objective is to construct a map $\phi(x)$ from $\Omega \subset \mathcal{R}^3$ to the unit interval:

$$\phi(\mathrm{x}): \quad \Omega \subset \mathcal{R}^3 \mapsto [0, 1], \tag{46}$$

such that iso-surfaces can be used as one family of coordinate surfaces belonging to a map from $\Omega \subset \mathcal{R}^3$ to the unit cube.

Let the functional $K[\phi]$ be defined on a bounded domain $\Omega \subset \mathcal{R}^3$ with Cartesian coordinates $\mathrm{x} = (x, y, z)^T$:

$$K[\phi] = \frac{1}{2} \int_\Omega \frac{1}{w_j(\mathrm{x})} (\mathrm{h}_j(\mathrm{x}) \cdot \nabla\phi)^2 \, d\Omega, \tag{47}$$

where the Einstein summation convention is applied and $\mathrm{h}_j(\mathrm{x}) \in R^3 \, (j = 1, 2, 3)$ and $\nabla = (\frac{\partial}{\partial x}, \frac{\partial}{\partial y}, \frac{\partial}{\partial z})$. In Eq. (47) $w_j \, (j = 1, 2, 3)$ are bounded, strictly positive, functions of the physical coordinates:

$$w_j(\mathrm{x}): \quad \Omega \in \mathcal{R}^3 \mapsto [\delta, \infty); \quad \delta > 0, \quad j = 1, 2, 3, \tag{48}$$

and it is assumed that the $\mathbf{h}_j(\mathbf{x})\,(j = 1,2,3)$ are nonzero and independent.

Functional K in Eq. (47) can be considered as an extension of the WLS formulation for 1D problems, see functional (41). Functional K^{**} in Eq. (41) includes the derivative of the object function, $\xi(x)$, with respect to the physical coordinate x. As an extension, functional K given by Eq. (47) includes three different components of the gradient of the object function ϕ determined by the vector functions $\mathbf{h}_j(\mathbf{x}), j = 1,2,3$. In addition, the single weight function $w(x)$ incorporated in functional K^{**} (41) is replaced by three separate weight functions $w_j(\mathbf{x})$, $j = 1,2,3$, in functional K given by Eq. (47) to enable anisotropic weighting of the components of the gradient of ϕ.

K can be rewritten in matrix vector notation:

$$K[\phi] = \frac{1}{2}\int_{\Omega}(M\nabla\phi)\cdot\nabla\phi\,d\Omega, \tag{49}$$

where M is a symmetric 3x3 matrix:

$$M = H\,W^{-1}\,H^T, \quad H = (\mathbf{h}_1\,\mathbf{h}_2\,\mathbf{h}_3), \quad W = diag(w_1, w_2, w_3). \tag{50}$$

From Eq. (47) and the assumption that the $\mathbf{h}_j(\mathbf{x})\,(j = 1,2,3)$ are nonzero and independent it follows that the integrand in (49) is positive for any $\nabla\phi \neq 0$. Because M is also real and symmetric, M is positive definite by definition (see e.g. ref. [75]).

Let on a part $\partial\Omega^D \subset \partial\Omega$ the function ϕ be specified:

$$\phi = \phi_0, \quad \mathbf{x} \in \partial\Omega^D, \tag{51}$$

then we will consider the following variational problem:

Variational Problem 3.1 *Find a function* $\phi(\mathbf{x}) : \Omega \subset \mathcal{R}^3 \mapsto \mathcal{R}$ *with* $\phi(\mathbf{x}) = \phi_0(\mathbf{x})$ *for* $\mathbf{x} \in \partial\Omega^D \subset \partial\Omega$ *such that the functional* $K[\phi]$ *given by Eq. (49) is minimised.*

Although we could refer to [17] and immediately state the equations that have to be satisfied by the function ϕ to extremise functional $K[\phi]$ given by Eq. (49), we prefer to present a derivation of these equations to direct attention to the fact that not only the Euler-Lagrange (EL) equation has to be satisfied but also the associated **natural boundary condition**.

Let $\tilde{\phi}$ be an arbitrary function within the class of admissible perturbation functions of the solution ϕ. Then:

$$K[\phi + \varepsilon\tilde{\phi}] = K[\phi] + \varepsilon \int_\Omega (M\nabla\phi) \cdot \nabla\tilde{\phi}\, d\Omega + \varepsilon^2 K[\tilde{\phi}], \quad \varepsilon \in \mathcal{R}. \tag{52}$$

The term that is linear in ε is the first variation of K that can be evaluated using the Divergence Theorem:

$$\int_\Omega (M\nabla\phi) \cdot \nabla\tilde{\phi}\, d\Omega = -\int_\Omega \tilde{\phi}\nabla \cdot (M\nabla\phi)\, d\Omega + \int_{\partial\Omega} \tilde{\phi}\mathbf{n} \cdot (M\nabla\phi)\, d\Gamma. \tag{53}$$

If K is minimised by the function ϕ then the condition

$$\left.\frac{\partial K}{\partial \varepsilon}\right|_{\varepsilon=0} = 0, \tag{54}$$

must be satisfied, hence the first variation (53) must be zero. Since both integrals on the right-hand side of (53) include the arbitrary function $\tilde{\phi}$, both integrals must be zero. The first integral at the right hand side of Eq. (53) is zero for all admissible functions $\tilde{\phi}$ if and only if its integrand is zero, resulting in the Euler-Lagrange (EL) equation (ref. [17]):

$$\nabla \cdot (M\nabla\phi) = 0, \quad \mathbf{x} \in \Omega. \tag{55}$$

Equation (55) is a second-order linear partial differential equation (PDE) which is elliptic since M is positive definite. If the smallest eigenvalue of M has a lower positive bound in Ω, the EL equation is even uniformly elliptic and the extremum principle of Hopf is valid (refs. [75], [53]).

The second integral at the right hand side of Eq. (53) is also zero for all admissible functions $\tilde{\phi}$ if and only if its integrand is zero. On the part $\partial\Omega^D$ of the boundary where ϕ is specified $\tilde{\phi}$ must be identically zero such that the compound function $\phi + \varepsilon\tilde{\phi}$ satisfies the correct boundary condition. On the remaining part $\{\partial\Omega \setminus \partial\Omega^D\}$ $\tilde{\phi}$ is not necessarily zero resulting in the so-called *natural boundary condition* (ref. [17]):

$$\mathbf{n} \cdot (M\nabla\phi) = 0, \quad \mathbf{x} \in \{\partial\Omega \setminus \partial\Omega^D\}, \tag{56}$$

where $\mathbf{n} \in \mathcal{R}^3$ denotes the outward unit normal on $\partial\Omega$. The combined conditions (55) and (56) are sufficient to extremise the functional K. Since M is positive definite the term in Eq. (52) that

is quadratic in ε is non-negative. Hence:

$$K[\phi + \varepsilon\tilde{\phi}] \geq K[\phi] \tag{57}$$

where the equality sign applies if and only if $\varepsilon = 0$. This proves that the stationary point of K is unique and consists of a minimum.

To relate the present analysis to formulations found in the literature the question arises whether it is possible to formulate functional K as a WLS functional in case M is an arbitrary positive definite matrix. Since M is real and symmetric there exists an orthogonal matrix R such that $\Lambda = R^{-1}\, M\, R$ is a diagonal matrix and the column vectors $\mathbf{r}_j\,(j = 1,2,3)$ of R form an orthogonal set of eigenvectors of M (ref. [75]). Because R is orthogonal $R^{-1} \equiv R^T$ and the eigenvectors are orthonormal:

$$\mathbf{r}_i \cdot \mathbf{r}_j = \delta^{ij}, \tag{58}$$

where δ^{ij} is the Kronecker delta. With these relations M can be decomposed:

$$M = R\,\Lambda\,R^T, \quad R = (\mathbf{r}_1\,\mathbf{r}_2\,\mathbf{r}_3), \quad \Lambda = diag(\lambda_1, \lambda_2, \lambda_3), \tag{59}$$

where $\lambda_j\,(j = 1,2,3)$ are the eigenvalues of M which are real and positive because M is positive definite. Hence the following WLS formulation is always possible:

$$K[\phi] = \frac{1}{2}\int_\Omega (M\nabla\phi)\cdot\nabla\phi\, d\Omega = \frac{1}{2}\int_\Omega \lambda_j\,(\mathbf{r}_j\cdot\nabla\phi)^2\, d\Omega. \tag{60}$$

A key element of the present problem formulation is the required compatibility of the natural boundary condition (56) with Neumann-like boundary condition:

$$\tau\cdot\nabla\phi = 0, \quad x \in \{\partial\Omega \setminus \partial\Omega^D\}, \tag{61}$$

where τ is a vector with a non-zero component in the direction of the unit outward normal, i.e.:

$$\tau \cdot \mathbf{n} \neq 0. \tag{62}$$

If (61) is applied it must be equivalent with Eq. (56) to make the functional K stationary. Because M is symmetric

$$\mathbf{n} \cdot (M \nabla \phi) = (M \mathbf{n}) \cdot \nabla \phi, \tag{63}$$

leading to the following *compatibility condition*:

$$M\mathbf{n} = \lambda \tau, \quad \lambda \neq 0, \quad \boldsymbol{x} \in \{\partial\Omega \setminus \partial\Omega^D\}. \tag{64}$$

In the special case that τ is identical to $\mathbf{n}$, then it follows from Eq. (64) that $\mathbf{n}$ must be an eigenvector of M on $\{\partial\Omega \setminus \partial\Omega^D\}$. Condition (64) imposes important restrictions on the construction of candidates for M.

3.2.2 Transformation

At several stages in the remainder of this thesis a transformation of the previously derived variational problem is carried out. The present section briefly presents such transformation from the physical domain $\Omega \subset \mathcal{R}^3$ to the unit cube Ω_α with Cartesian coordinates, say $\boldsymbol{\alpha} = (\alpha^1, \alpha^2, \alpha^3)^T$, and to derive the associated EL equations.

By using the identity:

$$\nabla \equiv J_\alpha^{-T} \nabla_\alpha, \tag{65}$$

with

$$J_\alpha^{-T} = (J_\alpha^{-1})^T, \quad \nabla_\alpha = (\frac{\partial}{\partial \alpha^1}, \frac{\partial}{\partial \alpha^2}, \frac{\partial}{\partial \alpha^3})^T, \tag{66}$$

and where J_α is the Jacobian matrix of the map from Ω_α to Ω, $(J_\alpha)^{ij} = \frac{\partial x^i}{\partial \alpha^j}$, functional K in (49) can be transformed to:

$$K[\phi] = \frac{1}{2} \int_{\Omega_\alpha} (M J_\alpha^{-T} \nabla_\alpha \phi) \cdot (J_\alpha^{-T} \nabla_\alpha \phi) |J_\alpha| d\Omega_\alpha. \tag{67}$$

Using the identity:

$$(MJ_\alpha^{-T}\nabla_\alpha\phi)\cdot(J_\alpha^{-T}\nabla_\alpha\phi) \equiv (J_\alpha^{-1}MJ_\alpha^{-T}\nabla_\alpha\phi)\cdot\nabla_\alpha\phi, \tag{68}$$

leads to:

$$K[\phi] = \frac{1}{2}\int_{\Omega_\alpha}(\tilde{M}\nabla_\alpha\phi)\cdot\nabla_\alpha\phi\, d\Omega_\alpha, \quad \tilde{M} = |J_\alpha|J_\alpha^{-1}MJ_\alpha^{-T}. \tag{69}$$

The Dirichlet condition, the EL equation and the natural boundary conditions are:

$$\phi = \phi_0, \quad \boldsymbol{\alpha} \in \partial\Omega_\alpha^D, \tag{70}$$

$$\nabla_\alpha\cdot(\tilde{M}\nabla_\alpha\phi) = 0, \quad \boldsymbol{\alpha} \in \Omega_\alpha, \tag{71}$$

and:

$$\mathbf{n}_\alpha\cdot(\tilde{M}\nabla_\alpha\phi) = 0, \quad \boldsymbol{\alpha} \in \{\partial\Omega_\alpha \setminus \partial\Omega_\alpha^D\}, \tag{72}$$

respectively, where $\mathbf{n}_\alpha \in \Omega_\alpha$ denotes the outward unit normal on $\partial\Omega_\alpha$.

3.2.3 Map of $\Omega \subset \mathcal{R}^3$ to the unit cube

In this section it is shown how the map of Ω to the unit cube $[0,1]^3$ is constructed by combination of three separate maps from Ω to the unit interval.

Assume that there exists some auxiliary map P from the unit cube C to the physical domain Ω which is one-to-one, continuous and invertible. This map P will only be used in the present section to formulate the boundary-value problem for the construction of the desired map from Ω to the unit cube C. The boundary of Ω can conveniently be expressed as the image of the boundary of the unit cube C under the map P:

$$\partial\Omega = P(\partial C), \quad C = [0,1]^3. \tag{73}$$

Moreover, the boundary $\partial\Omega$ can be split into six separate non-overlapping parts $\partial\Omega_i$, $i = 1,6$:

$$\partial\Omega_i = P(\partial C_i), \quad i = 1,2,...,6, \tag{74}$$

where

$$\partial C_1 = \{0\} \times (0,1) \times (0,1),$$

$$\partial C_2 = \{1\} \times (0,1) \times (0,1),$$

$$\partial C_3 = (0,1) \times \{0\} \times (0,1),$$

$$\partial C_4 = (0,1) \times \{1\} \times (0,1),$$

$$\partial C_5 = (0,1) \times (0,1) \times \{0\},$$

$$\partial C_6 = (0,1) \times (0,1) \times \{1\}.$$

Note that the auxiliary unit cube C and the auxiliary map P are only used to conveniently define the problem formulation for the desired map of Ω to the unit cube $[0,1]^3$.

The desired map from the physical domain Ω to the unit cube $[0,1]^3$ that we are looking for can now be defined by combination of three 1D maps $\xi(\mathbf{x})$, $\eta(\mathbf{x})$ and $\zeta(\mathbf{x})$ from Ω to the unit interval, which are solutions of the following three variational problems:

Variational Problem 3.2 *Find a function* $\xi(\mathbf{x})$, $\Omega \in \mathcal{R}^3 \mapsto [0,1]$ *with* $\xi = 0$ *for* $\mathbf{x} \in P(\partial C_1)$ *and* $\xi = 1$ *for* $\mathbf{x} \in P(\partial C_2)$, *(see Fig. 5), such that the functional* $K[\xi]$ *given by Eq. (49) is minimised,*

and

Variational Problem 3.3 *Find a function* $\eta(\mathbf{x})$, $\Omega \in \mathcal{R}^3 \mapsto [0,1]$ *with* $\eta = 0$ *for* $\mathbf{x} \in P(\partial C_3)$ *and* $\eta = 1$ *for* $\mathbf{x} \in P(\partial C_4)$, *(see Fig. 6), such that the functional* $K[\eta]$ *given by Eq. (49) is minimised,*

and

Variational Problem 3.4 *Find a function* $\zeta(\mathbf{x})$, $\Omega \in \mathcal{R}^3 \mapsto [0,1]$ *with* $\zeta = 0$ *for* $\mathbf{x} \in P(\partial C_5)$ *and* $\zeta = 1$ *for* $\mathbf{x} \in P(\partial C_6)$, *(see Fig. 7), such that the functional* $K[\zeta]$ *given by Eq. (49) is minimised.*

For completeness we note that these three separate variational problems can also be combined into a single compound variational problem:

Variational Problem 3.5 *Find functions*

$$\xi(\mathbf{x}), \Omega \in \mathcal{R}^3 \mapsto [0,1],$$

$$\eta(\mathbf{x}), \Omega \in \mathcal{R}^3 \mapsto [0,1],$$

$$\zeta(\mathbf{x}), \Omega \in \mathcal{R}^3 \mapsto [0,1],$$

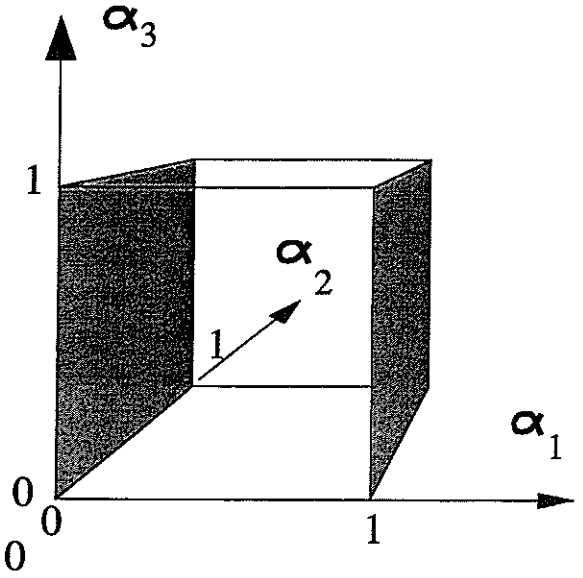

Fig. 5 Auxiliary unit cube C and indicated boundary parts ∂C_1 and ∂C_2 (shaded) used for specification of Variational Problem 3.2.

with

$$\xi = 0, \mathbf{x} \in P(\partial C_1),$$

$$\xi = 1, \mathbf{x} \in P(\partial C_2),$$

$$\eta = 0, \mathbf{x} \in P(\partial C_3),$$

$$\eta = 1, \mathbf{x} \in P(\partial C_4),$$

$$\zeta = 0, \mathbf{x} \in P(\partial C_5),$$

$$\zeta = 1, \mathbf{x} \in P(\partial C_6),$$

such that the functional

$$I[\xi, \eta, \zeta] = K[\xi] + K[\eta] + K[\zeta], \tag{75}$$

with $K[\ ]$ given by Eq. (49), is minimised.

By means of the analysis presented in section 3.2.1 the three variational problems 3.2, 3.3 and 3.4 can be transformed into three boundary value problems:

Boundary Value Problem 3.1 *Find a function $\xi(\mathbf{x}), \Omega \in \mathcal{R}^3 \mapsto [0, 1]$ that satisfies $\nabla \cdot (M \nabla \xi) =$*

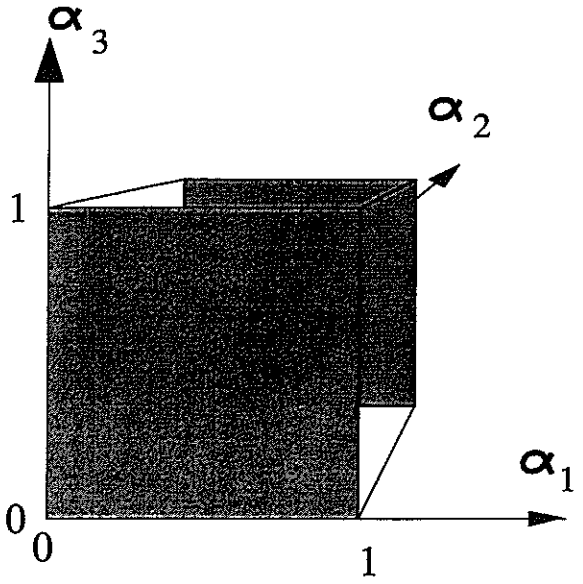

Fig. 6 Auxiliary unit cube C and indicated boundary parts ∂C_3 and ∂C_4 (shaded) used for specification of Variational Problem 3.3.

0 *for* $x \in \Omega$, *with the matrix* M *given by Eq. (50), under the Dirichlet conditions* $\xi = 0$ *for* $\mathbf{x} \in P(\partial C_1)$ *and* $\xi = 1$ *for* $\mathbf{x} \in P(\partial C_2)$, *and under the generalized Neumann condition* $\mathbf{n} \cdot (M \nabla \xi) = 0$ *for* $x \in \partial\Omega \setminus \{P(\partial C_1) \cup P(\partial C_2)\}$,

and

Boundary Value Problem 3.2 *Find a function* $\eta(\mathbf{x}), \Omega \in \mathcal{R}^3 \mapsto [0,1]$ *that satisfies* $\nabla \cdot (M \nabla \eta) = 0$ *for* $x \in \Omega$, *with the matrix* M *given by Eq. (50), under the Dirichlet conditions* $\eta = 0$ *for* $\mathbf{x} \in P(\partial C_3)$ *and* $\eta = 1$ *for* $\mathbf{x} \in P(\partial C_4)$, *and under the generalized Neumann condition* $\mathbf{n} \cdot (M \nabla \eta) = 0$ *for* $x \in \partial\Omega \setminus \{P(\partial C_3) \cup P(\partial C_4)\}$,

and

Boundary Value Problem 3.3 *Find a function* $\zeta(\mathbf{x}), \Omega \in \mathcal{R}^3 \mapsto [0,1]$ *that satisfies* $\nabla \cdot (M \nabla \zeta) = 0$ *for* $x \in \Omega$, *with the matrix* M *given by Eq. (50), under the Dirichlet conditions* $\zeta = 0$ *for* $\mathbf{x} \in P(\partial C_5)$ *and* $\zeta = 1$ *for* $\mathbf{x} \in P(\partial C_6)$, *and under the generalized Neumann condition* $\mathbf{n} \cdot (M \nabla \zeta) = 0$ *for* $x \in \partial\Omega \setminus \{P(\partial C_5) \cup P(\partial C_6)\}$

The results of this section are used in the next section to relate map constructions presented in the literature within the frame work of weighted least squares formulations.

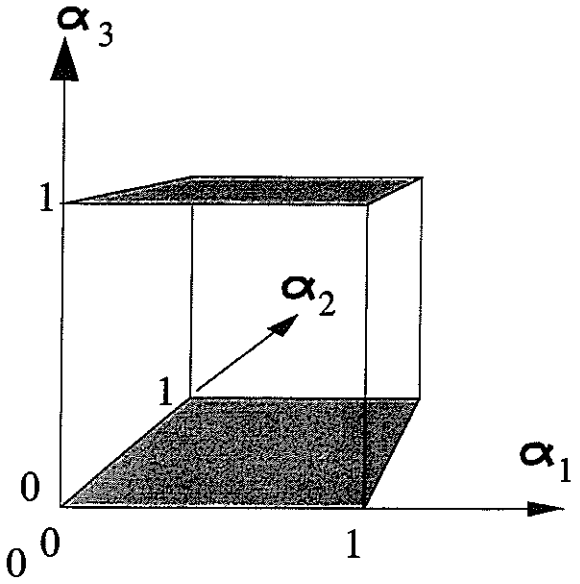

Fig. 7 Auxiliary unit cube C and indicated boundary parts ∂C_5 and ∂C_6 (shaded) used for specification of Variational Problem 3.4.

3.2.4 Direct formulation

In this section we will formulate a lemma with which the inverse formulation given by the boundary value problems 3.1, 3.2 and 3.3 for the map $\boldsymbol{\xi}(\mathbf{x})$, $\Omega \in \mathcal{R}^3 \mapsto [0,1]^3$ can be transformed into a direct formulation for the map $\mathbf{x}(\boldsymbol{\xi})$, $[0,1]^3 \mapsto \Omega \in \mathcal{R}^3$. The lemma is an extension of the method described in [65] for the interchange of the roles of the dependent and independent variables of a system of Poisson equations.

Lemma 3.1 *Let the map $\boldsymbol{\xi}(\mathbf{x}) : \Omega \subset \mathcal{R}^3 \mapsto [0,1]^3$ satisfy the system of decoupled linear PDE's*

$$(A\nabla)\cdot(B\nabla\xi^k) = P_k,\ k = 1,2,3,$$

then the inverse map $\mathbf{x}(\boldsymbol{\xi}) : [0,1]^3 \mapsto \Omega \subset \mathcal{R}^3$ satisfies the system of coupled nonlinear PDE's

$$\tilde{g}^{ij}\frac{\partial^2 x^k}{\partial\xi^i\partial\xi^j} + P_m\frac{\partial x^k}{\partial\xi^m} = Q_k,\ k = 1,2,3,$$

with

$$\tilde{g}^{ij} = a^{lm}b^{ln}\frac{\partial\xi^i}{\partial x^m}\frac{\partial\xi^j}{\partial x^n}$$

and

$$Q_k = a^{mn}\frac{\partial b^{mk}}{\partial x^n}.$$

Proof. Evaluation of the partial differential operator yields:

$$(A\nabla)\cdot(B\nabla\phi) = a^{ik}\frac{\partial}{\partial x^k}b^{ij}\frac{\partial\phi}{\partial x^j} = a^{ik}\frac{\partial}{\partial x^k}b^{ij}\frac{\partial\phi}{\partial\xi^m}\frac{\partial\xi^m}{\partial x^j}$$

$$= \frac{\partial \phi}{\partial \xi^m} a^{ik} \frac{\partial}{\partial x^k} b^{ij} \frac{\partial \xi^m}{\partial x^j} + a^{ik} b^{ij} \frac{\partial \xi^m}{\partial x^j} \frac{\partial}{\partial x^k} \frac{\partial \phi}{\partial \xi^m}.$$

The first term equals $\frac{\partial \phi}{\partial \xi^m} P_m$ because $(A\nabla) \cdot (B\nabla \xi^k) = P_k$ by assumption. The second term can be evaluated:

$$a^{ik} b^{ij} \frac{\partial \xi^m}{\partial x^j} \frac{\partial}{\partial x^k} \frac{\partial \phi}{\partial \xi^m} = a^{ik} b^{ij} \frac{\partial \xi^m}{\partial x^j} \frac{\partial \xi^n}{\partial x^k} \frac{\partial^2 \phi}{\partial \xi^n \partial \xi^m}$$

$$= \tilde{g}^{nm} \frac{\partial^2 \phi}{\partial \xi^n \partial \xi^m} = \tilde{g}^{mn} \frac{\partial^2 \phi}{\partial \xi^n \partial \xi^m} = \tilde{g}^{ij} \frac{\partial^2 \phi}{\partial \xi^i \partial \xi^j}.$$

Substitution of x^k for ϕ directly gives:

$$(A\nabla) \cdot (B\nabla x^k) = a^{il} \frac{\partial}{\partial x^l} b^{ij} \frac{\partial x^k}{\partial x^j} = a^{il} \frac{\partial}{\partial x^l} b^{ij} \delta^{kj} = a^{il} \frac{\partial b^{ik}}{\partial x^l} = a^{mn} \frac{\partial b^{mk}}{\partial x^n},$$

which proves the assertion. □

The result of this lemma is used in the next section where applications from the literature are reviewed.

3.3 Applications from the literature

3.3.1 Laplace maps

Brackbill and Saltzmann (ref. [9]) used a compound functional within a variational problem formulation for adaptive grid generation consisting of three functionals: one for smoothness, one for orthogonality and one for adaptation. In this section we will discuss only the smoothness functional:

$$I_S[\xi, \eta, \zeta] = \frac{1}{2} \int_\Omega \{ \|\nabla \xi\|^2 + \|\nabla \eta\|^2 + \|\nabla \zeta\|^2 \} \, d\Omega, \tag{76}$$

This functional can be written in WLS format (75) as:

$$I_S[\xi, \eta, \zeta] = K[\xi] + K[\eta] + K[\zeta], \tag{77}$$

with

$$K[\phi] = \frac{1}{2} \int_\Omega (M\nabla\phi) \cdot \nabla\phi \, d\Omega, \quad M = \begin{pmatrix} 1 & 0 & 0 \\ 0 & 1 & 0 \\ 0 & 0 & 1 \end{pmatrix}. \tag{78}$$

The EL equations (55) result in the Laplace equation for each of the computational coordinates ξ, η and ζ:

$$\nabla \cdot (\nabla \xi) = 0, \quad \nabla \cdot (\nabla \eta) = 0, \quad \nabla \cdot (\nabla \zeta) = 0, \quad \mathbf{x} \in \Omega. \tag{79}$$

The associated natural boundary conditions on those parts of the boundary where Dirichlet conditions are not specified are given by Eq. (56):

$$\begin{aligned} \mathbf{n} \cdot \nabla \xi &= 0, \quad x \in \partial\Omega \setminus \{P(\partial C_1) \cup P(\partial C_2)\} \\ \mathbf{n} \cdot \nabla \eta &= 0, \quad x \in \partial\Omega \setminus \{P(\partial C_3) \cup P(\partial C_4)\} \\ \mathbf{n} \cdot \nabla \zeta &= 0, \quad x \in \partial\Omega \setminus \{P(\partial C_5) \cup P(\partial C_6)\} \end{aligned} \tag{80}$$

which are ordinary Neumann conditions.

The direct formulation can readily be obtained by application of Lemma 3.1 to partial differential equations (79) with $A = I$, $B = I$ and $P_k = 0$, resulting in:

$$g^{ij} \frac{\partial^2 x^k}{\partial \xi^i \partial \xi^j} = 0, \tag{81}$$

where g^{ij} is the contra-variant metric tensor:

$$g^{ij} = \frac{\partial \xi^i}{\partial x^k} \frac{\partial \xi^j}{\partial x^k}, \tag{82}$$

which can be expressed in terms of the derivatives $\frac{\partial x^i}{\partial \xi^j}$, see [65] and [42].

3.3.2 Isotropic diffusion maps

Winslow (ref. [74]) introduced a single weight function into the smoothness functional of Brackbill and Saltzmann to account for smoothness as well as for adaptation. The functional is:

$$I[\xi, \eta, \zeta] = \frac{1}{2} \int_\Omega \frac{1}{w(\mathbf{x})} \{\|\nabla \xi\|^2 + \|\nabla \eta\|^2 + \|\nabla \zeta\|^2\} \, d\Omega. \tag{83}$$

This functional can be written in WLS format (75) as:

$$I[\xi, \eta, \zeta] = K[\xi; w] + K[\eta; w] + K[\zeta; w], \tag{84}$$

with

$$K[\phi;w] = \frac{1}{2}\int_\Omega (M\nabla\phi)\cdot\nabla\phi\, d\Omega, \quad M = \frac{1}{w}\begin{pmatrix} 1 & 0 & 0 \\ 0 & 1 & 0 \\ 0 & 0 & 1 \end{pmatrix}. \tag{85}$$

The EL equations (55) consist of identical isotropic diffusion equations for each of the computational coordinates ξ, η and ζ:

$$\nabla\cdot(\frac{1}{w}\nabla\xi) = 0, \quad \nabla\cdot(\frac{1}{w}\nabla\eta) = 0, \quad \nabla\cdot(\frac{1}{w}\nabla\zeta) = 0, \quad \mathbf{x}\in\Omega. \tag{86}$$

The associated natural boundary conditions on those parts of the boundary where Dirichlet conditions are not specified are given by Eqs. (80), which are again ordinary Neumann conditions.

The direct formulation can readily be obtained by application of Lemma 3.1 to partial differential equations (86) with $A = I$, $B = w^{-1}I$ and $P_k = 0$, resulting in:

$$g^{ij}\frac{\partial^2 x^k}{\partial\xi^i\partial\xi^j} + \frac{1}{w}\frac{\partial w}{\partial x^k} = 0, \tag{87}$$

where g^{ij} is the contra-variant metric tensor given by (82).

3.3.3 Weakly related isotropic diffusion maps

Eiseman [21] introduced an interesting extension to the approach of Winslow [74] by using different weight functions $w_j(\mathbf{x})$, $j = 1,2,3$, one for each coordinate direction, which enables anisotropic grid adaptation. The functional is:

$$I[\xi,\eta,\zeta] = \frac{1}{2}\int_\Omega \{\frac{1}{w_1}\|\nabla\xi\|^2 + \frac{1}{w_2}\|\nabla\eta\|^2 + \frac{1}{w_3}\|\nabla\zeta\|^2\}\, d\Omega, \tag{88}$$

This functional can be written in WLS format (75) as:

$$I[\xi,\eta,\zeta] = K[\xi;w_1] + K[\eta;w_2] + K[\zeta;w_3], \tag{89}$$

with $K[\phi; w]$ defined by Eq. (85). The EL equations (55) consist of weakly related isotropic diffusion equations, one for each of the computational coordinates ξ, η and ζ:

$$\nabla \cdot (\frac{1}{w_1}\nabla\xi) = 0, \quad \nabla \cdot (\frac{1}{w_2}\nabla\eta) = 0, \quad \nabla \cdot (\frac{1}{w_3}\nabla\zeta) = 0, \quad \mathrm{x} \in \Omega. \tag{90}$$

these equations are weakly related by the assumption that the weight functions $w_j(\mathrm{x}), j = 1,2,3$, are different, though all derived from the same scalar or vector function (e.g. an initial guess of the flow solution).

The associated natural boundary conditions on those parts of the boundary where Dirichlet conditions are not specified are given by Eqs. (80), which are again ordinary Neumann conditions.

The direct formulation cannot readily be obtained by application of lemma 3.1 since the differential operators in equations (90) are not identical. Therefore we first evaluate the PDE's by applying the chain rule of differentiation:

$$\begin{aligned} \nabla \cdot (\nabla\xi) &= P_1; \quad P_1 = \tfrac{1}{w_1}\nabla\xi \cdot \nabla w_1, \\ \nabla \cdot (\nabla\eta) &= P_2; \quad P_2 = \tfrac{1}{w_2}\nabla\eta \cdot \nabla w_2, \\ \nabla \cdot (\nabla\zeta) &= P_3; \quad P_3 = \tfrac{1}{w_3}\nabla\zeta \cdot \nabla w_3. \end{aligned} \tag{91}$$

Application of Lemma 3.1 to the evaluated system (91) yields:

$$g^{ij}\frac{\partial^2 x^k}{\partial\xi^i\partial\xi^j} + P_m\frac{\partial x^k}{\partial\xi^m} = 0, \tag{92}$$

where g^{ij} is the contra-variant metric tensor given by Eq. (82).

3.3.4 Harmonic maps

Harmonic maps with user-specified metric tensors for grid adaptation have been introduced by Dvinsky (ref. [19]) and reviewed by Brackbill (ref. [8]). In the present section harmonic maps are discussed within the frame work of the WLS formulation.

Let the functional E_0 be defined as:

$$E_0[\phi] = \frac{1}{2}\int_\Omega d^{ij}\frac{\partial\phi}{\partial x^i}\frac{\partial\phi}{\partial x^j}\sqrt{d}\,d\Omega, \tag{93}$$

where d^{ij} is the user-specified symmetric contravariant metric tensor in the coordinates $\mathbf{x}$ and $d = det\{d_{ij}\} > 0$. The covariant metric tensor of the Eucledian coordinates in the unit cube is the identity matrix and hence does not show up in the functional E_0. E can be rewritten in the matrix vector format (49):

$$E_0[\phi] = \frac{1}{2}\int_\Omega (M\nabla\phi)\cdot\nabla\phi\, d\Omega, \quad M^{ij} = \sqrt{d}\, d^{ij}. \tag{94}$$

The generation of an adaptive grid in Ω can be considered as a map from a three-dimensional Riemannian manifold in $\mathcal{R}^4$ described by the local coordinates $\mathbf{x}$ to the unit cube. The additional dimension with respect to $\Omega \subset \mathcal{R}^3$ can be obtained by defining a function Q on Ω to which the grid must be adapted (ref. [59]):

$$\Phi : \Omega \mapsto \mathcal{R}^4, \quad \Phi(x,y,z) = (x,y,z,Q(x,y,z))^T. \tag{95}$$

The Jacobian of the map (95) is:

$$J_\Phi = (\Phi_x, \Phi_y, \Phi_z)^T, \tag{96}$$

and hence the covariant tensor d_{ij} is:

$$d_{ij} = (J_\Phi {J_\Phi}^T)^{ij} = \delta^{ij} + \frac{\partial Q}{\partial x^i}\frac{\partial Q}{\partial x^j}, \quad d = det\{d_{ij}\} = 1 + \|\nabla Q\|^2. \tag{97}$$

The characteristic equation for the eigenvalues of d_{ij} is:

$$(\bar{\lambda} - d)(\bar{\lambda} - 1)^2 = 0, \tag{98}$$

with solutions $\bar{\lambda}_1 = d$ and $\bar{\lambda}_2 = 1$, respectively. The eigenspace belonging to $\bar{\lambda}_1$ is one-dimensional and is spanned by ∇Q, the gradient of Q. The eigenspace belonging to $\bar{\lambda}_2$ is two-dimensional and consists of all vectors in three-dimensional space that are normal to ∇Q. Hence, the metric tensor $\sqrt{d}\, d^{ij}$ has the same eigenspaces with eigenvalues $\lambda_1 = d^{-\frac{1}{2}}$ and $\lambda_2 = d^{\frac{1}{2}}$, respectively. With the above described expressions for the eigenvalues and eigenspaces the WLS formulation of E_0 is:

$$E_0[\phi] = \frac{1}{2}\int_\Omega \frac{1}{\sqrt{d}}(\mathbf{r}_1.\nabla\phi)^2 + \sqrt{d}\,\{(\mathbf{r}_2.\nabla\phi)^2 + (\mathbf{r}_3.\nabla\phi)^2\}\, d\Omega, \tag{99}$$

where the eigenvectors $\mathbf{r}_i$ $(i = 1, 2, 3)$ form an orthonormal set with $\mathbf{r}_1 = \frac{\nabla Q}{\|\nabla Q\|}$.

The harmonic map is established by minimising the 'total energy' functional:

$$E[\xi, \eta, \zeta] = E_0[\xi] + E_0[\eta] + E_0[\zeta], \tag{100}$$

where $\boldsymbol{\xi} = (\xi, \eta, \zeta)^T$ are the Cartesian ccordinates in the unit cube. The EL equations associated with the minimisation of $E[\xi, \eta, \zeta]$ are:

$$L_{LB}(\xi) = 0, \quad L_{LB}(\eta) = 0, \quad L_{LB}(\zeta) = 0, \tag{101}$$

where L_{LB} is the Laplace-Beltrami operator.

The associated natural boundary conditions on those parts of the boundary where Dirichlet conditions are not specified follow from Eq. (56):

$$\begin{aligned} \mathbf{n} \cdot (M \nabla \xi) &= 0, \quad x \in \partial\Omega \setminus \{P(\partial C_1) \cup P(\partial C_2)\} \\ \mathbf{n} \cdot (M \nabla \eta) &= 0, \quad x \in \partial\Omega \setminus \{P(\partial C_3) \cup P(\partial C_4)\} \\ \mathbf{n} \cdot (M \nabla \zeta) &= 0, \quad x \in \partial\Omega \setminus \{P(\partial C_5) \cup P(\partial C_6)\}. \end{aligned} \tag{102}$$

The WLS formulation of the 'total energy' functional E given by Eq. (100) is completely similar to Eq. (99).

3.4 Discussion

The maps that are applied in the literature and discussed in sections 3.3.1 to 3.3.4 can be checked on whether they satisfy a number of requirements, namely:

1. *The three PDE's that are derived from the chosen functional must be identical.* The regularity theorem that is presented in section 4.6 is based on the assumption that the PDE's for each of the computational coordinates are identical. Since the regularity of a map from $\Omega \subset \mathcal{R}^3$ to the unit cube depends on the relationship between the three computational coordinates it seems inevitable to require that the three PDE's be related, i.e. be identical.
2. *the PDE's must resemble anisotropic adaptation.* To enable an effective and efficient grid adaptation algorithm it should be possible to stretch cells differently in different directions.
3. *The matrix M must be a function of* $\mathbf{x}$ *only.* If the matrix M is also a function of $\boldsymbol{\xi}$ then the PDE's derived in the previous sections are not the EL-equations associated with the formulated variational problems.

4. *The compatibility condition (64) must be satisfied.* To impose the ordinary Neumann conditions and simultaneously minimise the chosen functional, the compatibility condition must be satisfied.

The various maps presented in sections 3.3.1 to 3.3.4 can be discussed in view of the above formulated four requirements.

Laplace maps. The PDE's that are derived from the smoothness functional in section 3.3.1 are all identical Laplace equations and are hence isotropic. The matrix M is the identity matrix and the compatibility condition (64) is satisfied.

Isotropic diffusion maps. The PDE's that are derived from the functional formulated by Winslow, see section 3.3.2, are identical isotropic diffusion equations. The matrix M is the identity matrix multiplied by a scalar function w, hence the compatibility condition (64) is satisfied. Requirement 3) can be satisfied by definition of w as a function of x only.

Weakly related Isotropic diffusion maps. The PDE's that are derived from the functional formulated by Eiseman, see section 3.3.3, are not identical isotropic diffusion equations. The three matrices included are identity matrices multiplied by the scalar functions w_i, $i = 1, 2, 3$, hence the compatibility condition (64) is satisfied. Looking at expression (88) for the functional to be minimised, the weight functions w_i, $i = 1, 2, 3$, are used to weigh the gradients $||\nabla \xi^i||$, $i = 1, 2, 3$. Hence it is natural to choose the weight functions as some norm of the components of the gradient of some function, e.g. the flow solution, in the direction of ξ^i. This implies, however, that the weight functions w_i, $i = 1, 2, 3$, are not functions of x only but are also functions of ξ, the solution of the variational problem. As a consequence Eqs. (90) are not the EL-equations associated with functional (88).

Harmonic maps. The PDE's that are derived from the functional formulated by Dvinsky, see section 3.3.4, are anisotropic and identical. The matrix is well-defined and expression (99) for the functional to be minimised enables a clear interpretation.

The component of $\nabla\phi$ in the direction ∇Q at one hand and the components of $\nabla\phi$ normal to ∇Q at the other hand are weighted with inversely proportional weights. These are consequences of the objective to generate a smooth grid in the Riemannian manifold formed by the four-dimensional vector field $(x, y, z, Q)^T$.

A complete extension to multiple functions Q_i, $i = 1, 2, .., N$ can be derived in a similar manner (ref. [59]). However, there is an important drawback: the compatibility condition (64) is not

satisfied by the metric tensor $\sqrt{d}\, d^{ij}$ for arbitrarily chosen functions Q. Hence if Neumann conditions are imposed along the domain boundary the functional E is not minimised and the claim to generate the smoothest possible map on the monitor surface can not be substantiated.

The satisfaction of requirements 1) to 4) formulated above, is summarised in table 1. The conclusion is that none of the discussed WLS functionals presented in the literature satisfy all of the requirements 1) to 4). This is the motivation for the work presented in the next chapter; the construction of a WLS functional that satisfies all four requirements formulated above.

Table 1 Comparison of WLS maps used in the literature

Maps	Anisotropic?	$M = M(\mathbf{x})$?	Compatiblity?	Identical PDE's?
Laplace	no	yes	yes	yes
ID	no	yes	yes	yes
WRID	yes	no	yes	no
Harmonic	yes	yes	no	yes

4 Compound Weighted Least Squares maps

4.1 Objective

The objective of the present chapter is to construct a compound WLS functional that satisfies all of the four requirements formulated in section 3.4. The idea is to map the physical domain to the unit cube by means of an auxiliary parametric map resulting in a parametrisation of the physical space Ω. The resulting parametric map can be chosen such that the compatibility condition (64) is satisfied.

Subsequently the auxiliary parametric domain, say Ω_p, is mapped by a WLS map to another unit cube which will be called the computational domain, say Ω_c. Hence, the map from the physical domain Ω to the computational domain Ω_c is constructed as a compound map consisting of two underlying maps, see Fig. 8.

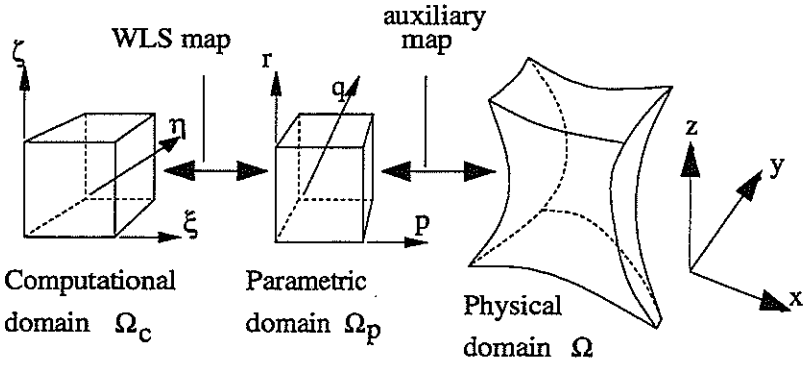

Fig. 8 Diagram of compound WLS map.

The compound map has the following properties:

1. If some map from the physical domain Ω to the unit cube is already available it can directly be used as the auxiliary map. This is the usual situation for grid adaptation; the existing grid that has to be adapted implicitly defines the auxiliary map to the unit cube.
2. Since the WLS map to be constructed maps the unit cube onto itself, the matrix included in the WLS functional can conveniently be chosen as a diagonal matrix.
3. If Neumann boundary conditions are imposed on the boundary of the parametric domain, and if the WLS map between the parametric domain and the computational domain is described by a WLS functional including a diagonal matrix, the compatibility condition is satisfied. This is explained in the present chapter.

One of the benefits of the variational formulation of a problem is the ability to interpret the resulting PDE's. In section 4.4 it is described how the compound WLS functional can be rewritten

to resemble the Equidisribution Principle for multi-dimensional problems. In addition it is shown in section 4.5 that the EL equations associated with the compound WLS functional can be written as averaged 1D Equidistribution Principles. Finally, section 4.6 describes an invertibility theorem for 2D problems.

4.2 General formulation

We start by formulating the WLS functional that upon minimisation defines the WLS map between the parametric domain Ω_p and the computational domain Ω_c . Let the functional $K[\phi]$ be defined as:

$$K[\phi] = \frac{1}{2}\int_{\Omega_p} (W^{-1}\nabla_p\phi)\cdot\nabla_p\phi\, d\Omega_p, \tag{103}$$

where $W(\mathbf{x})$ is a 3x3 diagonal matrix with strictly positive diagonal elements:

$$W(\mathbf{x}) = \begin{pmatrix} w_1(\mathbf{x}) & 0 & 0 \\ 0 & w_2(\mathbf{x}) & 0 \\ 0 & 0 & w_3(\mathbf{x}) \end{pmatrix} \quad w_i(\mathbf{x}) > 0, \quad i = 1,2,3, \tag{104}$$

and $\nabla_p = (\frac{\partial}{\partial p}, \frac{\partial}{\partial q}, \frac{\partial}{\partial r})^T$. The physical coordinates x are functions of the parametric coordinates $\mathbf{p} = (p,q,r)^T$ according to the auxiliary map. With this functional the following variational problem is defined:

Variational Problem 4.1 *Find a function* $\phi(\mathbf{p}) : \Omega_p \subset \mathcal{R}^3 \mapsto \mathcal{R}$ *with* $\phi(\mathbf{p}) = \phi_0(\mathbf{p})$ *for* $\mathbf{p} \in \partial\Omega_p^D \subset \partial\Omega_p$ *such that the functional* $K[\phi]$ *given by Eq. (103) is minimised.*

From section 3.2.2 we know that problem 4.1 is solved if the EL-equation

$$\nabla_p\cdot(W^{-1}\nabla_p\phi) = 0, \quad \mathbf{p}\in\Omega_p, \tag{105}$$

is solved while on that part of the boundary where no Dirichlet condition is imposed the associated natural boundary conditions are imposed:

$$\mathbf{n}_p\cdot(W^{-1}\nabla_p\phi) = 0, \quad \mathbf{p}\in\{\partial\Omega_p \setminus \partial\Omega_p^D\}, \tag{106}$$

where $\mathbf{n}_p \in \Omega_p$ denotes the outward unit normal on $\partial\Omega_p$. Since W is a diagonal matrix the EL-equation does not contain mixed partial derivatives. Since that Ω_p is a unit cube this enables

a clear interpretation of the functional $K[\phi]$, see sections 4.4 and 4.5.

It is further noted that because W is a diagonal matrix the natural boundary condition (106) is compatible with the ordinary Neumann condition since the compatibility condition (64) is satisfied on the complete boundary $\partial\Omega_p$:

$$W^{-1}n_p = \lambda n_p, \tag{107}$$

where $\lambda = w_1^{-1}$ on boundaries $p = 0$ and $p = 1$, $\lambda = w_2^{-1}$ on boundaries $q = 0$ and $q = 1$, and $\lambda = w_3^{-1}$ on boundaries $r = 0$ and $r = 1$. Here p, q and r are the coordinates in Ω_p. Hence, the natural boundary condition may be replaced by the ordinary Neumann condition:

$$\mathbf{n}_p \cdot \nabla_p \phi = 0, \quad \mathbf{p} \in \{\partial\Omega_p \setminus \partial\Omega_p^D\}. \tag{108}$$

This yields important implications for the boundary-value problem formulated in the physical domain Ω.

Transformation of the variational problem 4.1 to a formulation in the physical domain using a given auxiliary map $\mathbf{x}(\mathbf{p})$, $\Omega_p \subset \mathcal{R}^3$ is readily obtained by using the results of section 3.2.4. First functional (103) is rewritten as:

$$K[\phi] = \frac{1}{2}\int_\Omega (M\nabla\phi)\cdot\nabla\phi \, d\Omega, \quad M = \frac{1}{|J|}JW^{-1}J^T, \tag{109}$$

where the 3x3 matrix J is the Jacobian matrix of the auxiliary map:

$$J = (\mathbf{x}_p, \mathbf{x}_q, \mathbf{x}_r). \tag{110}$$

Then the transformed variational problem is:

Variational Problem 4.2 *Find a function* $\phi(\mathbf{x}) : \Omega \subset \mathcal{R}^3 \mapsto \mathcal{R}$ *with* $\phi(\mathbf{x}) = \phi_0(\mathbf{x})$ *for* $\mathbf{x} \in \partial\Omega^D \subset \partial\Omega$ *such that the functional* $K[\phi]$ *given by (109) is minimised.*

Section 3.2.4 learns that the transformed EL-equation is:

$$\nabla\cdot(M\nabla\phi) = 0, \quad \mathbf{x} \in \Omega, \tag{111}$$

and that the associated natural boundary condition is:

$$\mathbf{n} \cdot (M \nabla \phi) = 0, \quad \mathbf{x} \in \{\partial\Omega \setminus \partial\Omega^D\}, \tag{112}$$

where $\mathbf{n} \in \Omega$ denotes the outward unit normal on $\partial\Omega$ and $\partial\Omega^D$ is the image of $\partial\Omega_p^D$ under the auxiliary map $\mathbf{x}(\mathbf{p})$.

The compatibility of the natural boundary condition on $\Omega_p \setminus \partial\Omega_p^D$ with the ordinary Neumann condition suggests that the transformed natural boundary condition on $\Omega \setminus \partial\Omega^D$ is compatible with the transformation of the ordinary Neumann condition into a generalised Neumann condition in Ω under the map $\mathbf{x}(\mathbf{p})$.

To obtain such a transformation we first note that the auxiliary map $\mathbf{x}(\mathbf{p})$ is boundary conforming, i.e., the boundary $\partial\Omega_p$ is mapped to the boundary $\partial\Omega$. Then two of the column vectors of J are tangential to $\partial\Omega$ and the third one is not tangential to $\partial\Omega$, see Fig. 9.

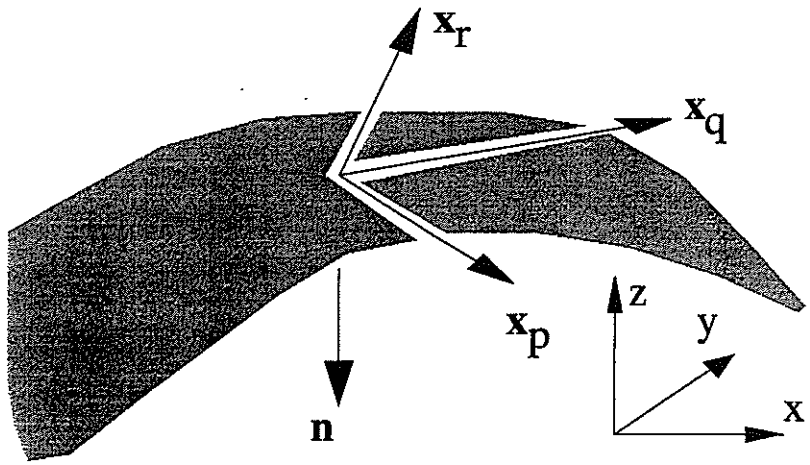

Fig. 9 Outward normal vector and components of the Jacobian matrix on $\partial\Omega$ associated with the auxiliary map $\mathbf{x}(\mathbf{p})$.

The following lemma shows that under these conditions the product of the matrix M and the unit normal $\mathbf{n}$ with respect to $\partial\Omega$ is equal to a constant times the column vector of J that is not coinciding with $\partial\Omega$:

Lemma 4.1 *Let a regular 3x3 matrix M be defined as $M = H\,W^{-1}\,H^T$ with $H = (\mathbf{h}_1, \mathbf{h}_2, \mathbf{h}_3)$ and $W = diag(w_1, w_2, w_3)$ with $w_j > 0$ for all $j \in \{1,2,3\}$, and let $\mathbf{n} \in \mathcal{R}^3$ be a nonzero vector. If there exists an integer $i \in \{1,2,3\}$ and a real $a \in \mathcal{R} \setminus \{0\}$ such that*

$$\mathbf{h}_j \cdot \mathbf{n} = a\delta^{ij}, \quad j \in \{1,2,3\},$$

then the product $M\mathbf{n}$ satisfies (without summation convention):

$$M\mathbf{n} = a{w_i}^{-1}\mathbf{h}_i.$$

Proof. The matrix vector product can be evaluated in three steps:

$$H^T\mathbf{n} = (\mathbf{h}_1 \cdot \mathbf{n}, \mathbf{h}_2 \cdot \mathbf{n}, \mathbf{h}_3 \cdot \mathbf{n})^T = a(\delta^{i1}, \delta^{i2}, \delta^{i3})^T,$$

$$W^{-1}H^T\mathbf{n} = a(\delta^{i1}{w_1}^{-1}, \delta^{i2}{w_2}^{-1}, \delta^{i3}{w_3}^{-1})^T,$$

$$HW^{-1}H^T\mathbf{n} = a\{\delta^{i1}{w_1}^{-1}\mathbf{h}_1 + \delta^{i2}{w_2}^{-1}\mathbf{h}_2 + \delta^{i3}{w_3}^{-1}\mathbf{h}_3\}$$

$$= a{w_i}^{-1}\mathbf{h}_i \quad \square$$

Hence, the compatibility condition (64) is satisfied if the column vector $\mathbf{x}_s$ of J, $s \in \{p,q,r\}$, that is not tangential to $\partial\Omega$, is used to specify the generalised Neumann condition (61):

$$\mathbf{x}_s \cdot \nabla\phi = 0, \quad \mathbf{x} \in \{\partial\Omega \setminus \partial\Omega^D\}, \quad \mathbf{x}_s \cdot \mathbf{n} \neq 0. \tag{113}$$

As a consequence, the orientation of curves $\phi = constant$ along the boundary $\partial\Omega \setminus \partial\Omega^D$ is identical to the orientation of curves $s = constant$, $s \in \{p,q,r\}$.

Before formulating of the complete boundary value problem that governs grid adaptation it is useful to note that the functional K given by Eq. (109) can be expressed as:

$$K[\phi] = \frac{1}{2}\int_\Omega \{\frac{(\mathbf{x}_p \cdot \nabla\phi)^2}{w_1} + \frac{(\mathbf{x}_q \cdot \nabla\phi)^2}{w_2} + \frac{(\mathbf{x}_r \cdot \nabla\phi)^2}{w_3}\}\frac{d\Omega}{|J|}. \tag{114}$$

Eq. 114 explicitly reveals the WLS character since the components of the gradient of ϕ in the directions of iso-parametric curves of the auxiliary parametric map are weighted with separate weight functions. From this observation it follows that the obvious choice is to take the weight functions in terms of derivatives of the monitor function(s) along the iso-parametric curves.

It is also noted that the functional K given by Eq. (103) can be expressed in the compact form:

$$K[\phi] = \frac{1}{2}\int_{\Omega_p} \{\frac{\phi_p^2}{w_1} + \frac{\phi_q^2}{w_2} + \frac{\phi_r^2}{w_3}\}\, d\Omega_p, \tag{115}$$

The complete boundary value problem formulation for adaptive grid generation can conveniently be formulated in the parametric domain Ω_p, based on minimisation of the compound functional (see section 3.2.3):

$$I_{CWLS}[\xi, \eta, \zeta] = K[\xi] + K[\eta] + K[\zeta], \tag{116}$$

with Dirichlet boundary conditions

$$\begin{aligned} &\xi(0,q,r) = 0,\ \xi(1,q,r) = 1, \\ &\eta(p,0,r) = 0,\ \eta(p,1,r) = 1, \\ &\zeta(p,q,0) = 0,\ \zeta(p,q,1) = 1. \end{aligned} \tag{117}$$

To solve this variational problem the associated EL equations

$$L(\xi) = \frac{\partial}{\partial p}(\frac{\xi_p}{w_1}) + \frac{\partial}{\partial q}(\frac{\xi_q}{w_2}) + \frac{\partial}{\partial r}(\frac{\xi_r}{w_3}) = 0, \tag{118}$$

$$L(\eta) = \frac{\partial}{\partial p}(\frac{\eta_p}{w_1}) + \frac{\partial}{\partial q}(\frac{\eta_q}{w_2}) + \frac{\partial}{\partial r}(\frac{\eta_r}{w_3}) = 0, \tag{119}$$

$$L(\zeta) = \frac{\partial}{\partial p}(\frac{\zeta_p}{w_1}) + \frac{\partial}{\partial q}(\frac{\zeta_q}{w_2}) + \frac{\partial}{\partial r}(\frac{\zeta_r}{w_3}) = 0, \tag{120}$$

must be solved subjected to a set of additional natural boundary conditions:

$$\begin{aligned} &\xi_q(p,0,r) = 0,\ \xi_q(p,1,r) = 0,\ \xi_r(p,q,0) = 0,\ \xi_r(p,q,1) = 0, \\ &\eta_p(0,q,r) = 0,\ \eta_p(1,q,r) = 0,\ \eta_r(p,q,0) = 0,\ \eta_r(p,q,1) = 0, \\ &\zeta_p(0,q,r) = 0,\ \zeta_p(1,q,r) = 0,\ \zeta_q(p,0,r) = 0,\ \zeta_q(p,1,r) = 0, \end{aligned} \tag{121}$$

Hence the objective to satisfy all of the conditions discussed in section 3.4 is met:

- The PDE's are identical,
- The PDE's are anisotropic,
- The matrix M is a function of x only, and
- The compatibility condition is satisfied.

4.3 Harmonically supported Weighted Least Squares map

A natural choice for the auxiliary parametric map satisfying the conditions of lemma 4.1 is the harmonic map obtained by minimising:

$$K_H[\phi] = \frac{1}{2}\int_\Omega \nabla\phi \cdot \nabla\phi \, d\Omega. \tag{122}$$

for which the EL-equations are:

$$L_H(p) = 0, \quad L_H(q) = 0, \quad L_H(r) = 0, \tag{123}$$

where L_H is the Laplace operator. The natural boundary condition for each of these harmonic maps is the Neumann boundary condition. Application of these Neumann conditions provides an auxiliary map that satisfies the the conditions of lemma 3.1.

In the remainder of this thesis the concept of harmonically supported WLS maps is not further considered since it is recognised that the initial grid that has to be adapted provides a suitable auxiliary parametric map with favourable properties. This is further explained in chapter 5.

4.4 Multiple 1D equidistribution interpretation in Ω_p

To demonstrate the connection between the variational problem formulated in section 103 and the equidistribution principle (33) presented in chapter 2 we will show that there exists an equivalent variational problem that involves functionals of the form (39) that explicitly express the *Equidistribution Principle.*

Consider the following functional as alternative for the functional given by Eq. (103):

$$\hat{K}[\phi, \mathbf{c}] = \frac{1}{2}\int_{\Omega_p} W(W^{-1}\nabla_p\phi - \mathbf{c}) \cdot (W^{-1}\nabla_p\phi - \mathbf{c}) \, d\Omega_p, \tag{124}$$

where $\mathbf{c} \in \mathcal{R}^3$ is a constant. This functional has some similarity with the 1D functional (39) which becomes clear when we express it in scalar notation:

$$\hat{K}[\phi, \mathbf{c}] = \frac{1}{2}\int_{\Omega_p} \sum_{i=0}^{3} w_i (\frac{1}{w_i}\frac{\partial\phi}{\partial p^{(i)}} - c^{(i)})^2 \, d\Omega_p. \tag{125}$$

To formulate the overall equivalent variational formulation we will first derive the EL equation

and natural boundary condition that are associated with functional $\hat{K}[\phi;\mathbf{c}]$. Eq. (124) can be expanded as:

$$\hat{K}[\phi,\mathbf{c}] = K[\phi] - \int_{\Omega_p} \mathbf{c}\cdot\nabla_p\phi\, d\Omega_p + \frac{1}{2}\int_{\Omega_p}(W\mathbf{c})\cdot\mathbf{c}\, d\Omega_p, \tag{126}$$

where the functional $K[\phi]$ is given by Eq. (103). Let $\tilde{\phi}$ be an admissible perturbation function of the solution ϕ. Then

$$\hat{K}[\phi+\varepsilon\tilde{\phi},\mathbf{c}] = K[\phi+\varepsilon\tilde{\phi},\mathbf{c}]$$

$$-\int_{\Omega_p}\mathbf{c}.\nabla_p\phi\, d\Omega_p - \varepsilon\int_{\Omega_p}\mathbf{c}\cdot\nabla_p\tilde{\phi}\, d\Omega_p + \frac{1}{2}\int_{\Omega_p}(W\mathbf{c})\cdot\mathbf{c}\, d\Omega_p, \tag{127}$$

and

$$\frac{\partial\hat{K}}{\partial\varepsilon} = \frac{\partial K}{\partial\varepsilon} - \int_{\Omega_p}\mathbf{c}\cdot\nabla_p\tilde{\phi}\, d\Omega_p. \tag{128}$$

Using the result (52) we find with $M = W^{-1}$:

$$\left.\frac{\partial K}{\partial\varepsilon}\right|_{\varepsilon=0} = \int_{\Omega_p} W^{-1}\nabla_p\phi\cdot\nabla_p\tilde{\phi}\, d\Omega_p. \tag{129}$$

Expression (128) can be put equal to zero to obtain the conditions for the functional $\hat{K}[\phi;\mathbf{c}]$ to become stationary:

$$\left.\frac{\partial\hat{K}}{\partial\varepsilon}\right|_{\varepsilon=0} = \int_{\Omega_p}(W^{-1}\nabla_p\phi - \mathbf{c})\cdot\nabla_p\tilde{\phi}\, d\Omega_p = 0. \tag{130}$$

By using the identity

$$(W^{-1}\nabla_p\phi - \mathbf{c})\cdot\nabla_p\tilde{\phi} \equiv \nabla_p\cdot\tilde{\phi}(W^{-1}\nabla_p\phi - \mathbf{c}) - \tilde{\phi}\nabla_p\cdot(W^{-1}\nabla_p\phi - \mathbf{c}), \tag{131}$$

and applying the divergence theorem we get from Eq. 130:

$$-\int_{\Omega_p}\tilde{\phi}\nabla_p\cdot(W^{-1}\nabla_p\phi - \mathbf{c})\, d\Omega_p + \int_{\partial\Omega_p}\tilde{\phi}\mathbf{n}\cdot(W^{-1}\nabla_p\phi - \mathbf{c})\, d\Gamma = 0 \tag{132}$$

From this expression we directly derive the expression for the EL equation as the condition which

ensures that the integrand of the volume integral in Eq. (132) is equal to zero for arbitrary $\tilde{\phi}$:

$$\nabla_p \cdot (W^{-1} \nabla_p \phi - \mathbf{c}) = 0, \quad \mathbf{p} \in \Omega_p \tag{133}$$

and the expression for the natural boundary condition as the condition which ensures that the integrand of the boundary integral in Eq. (132) is equal to zero for arbitrary $\tilde{\phi}$:

$$\mathbf{n} \cdot (W^{-1} \nabla_p \phi - \mathbf{c}) = 0, \quad \mathbf{p} \in \partial\Omega_p \setminus \partial\Omega_p^D, \tag{134}$$

see also section 3.2. Because $\mathbf{c}$ is a constant the EL-equation (133) associated with functional $\hat{K}$ is equivalent with the EL-equation (105) associated with functional K. To obtain equivalence of the natural boundary conditions (134) and (106) it is required that the following condition be satisfied:

$$\mathbf{n} \cdot \mathbf{c} = 0, \quad \mathbf{p} \in \partial\Omega_p \setminus \partial\Omega_p^D. \tag{135}$$

We will show for the problem formulation for the coordinate ξ of the computational domain that condition (135) can be satisfied.

If we minimise $\hat{K}[\xi, \mathbf{c}]$ with boundary condition (117) and take $\mathbf{c}$ of the form $\mathbf{c} = (c_1, 0, 0)^T$ then condition (135) is satisfied. Furthermore we can optimise functional $\hat{K}[\xi, \mathbf{c}]$ with respect to the scalar c_1 by requiring:

$$\frac{\partial \hat{K}}{\partial c_1} = 0. \tag{136}$$

From equation (126) we derive:

$$\hat{K}[\xi, (c_1, 0, 0)^T] = K[\xi] - c_1 \int_{\Omega_p} \xi_p d\Omega_p + \frac{1}{2} c_1^2 \int_{\Omega_p} w_1 d\Omega_p, \tag{137}$$

and:

$$\frac{\partial \hat{K}}{\partial c_1} = - \int_{\Omega_p} \xi_p d\Omega_p + c_1 \int_{\Omega_p} w_1 d\Omega_p. \tag{138}$$

So in order to satisfy condition (136) we find:

$$c_1 = \frac{\int_{\Omega_p} \xi_p d\Omega_p}{\int_{\Omega_p} w_1 d\Omega_p} = \frac{1}{\int_{\Omega_p} w_1 d\Omega_p}. \tag{139}$$

This expression for the constant c_1 is similar to expression (38) for the 1D case.

For the problem formulation for η and ζ similar expressions can be derived. For the η-problem we choose the form $\mathbf{c} = (0, c_2, 0)^T$ and for the ζ-problem we choose the form $\mathbf{c} = (0, 0, c_3)^T$.Now we can formulate the complete equivalent problem with respect to the functional I_{CWLS} (116) and boundary conditions (117). Retaining the boundary conditions (117) we replace I_{CWLS} by $\hat{I}_{CWLS}$ defined as:

$$\hat{I}_{CWLS}[\xi, \eta, \zeta, c_1, c_2, c_3] = \hat{K}[\xi, c_1] + \hat{K}[\eta, c_2] + \hat{K}[\zeta, c_3]. \tag{140}$$

As shown above this functional has the same EL-equations (118), (119) and (120), and natural boundary conditions (121) as the original functional I_{CWLS} in Eq. (116). To interpret the new functional $\hat{I}_{CWLS}$ we evaluate it to:

$$\begin{aligned} & \hat{I}_{CWLS}[\xi, \eta, \zeta, c_1, c_2, c_3] = \\ \tfrac{1}{2}\int_{\Omega_p}\{ \; & w_1(\frac{\xi_p}{w_1} - c_1)^2 + w_2(\frac{\xi_q}{w_2})^2 + w_3(\frac{\xi_r}{w_3})^2 \\ + \; & w_1(\frac{\eta_p}{w_1})^2 + w_2(\frac{\eta_q}{w_2} - c_2)^2 + w_3(\frac{\eta_r}{w_3})^2 \\ + \; & w_1(\frac{\zeta_p}{w_1})^2 + w_2(\frac{\zeta_q}{w_2})^2 + w_3(\frac{\zeta_r}{w_3} - c_3)^2\} \, d\Omega_p. \end{aligned} \tag{141}$$

This expression reveals the multiple equidistribution character of the problem formulation because minimisation of functional $\hat{I}_{CWLS}$ means that all terms in the integrand will be small in some optimal sense, with a tendency towards:

$$\begin{aligned} & \tfrac{\xi_p}{w_1} \to c_1, \quad \xi_q \to 0, \quad \xi_r \to 0, \\ & \eta_p \to 0, \quad \tfrac{\eta_q}{w_2} \to c_2, \quad \eta_r \to 0, \\ & \zeta_p \to 0, \quad \zeta_q \to 0, \quad \tfrac{\zeta_r}{w_3} \to c_3. \end{aligned} \tag{142}$$

Hence the variational problem formulated in section 4.2 tends to satisfy three separate 1D equidistribution principles, where each of the three computational coordinates ξ, η and ζ are preferably

uniformly adapted separately.

4.5 Averaged 1D equidistribution interpretation in Ω_p

Another way to show the connection between the 1D Equidistribution Principle and the variational formulation in section 4.2 is to integrate the EL-equation (118) over q and r, to integrate the EL-equation (119) over p and r and to integrate the EL-equation (120) over p and q using the natural boundary conditions (121). The result consists of three expressions:

$$\frac{\partial}{\partial p}\int_0^1\int_0^1 \frac{\xi_p}{w_1}\,dq\,dr = 0, \tag{143}$$

$$\frac{\partial}{\partial q}\int_0^1\int_0^1 \frac{\eta_q}{w_2}\,dp\,dr = 0, \tag{144}$$

and

$$\frac{\partial}{\partial r}\int_0^1\int_0^1 \frac{\zeta_r}{w_3}\,dp\,dq = 0. \tag{145}$$

These expressions are directly comparable to expression (43) that was derived for the 1D case since Eq. (143) indicates that the average of (ξ_p/w_1) taken over a p=constant plane is independent of the value of p.

4.6 Invertibility theorem for 2D problems

A critical aspect of grid generation and grid adaptation is the ability of the adaptation algorithm to produce grids that contain cells with positive volumes only. In other words the map from the computational domain to the physical domain must be one-to-one and have a Jacobian that is strictly positive everywhere except for a finite number of points where it may be zero. Assuming that these conditions are met by the map between the parametric domain Ω_p and the physical domain Ω it remains to be shown that the adaptive map between the computational domain Ω_c and the parametric domain Ω_p also satisfies this condition. For the 2D case where the computational and parametric domains both consist of the unit square it can be proven that for a large class of elliptic partial differential equations with appropriate boundary conditions the map is invertible. The relevant theorem has recently been developed by Clement, Hagmeijer and Sweers [14] and is listed below using the original notation of Ref. [14].

Let the open unit square $(0,1)\times(0,1)$ in $\mathcal{R}^2$ be denoted by S and the sides by Γ_1 to Γ_4 in the

following way:

$$\begin{cases} \Gamma_1 = \{0\} \times (0,1), \\ \Gamma_2 = (0,1) \times \{1\}, \\ \Gamma_3 = \{1\} \times (0,1), \\ \Gamma_4 = (0,1) \times \{0\} \end{cases}$$

Consider the problem:

Boundary Value Problem 4.1

$$(a)\begin{cases} Lu = 0 & in \quad S, \\ u = 0 & on \quad \Gamma_1, \\ u = 1 & on \quad \Gamma_3, \\ \frac{\partial u}{\partial n} = 0 & on \quad \Gamma_2 \cup \Gamma_4, \end{cases} \quad and \quad (b)\begin{cases} Lv = 0 & in \quad S, \\ v = 1 & on \quad \Gamma_2, \\ v = 0 & on \quad \Gamma_4, \\ \frac{\partial v}{\partial n} = 0 & on \quad \Gamma_1 \cup \Gamma_3, \end{cases} \tag{146}$$

where we are looking for a solution $(u,v) \in W^{2,p}(S) \times W^{2,p}(S)$ *with* $p \in (2,\infty)$.

For a domain in $\mathcal{R}^2$ with a Lipschitz boundary one has $W^{2,p}(S) \subset C^1(\bar{S})$ $p > 2$, see Theorem 7.26 of Ref. [25].

The operator L in (146) is given by:

$$L = a_1(x,y)\frac{\partial^2}{\partial x^2} + a_2(x,y)\frac{\partial^2}{\partial y^2} + b_1(x,y)\frac{\partial}{\partial x} + b_2(x,y)\frac{\partial}{\partial y}, \tag{147}$$

where the coefficients satisfy for some $c > 0$ and $\gamma \in (0,1)$

$$a_i \in C^{0,1}(\bar{S}), a_i \geq c > 0 \quad in \quad \bar{S}, \quad i = 1,2, \tag{148}$$

and

$$b_i \in C^{\gamma}(\bar{S}), \quad i = 1,2. \tag{149}$$

Theorem 4.1 *Problem (4.1) possesses exactly one solution* $(u,v) \in C^2(\bar{S})$. *Moreover* (u,v) *is a bijection from* $\bar{S}$ *(resp.* S*) onto itself and*

$$det\begin{pmatrix} u_x & u_y \\ v_x & v_y \end{pmatrix} > 0 \quad on \quad \bar{S}.$$

The proof of Theorem 4.1 is several pages long [14] and is not repeated here. The main fundament

of the proof is the use of the Carleman-Hartman-Wintner (CHW) Theorem (see [56]) which describes the structure of a solution to second order PDE's in the neighbourhood of critical points. Mainly because there is no straightforward higher dimensional extension of the CHW-Theorem it is not expected that Theorem 4.1 can be extended to hold for the three-dimensional cube.

4.7 Conclusions

The developed Compound Weighted Least Squares (CWLS) map described in the present chapter satisfies all of the four requirements formulated in section 3.4:

(i) Using the diagonal matrix W (104) with three different weight functions w_1, w_2 and w_3 provides anisotropic adaptation.

(ii) The matrix W is taken as a function of $\mathbf{x}$ while the obvious choice is to take the weight functions in terms of derivatives of the monitor function(s) along the iso-parametric curves, see expression (114).

(iii) In contrast to the WLS maps found in the literature, see Table 1, the present CWLS map satisfies the *compatibility condition* (64) as is proved by Lemma 4.1. This means that the natural boundary conditions of the variational problem 4.1 are equivalent to generalised Neumann boundary conditions. The exact form of these conditions can be controlled by the specific auxiliary map $\mathbf{x}(\mathbf{p})$ that is used.

(iv) Although the adaptation is anisotropic, the PDE's for the computational coordinates are identical. This is a direct consequence of using the same functional for each of the three computational coordinates.

In summary, Table 2 compares the methods found in the literature with the CWLS map.

Table 2 Comparison of the CWLS map with WLS maps used in the literature

Maps	Anisotropic?	$M = M(\mathbf{x})$?	Compatiblity?	Identical PDE's?
Laplace	no	yes	yes	yes
ID	no	yes	yes	yes
WRID	yes	no	yes	no
Harmonic	yes	yes	no	yes
CWLS	yes	yes	yes	yes

The challenge at this stage is to implement the theoretical concepts described in the present chapter such that robust and powerful adaptation algorithms are obtained that can be used for solving practical aerodynamic problems. This is the subject of the next two chapters.

5 Grid adaptation in 2D based on Compound Weighted Least Squares maps

In chapter 4 a mathematical frame work has been presented that can be used for the generation of coordinate systems that are suitable for grid adaptation. In this chapter we will use the described Compound Weighted Least Squares map to obtain an algorithm suitable for application to realistic Computational Fluid Dynamics (CFD) problems in two dimensions. Parts of this chapter have been published in [28].

In a typical aerodynamic study first a computational grid around the object of interest (e.g. a 2D airfoil) is generated followed by the calculation of the flow by solving the Navier-Stokes equations which describe conservation of mass, momentum and total energy per unit volume. A visual inspection of the calculated flow solution then will reveal areas that probably need higher grid resolution to enhance the flow details. These flow details may determine the accuracy of the overall flow calculation and show up in the accuracy with which the lift and drag of an airfoil are predicted. In this situation it is convenient to use a Compound Weighted Least Squares map for the generation of a new grid that is adapted to the calculated flow solution, where the original grid that was used initially for the flow computation provides a parametrisation of the physical domain.

Let $\Omega \subset \mathcal{R}^2$ be the physical domain in two-dimensional space on which the computational grid has to be adapted, and let $\Omega_c = [0,1]^2 \subset \mathcal{R}^2$ be the so-called computational domain. A boundary conforming curvilinear coordinate system in Ω can be defined by mapping Ω_c onto Ω such that the Cartesian computational coordinates $(\xi, \eta)^T$ in Ω_c are the curvilinear coordinates in Ω and are mapped onto the physical coordinates $(x, y)^T$ in Ω. The problem of grid adaptation is to find a suitable mapping from Ω_c to Ω. In this chapter it is assumed that there exists an initial grid with sufficient quality with respect to geometry resolution, orthogonality, and smoothness so that it has only to be adapted to the flow solution. To retain the characteristics of the initial grid in a global way we will use the initial grid for parametrisation of the physical domain based on the idea of Lee and Loellbach [44]. The concept of grid adaptation in the parametric domain is illustrated in Fig. 10.

Let the initial grid in the physical domain Ω be the image of a uniform Cartesian grid in the unit square $[0,1]^2 \subset \mathcal{R}^2$ under a map M. The Cartesian coordinates in the unit square denoted by $(p, q)^T$ serve as the parameters to describe the points in the physical domain; hence the unit square is called the parametric domain denoted by Ω_p. The idea is to adapt the Cartesian grid in the parametric domain Ω_p and to apply subsequently the map M to generate the adapted grid in the

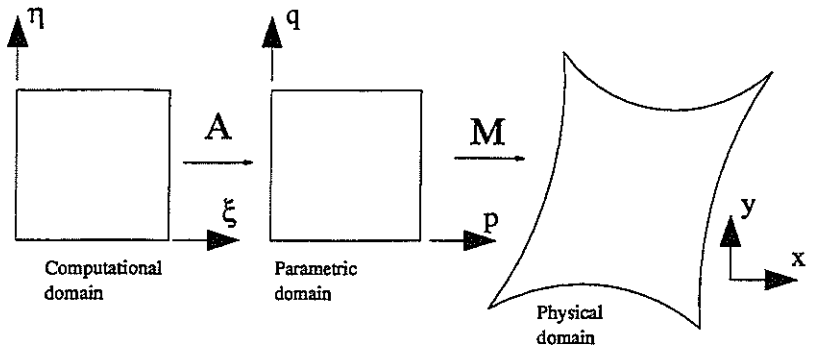

Fig. 10 Grid adaptation by using an adaptation map A that maps the computational domain onto the parametric domain.

physical domain.

An attractive feature of adaptation in the parametric domain is the natural preservation of the global features of the initial grid in the physical domain such as high resolution at parts of the geometry with high curvature. Hence, the initial grid can be considered to be pre-adapted to the geometry, whereas the new grid is in addition adapted to the flow solution.

The problem of grid adaptation in Ω_p can conveniently be formulated in terms of determination of a suitable map A that maps the Cartesian grid in the computational domain Ω_c to the adapted grid in Ω_p (see Fig. 10). Consequently, the adapted grid in the physical domain is the image of the Cartesian grid in Ω_c under the compound map $M \circ A$. Therefore the problem is to find the parametric coordinates p and q as functions of the computational coordinates ξ and η, which is the main topic of the next two sections.

5.1 Anisotropic Diffusion equations in parametric domain

To construct the adaptation map A we apply the theory developed in chapter 4 on the so-called Compound WLS map. It is derived in section 4.2 that such a map can be generated either by minimising a functional in the physical domain, or by minimising an equivalent functional in the parametric domain.

Let the functional $K[\xi(p,q), \eta(p,q)]$ be defined as (see Eqs. (115) and (116)):

$$K[\xi,\eta] = \frac{1}{2}\int_{\Omega_p} \{\frac{\xi_p^2+\eta_p^2}{w_1(\mathbf{p})} + \frac{\xi_q^2+\eta_q^2}{w_2(\mathbf{p})}\}\, d\Omega_p, \tag{150}$$

where the weight functions are strictly positive, bounded, differentiable functions of $(p,q)^T$. The map $(\xi(p,q),\eta(p,q))$ can now conveniently be defined as the map that minimises the functional K. To ensure that the map is boundary conforming the following set of essential boundary conditions is applied:

$$\xi(0,q)=0, \quad \xi(1,q)=1, \quad \eta(p,0)=0, \quad \eta(p,1)=1. \tag{151}$$

As is demonstrated in chapter 3 the above formulated variational problem requires that the Euler-Lagrange (EL) equations be satisfied:

$$\begin{aligned} &\frac{\partial}{\partial p}\frac{\xi_p}{w_1}+\frac{\partial}{\partial q}\frac{\xi_q}{w_2}=0, \\ &\frac{\partial}{\partial p}\frac{\eta_p}{w_1}+\frac{\partial}{\partial q}\frac{\eta_q}{w_2}=0. \end{aligned} \tag{152}$$

These equations are linear and decoupled partial differential equations for the functions $\xi(p,q)$ and $\eta(p,q)$ respectively. Equations (152) and (152) may be interpreted as anisotropic diffusion (AD) equations with diffusion coefficients w_1^{-1} and w_2^{-1} in p, and in q direction, respectively, and form the basis for specification of the inverse adaptation map A^{-1} in Fig. 10.

To complete the variational problem formulation the following set of natural boundary conditions have to be fulfilled:

$$\xi_q(p,0)=0, \quad \xi_q(p,1)=0, \quad \eta_p(0,q)=0, \quad \eta_p(1,q)=0. \tag{153}$$

5.2 Modified Anisotropic Diffusion equations in parametric domain

A disadvantage of grid adaptation in the parametric domain is the possible generation of excessive skew cells in the physical domain when the initial grid contains cells with aspect ratios that are much smaller or larger than one. To illustrate this, let ϕ be the angle between two lines of the adapted grid in the physical domain Ω with constant ξ and η, respectively, and let the initial grid in Ω be orthogonal:

$$\mathbf{x}_p \cdot \mathbf{x}_q = 0. \tag{154}$$

The angle ϕ can be expressed in terms of derivatives of x with respect to the computational coordinates ξ and η:

$$\phi = \arccos\left(\frac{\mathbf{x}_\xi \cdot \mathbf{x}_\eta}{\|\mathbf{x}_\xi\| \, \|\mathbf{x}_\eta\|}\right) \tag{155}$$

which upon substitution of the functions $p(\xi, \eta)$ and $q(\xi, \eta)$ can be written as

$$\phi = \arccos\left(\frac{p_\xi p_\eta + \alpha^2 q_\xi q_\eta}{\sqrt{p_\xi^2 + \alpha^2 q_\xi^2}\sqrt{p_\eta^2 + \alpha^2 q_\eta^2}}\right) \tag{156}$$

where α is proportional to the local aspect ratio of the initial grid in the physical domain:

$$\alpha = \frac{\|\mathbf{x}_q\|}{\|\mathbf{x}_p\|}. \tag{157}$$

From (156) it can be deduced that when the adapted grid in the parametric domain Ω_p is nearly orthogonal, i.e.,

$$\mathbf{p}_\xi \cdot \mathbf{p}_\eta = p_\xi p_\eta + q_\xi q_\eta \ll \sqrt{p_\xi^2 + q_\xi^2}\sqrt{p_\eta^2 + q_\eta^2} = \|\mathbf{p}_\xi\| \, \|\mathbf{p}_\eta\|, \tag{158}$$

the adapted grid in Ω is also nearly orthogonal when $\alpha \approx 1$. However, Eq. (156) shows that when $\alpha \ll 1$ or $\alpha \gg 1$ $\phi \approx 0$ when $p_\xi \, p_\eta \neq 0$ or $q_\xi \, q_\eta \neq 0$, respectively, i.e., the adapted grid in Ω is collapsed. Cells of large or small aspect ratios within the field of CFD occur commonly in boundary-layers. Most Navier-Stokes methods need orthogonal grids in boundary-layers; i.e., grid lines are required to originate from solid surfaces in the normal direction. Moreover, gradients in the normal direction are much larger than gradients in the tangential direction. Hence it is desirable that the grid in the boundary-layer is primarily adapted in the normal direction while the adaptation in the tangential direction is constrained by the orthogonality requirement. To obtain this property of the adaptation algorithm, the adaptation equations (152) and (152) are modified:

$$\begin{aligned} \lambda_1 \frac{\partial}{\partial p}\frac{\xi_p}{w_1} + \lambda_2 \frac{\partial}{\partial q}\frac{\xi_q}{w_2} &= 0, \\ \lambda_1 \frac{\partial}{\partial p}\frac{\eta_p}{w_1} + \lambda_2 \frac{\partial}{\partial q}\frac{\eta_q}{w_2} &= 0, \end{aligned} \tag{159}$$

where λ_1 and λ_2 are functions of p and q. It is noted that by this modification the PDE's are no longer the EL-equations associated with the functional (150). The functions λ_1 and λ_2 are taken

proportionally to the squares of the local spacings of the initial grid in Ω:

$$\lambda_1 \sim \|\mathbf{x}_q\|^2, \quad \lambda_2 \sim \|\mathbf{x}_p\|^2. \tag{160}$$

With this choice the ratio λ_1/λ_2 is proportional to the square of the cell aspect ratio:

$$\lambda_1/\lambda_2 \sim \alpha^2. \tag{161}$$

To illustrate the effect of the modification functions λ_1 and λ_2 let the edge $q = 0$ in the parametric domain Ω_p represent a solid wall in Ω and let the cells of the initial grid along the wall be orthogonal and have very small aspect ratios, i.e., $\alpha \ll 1$. As a consequence $\lambda_1 \ll \lambda_2$ and the modified equations (159) can be approximated as

$$\frac{\partial}{\partial q}\frac{\xi_q}{w_2} \approx 0, \quad \frac{\partial}{\partial q}\frac{\eta_q}{w_2} \approx 0. \tag{162}$$

Since the Neumann boundary conditions (153) are applied we have $\xi_q(p,0) = 0$ and consequently $\xi_q = 0$ for increasing q as long as approximation (162) is valid, i.e., as long as $\lambda_1 \ll \lambda_2$. hence the adapted grid in the boundary-layer is nearly orthogonal. A second implication of approximation (162) is that the equation for η (the second equation of (162)) is similar to Eq. (43) which shows that the grid in the boundary-layer is adapted in normal direction by one-dimensional equidistribution in normal direction of the product $w_2^{-1}\eta_q$.

Finally the boundary value problems based on the modified adaptation equations for the functions $\xi(p,q)$ and $\eta(p,q)$ can conveniently be formulated by means of the linear partial differential operator L defined as

$$L \equiv \Lambda \nabla_p \cdot W^{-1} \nabla_p \tag{163}$$

where ∇_p is the Nabla operator $(\frac{\partial}{\partial p}, \frac{\partial}{\partial q})^T$ and Λ and W are diagonal matrices:

$$\Lambda = \begin{pmatrix} \lambda_1 & 0 \\ 0 & \lambda_2 \end{pmatrix}, \quad W = \begin{pmatrix} w_1 & 0 \\ 0 & w_2 \end{pmatrix}, \tag{164}$$

With the operator L the two boundary-value problems for ξ and η are expressed as:

$$L_p[\xi] = 0, \quad (p,q)^T \in \Omega_p,$$

$$\xi(0,q) = 0, \quad \xi(1,q) = 1,$$
$$\xi_q(p,0) = 0, \quad \xi_q(p,1) = 0, \tag{165}$$

and

$$L_p[\eta] = 0, \quad (p,q)^T \in \Omega_p,$$
$$\eta(p,0) = 0, \quad \eta(p,1) = 1,$$
$$\eta_p(0,q) = 0, \quad \eta_p(1,q) = 0. \tag{166}$$

The weight functions w_1 and w_2 in (164) are specified in the next section.

5.3 Weight functions

In this section the weight functions w_1 and w_2 that control the solution of Eqs. (159) are specified. Two questions are important:

- how can the weight functions be chosen such that the accuracy of the numerical flow solution is improved upon obtaining the flow solution on the new adapted grid, and
- how is the specification of the weight functions influenced by formulating the adaptation problem in the parametric domain.

Both questions can be answered to some extent for one-dimensional problems with the flow solution characterised by a single scalar function.

Let $Q \in \mathcal{R}$ be a scalar function of $x \in [0, L] \subset \mathcal{R}$ that represents a flow solution in one-dimensional physical space, and let the adapted computational grid be determined by the one-dimensional equidistribution principle (30), which can be written as:

$$\xi_x = c\, w, \quad c^{-1} = \int_0^L w dx, \tag{167}$$

where c is an integration constant. The main goal of this section is to provide a smooth distribution of the flow solution over the computational domain, i.e., small values of $Q_{\xi\xi}$.

Let the weight function w be a positive function of x which ensures that $\xi_x > 0$. With $Q_x = Q_\xi \xi_x$ and $Q_{xx} = Q_{\xi\xi}\xi_x^2 + Q_\xi \xi_{xx}$, it is possible to express $Q_{\xi\xi}$ as:

$$Q_{\xi\xi} = \frac{1}{c^2 w^2} \left(Q_{xx} - \frac{w_x}{w} Q_x\right) . \tag{168}$$

hence when Q_x is positive for all $x \in [0, L]$, the second derivative is identically zero if the weight function is taken as $w = Q_x$.

An equivalent equidistribution statement can be formulated in the parametric domain by substitution of $\xi_x = \xi_p p_x$ into Eq. (167), $Q_x = Q_p p_x$ and dividing by p_x:

$$\xi_p = c\, w^*, w^* = Q_p. \tag{169}$$

In the particular case of positive Q_x, and taking $w = Q_x$ and $w^* = Q_p$, the formulation in the parametric domain is not only equivalent but also similar to the formulation in the physical domain. However, in practice it is not possible to take $w^* = Q_p$ since this leads to infinite grid spacing when $Q_p = 0$.

As an alternative, the equidistribution statement is modified to

$$\xi_p = c\, w^*, w^* = \sqrt{1 + Q_p^2}. \tag{170}$$

Consequently $w^* = 1$ when $Q_p = 0$ but $w^* \rightarrow |Q_p|$ when $Q_p^2 \gg 1$. The equivalent statement formulated in the physical domain is not similar any more:

$$\xi_x = c\, w, \quad w = \sqrt{p_x^2 + Q_x^2}. \tag{171}$$

When the flow solution is uniform, e.g., $Q_x \equiv 0$, the weight function w is equal to p_x and the initial grid is retained. This is in contrast with the situation that the equidistribution statement is directly formulated in the physical domain with p_x^2 replaced by unity, which results in a uniform grid when $Q_x \equiv 0$.

The analysis of one-dimensional problems presented above with the flow solution represented by a single scalar function can be used as a guide for an extension to two dimensions with the flow solution represented by a vector function. In 2D the weight functions w_1 and w_2 that govern the solution of equations (159) are chosen as

$$w_1 = \sqrt{1 + ||\boldsymbol{Q}_p||^2}, \quad w_2 = \sqrt{1 + ||\boldsymbol{Q}_q||^2}, \tag{172}$$

where $\boldsymbol{Q} \in \mathcal{R}^n$ represents the flow solution with all components scaled to $O(1)$ and where $||.||$ denotes the L_2 norm.

Defining w_1 and w_2 according to Eq. (172) implies that if the flow solution $\boldsymbol{Q}$ is a bilinear function of p and q, i.e.,

$$\boldsymbol{Q}_{pp} = 0, \quad \boldsymbol{Q}_{qq} = 0, \tag{173}$$

then the initial grid is optimal in the sense that the flow solution is as smooth as possible in the parametric domain. In that case the weight functions satisfy

$$\frac{\partial w_1}{\partial p} = 0, \quad \frac{\partial w_2}{\partial q} = 0, \tag{174}$$

such that the trivial solutions $\xi(p,q) \equiv p$, $\eta(p,q) = q$ for the boundary value problems (151), (153) and (159) are obtained. Hence, the initial optimal grid is retained.

5.4 Correction maps for 2D Airfoils

At this stage it is convenient to describe a set of additional maps that are necessary to adapt C-topology grids around two-dimensional airfoils; see fig. 11. The problem is that the grid line

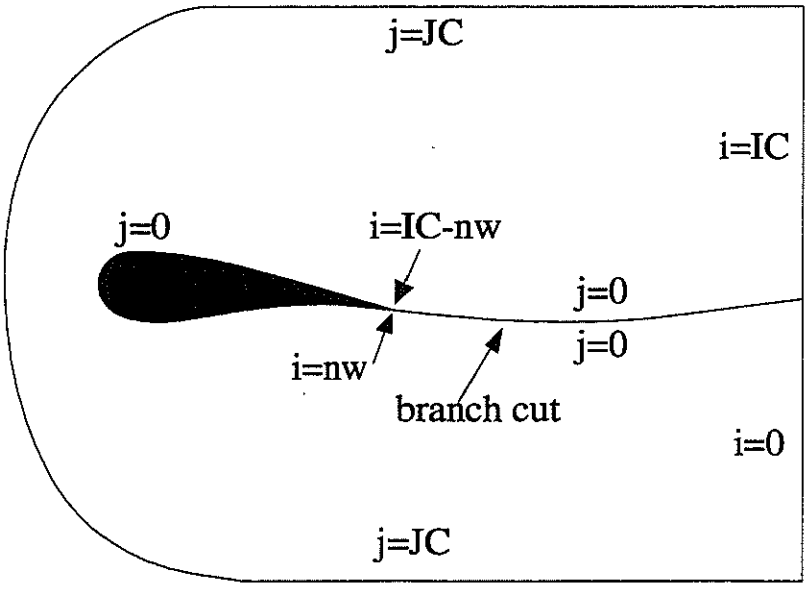

Fig. 11 C-topology around two-dimensional airfoil.

$i = i_0$ must be connected to the grid line $i = IC - i_0$ (IC is the number of cells in i-direction) if the first point $j = 0$ lies on the wake line, i.e., the part of the grid line $j = 0$ which does not belong to the airfoil contour. Formally the adaptation equations can be transformed to the physical domain and the roles of the physical coordinates acting as independent variables and

the computational coordinates acting as dependent variables can be interchanged analytically (see lemma 3.1). In this way the branch cut could be treated with complete continuity.

The computational method that is used in this study to solve the Reynolds-Averaged Navier-Stokes (RANS) equations, employs the Baldwin-Lomax turbulence model. This method requires that the wake center line coincides with the branch cut and that the grid be orthogonal across the viscous wake. The above-described branch cut treatment does not meet these requirements.

To meet the requirements of both grid continuity and orthogonality across the viscous wake, it is proposed to apply correction maps such that the initial adaptation map A is modified minimally. The position of the branch cut is pre-determined by the parametrisation of the physical domain and could be adapted to the actual position of the wake center line. It should be noted that application of correction maps is a consequence of the computational method requirements, not a consequence of using a parametric domain.

Two correction maps, C^{**} and C^{*}, are defined. The map C^{**} ensures that the grid line with $i = n_w$ and the grid line with $i = IC - n_w$, where n_w is the desired number of cells along the wake line, have common begin points at the trailing edge of the airfoil. The map C^{*} provides coinciding end points (continuity) along the rest of the wake line. Both maps are essentially one-dimensional,

$$C^{*} : (\xi, \eta) \mapsto (\xi^{*}, \eta), \quad C^{**} : (\xi^{*}, \eta) \mapsto (\xi^{**}, \eta), \tag{175}$$

hence, C^{*} and C^{**} are determined by the functions $\xi^{*}(\xi)$ and $\xi^{**}(\xi^{*})$, respectively.

The function $\xi^{**}(\xi^{*})$ is taken as

$$\xi^{**}(\xi^{*}) = a_3 \xi^{*3} + a_2 \xi^{*2} + a_1 \xi^{*} + a_0, \tag{176}$$

which minimises the integral

$$\int_0^1 \{\frac{d^2 \xi^{**}}{d\xi^{*2}}\}^2 \, d\xi^{*}. \tag{177}$$

The constants a_i, $i = 1, 2, 3$, are determined from four compatibility conditions:

$$\begin{aligned} \xi^{**}(0) &= 0, \\ \xi^{**}(\frac{n_w}{IC}) &= \xi_L^{**}, \\ \xi^{**}(1 - \frac{n_w}{IC}) &= \xi_R^{**}, \\ \xi^{**}(1) &= 1, \end{aligned} \tag{178}$$

with ξ_L^{**} and ξ_R^{**} implicitly defined by

$$p(\xi_L^{**}) = \frac{n_w}{IC}, \quad p(\xi_R^{**}) = 1 - \frac{n_w}{IC}. \tag{179}$$

Hence, upon application of C^* only, i.e., $\xi^* \equiv \xi$, both the lower and upper side of the wake contain n_w cells and the grid lines $i = n_w$ and $i = IC - n_w$ have common end points at the trailing edge. To obtain grid line continuity over the wake line, the function $\xi^*(\xi)$ is defined on the intervals $0 \leq \xi < n_w/IC$ and $1 - n_w/IC < \xi \leq 1$ by the implicit equation

$$p(\xi^{**}(\xi^*(\xi))) = \frac{1}{2}\{p(\xi^{**}(\xi)) + 1 - p(\xi^{**}(1 - \xi))\}, \tag{180}$$

where the right-hand side represents the mean of the upper and lower grid point distributions along the wake line upon application of C^* only. On the remaining interval $n_w/IC \leq \xi \leq 1 - n_w/IC$, $\xi^*(\xi)$ is taken as

$$\xi^*(\xi) = b_3\xi^3 + b_2\xi^2 + b_1\xi + b_0, \tag{181}$$

which minimises the integral

$$\int_0^1 \{\frac{d^2\xi^*}{d\xi^2}\}^2 \, d\xi. \tag{182}$$

and provides grid smoothness at the trailing edge if the constants b_i are determined from the following compatibility conditions:

$$\begin{aligned} \xi^*(\frac{n_w}{IC}) &= \frac{n_w}{IC}, \\ \xi^*(1 - \frac{n_w}{IC}) &= 1 - \frac{n_w}{IC}, \end{aligned}$$

$$\frac{d\xi^*}{d\xi}(\frac{n_w}{IC}) = \lim_{\xi \uparrow \frac{n_w}{IC}} \frac{d\xi^*}{d\xi}(\xi),$$
$$\frac{d\xi^*}{d\xi}(1-\frac{n_w}{IC}) = \lim_{\xi \downarrow 1-\frac{n_w}{IC}} \frac{d\xi^*}{d\xi}(\xi). \tag{183}$$

It is easily verified that the application of both C^* and C^{**} yields the following properties:

(i) $p(\xi^{**}(\xi^*(n_w/IC))) = n_w/IC$,
(ii) $p(\xi^{**}(\xi^*(1-n_w/IC))) = 1 - n_w/IC$, and
(iii) $p(\xi^{**}(\xi^*(\xi))) = 1 - p(\xi^{**}(\xi^*(1-\xi)))$
for $0 \leq \xi < n_w/IC$ and $1 - n_w/IC, \xi \leq 1$.

Properties (i) and (ii) ensure common end points at the trailing edge while property (iii) takes care of continuity over the wake line.

5.5 Discretisation and numerical solution method

Instead of analytically interchanging the dependent and independent variables of the grid adaptation equations (159) by application of lemma 3.1, which is commonly applied in the literature, the boundary-value problems (165) and (166) are directly solved for the functions $\xi(p,q)$ and $\eta(p,q)$ in this thesis. In a second additional step these functions are numerically inverted to the functions $p(\xi,\eta)$ and $q(\xi,\eta)$. An advantage of the present method compared to the ones found in the literature is that two decoupled, linear, PDE's are to be solved instead of two coupled, nonlinear, PDE's. A disadvantage is the need for an additional computational step to invert the functions $\xi(p,q)$ and $\eta(p,q)$.

Let the initial uniform rectangular grid in the parametric domain consist of IC cells in the p-direction and of JC cells in the q-direction, where IC and JC are positive integers. The differential operator L_p defined by Eq. (163) can be approximated by a second-order accurate difference operator L_p^h by replacing derivatives by central differences. At an interior grid point ($0 < i < IC$ and $0 < j < JC$) L_p^h is defined as:

$$\begin{aligned} L_p^h[.] \equiv\ & \beta_{north}(.)_{i,j+1} + \beta_{south}(.)_{i,j-1} \\ & + \beta_{centre}(.)_{i,j} \\ & + \beta_{east}(.)_{i+1,j} + \beta_{west}(.)_{i-1,j}, \end{aligned} \tag{184}$$

with

$$\begin{aligned}
\beta_{north} &= \frac{1}{\Delta q^2}\frac{2\lambda_2^{i,j}}{w_2^{i,j+1}+w_2^{i,j}},\\
\beta_{south} &= \frac{1}{\Delta q^2}\frac{2\lambda_2^{i,j}}{w_2^{i,j-1}+w_2^{i,j}},\\
\beta_{east} &= \frac{1}{\Delta p^2}\frac{2\lambda_1^{i,j}}{w_1^{i+1,j}+w_1^{i,j}},\\
\beta_{west} &= \frac{1}{\Delta p^2}\frac{2\lambda_1^{i,j}}{w_1^{i-1,j}+w_1^{i,j}},\\
\beta_{centre} &= -(\beta_{north}+\beta_{south}+\beta_{east}+\beta_{west}),
\end{aligned} \tag{185}$$

where the subscripts and superscripts i, j indicate at which node the functions are evaluated, with $\Delta p = 1/IC$ and $\Delta q = 1/JC$. The normal derivatives at the boundary $\partial\Omega_p$ are approximated by one-sided differences, e.g.,

$$\frac{\partial}{\partial p}(.)_{0,j} \approx \frac{1}{\Delta p}\{-\frac{3}{2}(.)_{0,j} + 2(.)_{1,j} - \frac{1}{2}(.)_{2,j}\}, \tag{186}$$

which is also second-order accurate. For the first derivative with respect to q a similar expression is used.

The system of linear equations that results from the above-described discretisations of the boundary-value problems (165) for $\xi(p,q)$ and (166) for $\eta(p,q)$ are solved by red-black Gauss-Seidel relaxation. A correction-storage multi-grid technique (see e.g. Refs. [11] and [73]) with fixed V-cycles is used to increase the rate of convergence.

The solution of the above-described linear system provides values for ξ and η in all points of the uniform grid in Ω_p and determines the inverse adaptation map A^{-1} of Fig. 10. The map A is determined in discrete form by a set of points $\mathbf{p}_{i,j} = (p_{i,j}, q_{i,j})^T$ that satisfies the following set of algebraic equations:

$$\boldsymbol{\xi}(\mathbf{p}_{i,j}) = (\frac{i}{IC}, \frac{j}{JC})^T, \quad i \in [0, IC], \quad j \in [0, JC], \tag{187}$$

where $\boldsymbol{\xi}(\mathbf{p}) = (\xi(\mathbf{p}), \eta(\mathbf{p}))^T$ is a piecewise bilinear interpolation of the points $\xi_{i,j}$ and $\eta_{i,j}$. When Eq. (187) is satisfied then for all points $(i/IC, j/JC)^T$ of a uniform grid in the computational domain Ω_c associated values of p and q are known, which determines the adaptation map A. In

order to find the set $\mathbf{p}_{i,j}$, the following iteration procedure is carried out:

$$\mathbf{p}_{i,j}^{n+1} = \mathbf{p}_{i,j}^{n} - \Delta t\{\boldsymbol{\xi}(\mathbf{p}_{i,j}^{n}) - (\frac{i}{IC}, \frac{j}{JC}\}^T. \tag{188}$$

This can be interpreted as an explicit time-stepping scheme with time step Δt ($\Delta t = 0.1$ in this chapter). The stationary solution of Eq. (188) satisfies Eq. (187).

Finally the two correction maps C^* and C^{**} of section 5.4 are applied and the obtained adapted grid in the parametric domain Ω_p is mapped to the physical domain Ω by the map M, see Fig. 10. At all stages piecewise linear or bilinear interpolation is used to approximate the maps C^*, C^{**}, A and M.

5.6 Examples of numerical grid adaptation

As a first example, the adaptation algorithm described in the previous section is applied to a problem representative for the interaction of an oblique shock and a boundary-layer. The "flow solution" is represented by a single scalar function $u(x, y)$,

$$u(x, y) = \tanh(10y) - \tanh(5(x - 2) - 10y), \tag{189}$$

on the rectangular domain $0 \leq x \leq 4$, $0 \leq y \leq 2$. The initial grid of 32x16 cells and a surface plot of u as a function of the computational coordinates ξ and η are shown in Fig. 12a in Fig. 13a respectively. Figures 189b-189d show the grid after 1,2, and 10 adaptations, respectively, where the first adapted grid is taken as the initial grid for the second adaptation, the second adapted grid is taken as the initial grid for the third adaptation and so on. The modification functions λ_1 and λ_2 in (159a) and (159b) have been taken as:

$$\lambda_1 = \|\mathbf{x}_q\|^2, \quad \lambda_2 = \|\mathbf{x}_p\|^2. \tag{190}$$

The first adapted grid shows the cell concentration at both the "shock" and the "boundary-layer". The effects of piecewise bilinear interpolation can be observed in the boundary-layer and some wiggles seem to be present which may be caused by odd-even decoupling in the discretised differential equations. These are minor flaws, however, and the adapted grid is acceptable. More adaptation cycles result in stronger cell concentrations and skew cells at the "shock", but they also show the robustness of the algorithm since the last adapted grid (Fig. 189d) is still a regular non-overlapping grid. Figures 13.a-13.d show the function u in the computational domains associated with the initial grid and the grids after 1,2, and 10 adaptations, respectively. Already after

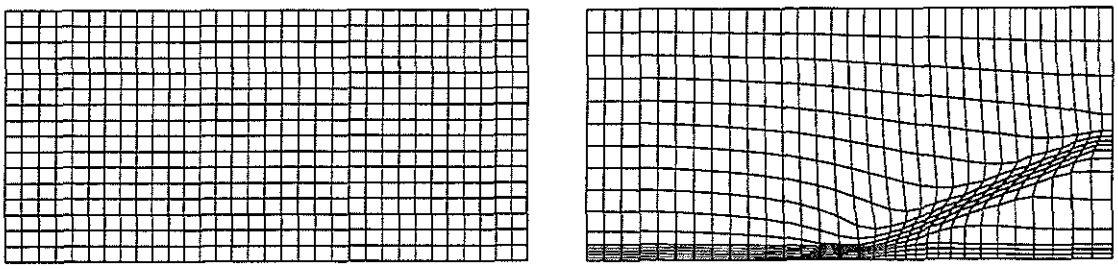

a) Initial grid.

b) Grid after one adaptation.

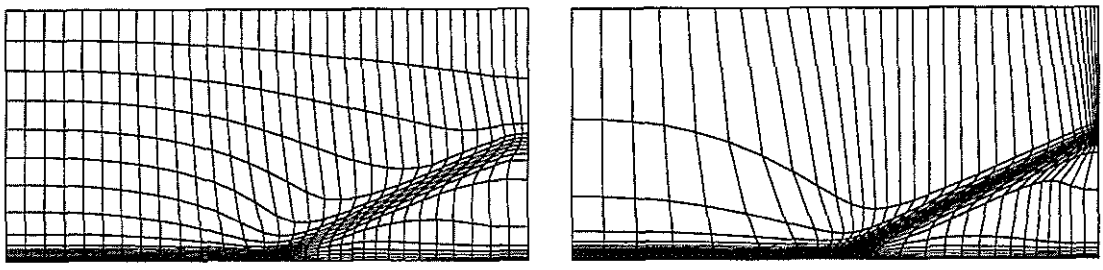

c) Grid after two adaptations.

d) Grid after ten adaptations.

Fig. 12 Initial grid and adapted grids for oblique-shock boundary-layer simulation.

one adaptation the gradient of u in the computational domain decreases significantly, and after 10 adaptations the "shock" and the "boundary-layer" are no longer evident as sharp gradients, because of the many points attracted to these features. Finally it may be noted that the first adaptation is the most effective one, see Figs. 13.a-13.d, while the following adaptations show less dramatic effects.

5.7 Applications to 2D aerodynamic problems

5.7.1 RAE2822 airfoil

Consider the adaptation of a C-topology grid around the RAE2822 airfoil to be used for the solution of the Reynolds-Averaged Navier-Stokes equations. The flow conditions are transonic: $M_\infty = 0.725$, $Re_\infty = 6.5 \times 10^6$, $\alpha = 2.44°$. Laminar-turbulent transition of the boundary-layer is enforced at a distance of 3% chord length from the leading edge both at the upper and the lower surface. The structured C-topology grid consists of 352×64 cells with 256 cells along the airfoil,

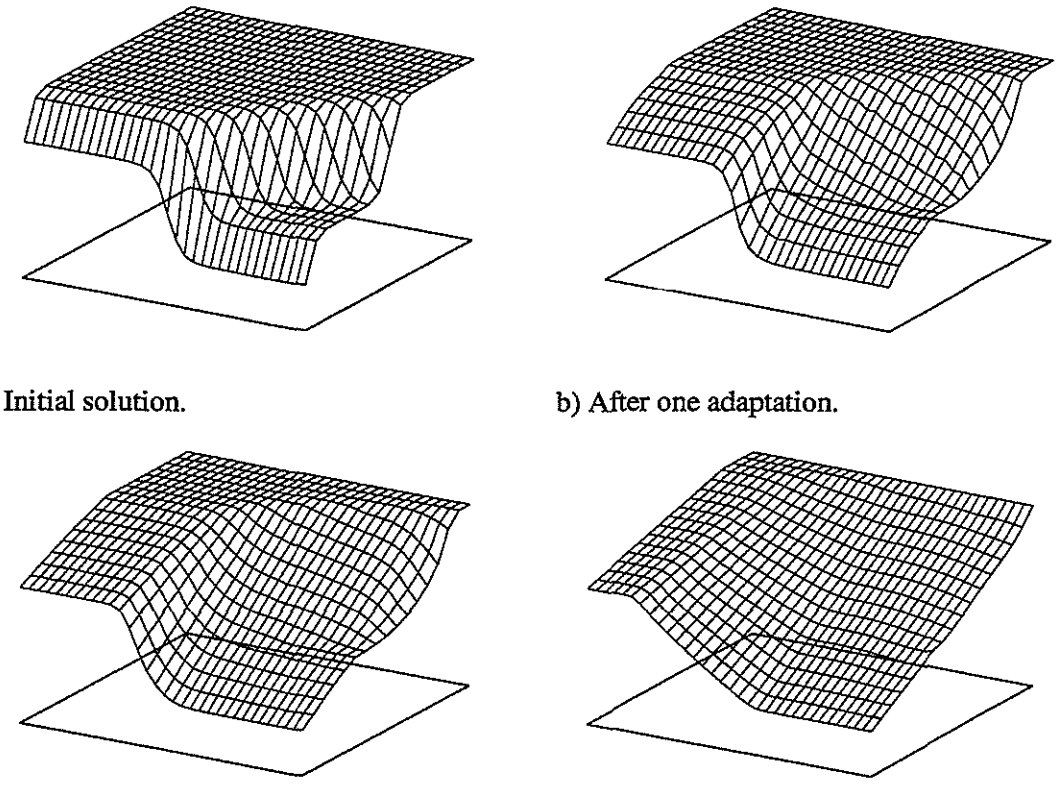

a) Initial solution.

b) After one adaptation.

c) After two adaptations.

d) After ten adaptations.

Fig. 13 Scalar monitor function $u(\xi, \eta)$ in the computational domains associated with the initial and adapted grids for oblique-shock boundary-layer type of flow field.

48 cells at both sides of the wake line, and 64 cells in the normal direction. The flow equations are solved with a vertex-based finite-volume scheme combined with a modified Baldwin-Lomax turbulence model, described by Brandsma [10].

Before discussing the adaptation results we have to choose the appropriate form of the modification functions λ_i, $i = 1, 2$, that control the adaptation equations in the boundary-layer (see Eq. (160)).

For each af the cases presented one single adaptation is carried out starting with an initial flow solution calculated on the initial grid. The initial grid is generated with an algebraic grid generator [10].

Fig. 14a shows the initial grid around the leading edge of the RAE2822 airfoil showing the initially highly stretched grid in the region near the airfoil where the boundary-layer is expected to develop.

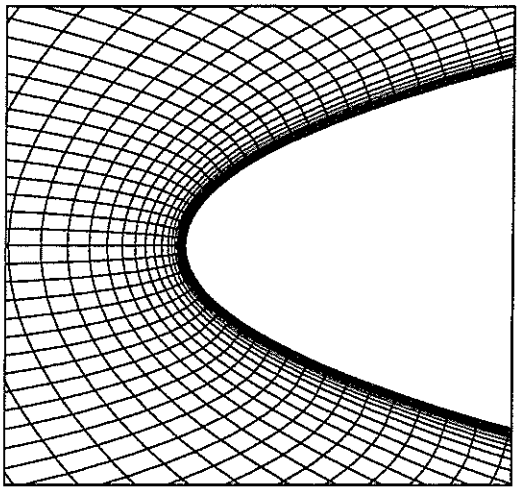

a) Initial grid.

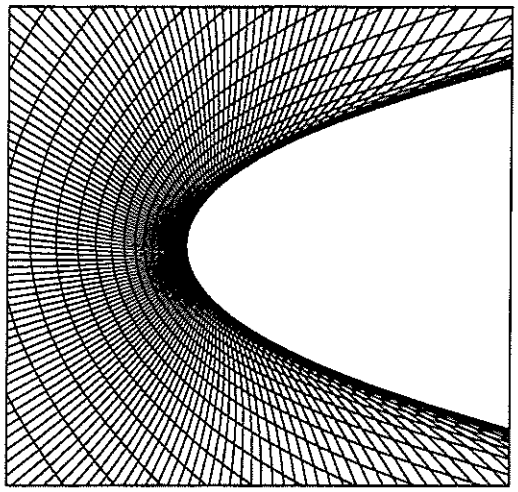

b) Adapted grid, $\lambda_1 \equiv 1$, $\lambda_2 \equiv 1$.

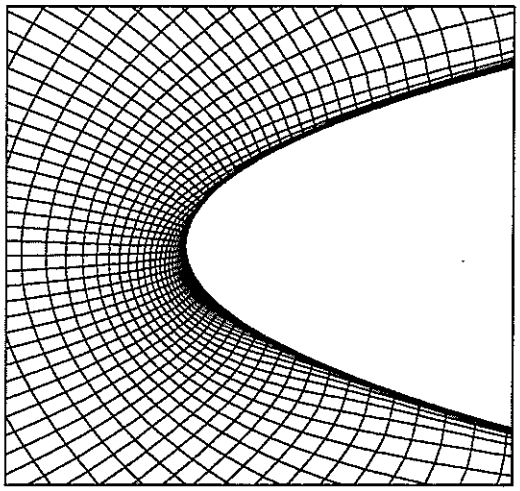

c) Adapted grid,
$\lambda_1 = \|\mathbf{x}_q\|$, $\lambda_2 = \|\mathbf{x}_p\|$.

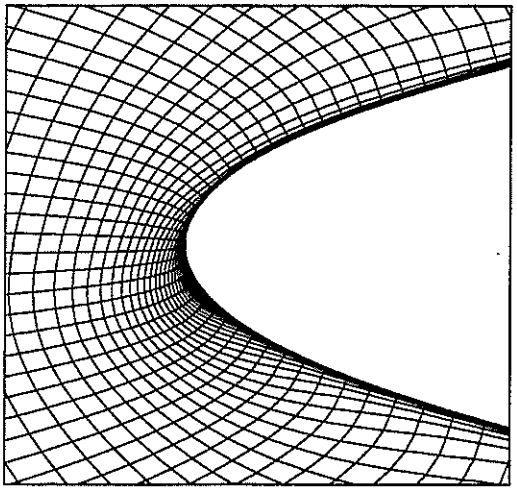

d) Adapted grid,
$\lambda_1 = \|\mathbf{x}_q\|^2$, $\lambda_2 = \|\mathbf{x}_p\|^2$.

Fig. 14 Initial and adapted grids around nose of RAE2822 airfoil using different modification functions.

Fig. 14b shows the adapted grid using $\lambda_1 \equiv 1$, $\lambda_2 \equiv 1$. It can be observed that the grid indeed is strongly adapted to the flow expansion above the airfoil nose, but has associated with it highly skewed cells. This is in agreement with the analysis of section 5.2.

When $\lambda_1 = \|\mathbf{x_q}\|$, $\lambda_2 = \|\mathbf{x_p}\|$ is chosen, see Fig. 14c, the adapted grid outside the boundary-layer region is improved significantly with respect to skewness; however, inside the boundary-layer (not shown) the grid is still skewed unacceptably. When $\lambda_1 = \|\mathbf{x_q}\|^2$, $\lambda_2 = \|\mathbf{x_p}\|^2$ is chosen, see Fig. 14d the adapted grid is also orthogonal inside the boundary-layer region (not shown) while the grid adaptation in normal direction dominates that in the direction along the airfoil. Unfortunately this choice of Λ results in a thinning out of cells in the tangential direction; compare Figs. 14a, 14b and 14d. In order to obtain both one-dimensional equidistribution in the normal direction inside the boundary-layer region as well as adaptation in the tangential direction, the latter controlled by the outer flow at the edge of the boundary-layer, the following choice for the modifications is proposed:

$$\lambda_1 = w_1^2\|\mathbf{x}_q\|^2, \quad \lambda_2 = w_2^2\|\mathbf{x}_p\|^2. \tag{191}$$

Because just outside the boundary-layer the component of the flow solution gradient in normal direction is much smaller than the flow solution gradient in tangential direction ($w_2 \ll w_1$), the adaptation in tangential direction dominates over the adaptation in normal direction when $\|\mathbf{x}_q\|/\|\mathbf{x}_p\|$ is not too small. The resulting adapted grid is depicted in Fig. 15a, which shows that

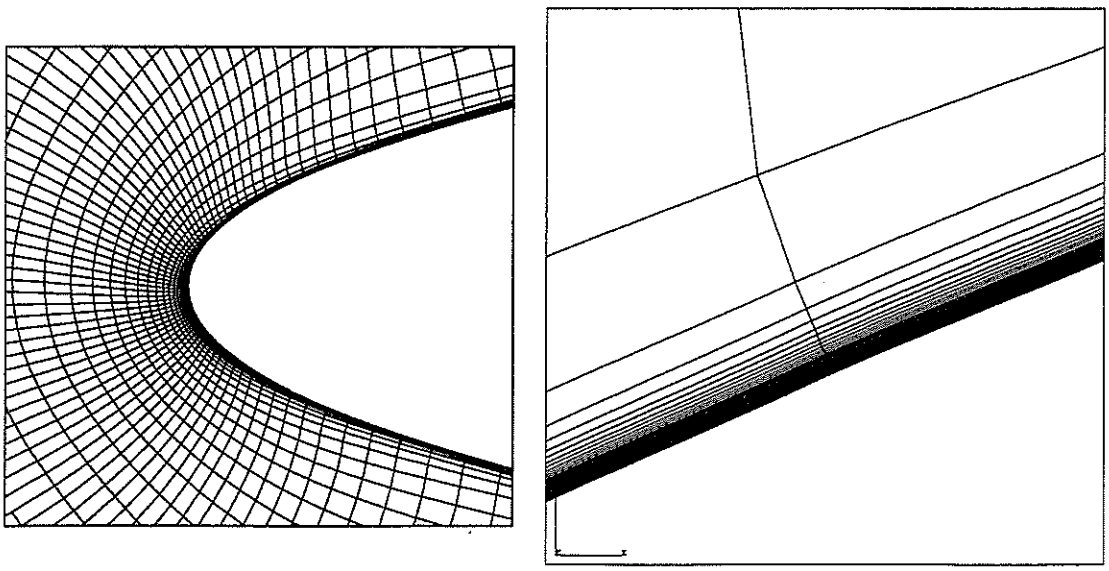

a) Adapted grid, $\lambda_1 = w_1^2\|\mathbf{x}_q\|$, $\lambda_2 = w_2^2\|\mathbf{x}_p\|$.

b) Adapted grid, close-up showing orthogonality.

Fig. 15 Adapted grid around nose of RAE2822 airfoil using alternative modification functions.

grid lines normal to the airfoil enter the boundary-layer region orthogonally, while simultaneously

around the leading edge the grid is significantly refined in the tangential direction, compare Figs. 14a and 15a. Inside the boundary-layer region the adapted grid is also orthogonal, see Fig. 15b. Hence choice (191) for the modification functions is used in the remainder of this chapter. Large

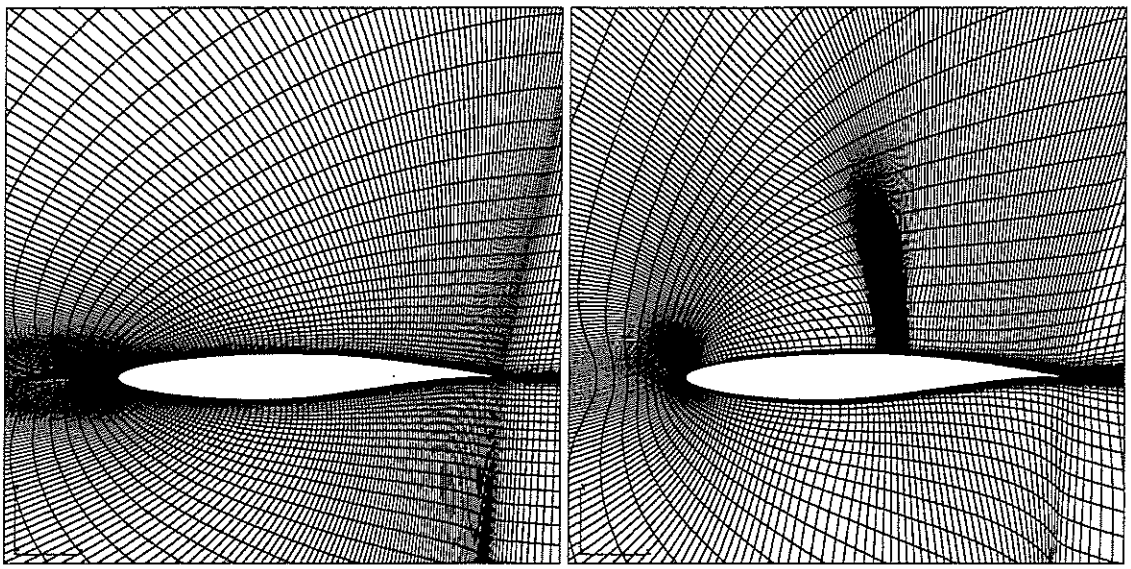

a) Initial grid (352 × 64 cells). b) Adapted grid (352 × 64 cells).

Fig. 16 Initial and adapted grid around RAE2822 airfoil (transonic flow conditions: $M_\infty = 0.725$, $Re_\infty = 6.5 \times 10^6$, $\alpha = 2.44°$).

parts of the initial and adapted grid are shown in Fig. 16. The execution time needed to solve the adaptation equations and to invert the inverse adaptation map amounts to about 75 CP seconds on the NEC SX-3 supercomputer (single processor), used for 1254 V-cycles on the ξ-equation, 974 V-cycles on the η-equation, and 961 iterations on the inversion equations to decrease the maximum residuals 11, 12, and 14 orders of magnitude, respectively. Typically a flow calculation requires approximately 3 minutes. The pressure distributions along the airfoil surface are shown in Figs. 17a-b , and the Mach number contours are given in Figs. 18a-b. Both the shock and the leading edge expansion are better resolved on the adapted grid. Behind the shock the probably spurious kink in the pressure distribution has disappeared. The Mach number distribution just outside the boundary-layer has become more uniform in the normal direction. The lift coefficient changed from 0.7714 to 0.7926 (2.7%), the drag coefficient changed from 0.01259 to 0.01248 (1 count), and the pitching coefficient changed from -0.09125 to -0.09399 (3%). A close-up of the grid in the shock region near the airfoil is presented in Fig. 19, showing a substantial improvement of the resolution in tangential direction. Simultaneously the resolution in normal direction is changed dramatically, reflecting the increasing thickness of the boundary-layer behind

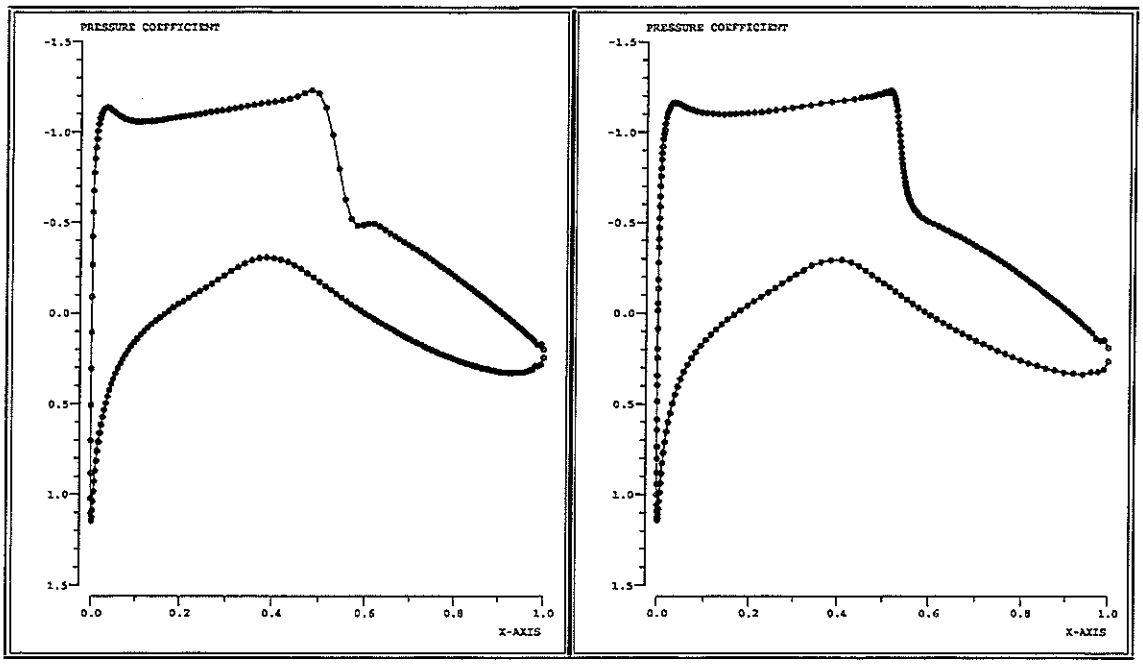

a) Initial grid (352 × 64 cells). b) Adapted grid (352 × 64 cells).

Fig. 17 Pressure distribution from solution on initial and on adapted grid around RAE2822 airfoil (transonic flow conditions: $M_\infty = 0.725$, $Re_\infty = 6.5 \times 10^6$, $\alpha = 2.44°$).

the shock. Figs. 20 and 21 show the Mach number and pressure coefficient distributions in that area. Both distributions have gained much more detail upon adaptation, such as the beginning of the development of a "λ-shock".

It is also interesting to see how the flow solution in the computational domain changes due to adaptation of the grid and the recalculation of the flow. In Figs. 22a-22b the Mach number distribution is depicted in the computational domain. Both the expansion region at the leading edge and the boundary-layer are more smoothly distributed in the adapted case (Fig. 22b). Initially, see Fig. 22a, the shock appears as a discontinuity both inside and outside the boundary-layer. Inside the boundary-layer the Mach number also jumps from high to low values but these jumps do not represent a shock in the physical sense because the flow in front of the jump is subsonic. After adaptation and recalculation the shock again appears as a discontinuity, but now outside the boundary-layer. This is in agreement with the observation that the flow is locally inviscid. Inside the boundary-layer the jump in the Mach number is decreased significantly due to the strong increase of grid resolution. Upon grid adaptation in the trailing-edge region the gradients in the computational domain are increased in the boundary-layer. This appears to be caused by

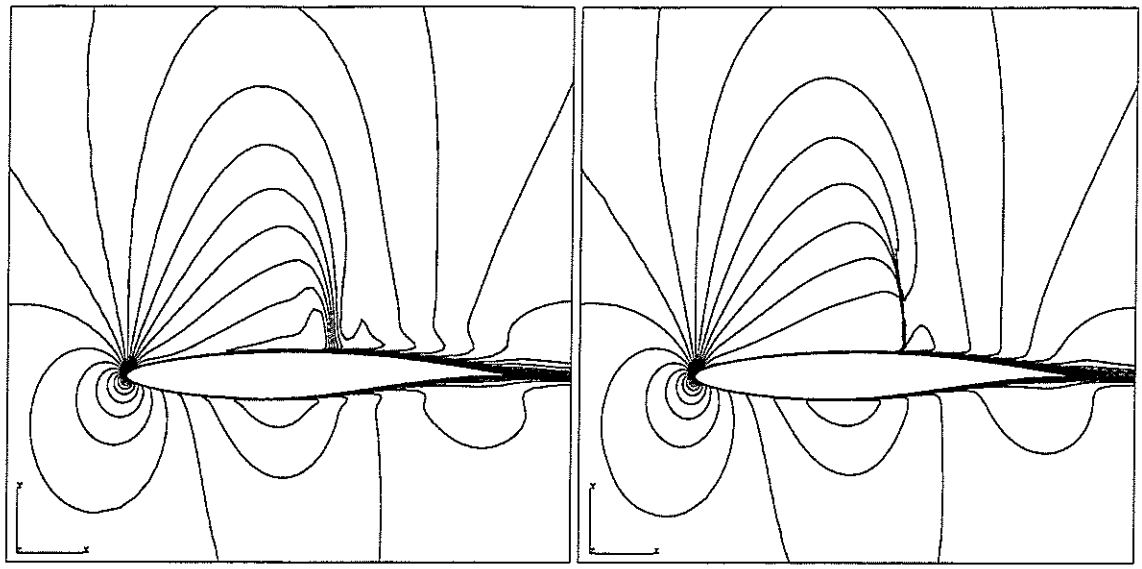

a) Initial grid (352 × 64 cells). b) Adapted grid (352 × 64 cells).

Fig. 18 Mach number distribution from solution on initial and on adapted grid around RAE2822 airfoil (transonic flow conditions: $M_\infty = 0.725$, $Re_\infty = 6.5 \times 10^6$, $\alpha = 2.44°$, $\Delta M = 0.05$*).*

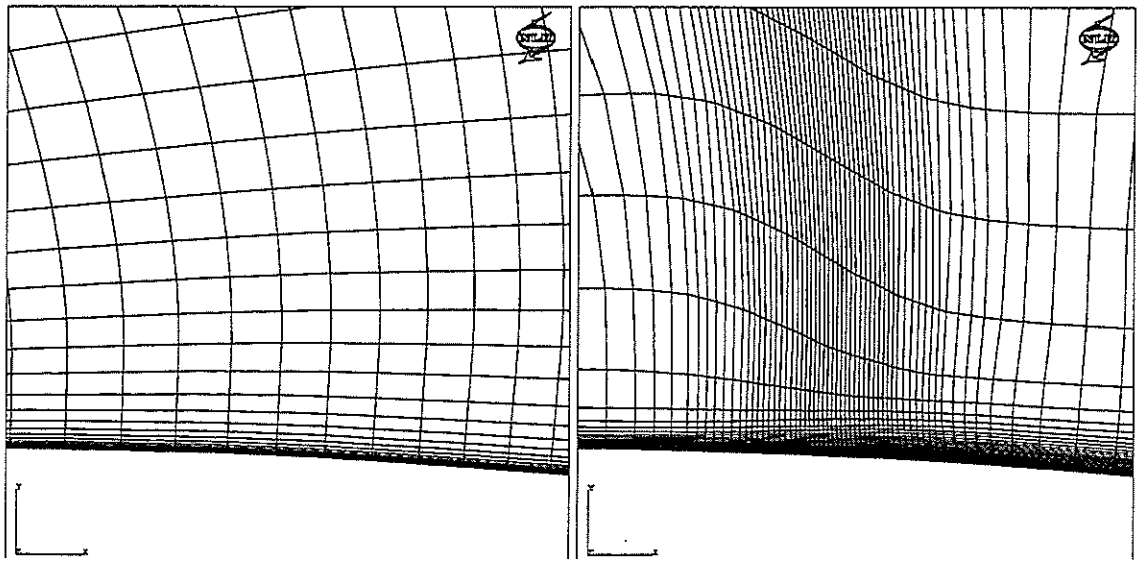

a) Initial grid (352 × 64 cells). b) Adapted grid (352 × 64 cells).

Fig. 19 Close-up of shock-region of initial and adapted grid around RAE2822 airfoil (transonic flow conditions: $M_\infty = 0.725$, $Re_\infty = 6.5 \times 10^6$, $\alpha = 2.44°$*).*

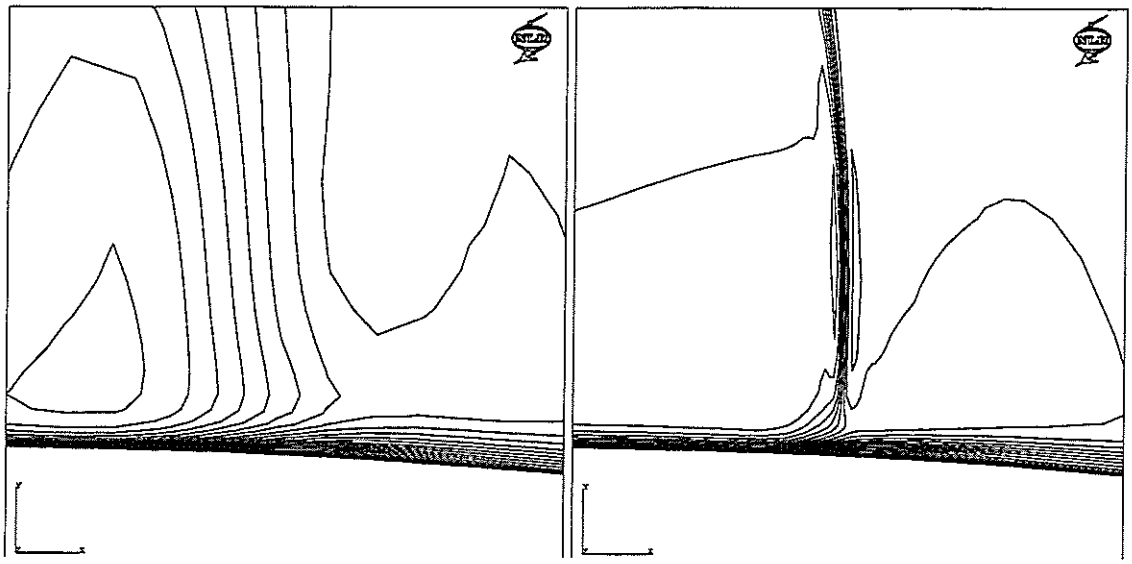

a) Initial grid (352 × 64 cells). b) Adapted grid (352 × 64 cells).

Fig. 20 Close-up of Mach number contours in shock-region for initial and for adapted grid around RAE2822 airfoil (transonic flow conditions: $M_\infty = 0.725$, $Re_\infty = 6.5 \times 10^6$, $\alpha = 2.44°$, $\Delta M = 0.05$*).*

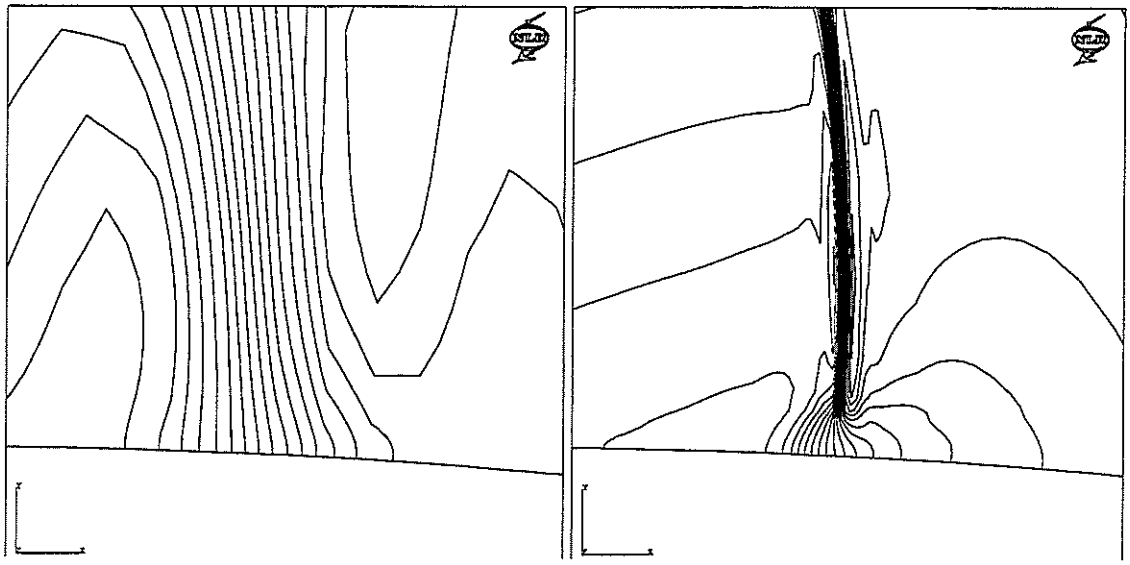

a) Initial grid (352 × 64 cells). b) Adapted grid (352 × 64 cells).

Fig. 21 Close-up of pressure coefficient contours in shock region for initial and for adapted grid around RAE2822 airfoil (transonic flow conditions: $M_\infty = 0.725$, $Re_\infty = 6.5 \times 10^6$, $\alpha = 2.44°$, $\Delta C_p = 0.05$*).*

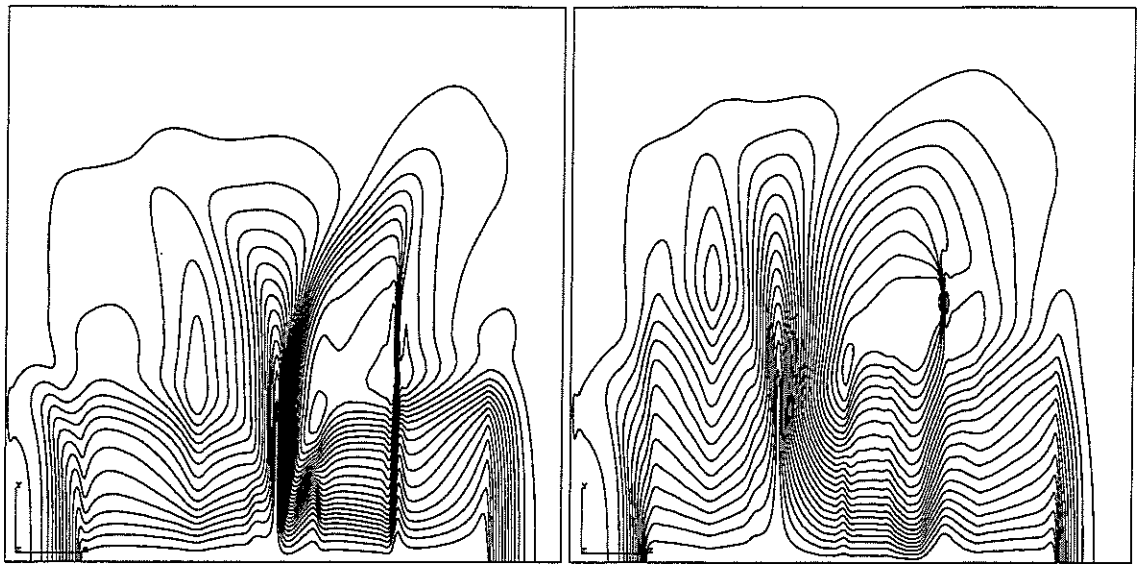

a) Initial grid (352 × 64 cells). b) Adapted grid (352 × 64 cells).

Fig. 22 Mach number distribution in the computational domain for solution on initial and adapted grid around RAE2822 airfoil (transonic flow conditions: $M_\infty = 0.725$, $Re_\infty = 6.5 \times 10^6$, $\alpha = 2.44°$, $\Delta M = 0.05$*).*

the modification function λ_1, which is less sensitive for the flow gradient component along the surface when the grid has locally very high cell aspect ratios while outside the boundary layer the flow gradient is relatively small. In Figs. 23a-23b the pressure-coefficient distribution in the computational domain is depicted. The same features as in the Mach number distributions can be observed. Note that across the boundary-layer the pressure is approximately constant which is in agreement with the results of boundary-layer theory.

In addition to the above described qualitative judgement of the grid adaptation results we can also make a comparison with results obtained on a globally refined grid involving twice as many points in each coordinate direction. In addition we can make a comparison with experimental data and with computational results obtained by other researchers. To enable such comparison we use slightly different flow conditions: $M_\infty = 0.734$, $Re_\infty = 6.5 \times 10^6$, $\alpha = 2.54°$, while again transition is fixed at 3% chord at both the upper and the lower side of the airfoil. The calculations described here have been taken from Ref. [52]. The experimental data set for this flow condition is described in [16]. The computational data set for this flow condition obtained by

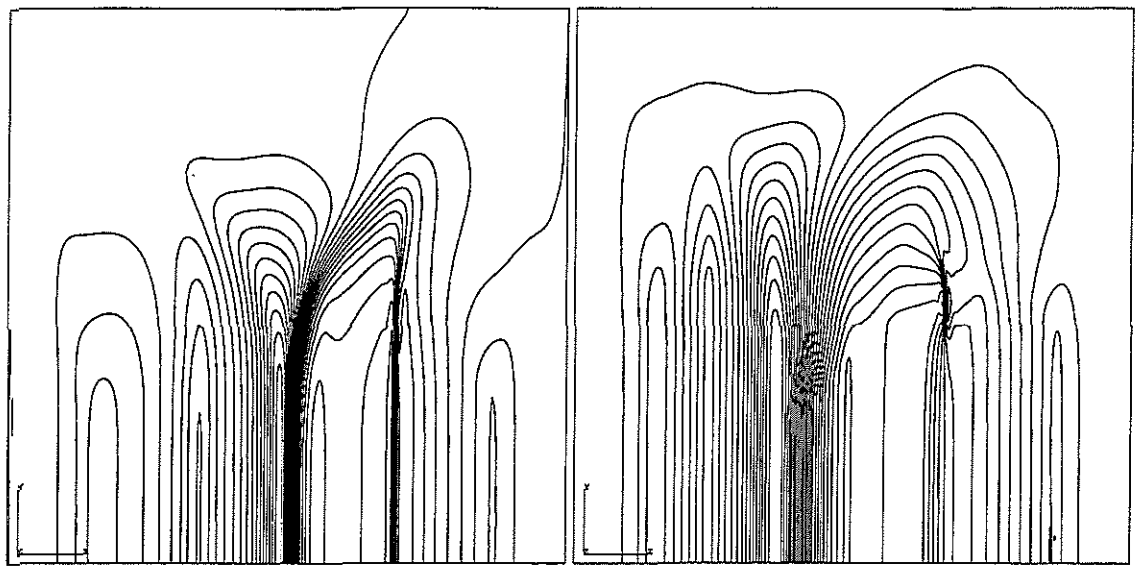

a) Initial grid (352 × 64 cells). b) Adapted grid (352 × 64 cells).

Fig. 23 Pressure distribution in the computational domain for solution on initial and adapted grid around RAE2822 airfoil (transonic flow conditions: $M_\infty = 0.725$, $Re_\infty = 6.5 \times 10^6$, $\alpha = 2.44°$, $\Delta C_p = 0.1$).

various European researchers within the EUROVAL project is described in [26]. The grids used by these researchers have been tuned several times based on visual inspection of the subsequently calculated flow solutions, and are considered to represent the state-of-the-art.

Starting with the pressure distribution, Fig.24 shows the present computational results obtained on the non-adapted medium grid, on the the adapted medium grid (one adaptation), on the non-adapted fine grid, and the results obtained from the wind tunnel measurements. In Fig.24 the pressure coefficient C_p is plotted as a function of the x-coordinate scaled by the chord-length ($x/c = 0$ at the leading edge, $x/c = 1$ at the trailing edge). The main differences between the various computed data sets occur around the suction peak at the leading edge of the airfoil and around the position of the shock wave. At both locations the data obtained on the adapted medium grid agree much better with the data obtained on the non-adapted fine grid. Comparison of the computational data with the wind-tunnel data does not show significant improvements.

The accuracy of the calculated pressure distributions directly influences the accuracy of the calculated aerodynamic force coefficients which are based on integration of the pressure and skin-friction distributions. Fig. 25 shows the various data sets in terms of the lift coefficient C_l

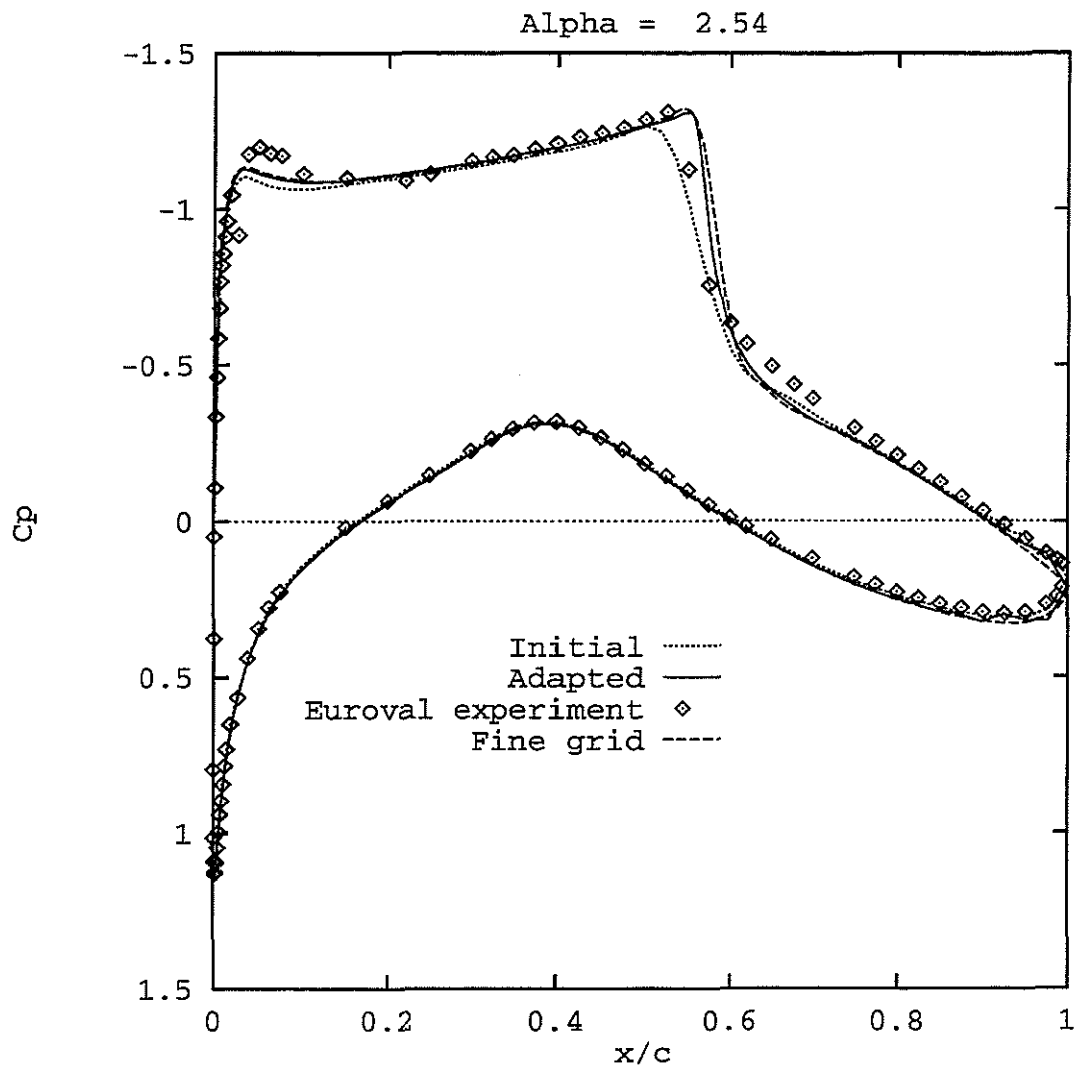

Fig. 24 Comparison of numerical and experimental data for the pressure distribution on the RAE2822 airfoil, $M_\infty = 0.734$, $Re_\infty = 6.5 \times 10^6$, $\alpha = 2.54°$.

as a function of the drag coefficient C_d. Two calculated $C_l - C_d$ polars consisting of nine flow conditions each are shown in Fig. 25: one obtained on a single non-adapted grid and one obtained on an adapted grids where each of the adapted grids is adapted to the flow condition at hand.

In addition to the already mentioned data sets obtained on the medium grids (both non-adapted and adapted), on the non-adapted fine grid and obtained from wind-tunnel measurements, Fig. 25 also shows the computational data from the EUROVAL project. The computational result on the non-adapted medium grid is significantly improved upon grid adaptation, both with respect to the

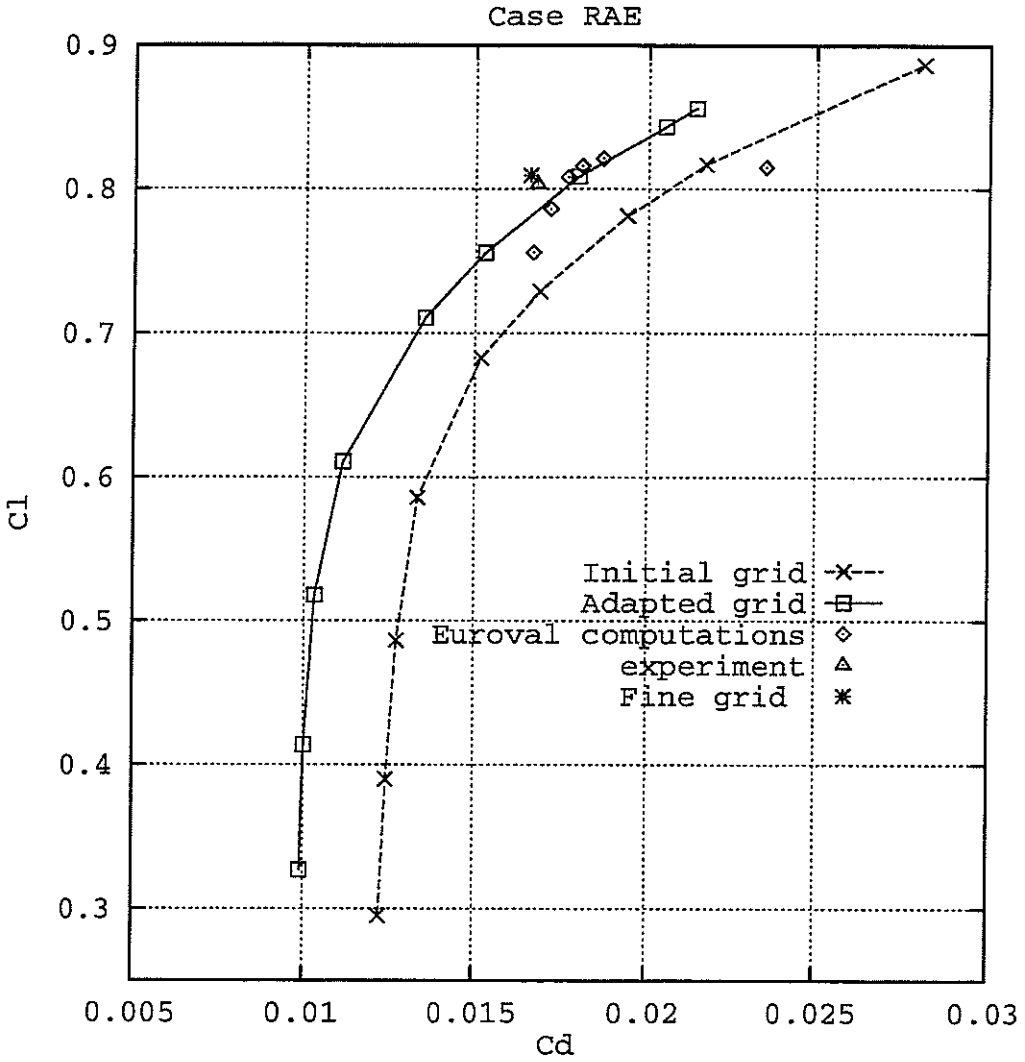

Fig. 25 Comparison of numerical and experimental polar data for the RAE2822 airfoil, $M_\infty = 0.734$, $Re_\infty = 6.5 \times 10^6$, $\alpha = 2.54°$, *transition fixed at 3% chord for all cases.*

experimental data and the non-adapted fine grid data. Many of the computational results from the EUROVAL project are very close to the calculated polar on the adapted medium grids. In fact this shows the potential benefit of automatic grid adaptation for industrial airframe design: the problem turnaround-time decreases dramatically. Starting with a medium grid with reasonable resolution and quality, grid adaptation enables one to obtain the same accuracy as on medium grids that are manually adapted in several steps by CFD experts. Since the adaptation is performed by an algorithm without user-interaction the problem turnaround time is very short.

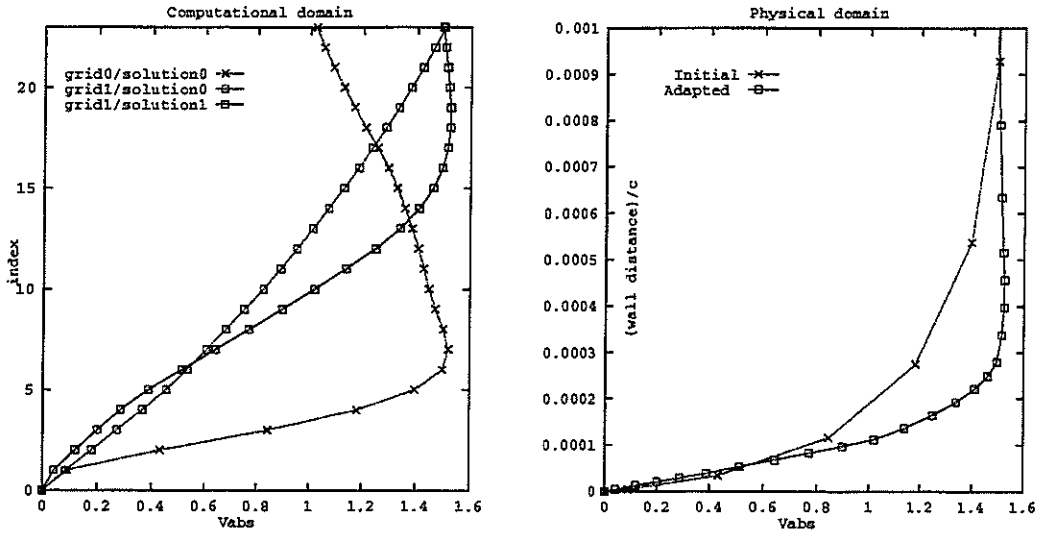

Fig. 26 Boundary-layer profiles in the computational domain (left) and in the physical domain (right), upper side of the RAE2822 airfoil, $x/c = 0.02$; $M_\infty = 0.734$, $Re_\infty = 6.5 \times 10^6$, $\alpha = 2.54°$. Upon adaptation the boundary-layer resolution increases from 6 to 20 points.

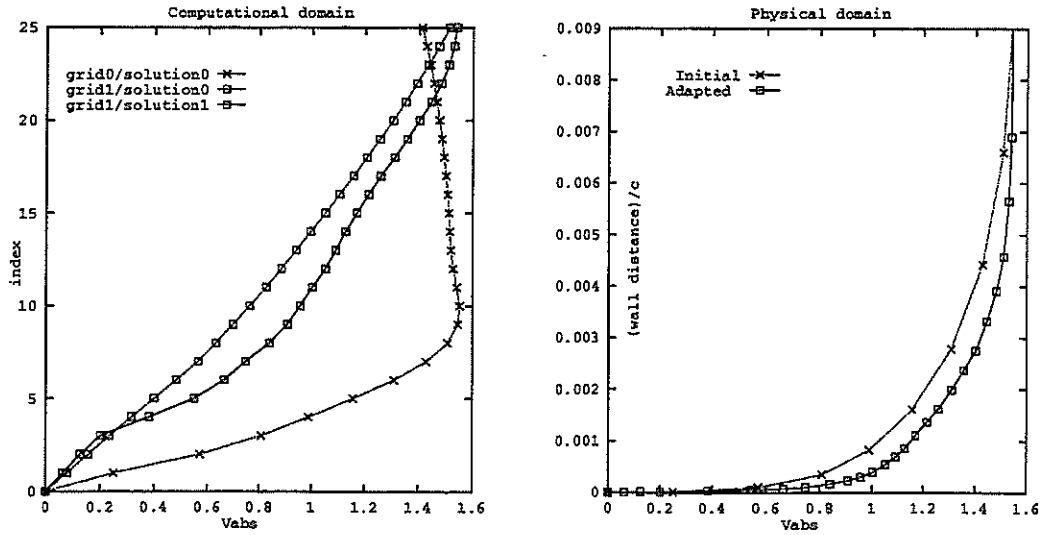

Fig. 27 Boundary-layer profiles in the computational domain (left) and in the physical domain (right), upper side of the RAE2822 airfoil, $x/c = 0.30$; $M_\infty = 0.734$, $Re_\infty = 6.5 \times 10^6$, $\alpha = 2.54°$. Upon adaptation the boundary-layer resolution increases from 10 to 25 points.

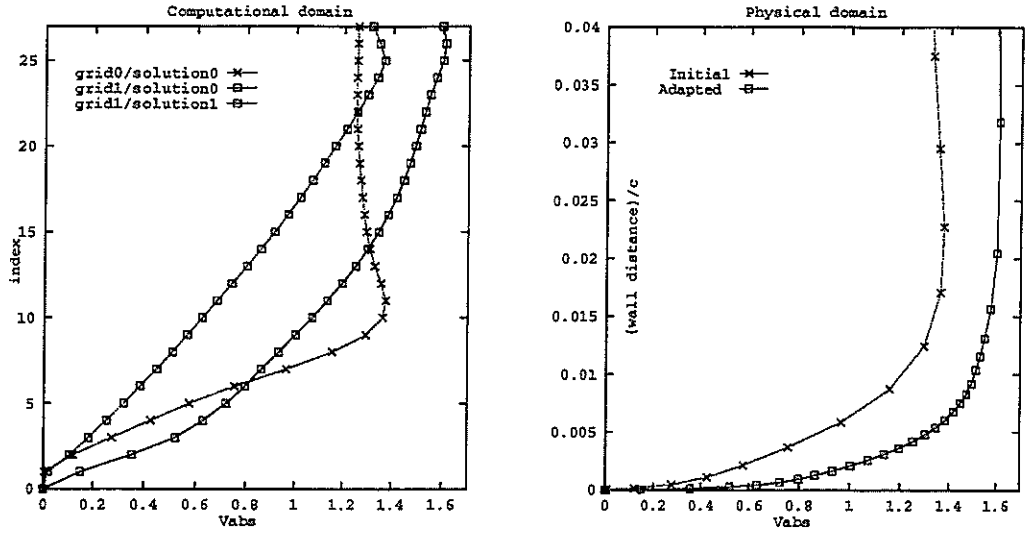

Fig. 28 Boundary-layer profiles in the computational domain (left) and in the physical domain (right), upper side of the RAE2822 airfoil, $x/c = 0.57$; $M_\infty = 0.734$, $Re_\infty = 6.5 \times 10^6$, $\alpha = 2.54°$. Upon adaptation the boundary-layer resolution increases from 10 to 25 points.

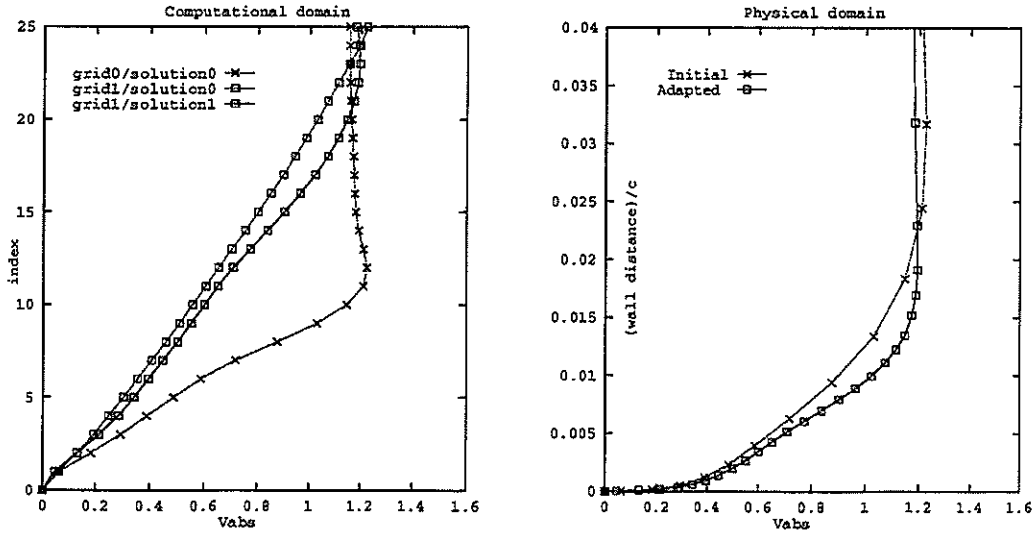

Fig. 29 Boundary-layer profiles in the computational domain (left) and in the physical domain (right), upper side of the RAE2822 airfoil, $x/c = 0.65$; $M_\infty = 0.734$, $Re_\infty = 6.5 \times 10^6$, $\alpha = 2.54°$. Upon adaptation the boundary-layer resolution increases from 11 to 23 points.

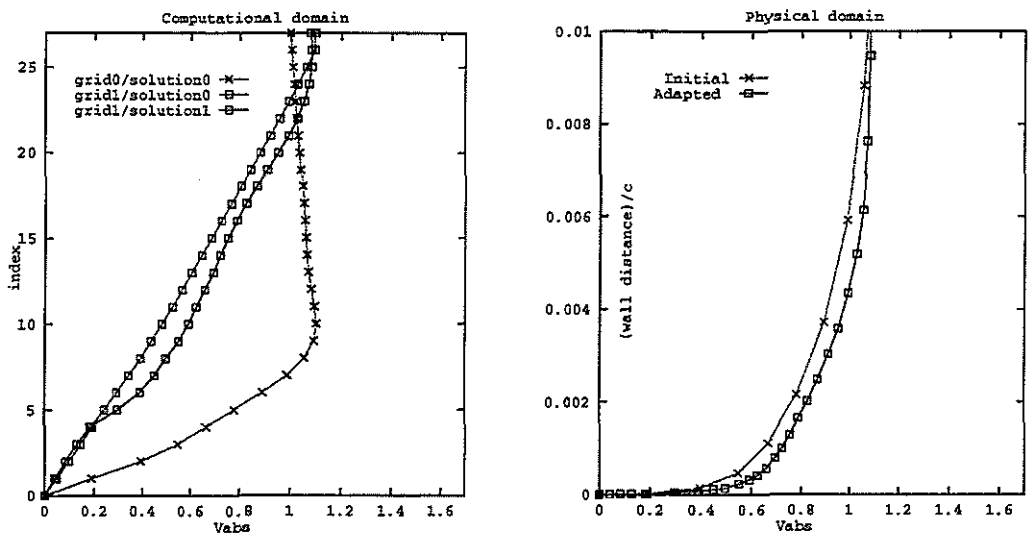

Fig. 30 Boundary-layer profiles in the computational domain (left) and in the physical domain (right), lower side of the RAE2822 airfoil, $x/c = 0.50$; $M_\infty = 0.734$, $Re_\infty = 6.5 \times 10^6$, $\alpha = 2.54°$. *Upon adaptation the boundary-layer resolution increases from 10 to 25 points.*

The main difference between the non-adapted and adapted grid results is the difference in the drag coefficient. This is not very surprising since the adaptation algorithm explicitly tunes the grid resolution normal to the airfoil surface to the boundary-layer solution profiles which vary quite strongly with the angle of attack. This suggests that the friction drag is calculated more accurately on the adapted grids than on the non-adapted grids.

To illustrate the adaptation in the boundary-layer region Figs. 26 to 30 show the velocity profiles for the reference flow condition at different values of x/c as a function of the grid point index (computational domain, normal direction) and as a function of the distance from the airfoil surface (physical domain, normal direction). The velocity values correspond to the magnitude of the velocity vector.

The profiles indicated as "grid0/solution0" correspond to the result obtained on the initial grid. The profiles indicated as "grid1/solution0" correspond to the solution on the initial grid interpolated onto the adapted grid. The profiles indicated as "grid1/solution1" correspond to the result obtained on the adapted grid.

In each of the figures Figs. 27 to 30 upon adaptation the number of grid points in the boundary-

layer is increased by roughly 150%. The profiles in the physical domain change significantly upon adaptation. At station $x/c = 0.57$ at the upper side of the airfoil, see Fig. 28, the velocity magnitude outside the boundary-layer also changed upon adaptation due to a shift in the position of the shock. The profiles in the computational domain change dramatically upon adaptation, all showing that the initial flow solution (calculated on the initial grid) becomes almost linear in the computational domain when interpolated to the adapted grid. The solution computed on the adapted grid partially loses the linear behaviour in the computational domain, indicating that more adaptation is required.

5.7.2 NLR8602 airfoil

In this section grid adaptation results obtained for the NLR8602 airfoil [52] are presented and compared to experimental data [54]. Fig. 31 shows the NLR8602 airfoil with a typical adapted grid. The airfoil is much thicker than the RAE2822 airfoil. The flow conditions are: $M_\infty = 0.65$, $Re_\infty = 9.5 \times 10^6$, with the angle of attack α ranging from $-2.94°$ to $4.41°$ while transition is fixed at locations on the upper and lower sides of the airfoil that differ for each of the angles of attack applied.

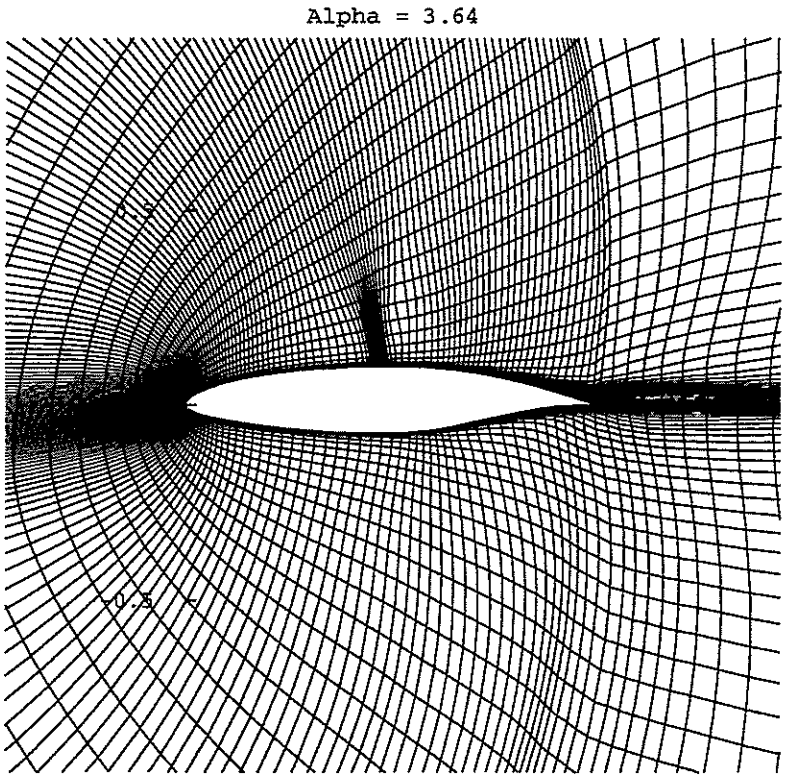

Fig. 31 Typical adapted grid around the NLR8602 airfoil for a transonic flow condition.

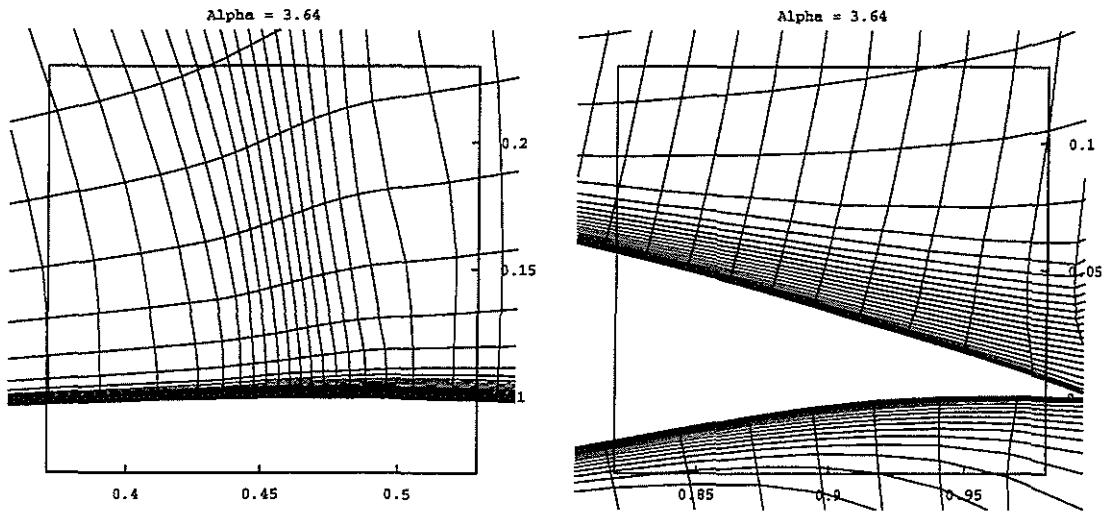

Fig. 32 Details of a typical adapted grid around the NLR8602 airfoil in the shock region (left) and in the trailing-edge region (right).

Details of the grid in the regions of the shock and the boundary-layer downstream of the shock are shown in Fig. 32. Travelling in downstream direction, the grid line density near the surface of the body gradually decreases, indicating an increasing boundary-layer thickness and a decreasing velocity gradient in the direction normal to the surface.

The pressure distributions obtained for the data points along the polar, with α ranging from $-2.94°$ to $4.41°$, can be divided in three categories:

- $\alpha < 0°$: the suction peak is on the lower side of the airfoil.
- $0° < \alpha < 1.83°$: no shock wave present.
- $\alpha > 1.83°$: shock wave present.

Typical C_p distributions of each of the three categories are plotted in Figs. 33 to 35. Besides a small area just aft of the shock wave (if applicable), for $\alpha > 0$ the adaptation invariably decreases the pressure coefficient on the upper side of the geometry and shows an increase on the lower side. When a shock wave is involved, it is steepened by the adaptation. This behaviour is very similar to what was observed for the case of the RAE2822 airfoil section.

For the present airfoil section, experimental pressure distributions are available for every angle of attack. In general, agreement of both the initial and the adapted solution with experimental data is not too good. The predicted pressure coefficient along the upper side of the airfoil is much lower than the one measured, while the predicted C_p along the lower side is higher than

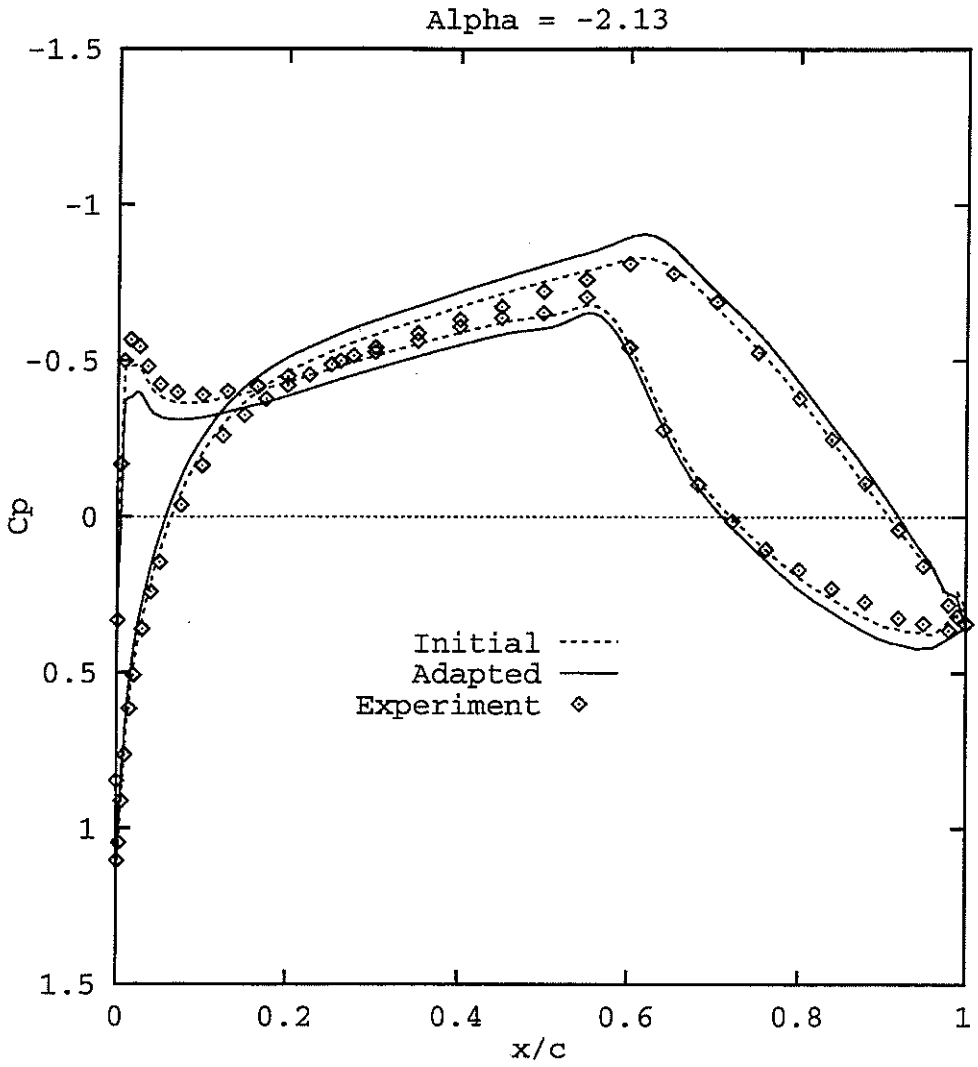

Fig. 33 Typical pressure distributions with suction peak on lower side of the NLR8602 airfoil for $\alpha < 0°$ *(*$M_\infty = 0.65$, $Re_\infty = 9.5 \times 10^6$*).*

the one measured. As a consequence, C_l will be overestimated. In particular, Fig. 35 shows that the computed shock location does not agree at all with the one in the experiment. Unfortunately adaptation slightly increases the differences between computed and measured data. The reason for the discrepancy are not known, but possible explanations are wind tunnel interference effects and uncertainty of the transition locations.

In Fig. 36 the lift coefficient C_l is plotted as a function of the drag coefficient C_d. Similar to the RAE2822 airfoil, this $C_l - C_d$ polar also shows that the values of C_l calculated on the adapted

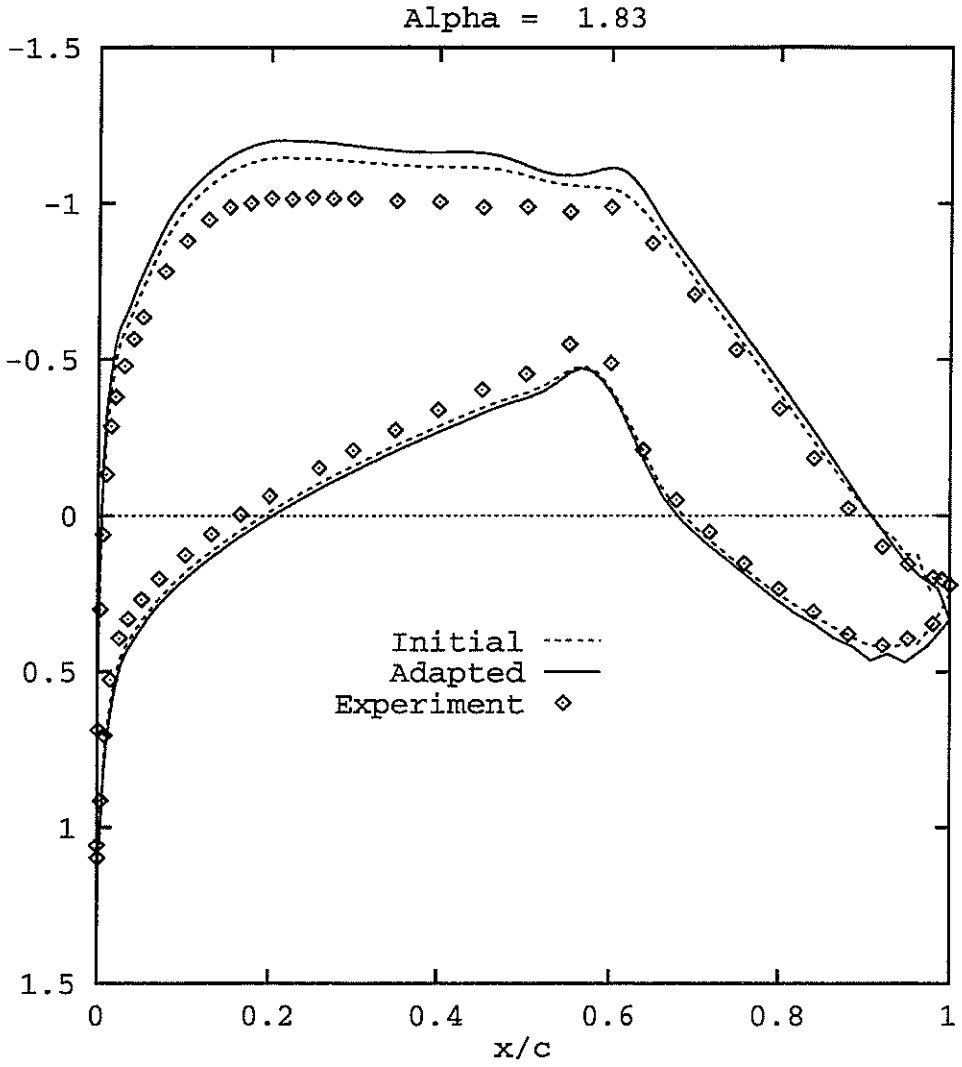

Fig. 34 Typical pressure distribution without shock wave on the NLR8602 airfoil for $0° < \alpha < 1.83°$ *(*$M_\infty = 0.65$, $Re_\infty = 9.5 \times 10^6$*).*

grids are higher than the values calculated on the non-adapted grids. Also the values of C_d calculated on adapted grids are lower than the values calculated on the non-adapted grids. The shape of both polars is very similar. Comparing the polar obtained from the numerical data with the polar obtained from the experimental data, the adaptation can be considered an improvement for negative and small angles of attack. For higher angles of attack the correlation is not satisfactory.

Fig. 37 shows the lift and drag coefficients as function of the angle of attack. The differences between the computed and measured coefficients slightly increase upon grid adaptation, which

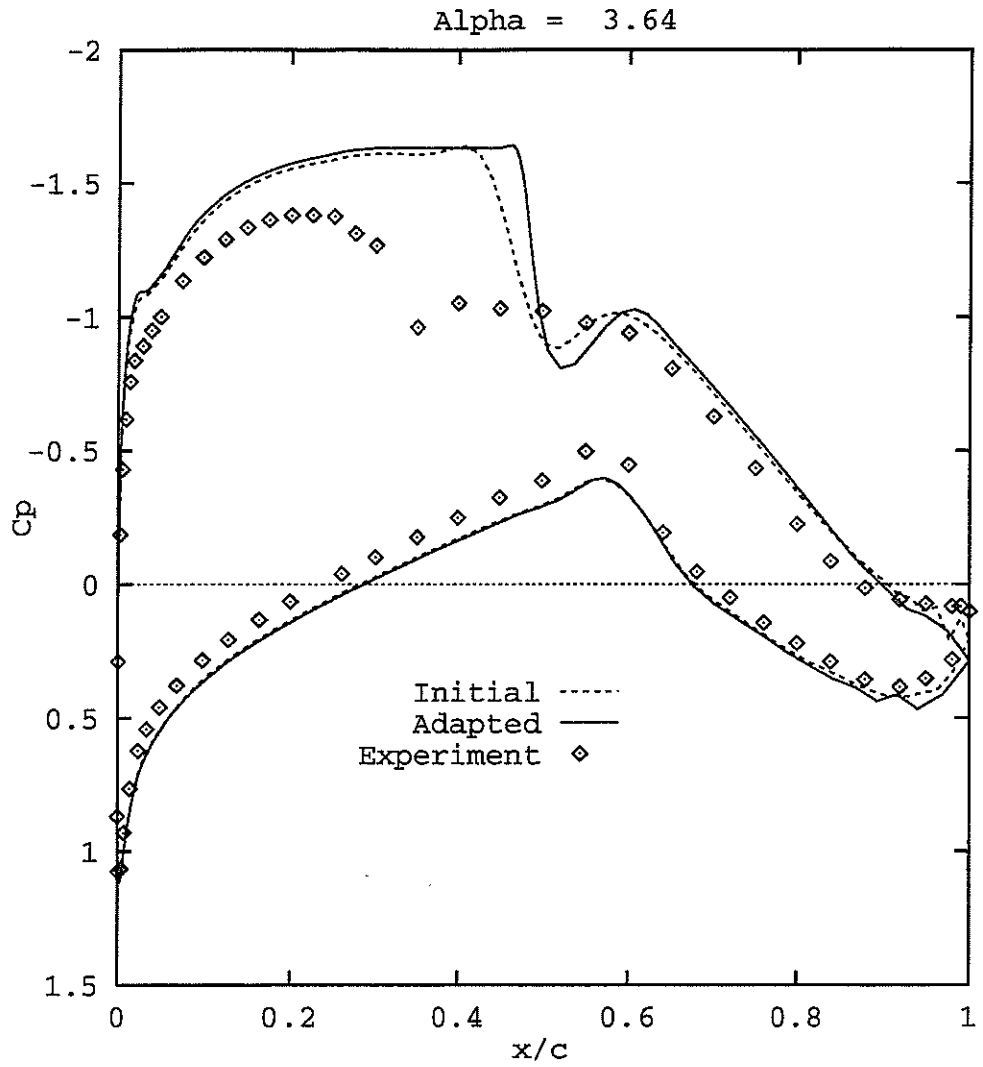

Fig. 35 Typical pressure distribution with shock wave on the NLR8602 airfoil for $\alpha = 3.64°$ *(*$M_\infty = 0.65$, $Re_\infty = 9.5 \times 10^6$*).*

is in agreement with the observations made for the pressure distributions. The drag coefficient prediction is strongly improved upon adaptation. It is noted that the drag coefficient heavily depends on the skin-friction distribution which is apparently better resolved on the adapted grid.

To assess the resolution of the boundary-layer velocity profiles, which determine the skin-friction distribution, Figs. 38, 39 and 40 show for $\alpha = 3.64°$ the profiles at various stations along the upper surface of the airfoil. The profiles obtained on the non-adapted grid and on the adapted grid are plotted in both the computational domain and the physical domain.

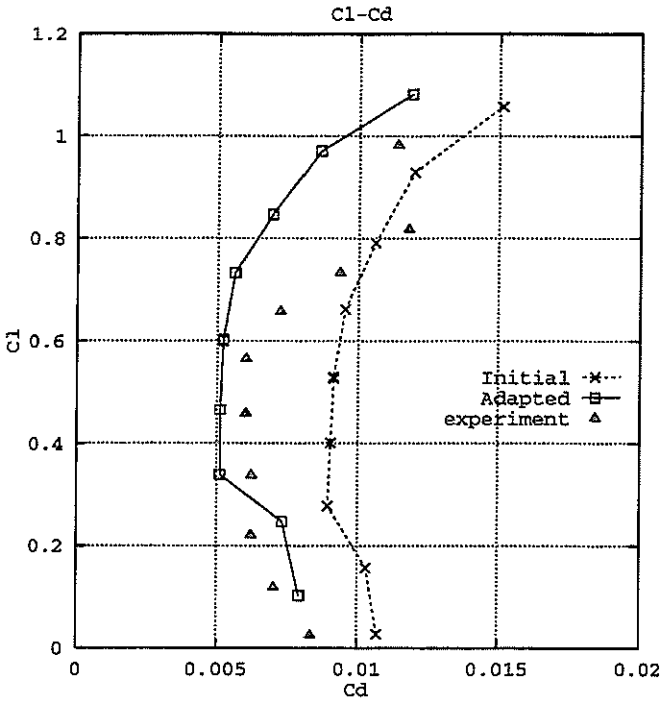

Fig. 36 Calculated polar data for the NLR8602 airfoil for angles of attack ranging from −2.94 to 3.64 degrees.

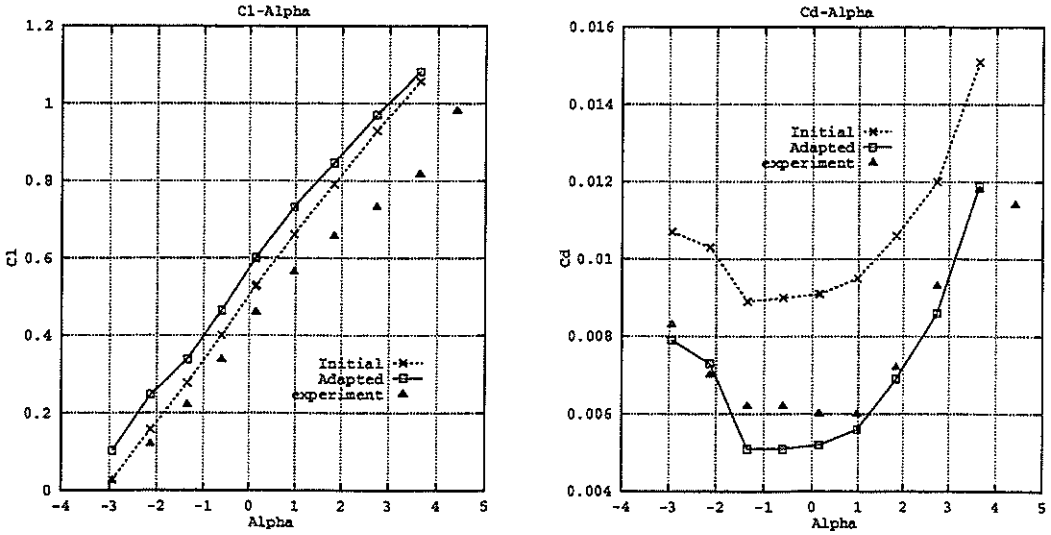

Fig. 37 Lift (left) and drag (right) coefficients as functions of the angle of attack showing improvement of the agreement between computational and experimental drag prediction upon adaptation.

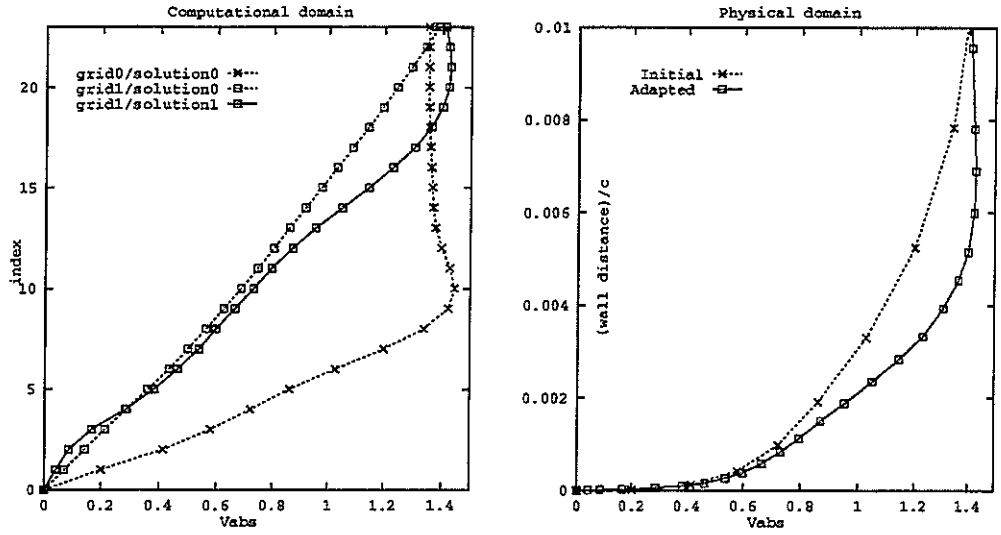

Fig. 38 Boundary-layer profiles in the computational domain (left) and in the physical domain (right), upper side of the NLR8602 airfoil, $x/c = 0.50$, $M_\infty = 0.65$, $Re_\infty = 9.5 \times 10^6$, $\alpha = 3.64°$. Upon adaptation the boundary-layer resolution increases from 10 to 20 points.

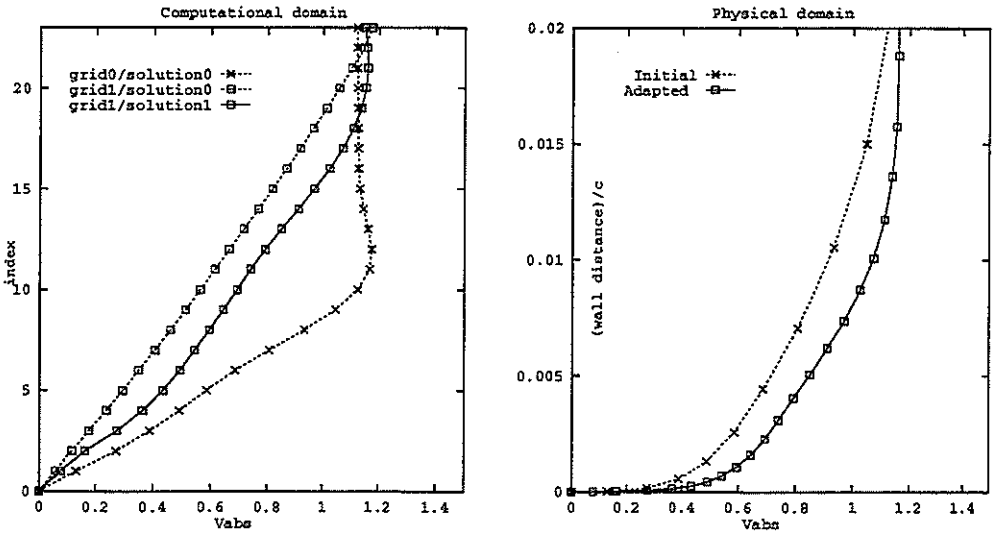

Fig. 39 Boundary-layer profiles in the computational domain (left) and in the physical domain (right), upper side of the NLR8602 airfoil, $x/c = 0.80$, $M_\infty = 0.65$, $Re_\infty = 9.5 \times 10^6$, $\alpha = 3.64°$. Upon adaptation the boundary-layer resolution increases from 11 to 21 points.

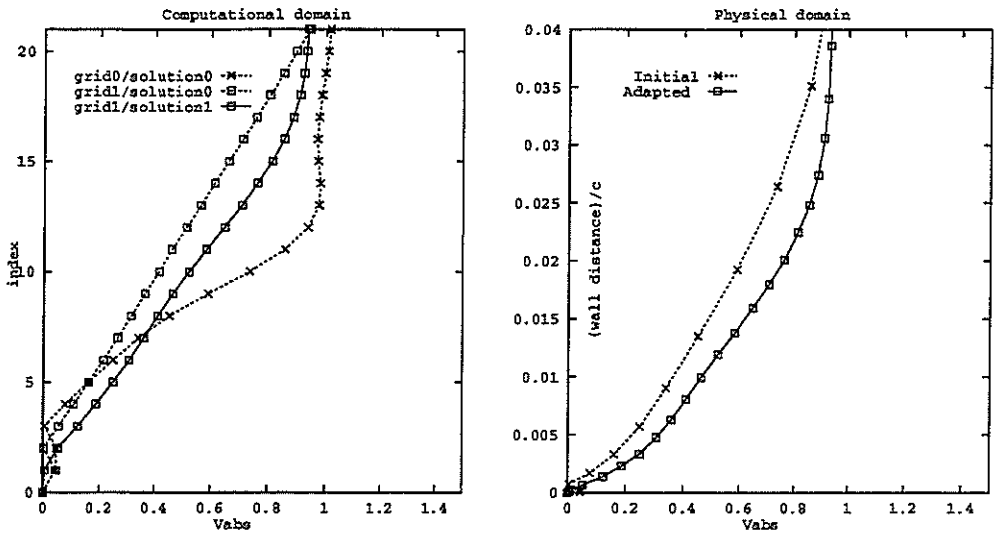

Fig. 40 Boundary-layer profiles in the computational domain (left) and in the physical domain (right), upper side of the NLR8602 airfoil, $x/c = 0.95$, $M_\infty = 0.65$, $Re_\infty = 9.5 \times 10^6$, $\alpha = 3.64°$, indicating reversed flow close to the surface.

We use the same notation as used in the previous section. The profiles indicated as "grid0/solution0" correspond to results obtained on the initial grid. The profiles indicated as "grid1/solution0" correspond to the solution on the initial grid interpolated onto the adapted grid. The profiles indicated as "grid1/solution1" correspond to results obtained on the adapted grid. The boundary-layer velocity profiles show basically the same trend as was observed in the previous section; grid adaptation and recalculation of the solution result in velocity profiles that are close to linear distributions in the computational domain.

5.8 Conclusions and discussion

A new adaptation algorithm for computational fluid dynamics problems has been developed, suitable for 2D airfoil problems. Four essential steps in the algorithm can be distinguished:

(i) The adaptation equations are formulated in the so-called parametric domain associated with the initial grid that is used as the basis of the adaptation.

(ii) The basic adaptation equations are derived from a variational formulation and can be interpreted as anisotropic diffusion equations.

(iii) The modified anisotropic diffusion equations are directly solved for the computational coordinates (ξ, η) as functions of the parametric coordinates (p, q) and the resulting map is numerically inverted.

(iv) The adaptation equations are modified to obtain the following desirable properties in boundary-layers:
- preservation of orthogonality,
- one-dimensional equidistribution of a weight function in the direction normal to the airfoil surface, and
- adaptation in the direction of the flow controlled by the outer flow.

Application to two aerodynamic test problems demonstrates that the developed grid adaptation algorithm is robust and generates heavily adapted grids around airfoils leading to significant improvement of the flow solution quality.

The quality improvement of the flow solution is apparent when comparing the flow solution obtained on a non-adapted medium and fine grid with the one obtained on the adapted medium grid. Upon adaptation of the medium grid the disagreement between the pressure distribution obtained on the non-adapted fine grid and the one obtained on the adapted medium grid largely disappear (see Fig. 24).

Also the agreement between our medium grid result and the medium grid results obtained by various European researchers improves significantly upon adaptation of our medium grid (See Fig. 25). It should be noted that the grids used by these researchers are the result of extensive tuning of the mesh characteristics to the obtained flow solutions, including numerous flow visualisations, grid generations and flow computations. Our non-adapted grid, however, is generated using an elliptic grid generator that only needs a rough estimate of the Reynolds number as input parameter. The purpose of the base medium grid is to resolve the geometry of the airfoil with sufficient accuracy and to provide a sufficient degree of smoothness and orthogonality. The Reynolds number estimate is used to specify the stretching of the grid in the direction normal to the airfoil surface, required to resolve the boundary-layer to some extent. The tuning of the grid is performed by the grid adaptation algorithm in a fully automatic way without user interference. This demonstrates a practical implication of grid adaptation: the problem turnaround time can be decreased dramatically.

Another indication of improved flow solution quality achieved by grid adaptation is the smoothness of the flow solution in the computational domain, indicating an improved resolution of the high gradient physical flow features. Increased smoothness is obtained in the region where the shock penetrates into the boundary-layer and in the region around the stagnation point near the leading edge (see Figs. 22 and 23). Almost optimal smoothness is obtained across the entire height of the

boundary-layer which is indicated by the linear velocity profiles in the computational domain that are found when the initial flow solution is interpolated onto the adapted grid (see Figs. 26 to 30 and Figs. 38 to 40). This observation is in agreement with the analysis in section 5.2 which shows that the adaptation normal to the airfoil surface is effectively one-dimensional. It is also noted, however, that the flow solution on the adapted grid introduces a deviation from the linear profiles, indicating that more adaptations may be required.

It is acknowledged that comparison of computational data with experimental data does not indicate that grid adaptation unconditionally leads to improvement of the correlation of predicted and measured aerodynamic data. In particular, the disagreement between the pressure distribution on the NLR8602 airfoil obtained from computation and the one measured increases upon grid adaptation. It is noted, however, that a number of uncertainties is involved.

(i) The flow is turbulent. This means that the flow is essentially unsteady and three-dimensional. In the computations the unsteadiness is accounted for by averaging the time-dependent Navier-Stokes equations in time and solving these quasi-steady equations for the time-averaged flow quantities. The number of unknowns in the time-averaged equations, however, is larger than the number of equations. Specifically the equations include the so-called Reynolds stresses which represent the effect of the high-frequency unsteadiness on the time-averaged flow quantities. The system of equations is closed by a so-called algebraic turbulence model which expresses the Reynolds stresses in terms of the time-averaged flow quantities. Such turbulence model, here the Baldwin-Lomax model, is empirical, partially based on knowledge of airfoil flows, and is subject to significant uncertainties.

(ii) The measurements have been carried out in wind tunnels where the airfoil is of finite span and is enclosed by four (sometimes partially) solid walls. The wind-tunnel data have been corrected to account for the effect of presence of wind-tunnel walls, but the determination of such corrections is a challenge in itself and is also subject to uncertainties.

The robustness of the grid adaptation algorithm is demonstrated by the substantial number of adapted grids that were used in the polar computations for the RAE2822 and NLR8602 airfoils. Each of these grids were adapted in a fully automatic way, i.e., completely without user interference. Although these grids are heavily adapted to the flow features that strongly vary with the changing upstream flow conditions, irregularities in the sense of grid overlap never occurred. This is in agreement with the invertibility theorem of Clement, Hagmeijer and Sweers [14] that is discussed

in the previous chapter.

The grids are heavily adapted at specific locations. In the shock region of the RAE2822 airfoil (see Fig. 19) the mesh size across the shock decreases by an order of magnitude while the mesh size normal to the airfoil surface is tuned to the strongly varying boundary-layer along the airfoil surface. Around the leading edge the mesh size along the airfoil surface decreases by a factor of 2 to 3 upon grid adaptation (see Figs. 14a and 15a). Finally the number of points across the boundary-layer typically increases by a factor of 2 or 3 (see Figs. 26 to 30 and Figs. 38 to 40). Evidently, the degree of adaptation depends on the quality of the initial grid.

We conclude by remarking that it appeared to be necessary to modify the Weighted Least Squares formulation developed in the previous chapters. By introducing modification functions in the PDE's, see section 5.2, we no longer minimise the WLS functional K given by Eq. (150) and it seems not possible to find the functional which has the modified PDE's (159) as the EL-equations. The pay-off of this compromise is that the adaptation method not only works for relatively simple model problems on rectangular domains, but is also applicable to realistic aerodynamic problems like airfoil flows involving cell aspect-ratios as high as 10,000.

6 Grid adaptation in 3D based on Compound Weighted Least Squares maps

In the present chapter we present an extension from 2D to 3D of the work presented in chapter 5. The objective is to achieve efficient adaptation of structured grids in three-dimensional space. Most of the 2D developments can be extended to 3D in a straightforward manner. But the behaviour of, for example, adapted grids along intersecting solid walls with boundary layers is not a priori clear. In section 6.2 arguments are given to expect that orthogonal grids will be generated in such regions. The introduction of correction maps for 2D aerodynamic problems around airfoils is extended to 3D aerodynamic problems around wings in section 6.6.

Let $\Omega \subset \mathcal{R}^3$ be the physical domain in three-dimensional space in which the computational grid has to be adapted, and let $\Omega_c = [0,1]^3 \subset \mathcal{R}^3$ be the so-called computational domain. A boundary conforming curvilinear coordinate system in Ω can be defined by mapping Ω_c onto Ω such that the Cartesian computational coordinates $(\xi, \eta, \zeta)^T$ in Ω_c are the curvilinear coordinates in Ω. The problem of grid adaptation is to find a suitable mapping from Ω_c to Ω. In this chapter it is assumed that there exists an initial grid with sufficient quality with respect to geometry resolution, orthogonality and smoothness, that merely has to be adapted to the flow solution at the specific flow conditions at hand. The initial grid is assumed to be generated by an experienced CFD specialist, and to have sufficient quality to obtain a converged solution with most of the flow features reasonably resolved. Such an initial grid would typically be used for all the flow conditions to be considered for the configuration investigated. Like the 2D development in the previous chapter the initial grid is used for parametrisation of the physical domain to retain the characteristics of the initial grid in a global way. The concept of grid adaptation in the parametric domain is illustrated in Fig. 41.

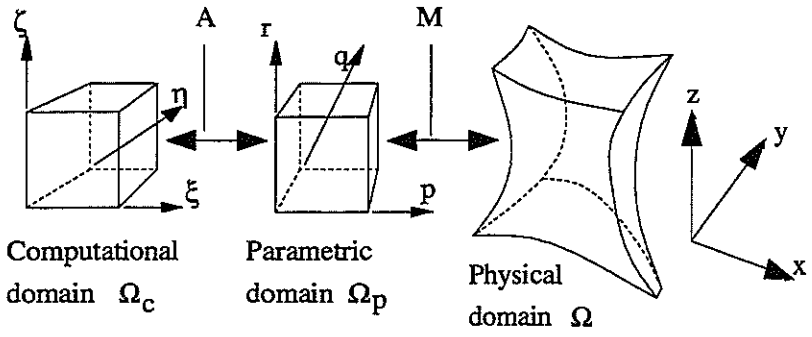

Fig. 41 Grid adaptation by using an adaptation map A that maps the computational domain onto the parametric domain.

Let the initial grid in the physical domain Ω be the image of a uniform Cartesian grid in the unit cube $[0,1]^3 \subset \mathcal{R}^3$ under a map M. The Cartesian coordinates in the unit square denoted by $(p,q,r)^T$ serve as the parameters to describe the physical domain; hence the unit cube is called the parametric domain denoted by Ω_p. The goal is to adapt the grid in the parametric domain Ω_p.

Once again it is stated that adaptation in the parametric domain enables preservation of the global features of the initial grid in the physical domain such as high resolution at geometry parts with high curvature. The initial grid can be considered to be pre-adapted to the geometry and the global features of the flow solution, whereas the regenerated grid is additionally adapted to details of the flow solution at the specific flow conditions considered.

The problem of grid adaptation in Ω_p can conveniently be formulated in terms of the determination of a suitable Weighted Least Squares map A that maps the Cartesian grid in the computational domain Ω_c to the adapted grid in Ω_p (see Fig. 41). Consequently, the adapted grid in the physical domain is the image of the Cartesian grid in Ω_c under the compound map $M \circ A$. Hence the problem is to find the parametric coordinates p, q and r as functions of the computational coordinates ξ, η and ζ, which is the main topic of the next two sections.

6.1 Anisotropic Diffusion equations in parametric domain

We start by introducing an extension of the functional (150) based on the generic functional (115):

$$K[\xi,\eta,\zeta] = \frac{1}{2}\int_{\Omega_p}\{\frac{\xi_p^2+\eta_p^2+\zeta_p^2}{w_1(\mathbf{p})}+\frac{\xi_q^2+\eta_q^2+\zeta_q^2}{w_2(\mathbf{p})}+\frac{\xi_r^2+\eta_r^2+\zeta_r^2}{w_3(\mathbf{p})}\}\,d\Omega_p, \tag{192}$$

where the weight functions are strictly positive, bounded, differentiable functions of $(p,q,r)^T$. The map $(\xi(p,q,r),\eta(p,q,r),\zeta(p,q,r))$ can now be defined as the map that minimises functional K. To assure that the map is boundary conforming the following set of essential boundary conditions is applied:

$$\begin{aligned}
&\xi(0,q,r)=0, \quad \xi(1,q,r)=1,\\
&\eta(p,0,r)=0, \quad \eta(p,1,r)=1,\\
&\zeta(p,q,0)=0, \quad \zeta(p,q,1)=1.
\end{aligned} \tag{193}$$

As is demonstrated in chapter 3 the above formulated variational problem requires that the Euler-Lagrange (EL) equations be satisfied:

$$\begin{aligned}
\frac{\partial}{\partial p}\frac{\xi_p}{w_1}+\frac{\partial}{\partial q}\frac{\xi_q}{w_2}+\frac{\partial}{\partial r}\frac{\xi_r}{w_3} &= 0,\\
\frac{\partial}{\partial p}\frac{\eta_p}{w_1}+\frac{\partial}{\partial q}\frac{\eta_q}{w_2}+\frac{\partial}{\partial r}\frac{\eta_r}{w_3} &= 0,\\
\frac{\partial}{\partial p}\frac{\zeta_p}{w_1}+\frac{\partial}{\partial q}\frac{\zeta_q}{w_2}+\frac{\partial}{\partial r}\frac{\zeta_r}{w_3} &= 0.
\end{aligned} \tag{194}$$

These equations are linear and decoupled partial differential equations for the functions $\xi(p,q,r)$, $\eta(p,q,r)$ and $\zeta(p,q,r)$, respectively, and may be interpreted as anisotropic diffusion (AD) equations with diffusion coefficients w_1^{-1}, w_2^{-1} and w_3^{-1}. They form the basis for determining the inverse adaptation map in Fig. 41.

To complete the variational problem formulation the following set of natural boundary conditions has to be fulfilled:

$$\begin{aligned}
&\xi_q(p,0,r)=0, \quad \xi_q(p,1,r)=0,\\
&\xi_r(p,q,0)=0, \quad \xi_r(p,q,1)=0,\\
&\eta_p(0,q,r)=0, \quad \eta_p(1,q,r)=0,\\
&\eta_r(p,q,0)=0, \quad \eta_r(p,q,1)=0,\\
&\zeta_p(0,q,r)=0, \quad \zeta_p(1,q,r)=0,\\
&\zeta_q(p,0,r)=0, \quad \zeta_q(p,1,r)=0.
\end{aligned} \tag{195}$$

6.2 Modified Anisotropic Diffusion equations in parametric domain

Following the skewness analysis of section 5.2 we introduce modification functions λ_i, $i=1,2,3$, to provide orthogonal grids in boundary layers:

$$\begin{aligned}
L_p[\xi] \equiv \lambda_1\frac{\partial}{\partial p}\frac{\xi_p}{w_1}+\lambda_2\frac{\partial}{\partial q}\frac{\xi_q}{w_2}+\lambda_3\frac{\partial}{\partial r}\frac{\xi_r}{w_3} &= 0,\\
L_p[\eta] \equiv \lambda_1\frac{\partial}{\partial p}\frac{\eta_p}{w_1}+\lambda_2\frac{\partial}{\partial q}\frac{\eta_q}{w_2}+\lambda_3\frac{\partial}{\partial r}\frac{\eta_r}{w_3} &= 0,\\
L_p[\zeta] \equiv \lambda_1\frac{\partial}{\partial p}\frac{\zeta_p}{w_1}+\lambda_2\frac{\partial}{\partial q}\frac{\zeta_q}{w_2}+\lambda_3\frac{\partial}{\partial r}\frac{\zeta_r}{w_3} &= 0.
\end{aligned} \tag{196}$$

where λ_1, λ_2 and λ_3 are functions of p,q and r which are taken proportional to the squares of the local mesh sizes of the initial grid in Ω:

$$\lambda_1 \sim \|\mathbf{x}_q\|^2\|\mathbf{x}_r\|^2, \quad \lambda_2 \sim \|\mathbf{x}_p\|^2\|\mathbf{x}_r\|^2, \quad \lambda_3 \sim \|\mathbf{x}_p\|^2\|\mathbf{x}_q\|^2. \tag{197}$$

To illustrate the effect of the modification functions λ_i let the surface $r = 0$ in the parametric domain Ω_p represent a solid wall in Ω and let the cells of the initial grid adjacent to the wall be orthogonal and have very small aspect ratios, i.e.

$$\|\mathbf{x}_r\| \ll \|\mathbf{x}_q\|, \quad \|\mathbf{x}_r\| \ll \|\mathbf{x}_p\|. \tag{198}$$

This situation is illustrated in Fig. 42a. As a consequence $\lambda_1 \ll \lambda_3$ and $\lambda_2 \ll \lambda_3$ and the modified equations can be approximated as

$$\frac{\partial}{\partial r}\frac{\xi_r}{w_3} \approx 0, \quad \frac{\partial}{\partial r}\frac{\eta_r}{w_3} \approx 0, \quad \frac{\partial}{\partial r}\frac{\zeta_r}{w_3} \approx 0. \tag{199}$$

Since the Neumann boundary conditions (195) are applied we have $\xi_r(p,q,0) = 0$ and consequently $\xi_r \approx 0$ for increasing r as long as approximation (199) is valid, i.e., as long as $\lambda_1 \ll \lambda_3$ and $\lambda_2 \ll \lambda_3$. The same is true for for η_r. Hence the adapted grid in the boundary layer is nearly orthogonal. A second implication of approximation (199) is that the equation for ζ (the third equation of Eqs. (199)) is similar to Eq. (43) which shows that the grid in the boundary layer is adapted in normal direction by one-dimensional equidistribution of the product $w_3^{-1}\zeta_r$.

So far the asymptotic behaviour near solid walls with boundary layers is completely similar to the situation in 2D. In 3D, however, we have the additional possibility of intersecting solid walls both with a boundary layer. Suppose that a boundary layer is present along the surface $p = 0$ and along the surface $r = 0$, see Fig. 42b. Then in the neighbourhood of the intersection $p = 0$, $r = 0$ we have

$$\|\mathbf{x}_r\| \ll \|\mathbf{x}_q\|, \quad \|\mathbf{x}_p\| \ll \|\mathbf{x}_q\|. \tag{200}$$

As a consequence $\lambda_2 \ll \lambda_1$ and $\lambda_2 \ll \lambda_3$ and the modified equations can be approximated as

$$\begin{aligned} \lambda_1\frac{\partial}{\partial p}\frac{\xi_p}{w_1} + \lambda_3\frac{\partial}{\partial r}\frac{\xi_r}{w_3} &\approx 0, \\ \lambda_1\frac{\partial}{\partial p}\frac{\eta_p}{w_1} + \lambda_3\frac{\partial}{\partial r}\frac{\eta_r}{w_3} &\approx 0, \end{aligned}$$

$$\lambda_1 \frac{\partial}{\partial p}\frac{\zeta_p}{w_1} + \lambda_3 \frac{\partial}{\partial r}\frac{\zeta_r}{w_3} \approx 0. \tag{201}$$

Hence only one term per equation can be neglected instead of two terms in the previous case of a boundary layer along one surface. Now the question is: will the adapted grid near the intersection be sufficiently orthogonal? This question can only be answered in a qualitative sense since the local solution of the grid adaptation equations depends on the global solution due to the ellipticity of the equations.

To assess the orthogonality question it is convenient to observe the solutions $\xi(p,q,r)$, $\eta(p,q,r)$ and $\zeta(p,q,r)$. As a reference we note that if upon adaptation planes of $p = constant$ would be mapped to planes of $\xi = constant$, planes of $q = constant$ would be mapped to planes of $\eta = constant$, and planes of $r = constant$ would be mapped to planes of $\zeta = constant$, then all angles of the initial grid in the physical domain are conserved within the adapted grid. For the the plane $q = constant$ depicted in Fig. 42b we note that in the neighbourhood of the intersection cells have aspect ratios that are of order unity and hence do not differ too much from the corresponding cells in the parametric domain. Hence, if it is assumed that the iso-ξ and iso-ζ surfaces are close to planes of $p = constant$ and $r = constant$, respectively, the angles of the initial grid in the physical domain are locally conserved within the adapted grid. Then the question remains whether the image of the plane $q = constant$ near the intersection under the adaptive map will be sufficiently close to a plane $\eta = constant$. To answer this question we assume that some distance away from the intersection in the parametric domain, see Fig. 42b, there exist lines in the iso-q plane of $p = \hat{p} > 0$ and $r = \hat{r} > 0$, respectively, along which approximations like Eqs. (201) are valid such that η is approximately constant along these lines. Since along curves $p = 0$ and $r = 0$ we have Neumann conditions for η, application of the maximum principle to the enclosed area between these four curves learns that η indeed is approximately constant in the enclosed area.

6.3 Weight functions and modification functions

The specification of the weight functions w_i, $i = 1,2,3$, and modification functions λ_i, $i = 1,2,3$, used for adaptation in 3D, is directly based on the functions used in 2D, see Eqs. (172) and (191), respectively.

As a natural extension of the weight functions given in Eq. (172) we take

$$w_1 = \sqrt{1 + \|\boldsymbol{Q}_p\|^2}, \quad w_2 = \sqrt{1 + \|\boldsymbol{Q}_q\|^2}, \quad w_3 = \sqrt{1 + \|\boldsymbol{Q}_r\|^2}, \tag{202}$$

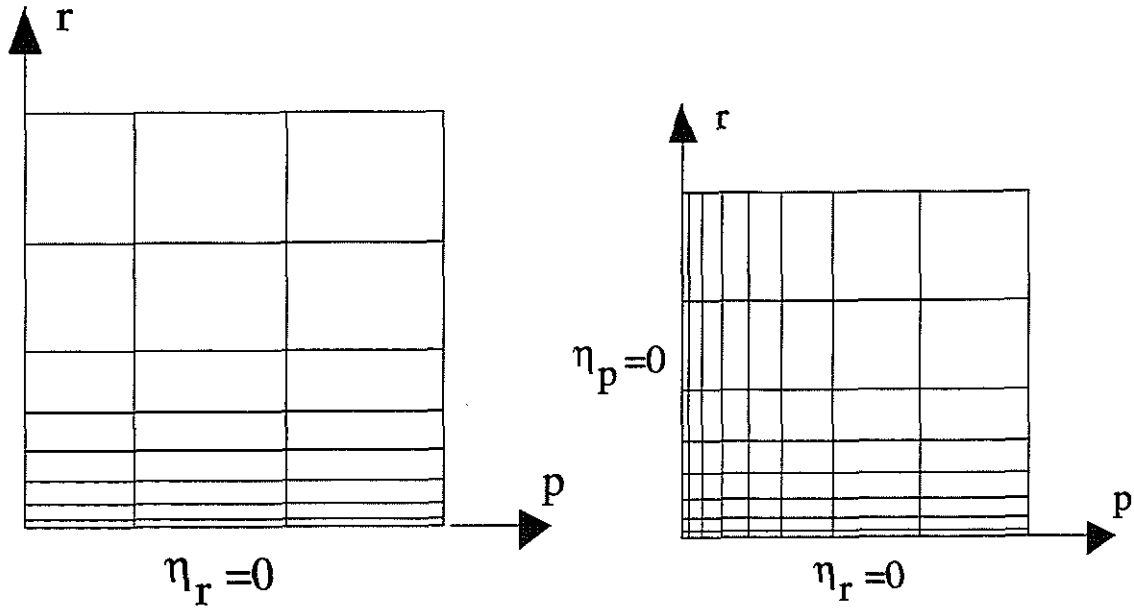

a) Single boundary layer.

b) Two intersecting boundary layers.

Fig. 42 Sketch of single boundary layer and two intersecting boundary layers in an iso-q plane.

where $\boldsymbol{Q} \in \boldsymbol{R}^n$ again represents the flow solution with all components scaled to $O(1)$ and where $\|.\|$ denotes the L_2 norm.

As a natural extension of the modification functions given in Eq. (191) we take

$$\lambda_1 = w_1^2\|\mathbf{x}_q\|^2\|\mathbf{x}_r\|^2, \quad \lambda_2 = w_2^2\|\mathbf{x}_p\|^2\|\mathbf{x}_r\|^2, \quad \lambda_3 = w_3^2\|\mathbf{x}_p\|^2\|\mathbf{x}_q\|^2. \tag{203}$$

6.4 Discretisation

The differential operator L_p defined in Eq. (196) is approximated by a second-order accurate difference operator L_p^h by replacing derivatives by central differences. In an interior grid point (i,j,k) L_p^h is defined as:

$$\begin{aligned} L_p^h[.] \equiv \quad & +\beta_{centre}(.)_{i,j,k} \\ & +\beta_{right}(.)_{i+1,j,k} + \beta_{left}(.)_{i-1,j,k} \\ & +\beta_{back}(.)_{i,j+1,k} + \beta_{front}(.)_{i,j-1,k} \\ & +\beta_{top}(.)_{i,j,k+1} + \beta_{bottom}(.)_{i,j,k-1}, \end{aligned} \tag{204}$$

with

$$
\begin{aligned}
\beta_{right} &= \frac{1}{\Delta p^2}\frac{2\lambda_1^{i,j,k}}{w_1^{i+1,j,k}+w_1^{i,j,k}},\\
\beta_{left} &= \frac{1}{\Delta p^2}\frac{2\lambda_1^{i,j,k}}{w_1^{i-1,j,k}+w_1^{i,j,k}},\\
\beta_{back} &= \frac{1}{\Delta q^2}\frac{2\lambda_2^{i,j,k}}{w_2^{i,j+1,k}+w_2^{i,j,k}},\\
\beta_{front} &= \frac{1}{\Delta q^2}\frac{2\lambda_2^{i,j,k}}{w_2^{i,j-1,k}+w_2^{i,j,k}},\\
\beta_{top} &= \frac{1}{\Delta r^2}\frac{2\lambda_3^{i,j,k}}{w_3^{i,j,k+1}+w_3^{i,j,k}},\\
\beta_{bottom} &= \frac{1}{\Delta r^2}\frac{2\lambda_3^{i,j,k}}{w_3^{i,j,k-1}+w_3^{i,j,k}},\\
\beta_{centre} &= -(\beta_{right}+\beta_{left}+\beta_{top}+\beta_{bottom}+\beta_{front}+\beta_{back})
\end{aligned}
\tag{205}
$$

where the subscripts and superscripts i, j, k indicate at which node the functions are evaluated, with Δp, Δq and Δr the mesh spacing of the uniform grid in the parametric domain. The normal derivatives at the boundary $\partial\Omega_p$ are approximated by first-order accurate one-sided differences.

The above described large system of linear equations is solved by means of GMRES relaxation [4]. The specific GMRES algorithm has been taken from the netlib.linalg library (ftp address: netlib2.cs.utk.edu) provided by the University of Tennessee and Oak Ridge National Laboratory. A correction-storage multi-grid technique [11] with fixed V-cycles is used to increase the rate of convergence.

Solution of the MAD equations results in the inverse adaptation map $\boldsymbol{\xi}(\mathbf{p})$. To re-invert this map to the adaptation map $\mathbf{p}(\boldsymbol{\xi})$ an iterative scheme like Eq. (188) could be used. In the present chapter however a more efficient direct method is applied.

We know from the solution of the MAD equations for each point $\mathbf{p}_{i,j,k}$ of the uniform hexahedral mesh in the parametric domain the associated values of the computational coordinates, i.e. the image of $\mathbf{p}_{i,j,k}$ in the computational domain. We divide each of the hexahedral cells of the uniform 3D grid in the parametric domain into six tetrahedra. We can map these tetrahedra easily to the computational domain by first taking the images of the vertices and assuming a locally linear map in the interior of the tetrahedron. Let a point in the tetrahedron in the parametric domain with

vertices $\mathbf{p}_i$, $i = 0, 1, 2, 3$ be given as:

$$\mathbf{p}(c_1, c_2, c_3) = \mathbf{p}_0 + \sum_{i=1}^{3} c_i(\mathbf{p}_i - \mathbf{p}_0), \tag{206}$$

with

$$0 \leq c_i \leq 1, \quad i = 1, 2, 3; \quad \sum_{i=1}^{3} c_i \leq 1. \tag{207}$$

We write its image in the computational domain likewise as:

$$\boldsymbol{\xi}(c_1, c_2, c_3) = \boldsymbol{\xi}_0 + \sum_{i=1}^{3} c_i(\boldsymbol{\xi}_i - \boldsymbol{\xi}_0), \tag{208}$$

where $\boldsymbol{\xi}_i$, $i = 0, 1, 2, 3$ are the images of $\mathbf{p}_i$. Our goal is to determine which points of a uniform mesh in the computational domain lie inside the image of the tetrahedron. We start by constructing in the computational domain the smallest possible cube around the image of the tetrahedron with faces of constant ξ, η and ζ, respectively. Then we calculate the values of c_i, $i = 1, 2, 3$ for each of the nodes of the uniform mesh that lie inside the cube. All of these nodes that satisfy criterion (207) lie inside the tetrahedron. Because we have the values of c_i, $i = 1, 2, 3$ we immediately have the inverse images of these points in the parametric domain by applying Eq. (206). Hence, by repeating this procedure for each of the hexahedral cells in the parametric domain we find all new points in the parametric domain associated with a uniform mesh in the computational domain.

6.5 Multiple adaptations

In this section we briefly discuss four different methods that can be used for multiple adaptations. The first method described is the most rigorous one but has associated with it a considerable amount of additional work on discretisation and solution algorithms. The second method discussed is the simplest and is applied in section 5.6 to the model problem representative for the interaction of an oblique shock and a boundary layer. The remaining two methods discussed are applied in sections 6.7.4 and 6.7.5, respectively, to realistic aerodynamic problems. It is acknowledged that the first method is favourable, but from an efficiency point of view the other less rigorous methods may be adequate for particular cases.

6.5.1 Transformed MAD equations in updated parametric domain

When the adaptation algorithm has been applied to an initial grid, the grid in the associated parametric domain is not uniform anymore. Hence when the flow solution is updated and the grid is to be adapted once more, the MAD equations have to solved on a non-uniform grid which leads to a more complex discretisation and a system of linear equations that is not diagonally dominant. As an alternative the PDE's can be transformed to a new parametric domain associated with the previously adapted grid where the grid is uniform. In the transformed equations, however, a full matrix instead of a diagonal matrix is involved (see section 3.2.2), which leads to the same linear system being not diagonally dominant.

6.5.2 Repetition of single-adaptation algorithm

The most simple alternative for the rigorous method described above is to repeat the single adaptation algorithm. This means that each previously adapted grid is considered a new 'initial grid' which can be associated with a new parametric domain. The direct consequence of this procedure is that we do not solve the same mathematical problem as is defined in section 6.5.2.

When the sequence of adaptations converges then the weight functions must satisfy:

$$\frac{\partial w_1}{\partial \xi} = 0, \quad \frac{\partial w_2}{\partial \eta} = 0,$$

which is a very special situation that cannot be expected to hold for arbitrary flow-fields. Therefore this method is abandoned.

6.5.3 Weight function including flow differences

When the exact flow solution is known one adaptation of the grid is sufficient because a second adaptation would be based on exactly the same flow solution. This raises the question whether it is possible to apply the repetition procedure described in the previous section but using different weight functions that monitor flow solution differences rather than the flow solution itself. In section 6.7.4 such a procedure is carried out for the computation of the transonic flow over a delta wing. Each time the grid is adapted the previous flow solution interpolated to the adapted grid is stored. After calculating the flow solution on the adapted grid the difference between the previous flow solution and the calculated flow solution is used in the weight functions for the next adaptation. Hence, when the flow solution does not change anymore the procedure has converged. It is again acknowledged that a different mathematical problem is solved. On the other hand the application described in section 6.7.4 shows that this method can be used for complex flow problems such as the flow around a delta wing involving several flow features.

6.5.4 Weight function including parametric map

A fourth alternative for multiple adaptations that we propose also employs the repetition procedure described in section 6.5.2 with alternative weight functions. To eliminate the essential problem of the repetition procedure of losing all information associated with the initial grid it is proposed to incorporate the parametric map into the weight functions as an additional monitor function. The effect is that at locations where the flow solution is uniform the weight functions are driven by the functions that describe the adapted grid in the parametric domain. This implies that the adaptation algorithm will generate a new adapted grid that is more uniform in the parametric domain. In the limit of infinitely many adaptations the initial grid will then be recovered. Although also in this case a different mathematical problem is solved. Application to the calculation of supersonic flow over a single-nozzle rocket, including the exhaust plume, shows that this method can be efficient for realistic problems involving supersonic flow. with complex shock-wave patterns.

6.6 Adaptation of 3D multi-block structured grids

In the 2D airfoil case it appeared that, although the C-type topology grid is essentially a single-block grid, the grid being connected to itself by a face-to-face connection introduces difficulties that are typical for a multi-block environment. The same is true for CO-topology grids around wings. Therefore we discuss a general approach towards the adaptation of multi-block grids which is then used to provide a useful algorithm to adapt CO-topology grids around wings.

6.6.1 General multi-block topology

Suppose we have the simplest possible 3D multi-block grid consisting of two blocks with a single common face. When we apply the adaptation algorithm to both blocks separately, the adapted grids of both blocks will not match in the common face. The question is how to correct both grids such that the grids in the common face match while the adapted grids in the two blocks are conserved as much as possible.

The question arises whether we can average the two non-matching grids in the common face to obtain a single grid that is a 'look-alike' of the two originals. We cannot simply average all nodes of the two grids that have identical indices since this does not guarantee that the averaged grid is non-overlapping. More specifically, when we average the maps that describe the two sets of computational coordinates it can not be proven that the Jacobian of the averaged map be non-zero everywhere.

We propose the following approach. Consider the two maps that describe both sets of computational coordinates in the common face as functions to which the initial non-adapted grid in the common face has to be adapted. The adaptation algorithm produces adapted grids that are such that the functions to which the grid is adapted tend to become linear in the computational domain of the adapted grid. This means that the gradients of the computational coordinates that describe the adapted grid will match the gradients of the functions that were used in the weight functions to drive the adaptation. In the case of grid averaging this means that the grid resulting from the averaging procedure will be dense at locations where both of the original grids are dense. If at a certain location one of the grids is dense while the other is relatively coarse, the grid resulting from the averaging procedure will be moderately dense.

The 2D adaptation algorithm is used to correct the initial, non-adapted, grid in the common face, so the invertibility theorem of Clement, Hagmeijer and Sweers presented in section 4.6 is applicable. This shows that the proposed correction procedure leads to an 'averaged' grid that is guaranteed to be regular and non-overlapping. Hence, this approach is used to 'average' two grids in common faces between adapted blocks. It should be noted, however, that when the two grids to be averaged are identical the present approach will not conserve these grids but will produce a 'similar' grid. These aspects are discussed in more detail in the next section.

Now the question arises how the adapted grids can be re-adapted in the two blocks to match the 'averaged' grid in the common face, while the originally adapted grids are largely conserved. Here we propose an approach that again uses the parametric domain concept. If each of the adapted grids is associated with its own parametric domain where each grid is uniform, the 'averaged' grid in the common face will appear as a non-uniform grid in one face of each of the parametric domains. The uniform grids can be adapted in these parametric domains to the non-uniform grid in their common face by simply shifting the family of straight grid lines that are normal to the face. This will cause the grids in the opposite faces to become non-uniform too. In order to keep the grids in the opposite faces fixed one could apply interpolation between the grids in the common face and its opposite faces to get the grid points in the interior of the blocks. This may lead, however, to excessive skewness of the resulting grid in the physical domain in case the non-adapted grid possesses highly stretched cells. Hence, by mapping the corrected grids back from the two parametric domains to the physical domain corrected grids are obtained in the two blocks that match at their common face. Moreover, the corrected grids will resemble the initially adapted grids because the grids have been corrected in their parametric domains which enables

conservation of global characteristics.

6.6.2 Averaging of two-dimensional grids in the unit square

In this section we will investigate how two different grids in the unit square can be 'averaged' such that the resulting grid contains characteristics of both grids in terms of cell-size distribution. It is required that when the two grids are identical, the 'averaged' grid is also identical to these grids. It is also required that when each of the two grids is regular (non-overlapping) that then the 'averaged' grid is also regular. For completeness it is noted that when the domain is not a unit square, transformation of the two grids to the unit square can be carried out first. Hence using the unit square as the domain does not cause a loss of generality.

We start by addressing the question whether any given grid can be obtained by solving a system of PDE's. Given a map $(\xi(p,q), \eta(p,q))$ from the unit square onto itself, we assume that there exists a matrix M such that:

$$\nabla_p \cdot (M \nabla_p \xi) = 0, \quad \nabla_p \cdot (M \nabla_p \eta) = 0. \tag{209}$$

Transformation of Eqs. (209) to the (ξ, η)-domain (see section 3.2.2) yields:

$$\nabla_\xi \cdot (\tilde{M} \nabla_\xi \xi) = 0, \quad \nabla_\xi \cdot (\tilde{M} \nabla_\xi \eta) = 0, \tag{210}$$

with:

$$\tilde{M} = |J| J^{-1} M J^{-T}, \quad J = \begin{pmatrix} p_\xi & p_\eta \\ q_\xi & q_\eta \end{pmatrix} = \begin{pmatrix} \xi_p & \xi_q \\ \eta_p & \eta_q \end{pmatrix}^{-1}. \tag{211}$$

Eqs. (210) are satisfied if we choose:

$$\tilde{M} = I = \begin{pmatrix} 1 & 0 \\ 0 & 1 \end{pmatrix}, \tag{212}$$

leading to definition of matrix M:

$$M = \frac{1}{|J|} J J^T. \tag{213}$$

Eqs. (209) and (213) are associated with a harmonic map as described in section 3.3.4 when the

monitor function Φ is taken as:

$$\Phi(p,q) = (\xi,\eta)^T. \tag{214}$$

Following the construction of the harmonic map we take the matrix M as:

$$M = \sqrt{|J_\Phi J_\Phi{}^T|}\, J_\Phi{}^{-T} J_\Phi{}^{-1}, \quad J_\Phi = (\Phi_p, \Phi_q)^T. \tag{215}$$

This finally leads to Eq. (213) by noting that:

$$J_\Phi \equiv J^{-T}. \tag{216}$$

Hence, the conclusion is that any given map from the unit square onto itself can be obtained as the solution of a harmonic map if the functions that define the given map are used as the monitor functions in the metric tensor. In other words reconstruction of a given map on the unit square can be considered as the adaptation of an initially uniform map in the unit square to monitor functions that consist of the functions describing the given map.

Based on the above results it is easy to construct an algorithm for the averaging of two given maps, say $(\xi_1(p,q), \eta_1(p,q))$ and $(\xi_2(p,q), \eta_2(p,q))$. The averaged map is defined as an harmonic map based on the following monitor function Φ:

$$\Phi(p,q) = (\xi_1, \eta_1, \xi_2, \eta_2)^T. \tag{217}$$

At this stage the first objective is reached: to enable grid averaging in such a way that when the two maps are identical they are also identical to the resulting harmonic map.

The second objective, to obtain a regular 'averaged' grid assuming that the two initial grids are both regular (non-overlapping) is not reached yet since an invertibility theorem is not available for harmonic maps. The a priori guarantee of producing a regular 'averaged' grid is of high priority in view of robustness, therefore it is proposed to use an alternative averaging algorithm. The 2D MAD equations (159) are used to construct the averaged map by again using the functions that describe the two given grids as monitor functions. In other words: the weight functions are specified in the MAD equations as:

$$w_1 = \sqrt{\|\Phi_p\|^2}, \quad w_2 = \sqrt{\|\Phi_q\|^2}, \tag{218}$$

with Φ given in Eq. (217). Note that due to the assumption that the initial mappings are regular and have positive Jacobians everywhere, i.e.:

$$w_1 > 0, \quad w_2 > 0. \tag{219}$$

It is noted that with this alternative averaging algorithm the requirement that the two initial maps be conserved when they are identical is not fulfilled. On the other hand the 'averaged' grid will be such that the monitor functions are smoothly distributed over the grid points. Therefore this averaging method is used for matching grids in common faces between different blocks.

6.6.3 Single-block topology around wings

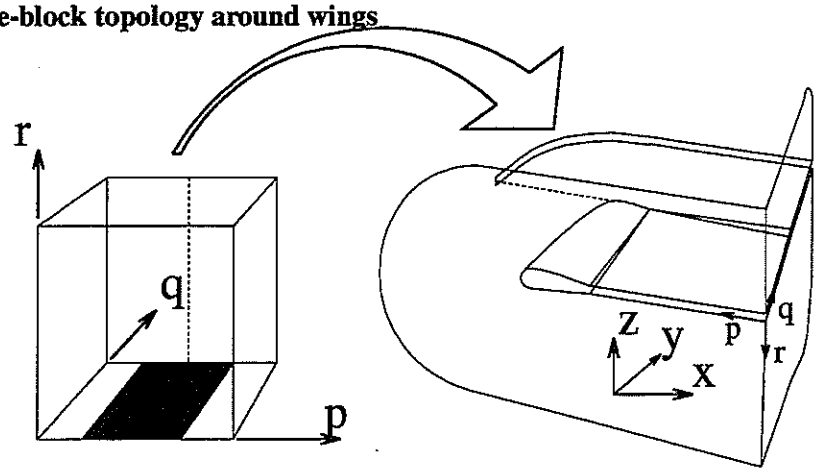

Fig. 43 Single block CO-topology with the shaded region in the cube corresponding to the wing surface.

In figure 43 the CO-topology of a single block around a wing is depicted as a map from a unit cube. The central part of the bottom face of the cube is mapped onto the wing surface while the remaining parts of the bottom face are mapped onto the upper and lower side of the wake surface, respectively. The back face of the cube is mapped onto the upper and lower side of the horizontal plane outboard of the wing. Hence two face-to-face connections are present: the off-centre parts of the bottom face and the two halfs of the back face.

To adapt the grid in the physical domain one has to adapt the grid in the unit cube which is considered as the parametric domain, see Fig. 41. But in view of the above described face-to-face connections, adaptation of the grid in the parametric domain will not result in an acceptable grid in the physical domain. This can easily be understood by noting that the adapted grid in the two off-centre parts of the bottom face of the parametric domain will be different and non-symmetric.

Also the trailing edge of the wing will not coincide with a grid line anymore in the adapted grid. Finally the adapted grid in the back plane of the unit cube will not be symmetric with respect to the vertical line that divides the back plane in two halfs. These mismatches are similar to the ones encountered in the adaptation of multi-block grids where adapted grids in adjacent blocks have to match at the block-interfaces.

The adaptation of the CO-type single-block topology depicted in Fig. 43 is performed in steps:

1) The basic adaptation map is applied by solving the MAD equations (196) in the parametric domain.
2) The back face grid is made symmetric. The functions that describe the back face grid and its image with respect to the $p = \frac{1}{2}$ plane are substituted in the weight functions of the 2D MAD equations (159). Solution of these equations leads to a symmetric re-adapted grid that resembles the characteristics of the originally adapted grid.
3) The bottom face grid is corrected. The off-centre parts are symmetrised using a similar approach that has been used to symmetrise the back plane grid. The centre part is also corrected to be boundary conforming along the two straight lines that correspond to the trailing edge. This is also done by the approach described in the previous section; a uniform grid in the centre part section (which is boundary conforming) is adapted to the functions that describe the initially adapted grid in that part of the face.
4) The grids in the three parts of the bottom plane are matched along the trailing edge lines, again using adaptation in local parametric domains.
5) The back face and the bottom face are matched at their intersection.
6) The block interior grid is matched to the bottom face (see previous section).
7) The block interior grid is matched to the back face (see previous section).

In all steps correction (or re-adaptation) is performed in a local parametric domain that is associated with a part of the current grid. So in each step the characteristics of the grid are more or less conserved. It is acknowledged that the above described correction steps are topology-dependent and also that the result depends on the order of the steps taken. For example, the sixth and seventh step can be interchanged leading to a slightly different result. To obtain a robust algorithm for the adaptation of CO-topology grids around wings, however, the above described approach is adequate which is demonstrated in section 6.7.

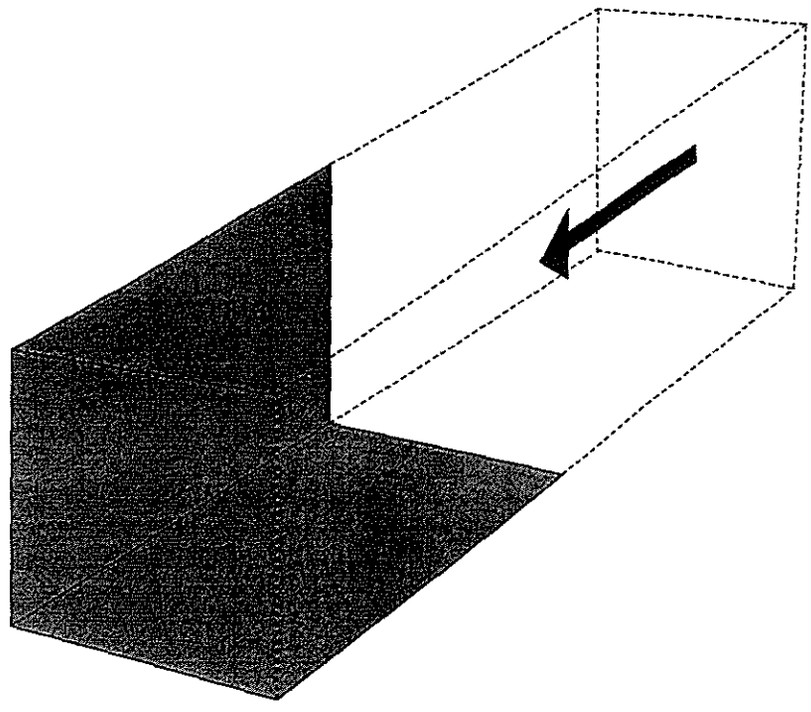

Fig. 44 Rectangular flow domain containing two intersecting solid walls (shaded).

6.7 Applications to 3D aerodynamic problems

6.7.1 Viscous corner flow

To test the modification functions and the asymptotic analysis for the boundary-layer along intersecting solid surfaces (see section 6.2) we start with the adaptation of an initially orthogonal grid within the flow domain depicted in Fig. 44. The flow domain consists of a box containing two flat plates that are connected at a common edge. The direction of the oncoming viscous flow is parallel to both plates on which interacting boundary-layers develop. The boundary layers start to develop at the leading edges of the two plates which are located at 50% length of the box. On all other faces and parts of faces of the box that are parallel to the flow direction symmetry conditions are imposed. If four of these flow domains are combined, one obtaines the flow through one cell of an infinite uniform (honeycomb-type of) mesh consisting of infinitesimally thin plates.

A global impression of the adapted grid is presented in Fig. 45 showing the high grid-point densities along the faces of the flow domain where the boundary layers are expected and at the leading edges of both plates. In Fig. 46 a close-up of the adapted grid shows that iso-ξ lines are not excessively skew confirming the validity of the qualitative arguments that are used in section 6.2. In Fig. 47 the same close-up is shown but an additional iso-ξ surface is shown to demonstrate that within this grid plane the grid is nearly orthogonal, even in the neighbourhood of the intersection

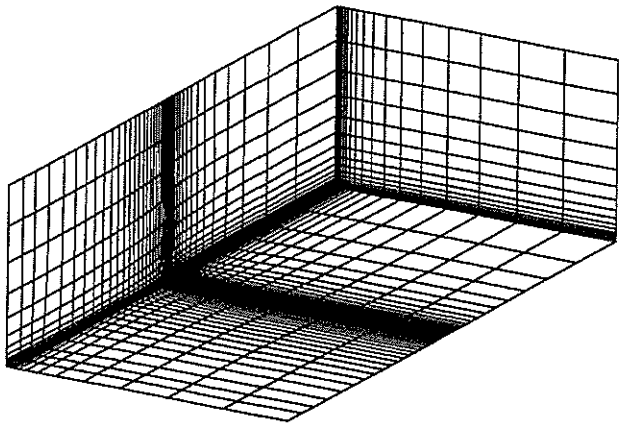

Fig. 45 Rectangular flow domain with impression of adapted grid showing boundary-layer and leading-edge resolution.

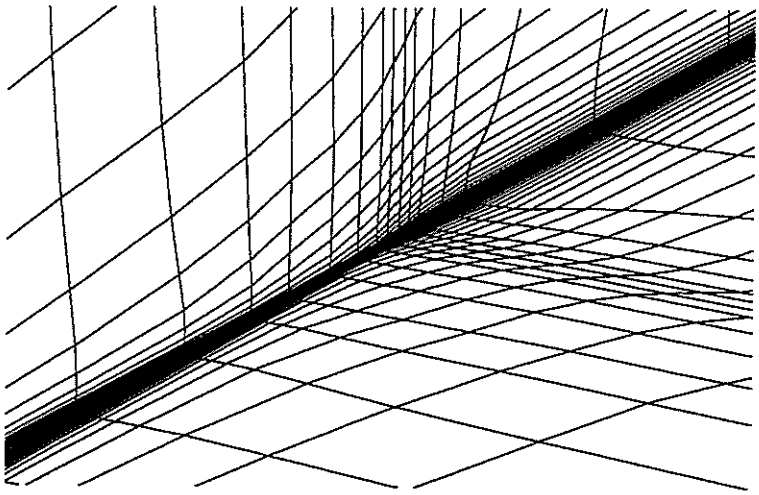

Fig. 46 Close-up of adapted grid near the leading edge and near the intersection of the two solid walls.

of the two plates.

The conclusion is that the modification functions that are proposed in section 6.2 are adequate to deal with boundary layers along intersecting solid surfaces.

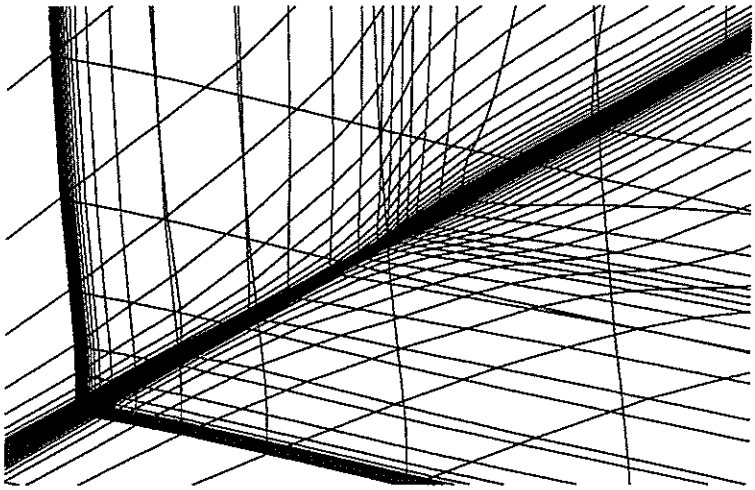

Fig. 47 Close-up of adapted grid near the leading edge and near the intersection of the two solid walls including iso-ξ plane.

6.7.2 ONERA M6 wing

To demonstrate the grid adaptation algorithm results are presented for the ONERA M6 wing at transonic flow conditions [55]. calculations on non-adapted as well as adapted grids have been performed, on medium and fine grids, and for three different Reynolds numbers, see table 3. For each case the NLR flow simulation system ENFLOW has been used, [7],[59],[38], to generate the initial grid and to calculate the flow solutions on the various grids. All solutions converged to a sufficient degree of accuracy.

Fig. 48 shows the medium grid (Fig. 48a) and the adapted medium grid on the wing upper surface (Fig. 48b) as well as the calculated pressure coefficient (C_p) distributions (Fig. 48c and 48d). Adaptation at the leading edge, trailing edge, shock position and tip are evident resulting in a more

Table 3 Cases considered for ONERA M6 wing (n=non-adapted, a=adapted) $M_\infty = 0.84$, $\alpha = 3.06°$, fixed transition at 3% chord.

	medium $128 \times 24 \times 32$	fine $256 \times 48 \times 64$
$Re_\infty = 3 \times 10^6$	n,a	n
$Re_\infty = 11.7 \times 10^6$	n,a	n
$Re_\infty = 48 \times 10^6$	n,a	n

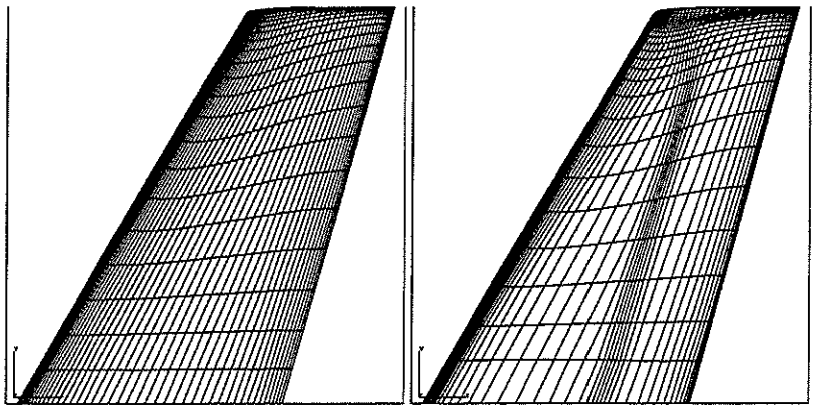

a) non-adapted grid b) adapted grid

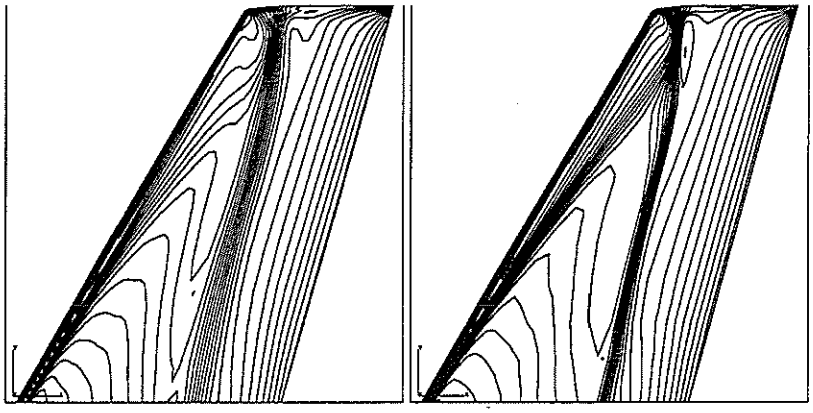

c) C_p on non-adapted grid d) C_p on adapted grid

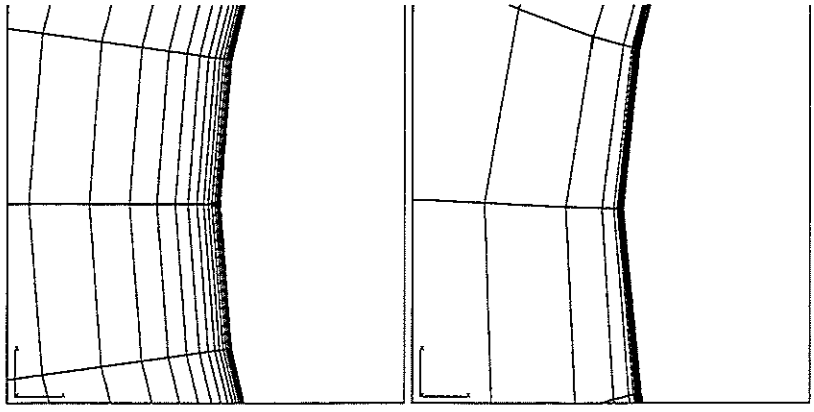

e) non-adapted grid, nose f) adapted grid, nose

Fig. 48 Non-adapted and adapted medium grid, (a) and (b), and C_p-distributions ($\Delta C_p = 0.05$), (c) and (d), on wing upper surface, and close-ups of non-adapted and adapted grid near the leading edge in the symmetry plane, (e) and (f), $M_\infty = 0.84$, $\alpha = 3.06°$, fixed transition at 3% chord, $Re_\infty = 11.7 \times 10^6$.

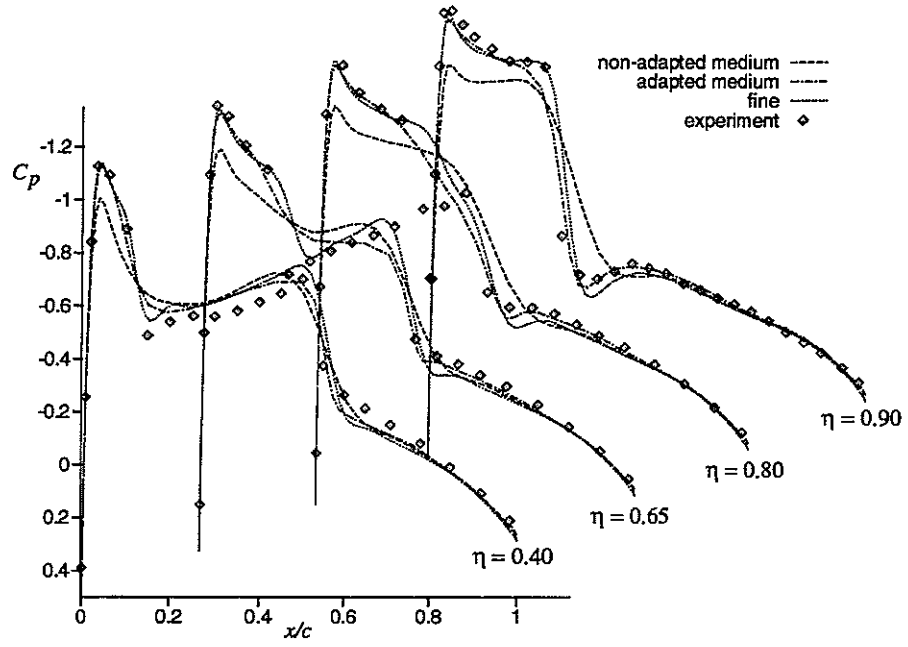

Fig. 49 Upper surface pressure distributions (C_p) on non-adapted and adapted grids compared to fine grid result and experimental data, $M_\infty = 0.84$, $\alpha = 3.06°$, fixed transition at 3% chord, $Re_\infty = 11.7 \times 10^6$.

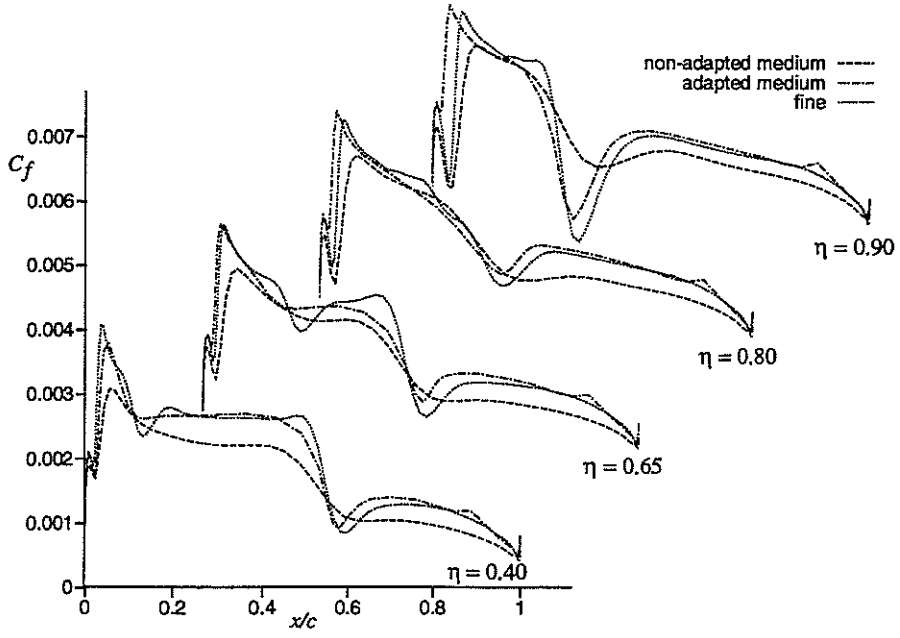

Fig. 50 Skin-friction distributions (C_f) on non-adapted and adapted grids compared to result on fine grid , $M_\infty = 0.84$, $\alpha = 3.06°$, fixed transition at 3% chord, $Re_\infty = 48 \times 10^6$.

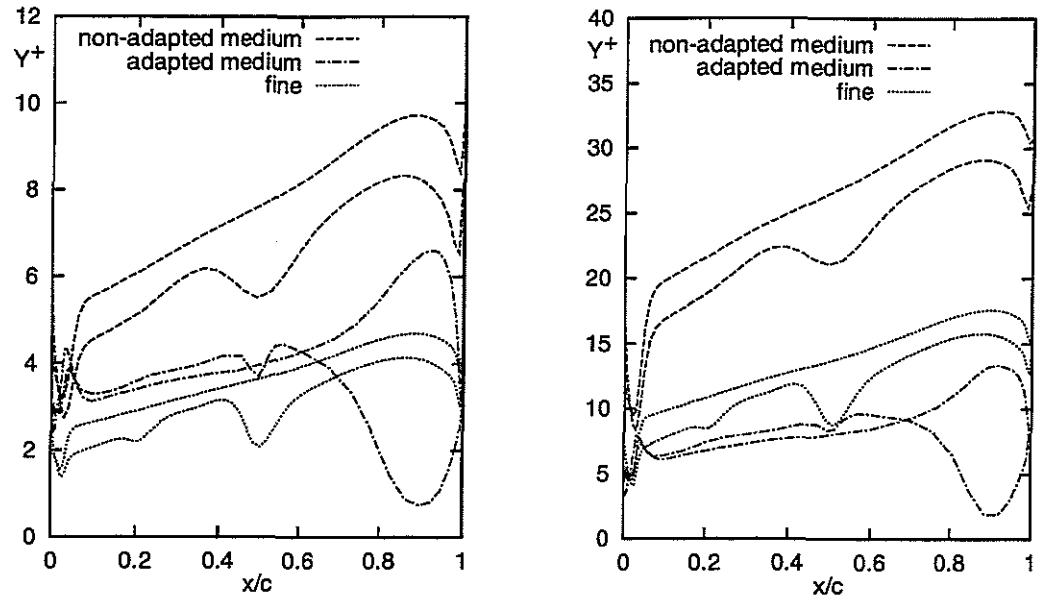

a) $Re = 11.7 \times 10^6$ b) $Re = 48 \times 10^6$

Fig. 51 Law-of-the-wall coordinate y^+ of first grid point above the surface along the 65% span cross section of various grids, $M_\infty = 0.84$, $\alpha = 3.06°$, fixed transition at 3% chord.

pronounced shock system and better resolution of the merging of the fore and aft shock. Details of the adaptation near the nose in the symmetry plane (Figs.48e and 48f) show concentration in the boundary layer with a clear transition to the outer flow field region.

The C_p distributions on the upper side at various cross sections of the wing are depicted in Fig. 49. The results on the non-adapted and adapted grid are compared to the fine grid result as well as experimental data. The suction peak at the leading edge and the downstream expansion zone as apparent in the fine grid result and the experimental data is fully captured in the solution obtained on the adapted medium grid, while on the non-adapted medium grid these flow features are not captured very well.

The skin-friction (C_f) distributions on the upper side of the wing at various cross sections of the wing are presented in Fig. 50 for $Re_\infty = 48 \times 10^6$. Along the whole upper surface adaptation results in significant improvements. It is also visible how the laminar-turbulent transition line shifts upstream upon adaptation. This is caused by the flow solver that uses user-specified transition positions in terms of grid line index. Hence, when the grid changes due to adaptation the transition location also changes.

The influence of grid adaptation on the resolution of the boundary layer is explicitly demonstrated

in Fig. 51 showing the 'law-of-the-wall' coordinate y^+ of the first grid point above the wing surface at the 65% span cross section. For the $Re_\infty = 11.7 \times 10^6$ case the y^+ distribution over the grid is significantly improved upon adaptation compared to the non-adapted medium grid. For the $Re_\infty = 48 \times 10^6$ case the improvement is even stronger: the adapted medium grid resolves the boundary layer better than the fine grid and the y^+ values are reduced by roughly 30%. The stronger effect for the high Reynolds number case is not unexpected since the initial grids have been generated for the $Re_\infty = 11.7 \times 10^6$ case by CFD experts with a state-of-the-art elliptic grid generator. From Fig. 51a we learn that even such a special-purpose grid can be automatically modified to improve the y^+ resolution by roughly 50%, i.e. equal to the improvement obtained on the grid that is twice as fine in each direction and therefore takes three to four times as much computing time to produce a solution.

The influence of grid adaptation on the aerodynamic coefficients is shown in Fig. 52 which shows the lift (C_L), total drag (C_D), friction drag (C_{Df}), and pitching moment (C_M) coefficients as calculated on the non-adapted and adapted medium grids, and on the fine grid, for three different Reynolds numbers. Globally grid adaptation results in an improvement of the medium-grid coefficient predictions when the fine grid results are taken as measure for comparison. More specifically the drag coefficient, see Fig. 52b, is strongly improved: the gap of 25 counts (1 count $\equiv 10^{-4}$) between the medium and fine grid results is reduced to 6 counts upon grid adaptation. This is still not accurate enough for practical problems but it should be mentioned that the medium grid contains only about 100,000 points. Especially the friction drag is improved upon grid adaptation, see Fig. 52c, and only differs by one count from the fine-grid result. It is also remarkable that the adapted medium-grid results and the fine-grid results have the same type of dependency on the Reynolds number. In this respect the non-adapted medium-grid solution is apparently not fully representative for the exact solution.

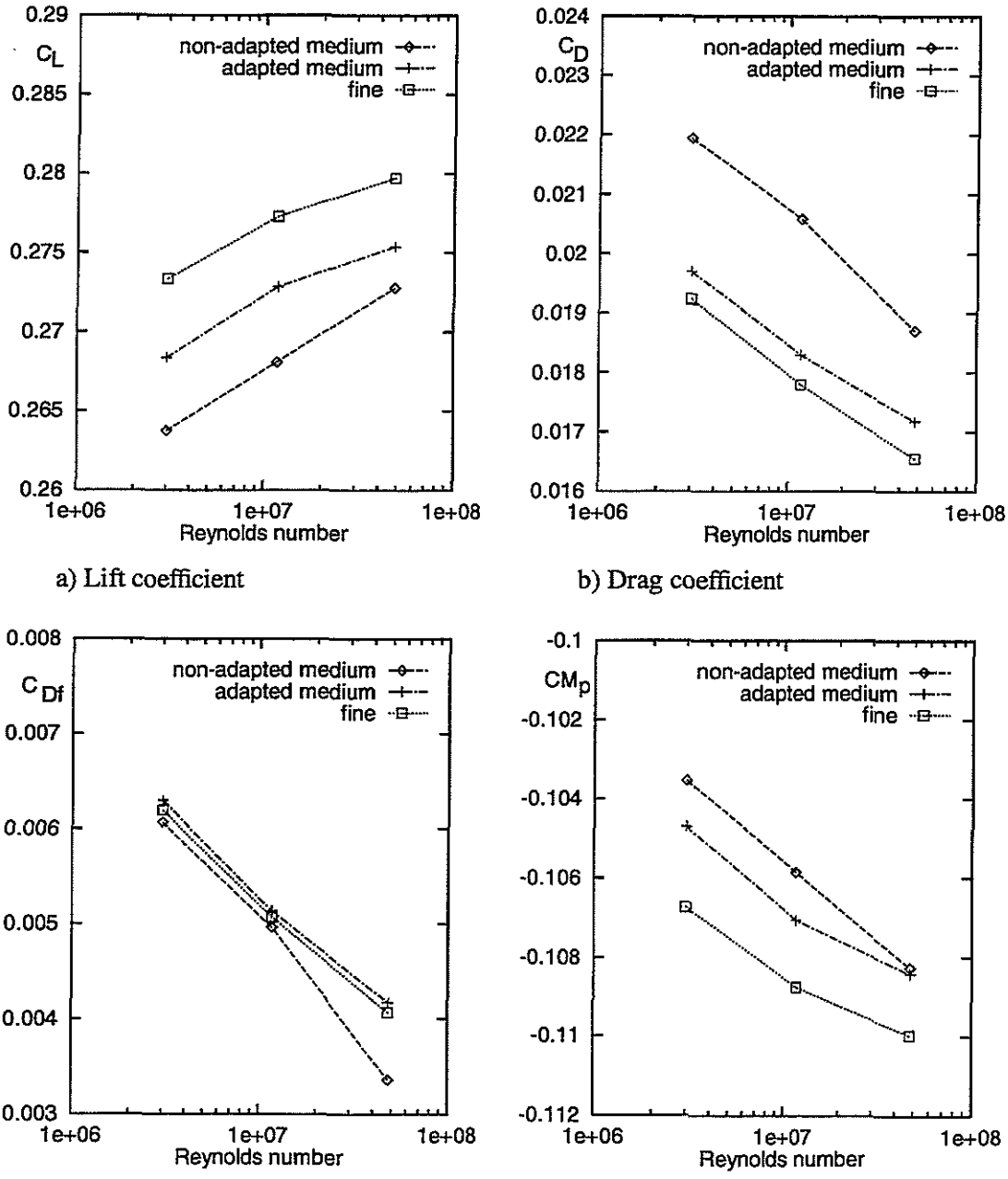

a) Lift coefficient

b) Drag coefficient

c) Friction drag coefficient

d) Pitching coefficient

Fig. 52 Force coefficients as function of Reynolds number obtained for non-adapted and adapted medium grids and obtained for fine grid, $M_\infty = 0.84$, $\alpha = 3.06°$, fixed transition at 3% chord.

6.7.3 DLR F4 wing/body

To illustrate that the developed adaptation algorithm is applicable for wing-body configurations the present section describes the grid adaptation results for a CO-type single-block structured grid around the DLR F4 wing-body configuration, see Fig. 53.

A medium resolution grid of $128 \times 24 \times 44$ cells (over 145,000 nodes) in stream-wise, span-wise and normal direction, respectively, is used. The upstream flow conditions are a Mach number of $M_\infty = 0.75$, a Reynolds number of $Re_\infty = 3 \times 10^6$, an incidence of $\alpha = 0.93°$. Fixed laminar-turbulent transition at 3% chord along the wing is employed, while the body surface is treated as inviscid (slip condition).

The initial and adapted medium grids and the corresponding C_p-distributions are shown in figures Figs. 53 to 56. The shock resolution is improved on the adapted grid and also it is observed that grid lines have been moved towards the shock wave as well as into the boundary-layer.

It should be noted that the grid line forming the intersection of the symmetry plane and the fuselage should not be moving during adaptation of the grid. At present, however, this is not accounted for yet by the algorithm. The results presented in this section therefore only serve to indicate the potential applicability of the grid adaptation algorithm to CO-type single-block topologies around wing-body configurations.

The 145,000 node grid for a wing body configuration is a medium grid which is rather coarse for obtaining a numerical solution of the Reynolds-averaged Navier-Stokes equations. Specifically in the span-wise direction the present grid is much too coarse so in the present study it merely serves as an illustration. For the DLR F4 wing-body configuration an adequate medium grid would contain in the order of 500,000 to 1 million nodes.

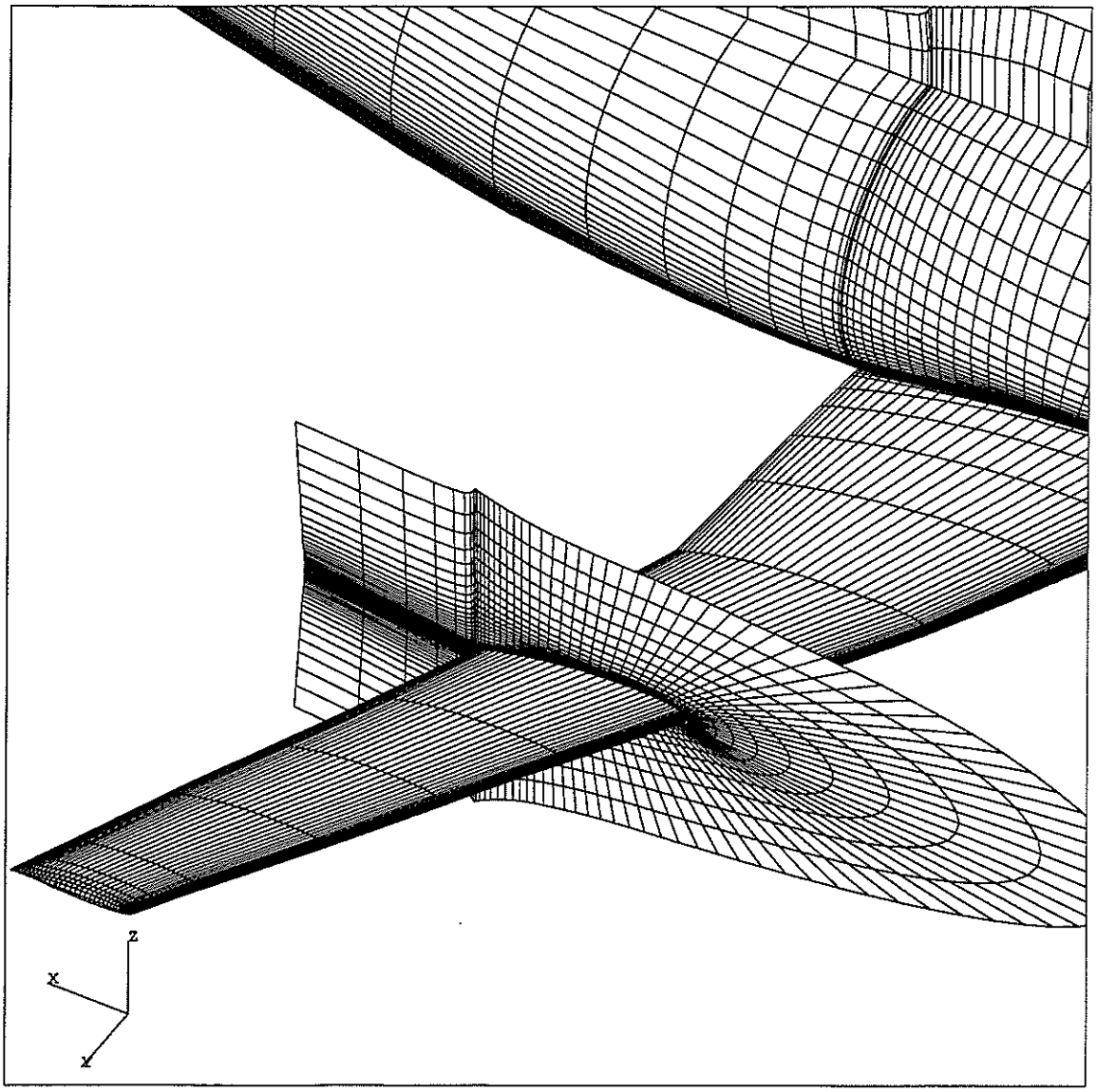

Fig. 53 Non-adapted grid for the DLR F4 wing-body configuration ($M_\infty = 0.75$, $Re_\infty = 3 \times 10^6$, $\alpha = 0.93°$, fixed transition at 3% chord).

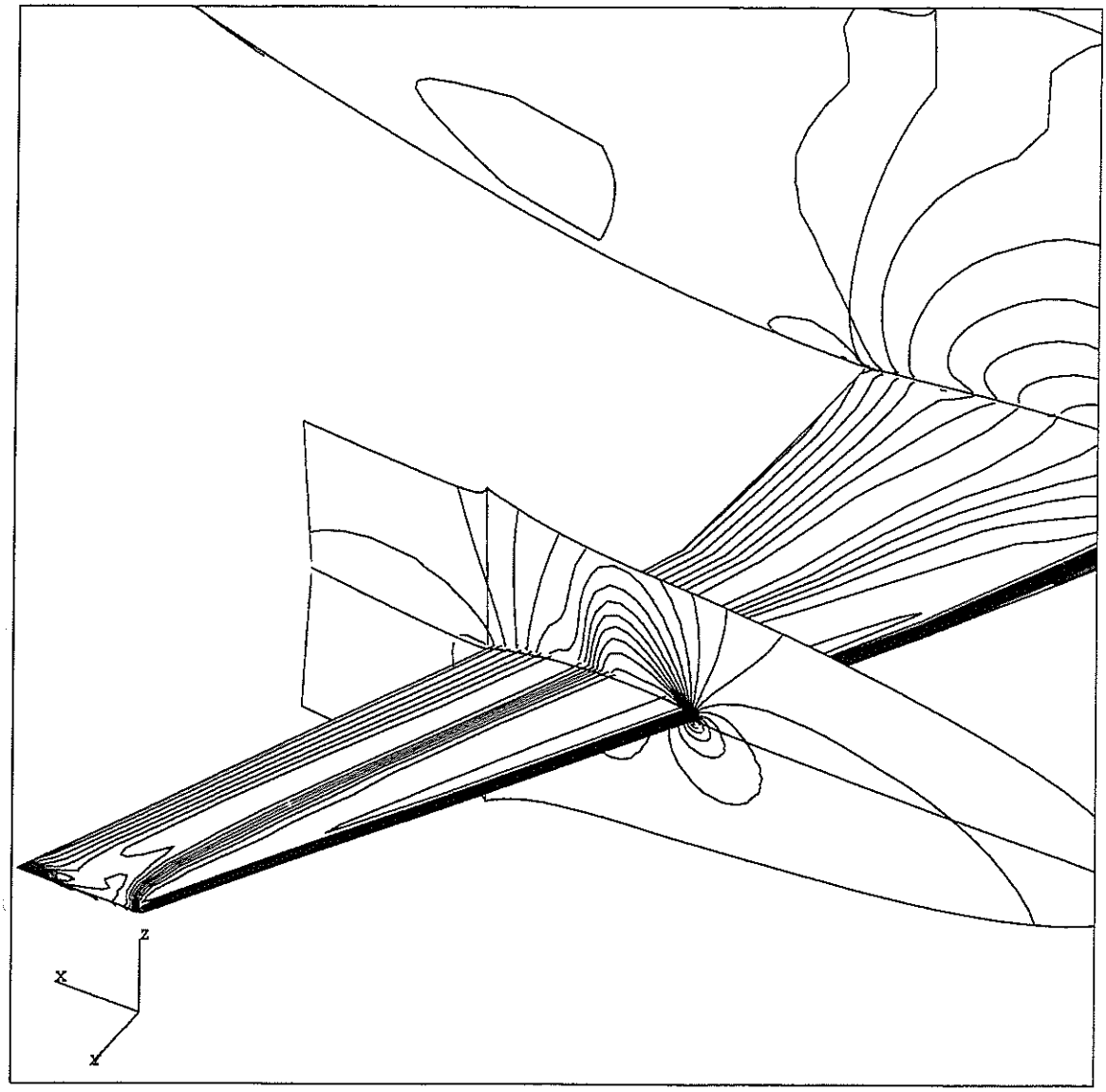

Fig. 54 C_p*-distribution obtained on non-adapted grid for the DLR F4 wing-body configuration (*$M_\infty = 0.75$, $Re_\infty = 3 \times 10^6$, $\alpha = 0.93°$, *fixed transition at 3% chord,* $\Delta C_p = 0.1$*).*

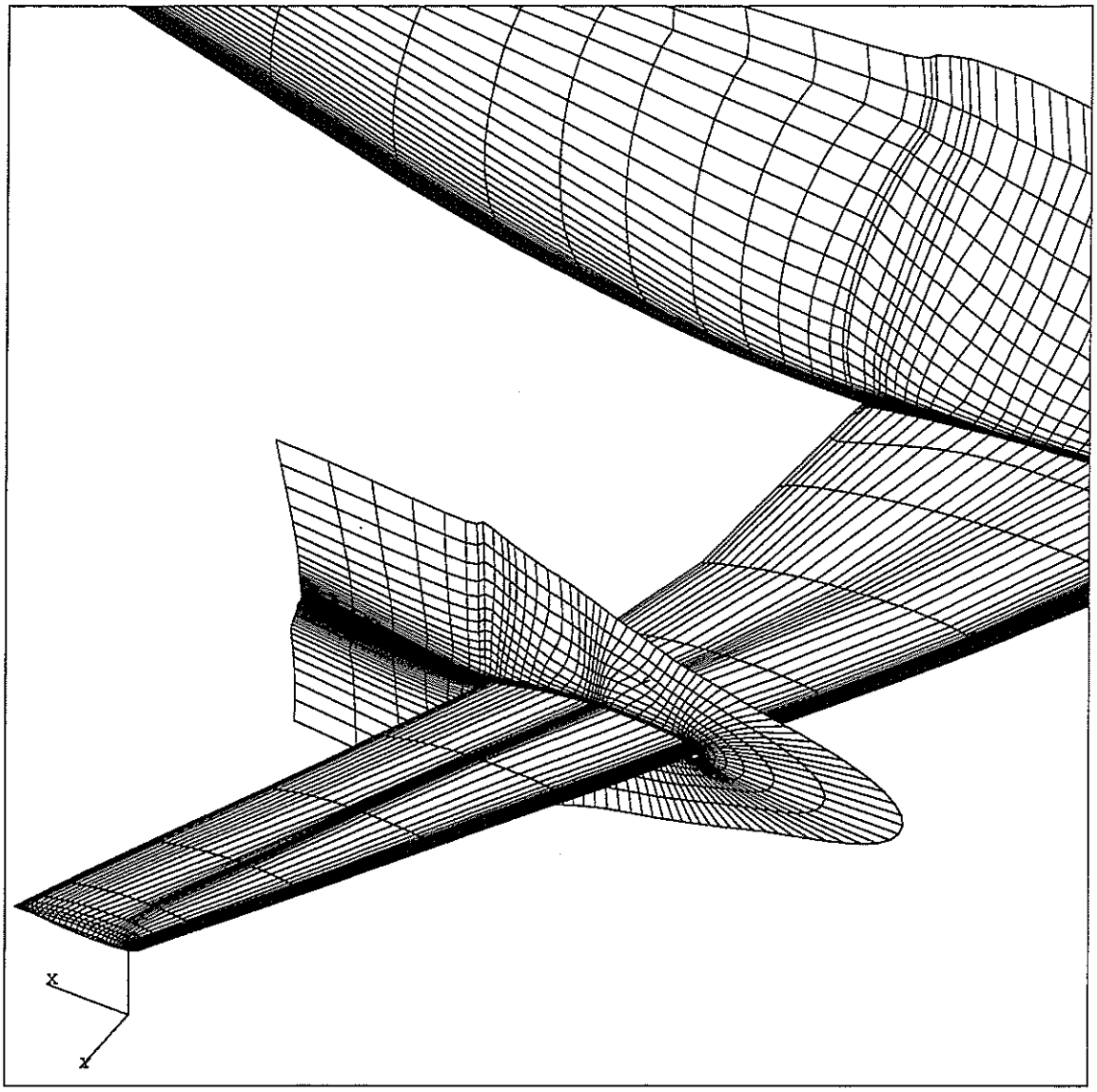

Fig. 55 Adapted grid for the DLR F4 wing-body configuration ($M_\infty = 0.75$, $Re_\infty = 3 \times 10^6$, $\alpha = 0.93°$, fixed transition at 3% chord).

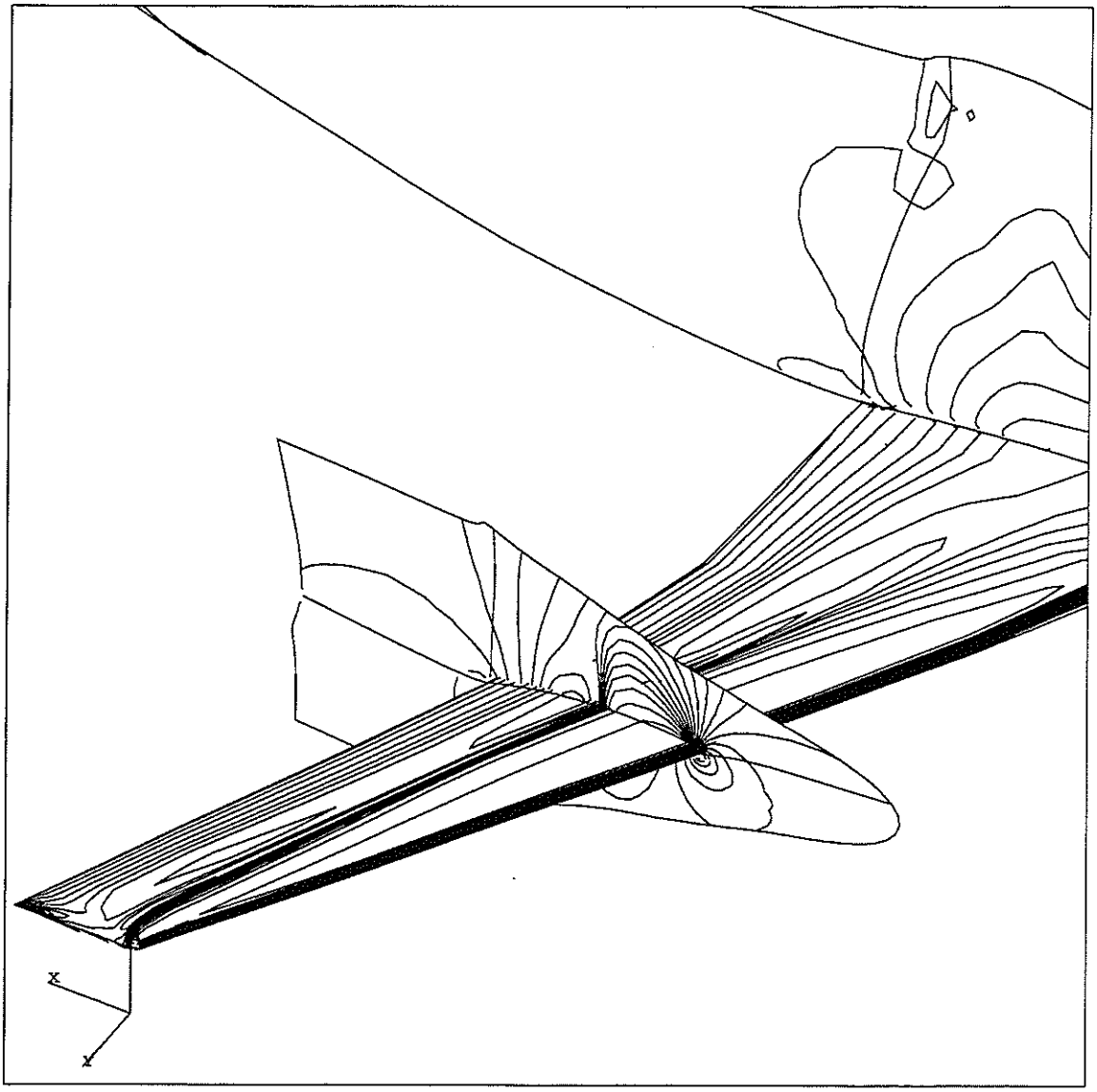

Fig. 56 C_p*-distribution obtained on adapted grid for the DLR F4 wing-body configuration* ($M_\infty = 0.75$, $Re_\infty = 3 \times 10^6$, $\alpha = 0.93°$, *fixed transition 3% chord,* $\Delta C_p = 0.1$).

6.7.4 Generic Delta wing

In the present section adaptation results are presented for the transonic flow around a delta wing, a configuration generic for the wing of fighter aircraft. The results are obtained within the framework of NLR's contribution to the TA15 research programme of the Western European Armaments Group (WEAG-TA15) as described in [1]. The cropped delta wing has a leading edge sweep of 65°, a sharp leading edge and a rounded tip. The flow condition used is: $M_\infty = 0.85$, $Re_\infty = 48 \times 10^6$, $\alpha = 10°$, and the flow is assumed to be turbulent everywhere. The flow solutions are solutions of the Navier-Stokes equations. Two grid resolutions are used: a coarse CO-grid of 66,297 points and a medium CO-grid of 505,440 points. The coarse CO-grid is a subset of the medium grid with half the number of points in each coordinate direction. In contrast to the previous examples, where only one adaptation per grid has been carried out, the present example involves five adaptations. Each subsequent adaptation uses the previous adapted grid as the 'initial' grid (see section 6.5.3). To prevent excessive adaptation and loosing too much information from the true initial grid, each new adaptation is based on the difference between the flow solution obtained on the current grid and that obtained on the previous grid (see section 6.5.3).

For the upper surface of the wing Fig. 57 shows the initial coarse grid and the adapted coarse grids after 1, 3 and 5 adaptations, respectively. The main vortex that is generated by leading-edge flow separation causes the grid to become denser in the region adjacent to the leading edge. This is also illustrated in Fig. 58 which shows the same grids in a cross-flow plane at approximately 60% root chord. In addition to adaptation in tangential direction the grid is also strongly adapted in normal direction.

The initial grid in Figs. 57 and 58 is typical for the current practice in CFD. Near the surface the grid is dense to accommodate boundary-layer resolution. Away from the surface the grid smoothly stretches in normal direction to cells that have aspect ratios of about 1. In this case such a grid is reasonably adequate in the region away from the neighbourhood of the vortex. The distribution of grid points along grid lines normal to the upper surface that cross both the boundary-layer and the vortex, however, has to be tuned carefully to accommodate resolution of both flow phenomena. The adapted grids shown in Fig. 58 suggest that this is exactly what the adaptation algorithm is trying to do.

Fig. 59 shows the comparison of the computed surface pressure distributions in the cross-section at 60% root chord. It appears that upon adaptation the C_p suction peak on the upper side of the wing shifts away from the leading edge and the secondary separation is better resolved. During

this shift the peak is reduced by approximately 10% and the gradients are increased. Fig. 60 shows a comparison of the C_p distributions obtained on the initial coarse grid, on the coarse grid after five adaptations, on the medium grid, and the one obtained from measurements. It shows that the shift of the C_p peak away from the leading edge is in line with the results obtained on the medium grid and the measurements. Also the pressure distribution between the symmetry plane and the suction peak is better predicted. The suction peak associated with the vortex resulting from the secondary separation that shows up in the medium grid result (small C_p peak between the high peak and the leading edge) is not present in the solution on the adapted coarse mesh. This suggests that the secondary vortex is better resolved on the medium grid than on the adapted coarse grid, i.e. more compact on the medium grid than on the adapted coarse grid.

Figs. 61 and 62 show the same comparisons as Figs. 59 and 60 but for the sections at 90% of the root chord. Again it is observed that adaptation leads to a shift of the C_p peak away from the tip, see Fig. 61, which is in line with the medium grid result and the measurements. The magnitude of the peak, however, is too low.

Also one adaptation of the medium grid has been carried out. In Figs. 63 and 64 the results obtained on the adapted medium grid are compared with the non-adapted medium-grid result and the measurements. At both cross-sections (at 60% and 90% of the root chord) the shift of the C_p peak due to the primary vortex is again evident which leads to better agreement with the measurements. At the 60% cross-section it appears that upon adaptation secondary separation occurs close to the location where it occurs in the measurement, but in the region between the suction peak and the leading edge the solution needs improvement. An explanation of these results may be that the adaptation algorithm cannot handle the multiple flow features present in the flow such as the separating boundary layer, the leading edge shear layer, the primary vortex and the secondary vortex. A further possible explanation may be that the Baldwin-Lomax turbulence model cannot cope adequately with the interaction of the secondary vortex and the boundary layer.

In conclusion adaptation-results show trends towards better agreement with the experimental results, especially with respect to the location of the peak in the C_p distribution. It is also recognised, however, that the agreement with the measurements is not improved everywhere upon adaptation. In particular the level of the C_p peak and the representation of the secondary vortex are not improved. It should also be noted that seen in the light of the strong interaction of the various flow features the overall number of nodes used is not very high.

At the 90% cross-section upon adaptation the distribution between the C_p peak and the tip shows

less agreement with the measurements than before adaptation.

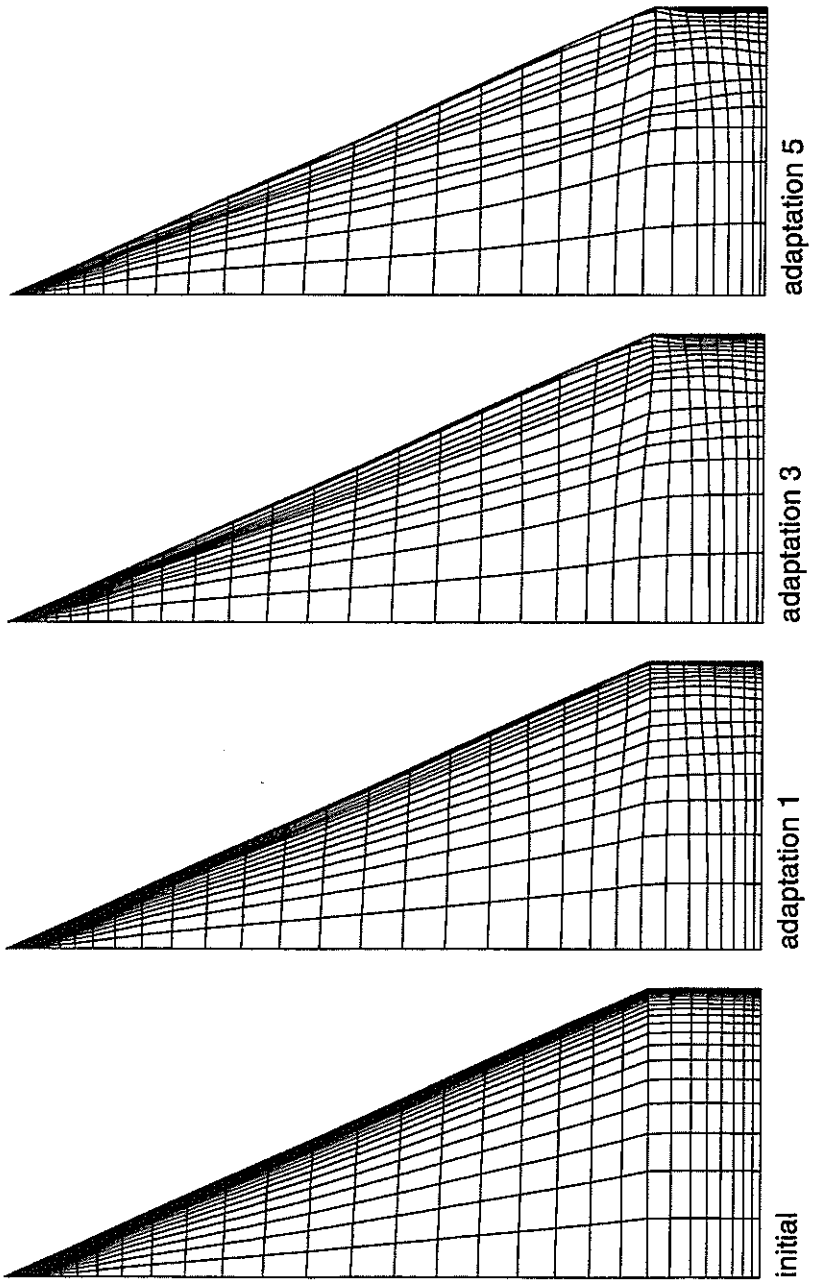

Fig. 57 Top view of adapted coarse grid for the upper side of the generic delta wing ($M_\infty = 0.85$, $Re_\infty = 48 \times 10^6$, $\alpha = 10°$, turbulent flow).

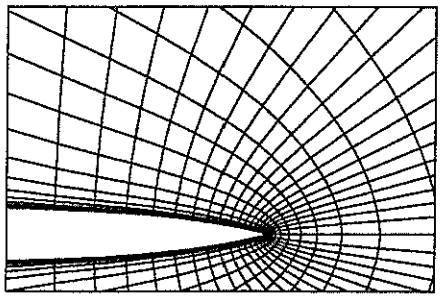

initial

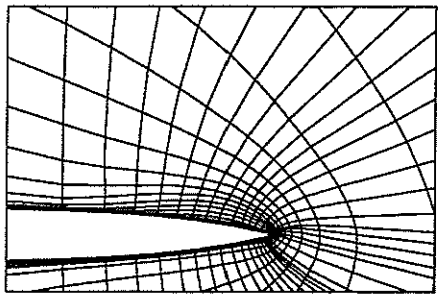

adaptation 1

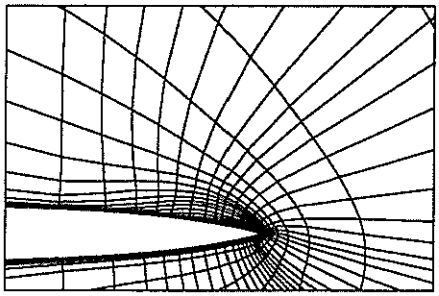

adaptation 3

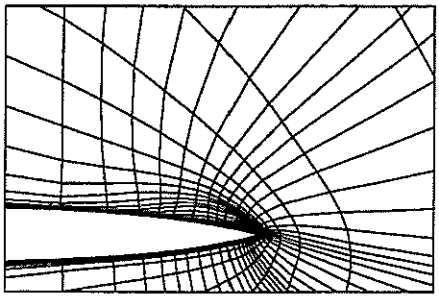

adaptation 5

Fig. 58 Cross-sectional view of adapted coarse grids around the leading edge of the generic delta wing at approximately 60% of the root chord ($M_\infty = 0.85$, $Re_\infty = 48 \times 10^6$, $\alpha = 10°$ turbulent flow).

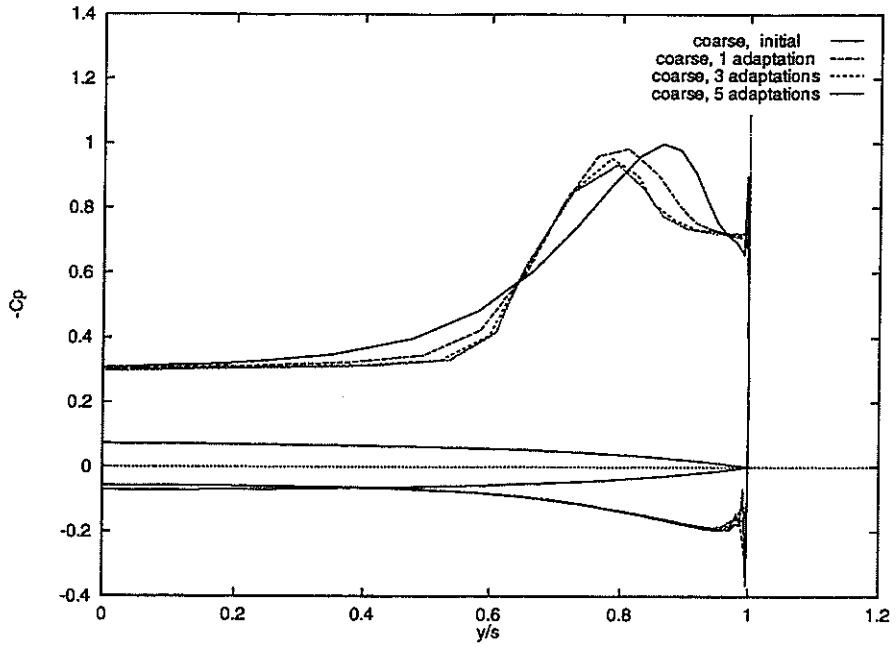

Fig. 59 Pressure distributions obtained for initial and adapted coarse grids at 60% root chord ($M_\infty = 0.85$, $Re_\infty = 48 \times 10^6$, $\alpha = 10°$ turbulent flow).

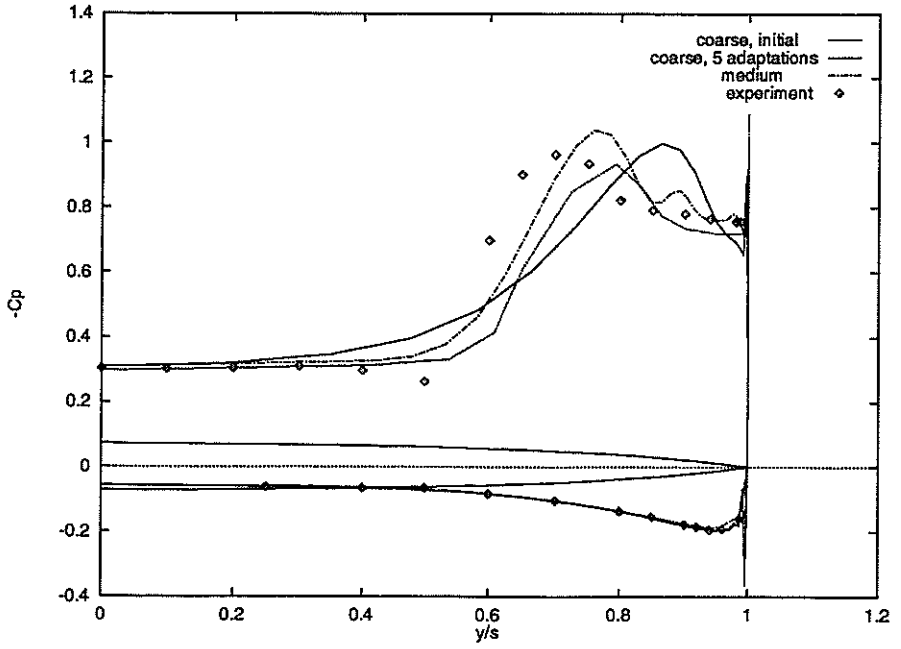

Fig. 60 Pressure distributions obtained for initial and five times adapted coarse grids, on medium grid, and from measurements, at 60% root chord ($M_\infty = 0.85$, $Re_\infty = 48 \times 10^6$, $\alpha = 10°$ turbulent flow).

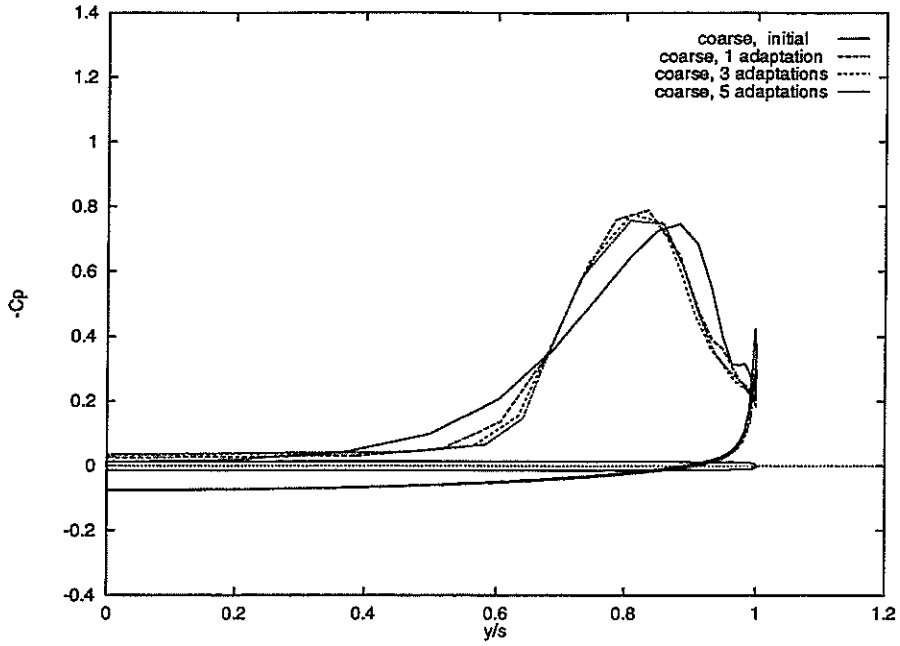

Fig. 61 Pressure distributions obtained for initial and adapted coarse grids at 90% root chord ($M_\infty = 0.85$, $Re_\infty = 48 \times 10^6$, $\alpha = 10°$ turbulent flow).

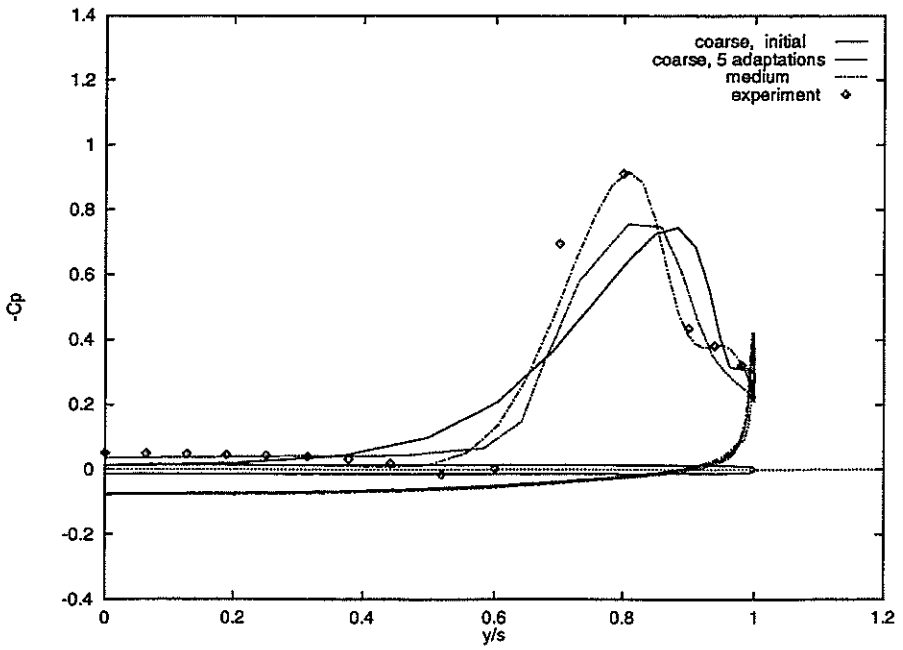

Fig. 62 Pressure distributions obtained for initial and five times adapted coarse grids, on medium grid, and from measurements, at 90% root chord ($M_\infty = 0.85$, $Re_\infty = 48 \times 10^6$, $\alpha = 10°$ turbulent flow).

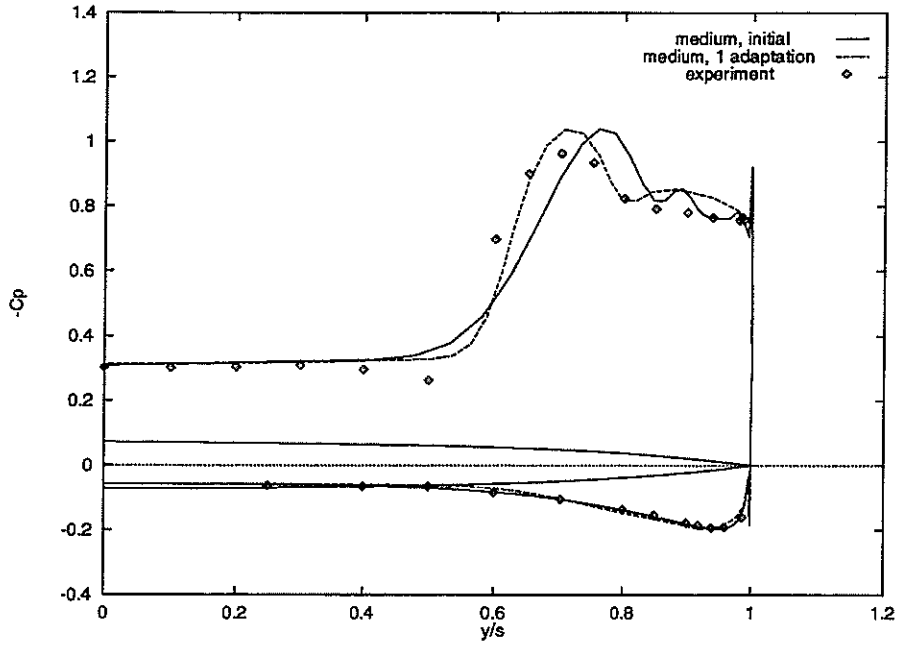

Fig. 63 Pressure distributions obtained for initial and adapted fine grids, and from measurements, at approximately 60% root chord. ($M_\infty = 0.85$, $Re_\infty = 48 \times 10^6$, $\alpha = 10°$ turbulent flow)

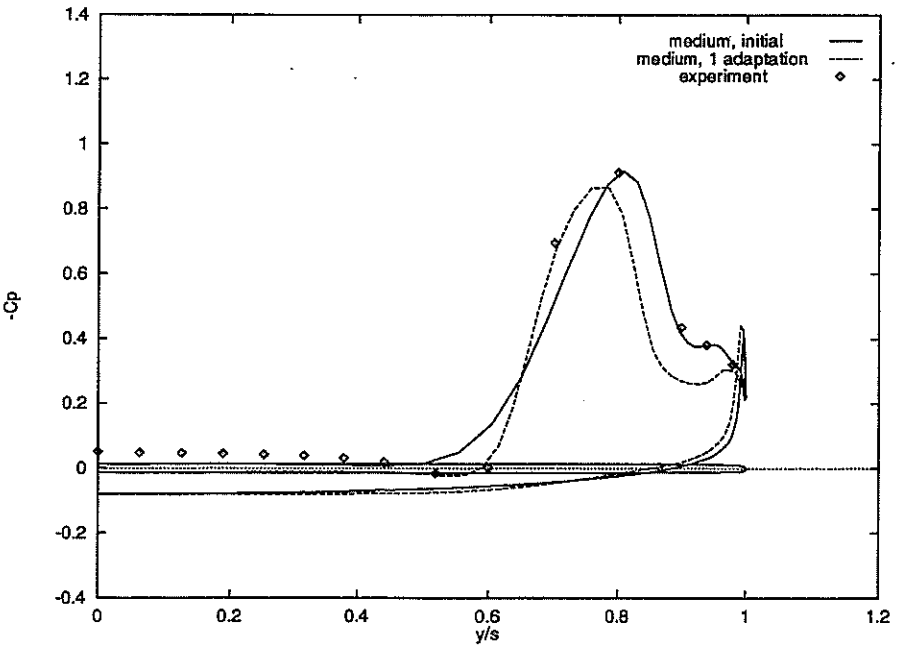

Fig. 64 Pressure distributions obtained for initial and adapted fine grids, and from measurements, at approximately 90% root chord. ($M_\infty = 0.85$, $Re_\infty = 48 \times 10^6$, $\alpha = 10°$ turbulent flow)

6.7.5 Single-nozzle rocket

In the present section grid adaptation is applied to the complex aerodynamic problem of a single-nozzle rocket flying at supersonic speed. The basic question related to this problem is whether the pressure at the base of the rocket can be predicted accurately. The work presented has been carried out at NLR under a contract awarded by the European Space Agency as a contribution to the ESA FESTIP programme [32].

Fig. 65 shows the configuration of the rocket including the single nozzle. The geometry of the configuration is axi-symmetric. It consists of a blunted-cone forebody combined with a cylindrical afterbody and a flat base. The nozzle has a cylindrical outer shape and a conical inner shape. The dimensions of the configuration in Fig. 65 are specified in Table 4. The flight conditions considered are:

- Mach number: $M_\infty = 3$,
- Reynolds number: $Re_\infty = 7.4 \times 10^6$,
- zero incidence,
- plume total-pressure ratio: $p_{t_{plume}}/p_{t_\infty} = 5.44$
- plume total-temperature ratio: $T_{t_{plume}}/T_{t_\infty} = 1$,
- forced transition at 21% length of the rocket measured from the nose of the blunted cone.

The flow simulation is based on the Thin-Layer Navier-Stokes (TLNS) equations including the Baldwin-Lomax turbulence model for the forebody and afterbody flow. Downstream of the base the turbulent eddy viscosity is kept fixed at a value of 100 times the free-stream dynamic viscosity. Two results are discussed: one obtained on a non-adapted medium grid and a second one obtained on a twice adapted medium grid. Both grids consist of approximately 15,000 cells. For comparison reasons an additional computation on a fine grid has been carried out. The medium grid and the fine grid are related in that each cell of the medium grid consists of four cells of the fine grid. So no refinement has been carried out in the azimuthal direction. The geometry is axi-symmetric and it is assumed that for the condition considered the flow is also axi-symmetric. However, the flow solution is obtained with the flow solver for fully 3D flow.

Table 4 Dimensions of single-nozzle rocket

D/L	R_N/L	$\Psi(^\circ)$	d/L	n/L	t/L	r/L	d/D
0.26765	0.0401	22	0.0878	0.0878	0.02676	-	0.328

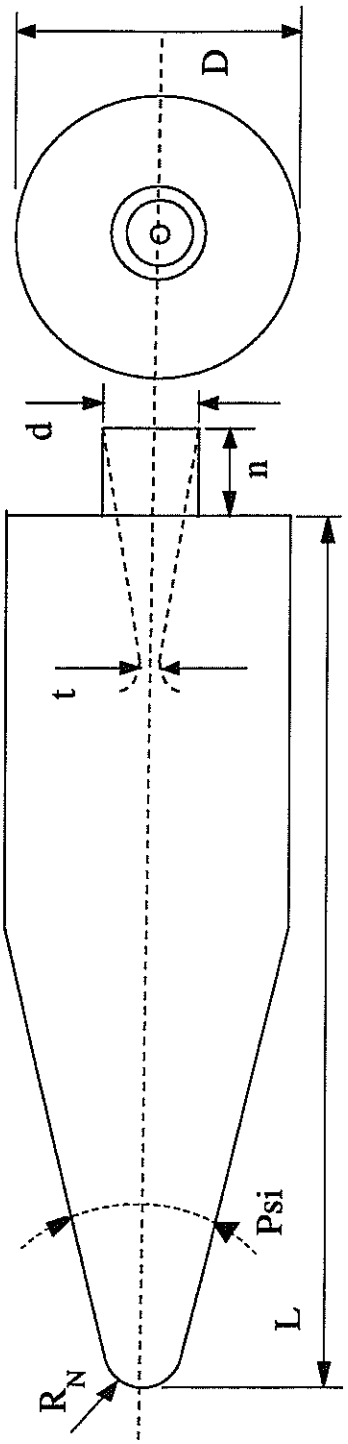

Fig. 65 Single-nozzle rocket configuration consisting of a blunted-cone/cylinder combination (BCCC).

Figs. 66 and 67 show an overview of the initial axi-symmetric grid and the obtained flow solution in terms of the Mach number distribution. The initial grid is basically smooth with additional clustering of points near solid walls and in the base region. Note that the grid is constructed such that it will contain the bow shock of the configuration at this Mach number. The grid consists of 11 blocks comprising a total of 42,000 nodes in each of the two azimuthal planes. The Mach number contours show the bow shock in front of the blunted cone, the expansion fan at the transition between the conical and the cylindrical part, and the complicated base flow comprising of shear layers, expansion fans and an oblique shock.

Figs. 68 and 69 show an overview of the twice adapted grid and the obtained flow solution in terms of the Mach number distribution respectively. The adapted grid shows clustering at the location of the flow features mentioned above. It should be noted that the adaptation is carried out in only one grid coordinate direction, i.e. in radial direction only. This implies that grid adaptation is allowed in the direction normal to the surface of the rocket and normal to the base centerline, but not in the direction normal to the base. Adaptation in two directions is also possible but would require a significant effort in terms of multi-block corrections, as discussed in section 6.6. Moreover, the majority of flow features to be captured are elongated in stream-wise direction such that adaptation in only one coordinate direction will be sufficient. This is illustrated by the Mach number contours in Fig. 69 showing improved resolution of shocks, expansion fans and shear-layers. A close-up of the stagnation area around the nose is given in Figs. 70 and 71. The Mach contours obtained for the initial grid hardly represent a bow shock, showing non-physical behaviour at the stagnation point and very poor resolution of the oblique part of the shock. The twice adapted grid is heavily clustered at the position of the shock while the boundary layer resolution is maintained. The size of the cells upstream of the bow shock is increased by approximately 250%, while the size of cells downstream of the shock is approximately unaltered. This is understandable since the flow upstream of the bow shock is uniform. The Mach contours obtained for the twice adapted grid show a dramatical improvement of the shock resolution and the flow solution at the stagnation point.

Figs. 72 to 75 show the grids and Mach contours in the base region. The initial grid is chosen fairly uniform in order to capture flow features like free shear-layers. The adapted grid is clearly clustered at several flow features such as the expansion fan and the shear-layer originating from the edge of the cylindrical afterbody, the strong oblique recompression shock initiated by the sudden change of the shear-layer direction induced by the plume, the plume boundary, and finally the barrel shock inside the exhaust plume. Comparison of the Mach number contours obtained for the initial and twice-adapted grids learns that all of these flow features are significantly better

resolved on the adapted grid.

Fig. 76 shows a close-up of the grids in the base region where the cylindrical/conical nozzle is clearly visible. The adapted grid indicates the location of the free shear-layer and of the exhaust-plume boundary. Fig. 77 shows some stream lines from the (axi-symmetric) solution for both grids. One stream line forms a closed contour indicating a large recirculation zone near the base. Also note another closed contour indicating a much smaller recirculation zone in the corner of the base and the nozzle. Another stream line indicates the plume boundary showing irregularities on the initial grid which are not present on the adapted grid. Also the angle of the free shear layer that originates from the edge of the cylindrical afterbody changes slightly upon adaptation. This is important since this angle determines the base pressure.

In Fig. 78 the base pressure distribution, normalised by the upstream static pressure, is plotted against the radial coordinate normalised by the base radius. Five distributions are compared:

(1) result obtained for initial medium grid
(2) result obtained for adapted medium grid
(3) result obtained for twice-adapted medium grid
(4) result obtained for non-adapted fine grid
(5) result obtained from measurements [3].

The difference between the results obtained for the initial medium grid and the non-adapted fine grid amounts to approximately 30%. The results obtained for the adapted medium grid and the twice-adapted medium grid are almost equal and closer to the non-adapted fine grid result. The increase of the base pressure upon adaptation is in agreement with the change of the shear-layer angle mentioned before. Compared to the measurements the data obtained on the adapted grids correlate very well.

Finally Fig. 79 shows the convergence history of the flow solution procedure on the medium grids. The first 15,000 iterations have been carried out on the initial medium grid resulting in a limit cycle, possibly suggesting that the flow solution is not steady. The curve starting at 15,000 iterations is the convergence history of the flow solution procedure on the medium grid upon one adaptation, which shows excellent convergence well below the level of the limit cycle. The curve starting at 17,000 iterations is the convergence history of the flow solution procedure on the medium grid upon two adaptations, which shows even better convergence. Hence, grid adaptation may lead in some cases not only to an improved flow solution but also to better convergence of the solution procedure.

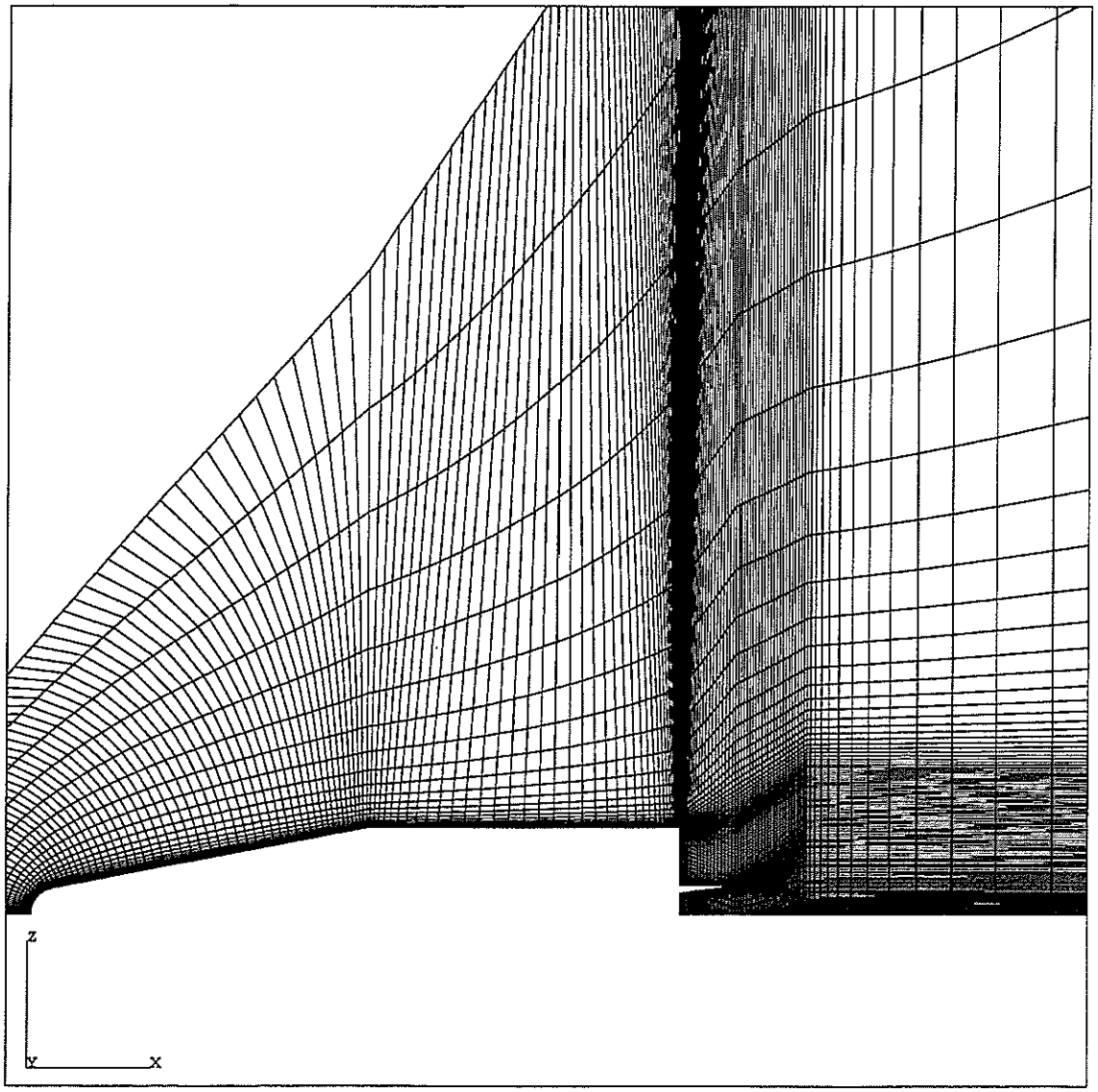

Fig. 66 Overview of initial grid around single-nozzle rocket configuration ($M_\infty = 3.0$, $Re_\infty = 7.4 \times 10^6$).

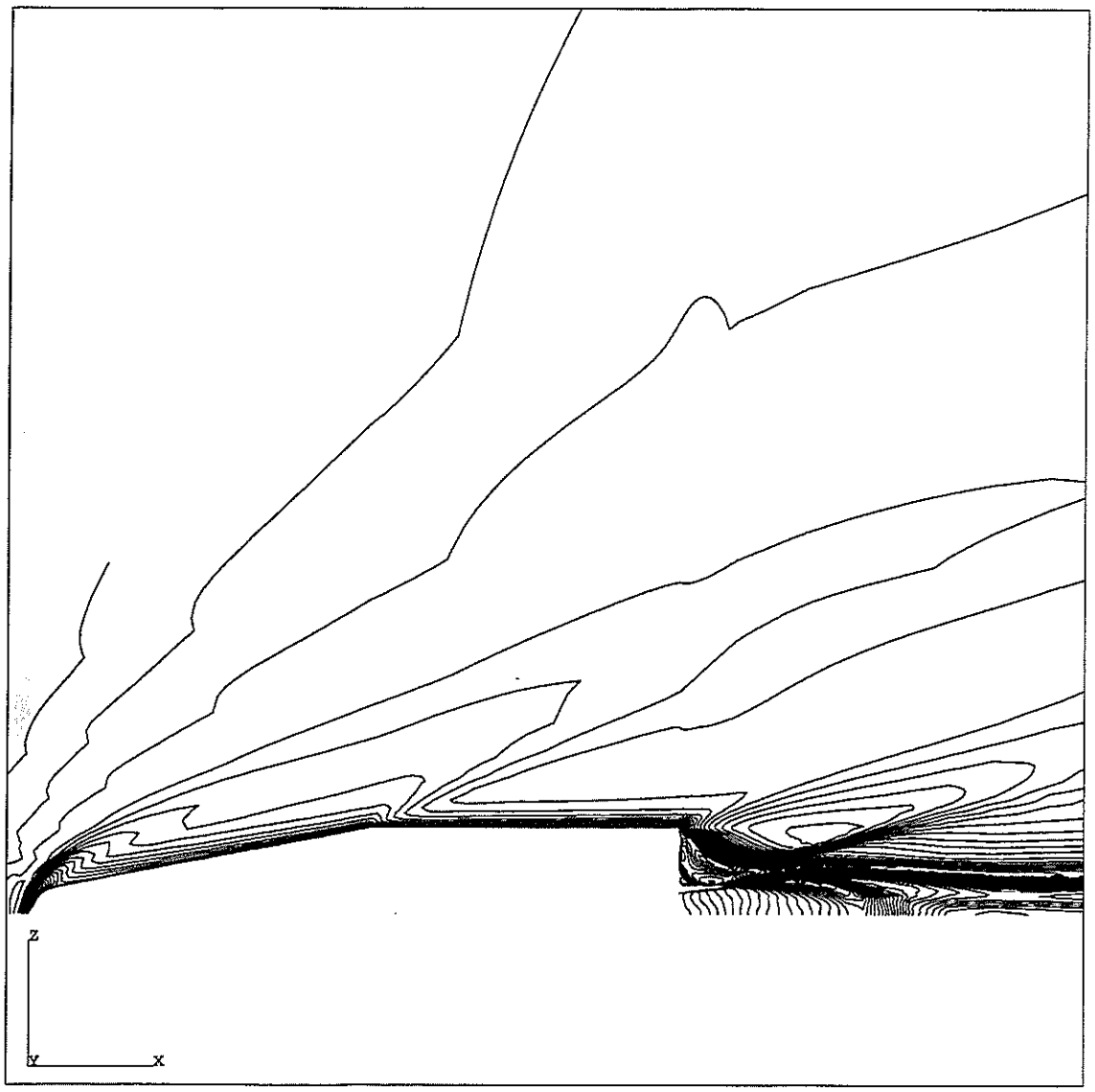

Fig. 67 Overview of Mach number distribution obtained for the initial grid around single-nozzle rocket configuration ($M_\infty = 3.0$, $Re_\infty = 7.4 \times 10^6$, $\Delta M = 0.1$).

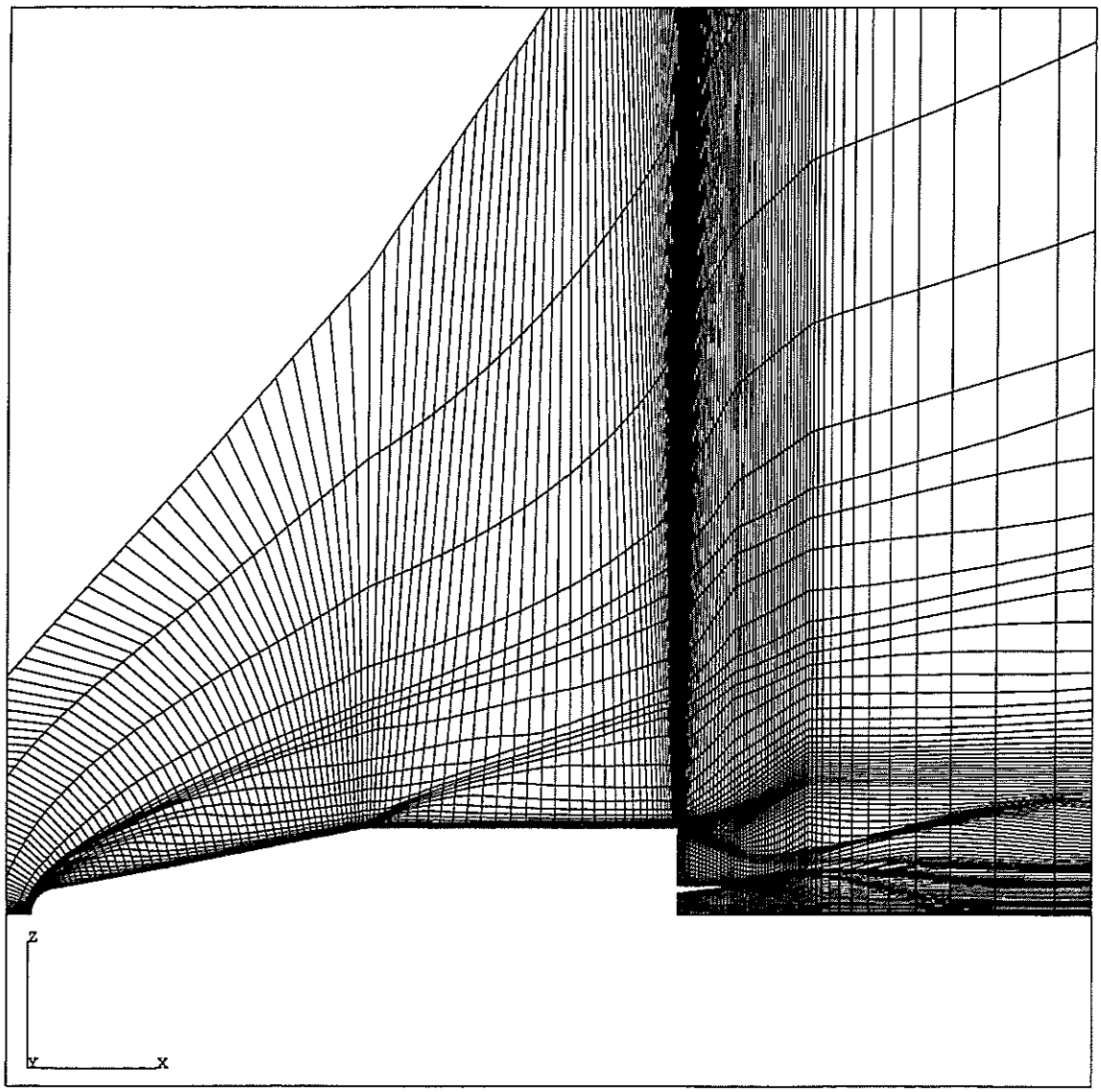

Fig. 68 Overview of twice adapted grid around single-nozzle rocket configuration ($M_\infty = 3.0$, $Re_\infty = 7.4 \times 10^6$).

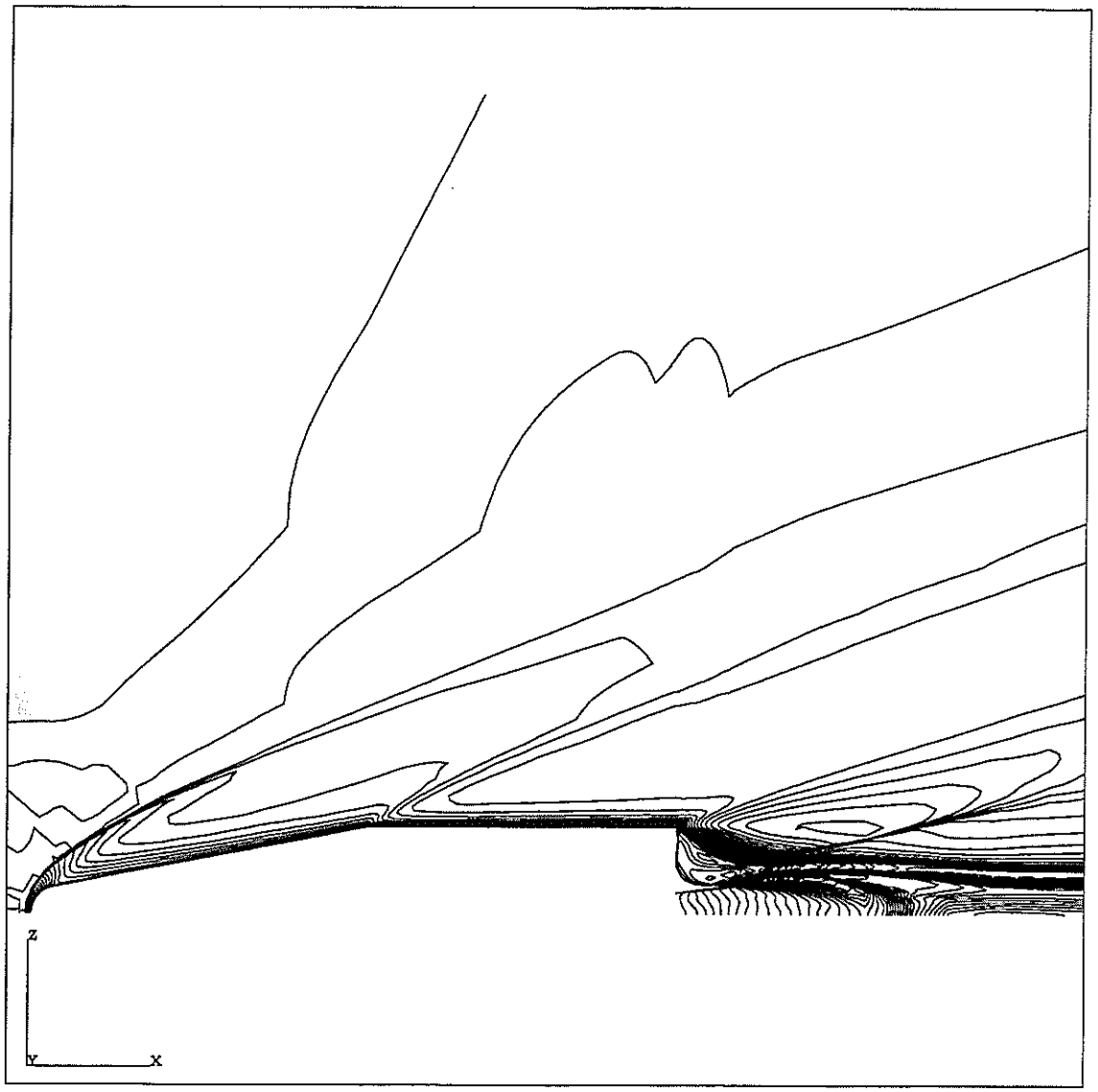

Fig. 69 Overview of Mach number distribution obtained for the twice adapted grid around single-nozzle rocket configuration ($M_\infty = 3.0$, $Re_\infty = 7.4 \times 10^6$, $\Delta M = 0.1$).

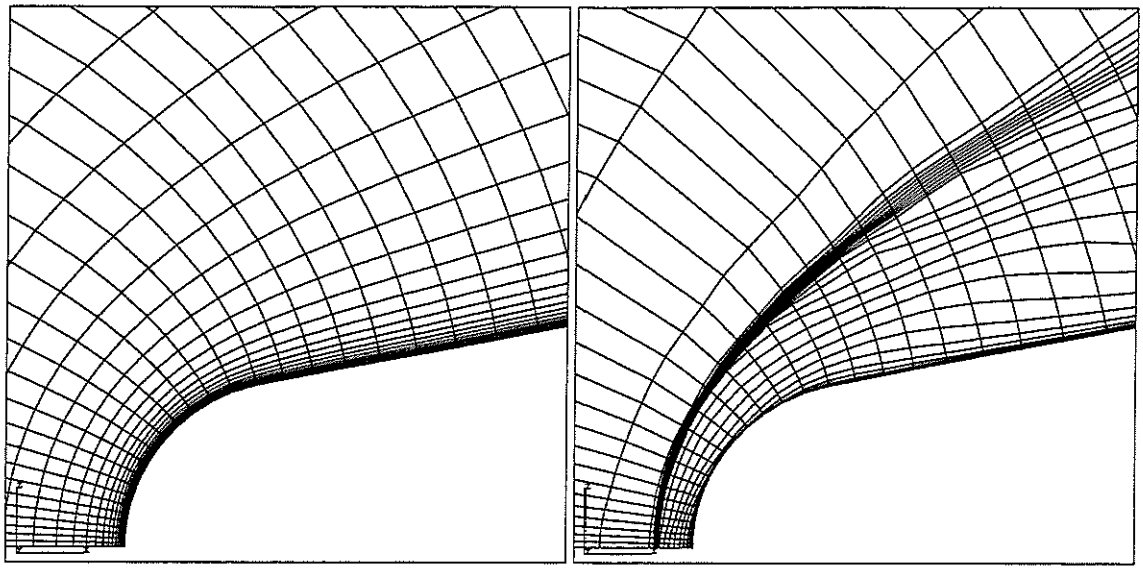

a) initial grid b) twice adapted grid

Fig. 70 Stagnation area of initial and twice adapted grid around single-nozzle rocket configuration ($M_\infty = 3.0$, $Re_\infty = 7.4 \times 10^6$).

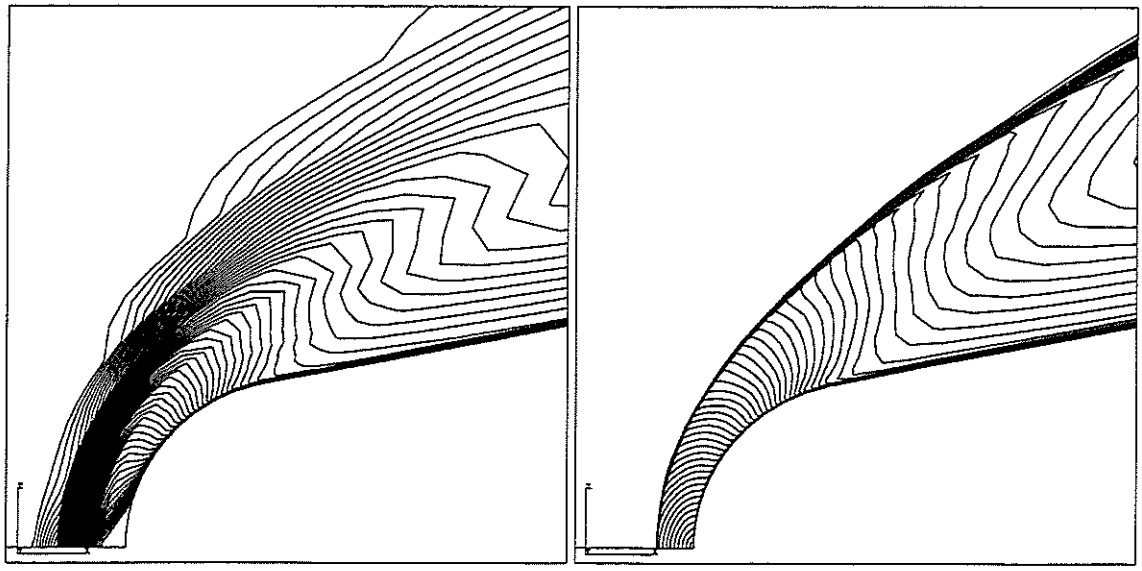

a) on initial grid b) on twice adapted grid

Fig. 71 Mach number distribution in stagnation area obtained for the initial and twice adapted grids around single-nozzle rocket configuration ($M_\infty = 3.0$, $Re_\infty = 7.4 \times 10^6$, $\Delta M = 0.05$).

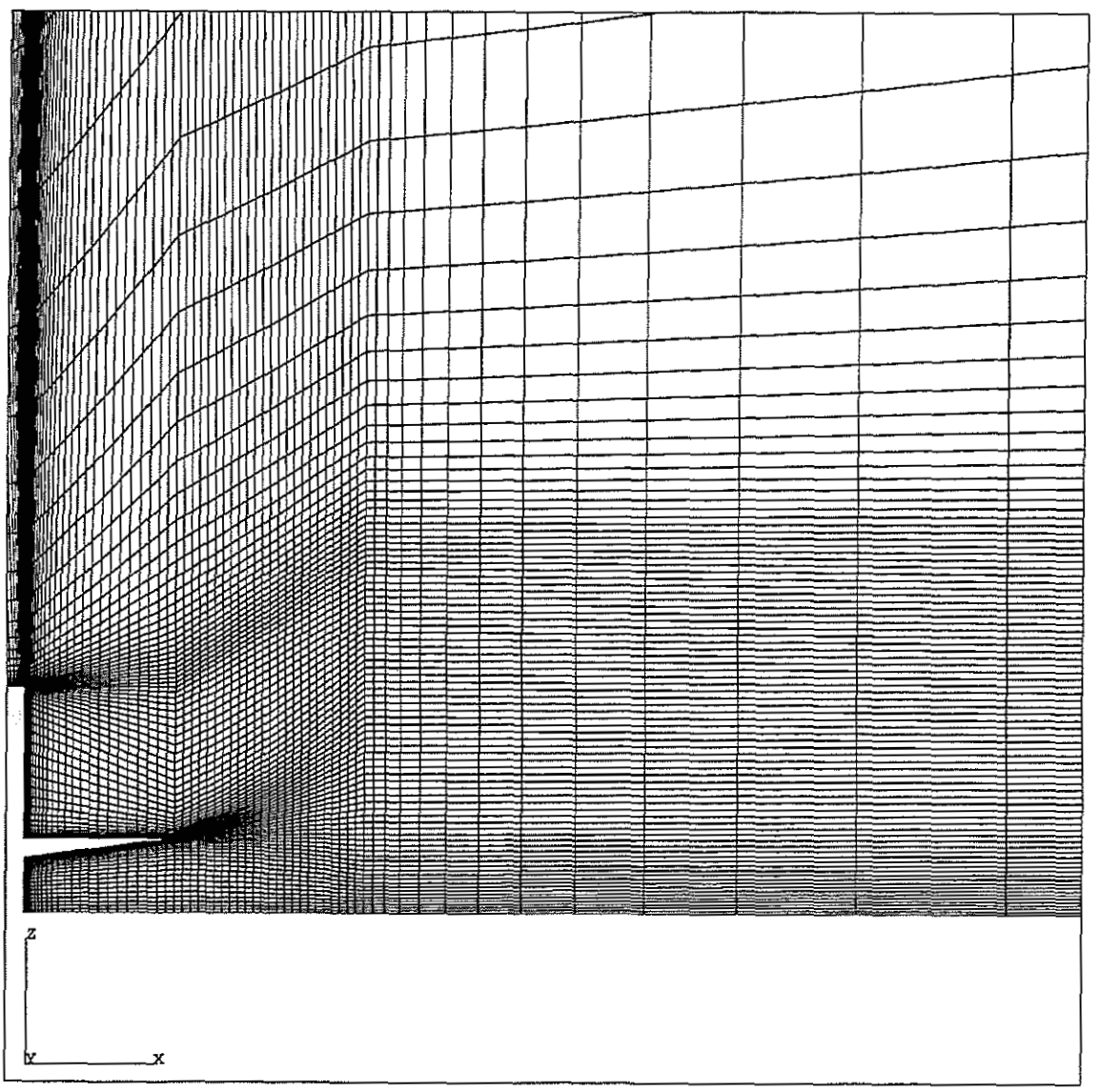

Fig. 72 Base area of initial grid around single-nozzle rocket configuration ($M_\infty = 3.0$, $Re_\infty = 7.4 \times 10^6$).

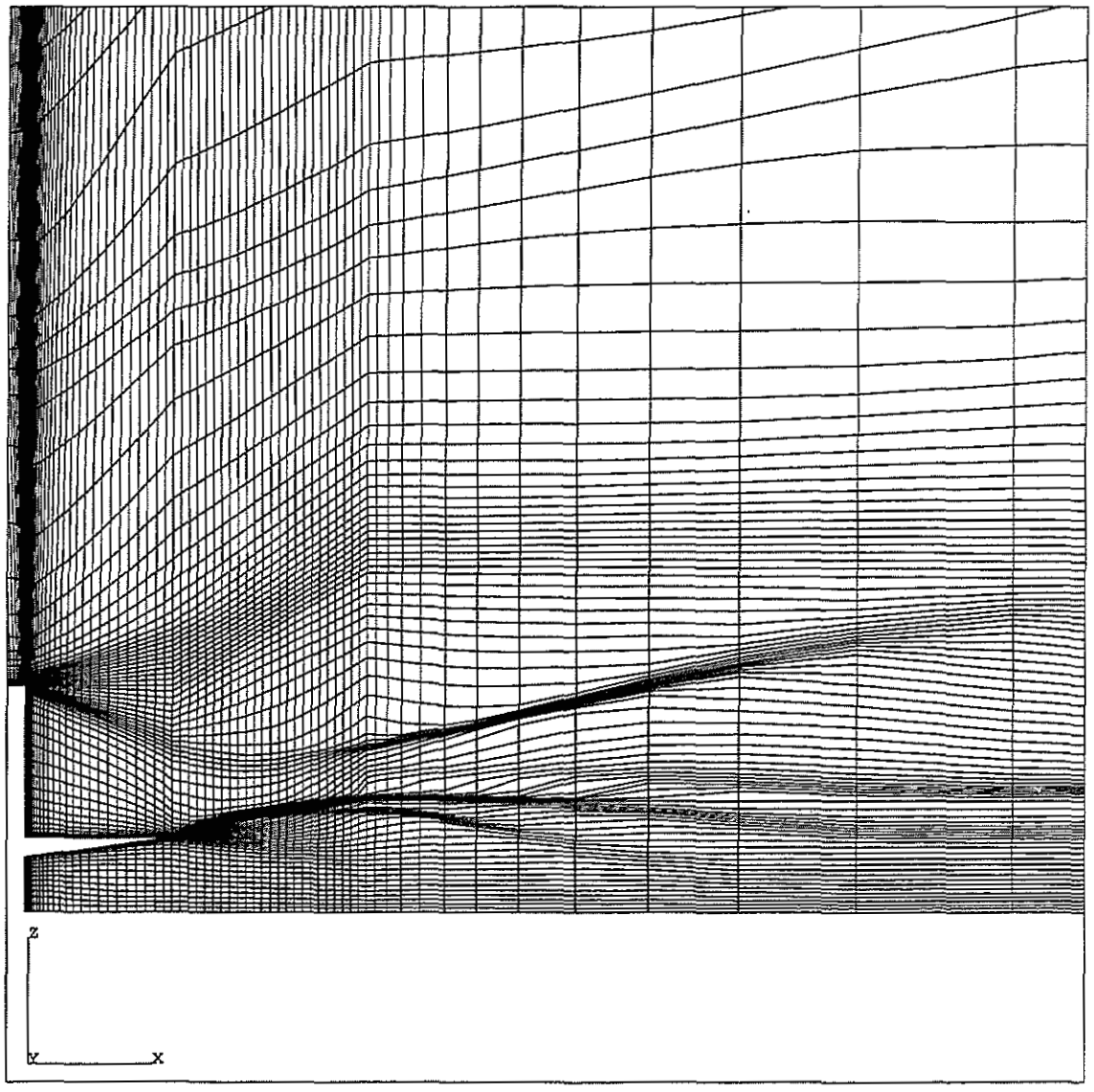

Fig. 73 Base area of twice adapted grid around single-nozzle rocket configuration ($M_\infty = 3.0$, $Re_\infty = 7.4 \times 10^6$).

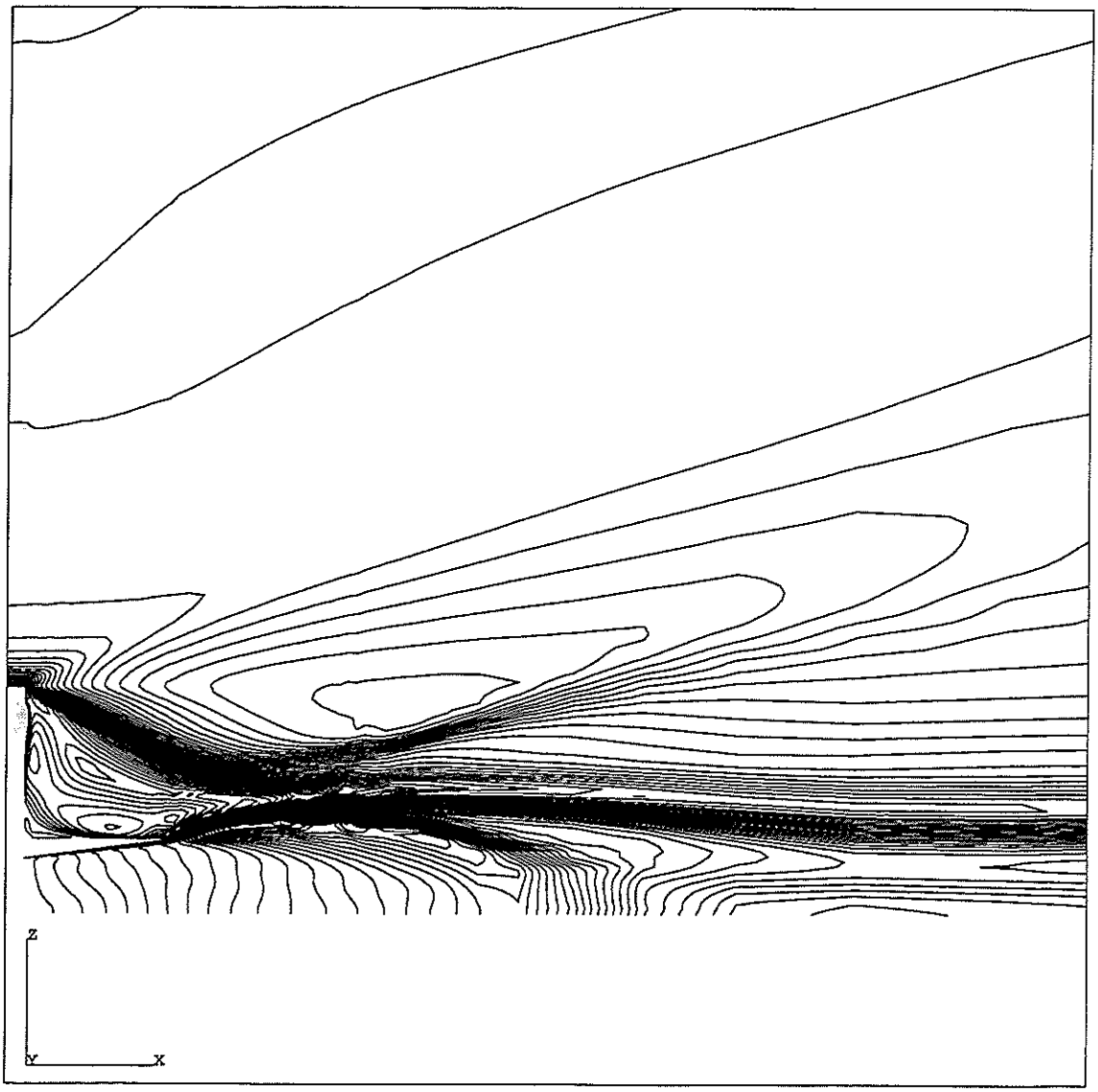

Fig. 74 Mach number distribution in base area obtained for the initial grid around single-nozzle rocket configuration ($M_\infty = 3.0$, $Re_\infty = 7.4 \times 10^6$, $\Delta M = 0.1$).

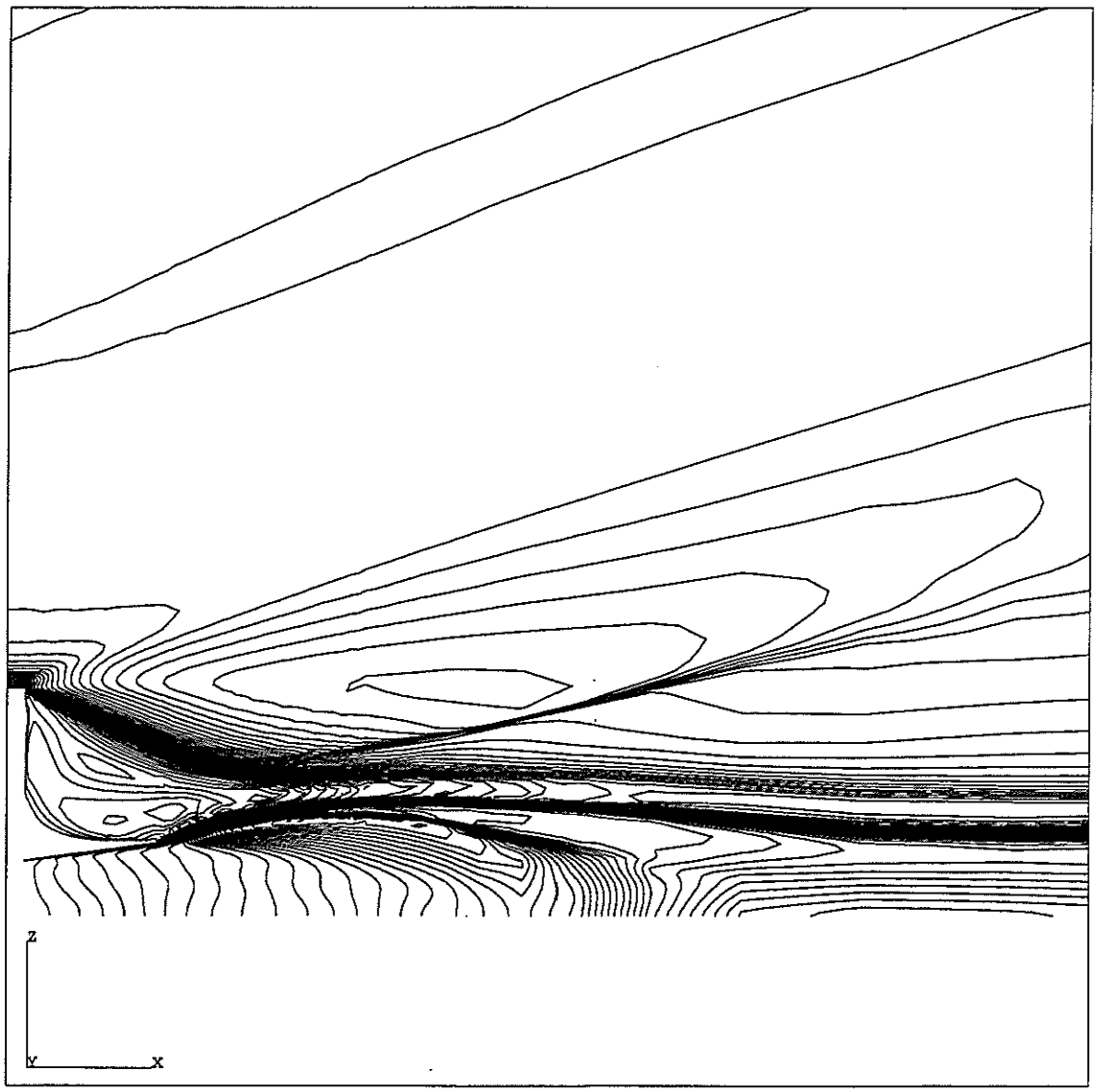

Fig. 75 Mach number distribution in base area obtained for the twice adapted grid around single-nozzle rocket configuration ($M_\infty = 3.0$, $Re_\infty = 7.4 \times 10^6$, $\Delta M = 0.1$).

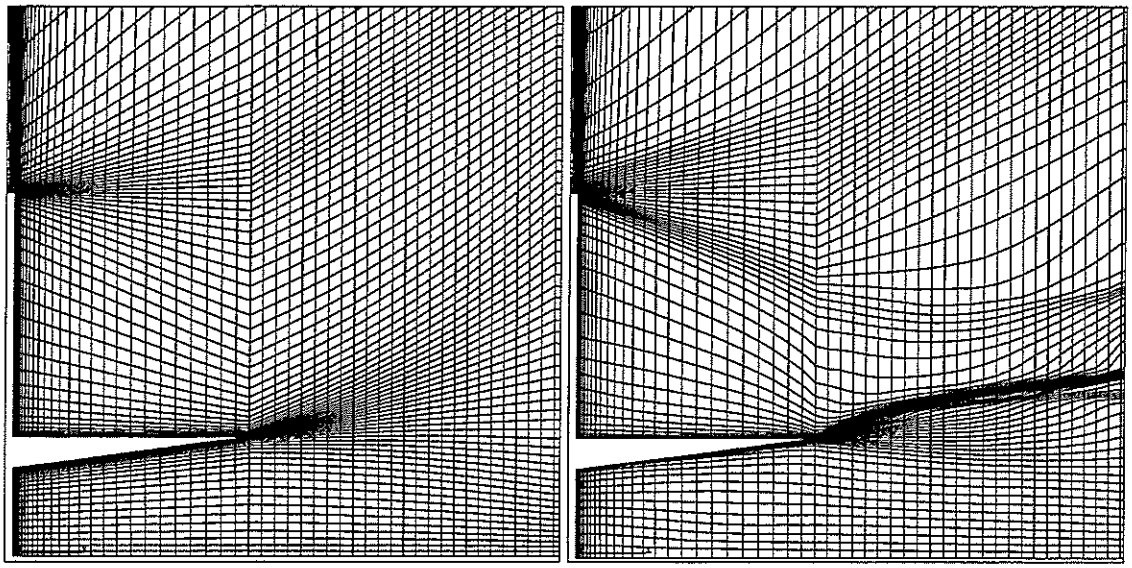

a) initial grid b) twice adapted grid

Fig. 76 Base area close-up of initial and twice adapted grid around single-nozzle rocket configuration ($M_\infty = 3.0$, $Re_\infty = 7.4 \times 10^6$).

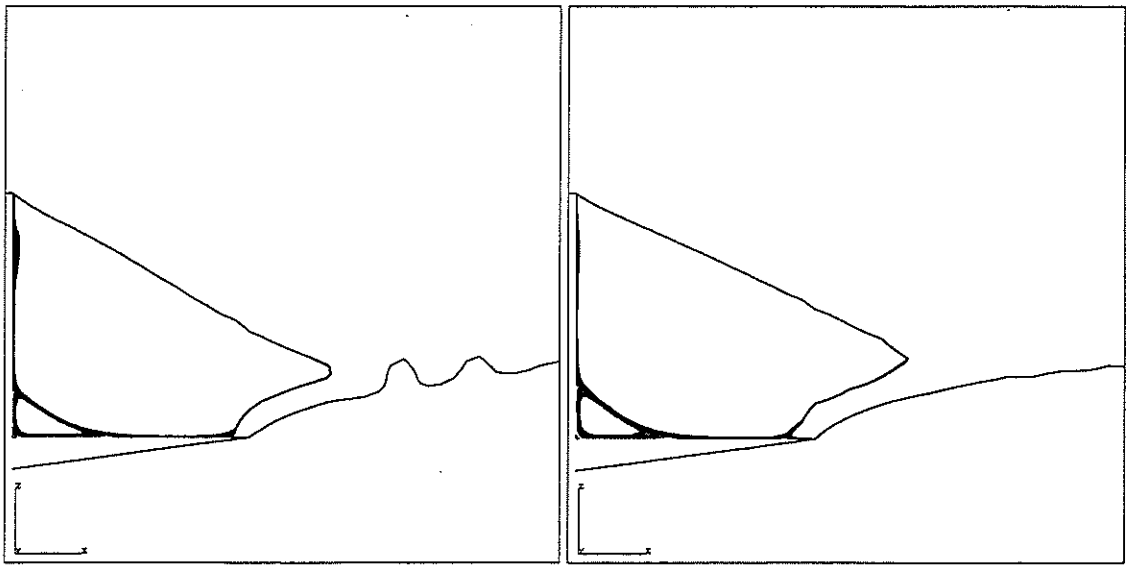

a) initial grid b) twice adapted grid

Fig. 77 Stream lines in base area obtained for the initial and twice adapted grids around single-nozzle rocket configuration ($M_\infty = 3.0$, $Re_\infty = 7.4 \times 10^6$).

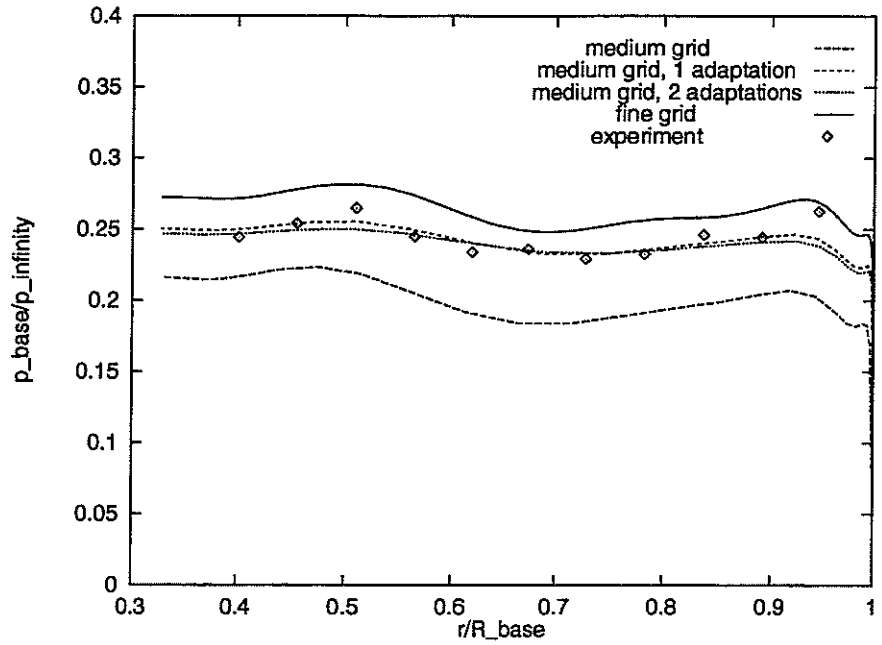

Fig. 78 Base pressure distribution obtained on medium grids (0, 1 and 2 adaptations), on fine grid, and from measurements (TU-Delft) ($M_\infty = 3.0$, $Re_\infty = 7.4 \times 10^6$)

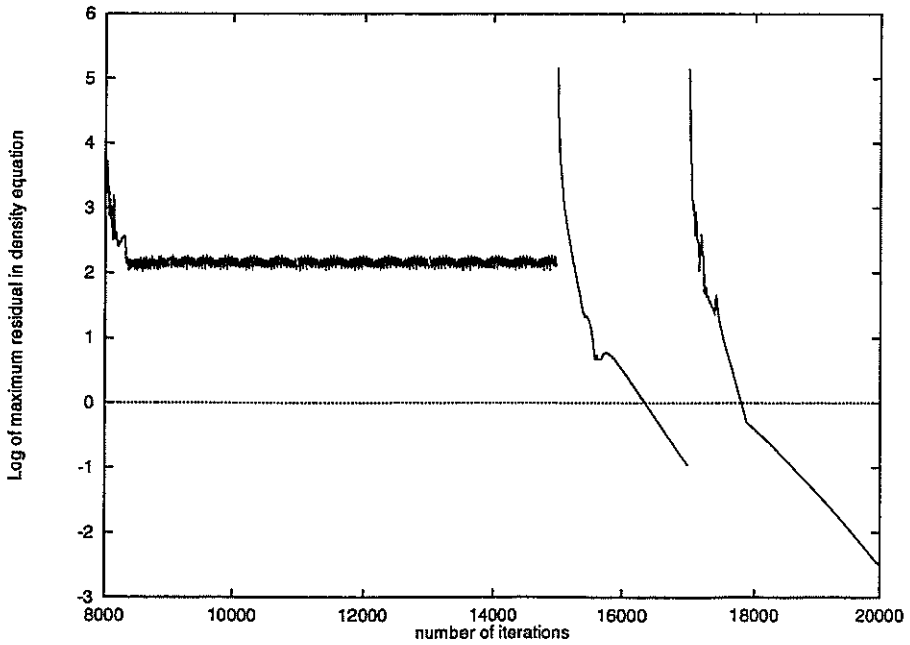

Fig. 79 Convergence history on initial grid, once adapted and twice adapted grid.

6.8 Conclusions

The 2D-grid adaptation algorithm developed in chapter 5 has been extended towards a 3D-grid adaptation algorithm. The concept of using modification functions to obtain desirable properties of the adapted grid in boundary-layers has been transferred from 2D to 3D. Both the qualitative arguments of section 6.2 and the numerical examples presented in section 6.7 show that the modification functions used (Eq. 203) are effective in 3D problems. This is illustrated by the following properties of the adapted grids in boundary-layers:

- preservation of orthogonality,
- one-dimensional equidistribution of a weight function in normal direction to the surface, and
- adaptation in flow direction is controlled by the flow just outside the boundary-layer.

Hence, it appears that the algorithm for adaptation of 3D-grids has the same desirable properties in boundary-layers as in the 2D case, see section 5.7.2.

A significant effort was required to maintain compatibility (C^0-continuity) across re-entrant boundaries of single-block grids and in general between blocks of an adapted multi-block grid. A general solution for this problem has not been presented but a practical solution has been proposed, implemented and applied. A multi-block grid is first adapted on a block-by-block basis introducing discontinuities between grids in neighbouring blocks. Next a correction algorithm is applied which:

(i) constructs "averaged" grids in block faces belonging to pairs of blocks, and
(ii) subsequently adjusts the block-interior grids to the corrected grids in the common faces.

A key item in this correction algorithm is the averaging of two different grids in a single common face. The two grids are defined by four computational coordinates (two for each grid), which are considered as monitor functions used in the adaptation of the original, initial non-adapted, grid in the specific block face. For this the 2D adaptation algorithm is employed. Since the theorem of Clement, Hagmeijer and Sweers presented in section 4.6 is applicable, this leads to an "averaged" grid that is guaranteed to be regular and non-overlapping.

The 3D grid adaptation algorithm has been demonstrated by application to a variety of aerodynamic problems, ranging from transonic flow around a transport wing and a wing/body configuration to the transonic flow around a fighter-type delta wing and supersonic flow around a rocket-propelled

launcher vehicle. In general it is clear that on adapted grids shocks, leading-edge expansion regions and boundary-layers are better resolved leading to improvements in the local pressure and skin-friction distribution. It is also clear, however, that improvements at one location may be accompanied by detrimental effects somewhere else.

7 Summary, conclusions and recommendations

The present study shows how a robust grid adaptation algorithm suitable for multi-dimensional aerodynamic problems can be developed starting from the *one-dimensional equidistribution principle*:

$$(weight\ \ function) \times (meshsize) = constant.$$

It is shown that the equidistribution principle can be formulated in various ways which are mathematically interrelated (section 1.1). These formulations, ranging from variational statements that prescribe a functional to be minimised to evolutionary statements that directly prescribe node movements, have been used in the literature.

One of the variational statements pertains to minimising (41):

$$K[\xi(x)] = \frac{1}{2}\int_0^L \frac{{\xi_x}^2}{w(x)}dx.$$

In this formulation the computational coordinate ξ is obtained as a function of the physical coordinate x controlled by the weight function $w(x)$. This formulation is used for extension from one dimension to multiple dimensions minimising a Weighted Least Squares functional (47):

$$K[\phi] = \frac{1}{2}\int_\Omega \frac{1}{w_j(\mathbf{x})}\left(\mathbf{h}_j(\mathbf{x})\cdot\nabla\phi\right)^2 d\Omega,$$

with $\phi = \xi$, $\phi = \eta$ and $\phi = \zeta$, for each of the three coordinates, respectively. The corresponding Euler-Lagrange equations are linear partial differential equations for the computational coordinates $\boldsymbol{\xi}$ as functions of the physical coordinates $\mathbf{x}$ controlled by three separate weight functions $w_j(\mathbf{x})$, $j = 1,2,3$, see Eq.s (50) and (55).

Four sets of partial differential equations that are frequently cited in the literature can be cast in the Weighted Least Squares format presented (section 3.3). Each of these methods satisfies a subset of the four requirements that have been identified as being essential for the map $\boldsymbol{\xi}(\boldsymbol{x})$ (Table 1, section 3.4), none of these methods satisfies all four requirements simultaneously. This is the motivation for the development of the so-called Compound Weighted Least Squares functional.

Introduction of a parametric domain associated with the given initial grid and application of the Weighted Least Squares functional in this domain is equivalent to application of the Compound Weighted Least Squares functional in the physical domain (see Fig. 8). It is demonstrated that this functional satisfies all four requirements simultaneously (see Table 2). To interpret the functional an equivalent functional (141) is derived that resembles the multi-dimensional extension of the one-dimensional equidistribution principle. It is also shown that application of the compound functional is equivalent to one-dimensional equidistribution in an grid-plane averaged way (Eqs. (143) to (145)). Finally it is highly significant that there exists an invertibility theorem, recently developed by Clement, Hagmeijer and Sweers, that guarantees that the generated map between the computational domain and the physical domain is invertible (section 4.6). For the adapted grid this means that it is non-overlapping assuming that discretisation errors are sufficiently small. The significance of this theorem follows from the observation that the avoidance of grid overlap is one of the major concerns in CFD applications.

Application of the developed grid-adaptation algorithm to two-dimensional aerodynamic problems requires a modification of the partial differential equations (see section 5.2) in order to obtain desirable properties in boundary-layers:

- preservation of orthogonality,
- one-dimensional equidistribution of a weight function in the direction normal to the surface of the airfoil, and
- adaptation in the direction of the flow controlled by the outer flow.

It is shown by application of the modified algorithm to a series of 2D flow problems (section 5.7) that it is robust and that grid adaptation leads to:

- an improved flow solution when compared to the flow solution obtained on a grid that contains four times as many nodes,
- a smooth flow solution in the computational domain,
- an approximately linear velocity profile in those parts of the computational domain that correspond to boundary-layers in the physical domain.

These observations indicate that the quality of the flow solution is improved upon grid adaptation.

Similar modifications to obtain desirable properties in 2D boundary-layers can be applied to the equations for grid adaptation in 3D (section 6.1). It is demonstrated that grids in the vicinity of

intersecting walls are adapted in such a way that orthogonality is conserved in the boundary-layer on each wall.

Four different methods for multiple adaptations have been described briefly (section 6.5) and two of these methods have been applied to 3D aerodynamic problems. Also discussed is the way in which multi-block grids can be adapted with the developed grid adaptation algorithm which is basically an algorithm for single-block grids. It appears that block-by-block adaptation leads to grid-discontinuity in block-interfaces. This is solved by developing an averaging map for the two different grids at each side of the interface and subsequently correcting the grid in the block-interior to the corrected grid in the block-faces. The correction algorithm for the block-interior grid, however, has not yet been developed fully to a general algorithm. The adaptation of a single-block topology grid around wings is explained in detail (section 6.6.3) including the correction mappings.

The 3D adaptation algorithm has been applied to a variety of aerodynamic problems. For each of these problems grid-overlap has not occurred, which again demonstrates the robustness of the developed algorithm. The improvement of the flow-solution quality has been assessed by comparison to results obtained on denser grids as well as by comparison to experimental data. In most cases improvement is evident but for the delta-wing case further investigation is desirable. The adaptation of the multi-block axi-symmetric grid around a single-nozzle rocket configuration has been successful in that it enables a fully converged flow solution. It also results in better agreement with the flow solution obtained on a fine grid and with experimental data.

In conclusion it is noted that each of the four objectives formulated in section 1.5 has been met in this study. The complete path has been traveled, starting from a review of first principles, extending these principles towards 2D and 3D formulations, and accomplishing the development of a robust grid-adaptation algorithm demonstrated by application to realistic aerodynamic problems. The relevance of the these results to the aerodynamic analysis and design practice is still limited to generic configurations like wings, wing/body combinations and rockets. The main obstacle for application of the obtained grid adaptation algorithm to more complex geometries is the lack of

a robust and reliable algorithm for the matching of block-by-block adapted grids. On the other hand, the multi-block adaptation problem might be solved by introducing flow solvers that do not require grid-continuity at block-interfaces which enables pure block-by-block adaptation.

1. M.T. Arthur, W. Kordulla, F.J. Brandsma, and N. Ceresola. Grid Adaptation in Vortical Flow Simulations. In *AIAA 97-2308*, Atlanta, GA, June 23-25 1997.
2. T.J. Baker. Mesh Adaptation Strategies for Problems in Fluid Dynamics. *Finite Elements in Analysis and Design*, 25:243–273, 1997.
3. W.J. Bannink, P.G. Bakker, and E.M. Houtman. Experimental Investigation of Base Flow and Exhaust Plume Interaction. Technical Report (in progress), Delft Universtity of Technology, 1996.
4. R. Barrett, M. Berry, T. Chan, J. Demmel, J. Donato, J. Dongarra, V. Eijkhout, R. Pozo, C. Romine, and H. van der Vorst. *Templates for the Solution of Linear Systems: Building Blocks for Iterative Methods*. SIAM Publications, 1993.
5. R.A. Benson and D.S. McRae. A Solution-Adaptive Mesh Algorithm for Dynamic/Static Refinement of Two and Three Dimensional Grids. In *3rd International Conference on Numerical Grid Generation in Computational Fluid Dynamics and Related Fields*, Barcelona, Spain, 1991. North Holland, New York.
6. M.J. Bockelie and R.E. Smith. An Adaptive Grid Method for Computing the High Speed 3D Viscous Flow about a Re-entry Vehicle. In *AIAA-92-2685*, 1992.
7. J.W. Boerstoel. ENFLOW a System of CFD Codes for Industrial CFD Analysis of Flows around Aircraft Including Propulsion Systems Modelling. Technical Report NLR CR 93519 L, National Aerospace Laboratory, 1993.
8. J.U. Brackbill. An Adaptive Grid with Directional Control. *Journal of Computational Physics*, 108:38–50, 1993.
9. J.U. Brackbill and J.S. Saltzman. Adaptive Zoning for Singular Problems in Two Dimensions. *Journal of Computational Physics*, 46:342–368, 1982.
10. F.J. Brandsma. in: EUROVAL- A European Initiative on Validation of CFD Codes, ed. W. Haase et. al. *Notes on numerical fluid mechanics*, 42, 1993.
11. A. Brandt. Multi-Level Adaptive Solutions to Boundary-Value Problems. *Mathematics of computation*, 31(138):333–390, 1977.
12. D. Catherall. An Assessment of the Advantage of Adaptivity on Structured Grids. In *4th International Conference on Numerical Grid Generation in Computational Fluid Dynamics and Related Fields*, Swansea, UK, 6-8th April 1994.
13. D. Catherall. Adaptivity via Mesh Movement with Three-Dimensional Block-Structured Grids. In *5th International Conference on Numerical Grid Generation in Computational Fluid Dynamics and Related Fields*, Starkville, Mississippi, 1-5th April 1996.
14. Ph. Clement, R. Hagmeijer, and G. Sweers. On the Invertibility of Mappings Arising in 2D Grid Generation Problems. *Numerische Mathematik*, 73-01:37–52, 1996.

15. W.C. Connett, R.K. Agarwal, A.L. Schwartz, and J.A. Wheeler. An Adaptive-Grid Technique for the Solution of Navier-Stokes Equations. In *AIAA-90-1605*, Seattle, Washington, June 18-20 1990.
16. P.H. Cook, M.A. MacDonald, and M.C.P.Firmin. Aerofoil 2822 - Pressure Distributions, Boundary Layer and Wake Measurements. *AGARD AR 138*, 1979.
17. R. Courant and D. Hilbert. *Methods of Mathematical Physics*, volume I. Wiley, New York, 1989.
18. G. Coussement. Euler-Lagrange Formulation of a Mesh Optimisation and Adaptation Method and Unification with some Other Popular Methods. In *5th International Conference on Numerical Grid Generation in Computational Fluid Dynamics and Related Fields*, Starkville, Mississippi, April 1-5 1996.
19. A.S. Dvinsky. Adaptive Grid Generation from Harmonic Maps on Riemannian Manifolds. *Journal of Computational Physics*, 95:450–476, 1991.
20. P.R. Eiseman. Adaptive Grid Generation by Mean Value Relaxation. *Journal of fluids engineering*, 107:477–483, 1985.
21. P.R. Eiseman. Adaptive Grid Generation. *Computer Methods in Applied Mechanics and Engineering*, 64:321–376, 1987.
22. P.R. Eiseman. Grid Generation for the Solution of Partial Differential Equations. Technical Report 87-57, ICASE, 1987.
23. P.R. Eiseman. The Fundamentals of Adaptive Grid Movement. In *Numerical Grid Generation, VKI Lecture Series 1990-06*, Rhode Saint Genese, Belgium, June 11-15 1990.
24. P.R. Eiseman and M.J. Bockelie. Adaptive Grid Solution for Shock Vortex Interaction. In *Eleventh International Conference on Numerical Methods in Fluid Dynamics*, Williamsburg, Va., June 27-July 1 1988.
25. D. Gilbarg and N.S. Trudinger. *Elliptic Partial Differential Equations of Second Order*, volume 2^{nd} edition. Springer Verlag, Berlin, Heidelberg, New York, Tokyo, 1983.
26. W. Haase et. al.(eds). in: EUROVAL- a European Initiative on Validation of CFD Codes. *Notes on numerical fluid mechanics*, 42, 1993.
27. R. Hagmeijer. Anisotropic Grid Adaption Based on Diffusion Equations. In *4th International Conference on Numerical Grid Generation in Computational Fluid Dynamics and Related Fields*, Swansea, UK, 6-8th April 1994.
28. R. Hagmeijer. Grid Adaption Based on Modified Anisotropic Diffusion Equations Formulated in the Parametric Domain. *Journal of Computational Physics*, 115:169–183, 1994.
29. R. Hagmeijer and J.C. Kok. Adaptive 3D Single-Block Structured Grids for the Computation of Viscous Flows around Wings. In *5th International Conference on Numerical Grid Generation in Computational Fluid Dynamics and Related Fields*, Starkville, Mississippi, April 1-5 1996.

30. R. Hagmeijer and J.C. Kok. Adaptive Generation of Structured Grids, Part 1: Introduction and State-of-the-art. *VKI Lecture Series: 27th Computational Fluid Dynamics*, March 25-29, 1996.
31. R. Hagmeijer and J.C. Kok. Adaptive Generation of Structured Grids, Part 2: Weighted Least Squares Formulation. *VKI Lecture Series: 27th Computational Fluid Dynamics*, March 25-29, 1996.
32. R. Hagmeijer, B. Oskam, B. Arlinger, and P. Bakker. Definition of Numerical and Experimental Activities for Critical Point Assessment: Base Flow Predictions. Technical Report CR 96285, National Aerospace Laboratory NLR, 1996.
33. D.J. Hall and D.W. Zing. Viscous Airfoil Computations using Adaptive Structured Grids. In *AIAA-94-2334*, Colorado Springs, Colorado, June 20-23 1994.
34. T.L. Henderson, W. Huang, K.D. Lee, and Y.K. Choo. Three-Dimensional Navier-Stokes Calculations using Solution-Adapted Grids. In *AIAA-93-0431*, Reno, Nevada, January 11-14 1993.
35. J.D. Hoffman. Relationship Between the Truncation Errors of Centered Finite-Difference Approximations on Uniform and Nonuniform Meshes. *Journal of Computational Physics*, 46:469–474, 1982.
36. A.D. Harvey III, S. Acharya, and S.L. Lawrence. A Solution-Adaptive Grid Procedure for the Three-Dimensional Parabolized Navier-Stokes Equations. In *AIAA-91-0104*, Reno, Nevada, January 7-10 1994.
37. O.P. Jaquotte, G. Coussement, F. Desbois, and Ch. Gaillet. Contribution to the Development of a Multiblock Grid Optimisation and Adaptation Code. In N.P. Weatherill, M.J. Marchant, and D.A. King, editors, *Notes on Numerical Fluid Mechanics, vol 44*. Vieweg, 1993.
38. J.C.Kok, M. Amato, S. Bosse, and A. Kassies. Numerical Design of ENSOLV; a Code for the Numerical Simulation of 3D Flows using the Thin-Layer Navier-Stokes and Euler Equations. Technical Report NLR CR 93152 L, National Aerospace Laboratory, 1993.
39. L. Kania. Three-Dimensional Adaptive Grid Generation with Applications in Nonlinear Fluid Dynamics. In *AIAA-92-0661*, Reno, Nevada, January 6-9 1992.
40. H.J. Kim and J.F. Thompson. Three Dimensional Adaptive Grid Generation on a Composite Block Grid. In *AIAA-88-0311*, Reno, Nevada, January 11-14 1988.
41. G.H. Klopfer. Solution Adaptive Meshes with a Hyperbolic Grid Generator. In *Numerical grid generation in computational fluid dynamics '88; proceedings of the second international conference*, Miami Beach, Florida, December 1988.
42. P. Knupp and S. Steinberg. *Fundamentals of Grid Generation*. CRC press, 1993.
43. D. Lee and Y.M. Tsuei. A Formula For Estimation of Truncation Errors of Convection Terms in a Curvilinear Coordinate System. *Journal of Computational Physics*, 98:90–100, 1992.

44. K.D. Lee and J.M. Loellbach. A Mapping Technique for Solution of Adaptive Grid Control. In *AIAA-89-2178*, Seattle, WA, July 1989.
45. B.P. Leonard. Comparison of Truncation Error of Finite-Difference and Finite-Volume Formulations of Convection Terms. Technical Report NASA TM 105861, Institute for Computational Mechanics in Propulsion, Lewis Research Center, 1992.
46. P.V. Luong, J.F. Thompson, and B. Gatlin. Adaptive EAGLE: Solution-Adaptive and Quality-Enhancing Multi-Block Grids for Arbitrary Domains. In *AIAA-91-1593-CP*, 1991.
47. P.V. Luong, J.F. Thompson, and B. Gatlin. Solution-Adaptive and Quality-Enhancing Grid Generation. *Journal of Aircraft*, 30(2):227–234, 1993.
48. C.W. Mastin. Error Induced by Coordinate Systems. In *Numerical grid generation*, Elsevier Science Publishing Company, 1982.
49. K. Nakahashi and G.S. Deiwert. A Practical Adaptive-Grid Method for Complex Fluid-Flow Problems. *AIAA Journal*, 24:948–954, June 1986.
50. S.P. Pao and K.S. Abdol-Hamid. Grid Adaptation to Multiple Functions for Applied Aerodynamics Analysis. In A.S. Arcilla, J. Hauser, P.R. Eiseman, and J.F. Thompson, editors, *Numerical Grid Generation in Computational Fluid Dynamics and Related Fields*. Elsevier Science Publishers B.V., 1991.
51. M.-C. Le Pape, O.-P. Jacquotte, and Ph. Guillen. A 3D Structured Multiblock Mesh Adaptation Method using a Variational Principle. In *to appear in Notes on Numerical Fluid Mechanics, in progress*, Vieweg, 1996.
52. A.K. Poortman. Evaluation and Extension of a Grid Adaptation Algorithm in a 2D Flow Simulation Code. Technical Report Memorandum M-750, Department of Aerospace Engineering, Delft University of Technology, 1996.
53. M.H. Protter and H.F. Weinberger. *Maximum Principles in Differential Equations*. Prentice Hall, Englewood Cliffs N.J., 1967.
54. D. Rozendal. Natural Laminar Flow Experiments on a 17.4 % Thick Airfoil in the NLR High Speed Wind Tunnel. Technical Report NLR CR 91328 L, National Aerospace Laboratory NLR, The Netherlands, 1991.
55. V. Schmitt and F. Charpin. *Experimental Data Base for Computer Program Assessment*, volume AGARD-AR-138. Advisory Group for Aerospace Research & Development, Neuilly-sur-Seine, France, 1979.
56. F. Schulz. *Regularity Theory for Quasilinear Elliptic Systems and Monge-Ampère Equations in Two Dimensions*, volume 1445. Springer Lecture Notes, 1990.
57. J.W. Slater, M.S. Liou, and R.G. Hindman. An Approach for Dynamic Grids. In *AIAA-94-0319*, Reno, Nevada, January 10-13 1994.

58. B.K. Soni and J.C. Yang. General Purpose Adaptive Grid Generation System. In *AIAA-92-0664*, Reno, Nevada, January 6-9 1992.
59. S.P. Spekreijse. Elliptic Grid Generation Based on Laplace Equations and Algebraic Transformations. *Journal of Computational Physics*, 118:38–61, 1995.
60. S.P. Spekreijse, R. Hagmeijer, and J.W. Boerstoel. Adaptive Grid Generation by using the Laplace-Beltrami Operator on a Monitor Surface. In *5th International Conference on Numerical Grid Generation in Computational Fluid Dynamics and Related Fields*, Starkville, Mississippi, April 1-5 1996.
61. E. Süli. The Accuracy of Cell Vertex Finite Volume Methods on Quadrilateral Meshes. *Mathematics of Computation*, 59(200):359–382, 1992.
62. J.F. Thompson. A Survey of Dynamically-Adaptive grids in the Numerical Solution of Partial Differential Equations. In *AIAA-84-1606*, Snowmass, Colorado, June 25-27 1984.
63. J.F. Thompson. A General Three-Dimensional Elliptic Grid Generation System on a Composite Block Structure. *Computer Methods in Applied Mechanics and Engineering*, 64:377, 1987.
64. J.F. Thompson and C.W. Mastin. Order of Difference Expressions in Curvilinear Coordinate Systems. *Journal of Fluids Engineering*, 107:241–250, 1985.
65. J.F. Thompson, Z.U.A. Warsi, and C.W. Mastin. *Numerical Grid Generation: Foundations and Applications*. North-Holland, Elsevier, New York, 1985.
66. J.F. Thompson and N.P. Weatherill. Aspects of Numerical Grid Generation: Current Science and Art. In *AIAA-93-3539-CP*, 1993.
67. Y. Tu and J.F. Thompson. Three-Dimensional Solution-Adaptive Grid Generation on Composite Configurations. *AIAA Journal*, 29(12):2025–2026, 1991.
68. E. Turkel, S. Yaniv, and U. Landau. Accuracy of Schemes for the Euler Equations with Non-Uniform Meshes. Technical Report 85-59, Institute for Computer Applications in Science and Engineering, 1985.
69. J.J.W. van der Vegt. Anisotropic Grid Refinement using an Unstructured Discontinuous Galerkin Method for the Three-Dimensional Euler Equations of Gas Dynamics. Technical Report TP 95235 U, National Aerospace Laboratory NLR, 1995.
70. J.J.W. van der Vegt and H. van der Ven. Hexahedron Based Grid Adaptation for Future Large Eddy Simulation. Technical Report TP 95514 U, National Aerospace Laboratory NLR, 1995.
71. H. van der Ven and J.J.W. van der Vegt. Experiences with Advanced CFD Algorithms on NEC SX-4. Technical Report TP 96575 L, National Aerospace Laboratory NLR, 1996.
72. Z.U.A. Warsi and J.F. Thompson. Application of Variational Methods in the Fixed and Adaptive Grid Generation. *Computers Math. Applic.*, 19(8/9):31–41, 1990.
73. P. Wesseling. *An Introduction to Multigrid Methods*. John Wiley and Sons, 1992.

74. A. Winslow. *Adaptive Mesh Zoning by the Equipotential Method.* UCID-19062, Lawrence Livermore National Laboratories, 1981.

75. D.M. Young. *Iterative Solution of Large Linear Systems.* Academic Press, New York and London, 1971.